



Comprendre le monde,  
construire l'avenir®



UNIVERSITÉ PARIS-SUD

ÉCOLE DOCTORALE : Ondes et Matière

Laboratoire Charles Fabry,

Institut d'Optique Graduate School

*DISCIPLINE : PHYSIQUE*

**THÈSE DE DOCTORAT**

soutenue le 18/12/2012

par

**Marie PIRAUD**

Localisation d'Anderson d'ondes de matière  
dans un désordre corrélé : de 1D à 3D

Anderson localization of matter waves in correlated disorder:  
from 1D to 3D.

**Composition du jury :**

<i>Directeur de thèse :</i>	Laurent SANCHEZ-PALENCIA
<i>Rapporteurs :</i>	Bart VAN TIGGELEN Patrizia VIGNOLO
<i>Examineurs :</i>	Robin KAISER Gilles MONTAMBAUX Georgy SHLYAPNIKOV
<i>Membre invité :</i>	Alain ASPECT



---

# Remerciements

Les travaux de thèse présentés dans ce manuscrit ont été effectués au laboratoire Charles Fabry à Palaiseau (France). Ce laboratoire est une unité mixte de recherche de l'Université Paris-Sud et du CNRS. Ils ont été financés par l'École Normale Supérieure de Cachan puis par un contrat doctoral de l'Université Paris-Sud (issu d'une Allocation Spécifique), ainsi qu'un monitorat à l'Institut d'Optique *Graduate School*.

Je tiens tout d'abord à remercier très sincèrement Laurent SANCHEZ-PALENCIA pour avoir dirigé cette thèse. Il me semble que son encadrement a été parfaitement adapté. Tout en guidant mon travail, j'ai toujours senti que Laurent me faisait confiance. Il a toujours été disponible pour répondre aussi bien à mes questions qu'à mes doutes, et a été attentif à me procurer un bon environnement de travail et à me former aux différentes activités d'un chercheur, notamment en me permettant d'aller à plusieurs écoles d'été et conférences. Je lui suis simplement reconnaissante d'avoir fait en sorte que cette thèse se déroule dans les meilleures conditions possibles, et j'espère que le résultat a été à la hauteur de ses espérances. Au cours de cette thèse nous avons travaillé avec Luca PEZZÉ. Luca est autant sympathique que compétent et efficace, ça a été très agréable ; je le remercie donc énormément.

Ce travail a donné lieu à une collaboration fructueuse avec des expérimentateurs du groupe. Je remercie Alain ASPECT, qui a mené ce projet avec beaucoup d'intérêt, qui nous transmet sa passion pour la physique et ses connaissances, et qui accepte aussi de jouer le rôle de conseiller en ressources humaines par moments. Je remercie Philippe BOUYER et Vincent JOSSE pour ce projet commun, ainsi que les acteurs de l'équipe « Pince » : Fred JENDRZEJEWSKI, Kilian MULLER, Alain BERNARD et Patrick CHEINET. Pendant plusieurs mois nous avons partagé espoirs, déceptions, doutes et joies. Merci de votre implication, et d'avoir le courage et la patience de réaliser des expériences aussi pointues !

Je remercie Patrizia VIGNOLO et Bart VAN TIGGELEN qui ont gentiment accepté d'être mes rapporteurs. Merci de l'intérêt que vous portez à notre travail et d'avoir lu avec attention ce manuscrit. Je remercie Gilles MONTAMBAUX, Gora SHLYAPNIKOV et Robin KAISER d'avoir accepté de faire partie de mon jury de thèse. Merci à tous pour les discussions que nous avons eues.

Je remercie Pierre CHAVEL et Christian CHARDONNET, les directeurs successifs du laboratoire, qui sont attentifs au bien-être de chacun et plus particulièrement des doctorants.

Je remercie toutes les personnes avec qui nous avons discuté de notre travail. Je pense en particulier à Bart VAN TIGGELEN et Peter WOELFLE, qui nous ont éclairés sur plusieurs points théoriques, et à Pierre CHAVEL, Jean-Jacques GREFFET et David CLÉMENT que nous avons consultés pour des questions pointues d'optique.

Je remercie les membres du groupe de théorie : Laurent, Luca, Pierre LUGAN et Ben HAMBRECHT, qui m'ont accueillie avec enthousiasme, puis le groupe a été rejoint par Tung-Lam DAO, Thomas KOFFEL, Samuel LELLOUCH, Giuseppe CARLEO, Guilhem BOERIS et

Lih-King LIM. Nous avons partagé de nombreux repas à la cantine et pauses café et parfois un bureau. Merci à tous pour votre bonne humeur car l'ambiance a toujours été fort sympathique. Merci en particulier à Pierre pour m'avoir convaincue de venir, à Ben et Lam pour leurs nombreux coups de pouces avec Ubuntu, et à Giuseppe et Guilhem pour leurs conseils en gastronomie italienne.

Je remercie Thibaut JACQMIN, Baptiste ALLARD, Thomas PLISSON, Fred JENDRZEJEWSKI et Vincent MÉNORET, les thésards de mon année avec qui nous avons beaucoup partagé, écoles d'été, sorties sympas et séances de sport notamment. Merci à Raphael LOPES et Josselin RUAUDEL qui ont accepté de m'aider à organiser les « Journées des DOCTORANTS d'Atomes Froids ». Et merci à tous les autres membres passés et actuels du groupe d'optique atomique et du labo. La liste des personnes avec qui j'ai passé de bons moments ou qui m'ont donné des coups de main durant cette thèse serait beaucoup trop longue.

Je remercie les membres du service info de l'Institut : Laurent LECLERC, Gilbert LUCAS et Loïc BLOT qui ont toujours répondu présents pour nous aider à résoudre nos problèmes. Je remercie les administrateurs de la GMPCS-Lumat : Georges RASEEV et Philippe DOS SANTOS, ainsi que Mondher BESBES pour leur aide patiente à propos de ce cluster. Je remercie aussi tous les membres de l'administration de l'Institut qui s'arrange toujours pour répondre à nos demandes, même dans l'urgence.

Enfin, j'ai eu l'occasion d'enseigner à l'Institut d'Optique avec des gens passionnés et très compétents. Je remercie notamment Lionel JACUBOWIEZ, François BALEMBOIS, François MARQUIER, Karen PERRONET, Delphine SACCHET, Louis DANIAULT, Xavier DÉLEN, et Loïc DEYRAT, ainsi que Thierry AVIGNON et Cédric LEJEUNE qui font un travail formidable au service des TPs.

# Contents

<b>Introduction</b>	<b>9</b>
<b>1 Waves in disorder: from condensed matter to ultra-cold atoms</b>	<b>15</b>
1.1 From condensed matter systems to waves in disordered media . . . . .	17
1.1.1 Disorder in solids . . . . .	17
1.1.2 Link with other waves . . . . .	18
1.1.3 Models of disordered systems . . . . .	19
1.2 Wave transport and Anderson localization . . . . .	21
1.2.1 Waves, coherence and randomness . . . . .	22
1.2.2 Scaling theory of localization . . . . .	27
1.2.3 Anderson localization in correlated disorder . . . . .	29
1.2.4 Disorder and interactions . . . . .	30
1.3 Ultra-cold atoms in disorder . . . . .	31
1.3.1 Quantum simulators/ assets . . . . .	32
1.3.2 Controlled Disorder . . . . .	33
1.3.3 State of the art . . . . .	34
<b>2 Quantum transport theory</b>	<b>37</b>
2.1 Green functions . . . . .	41
2.2 Properties of the disordered medium . . . . .	42
2.3 Propagation of the Wigner function . . . . .	45
2.4 Conductivity and Einstein relation . . . . .	48
<b>3 Speckle Potentials: A model of controlled disorder</b>	<b>51</b>
3.1 Introduction to speckle theory . . . . .	54
3.1.1 Realization of a speckle pattern . . . . .	54
3.1.2 Statistical properties . . . . .	55
3.2 Standard examples . . . . .	58
3.2.1 Uniformly illuminated apertures . . . . .	59
3.2.2 Gaussian laser beam shone onto infinite plate . . . . .	62
3.2.3 Further considerations . . . . .	62
3.3 Numerical implementation . . . . .	63
<b>4 Localization in one-dimensional speckle potentials</b>	<b>65</b>
4.1 Anderson localization of a single energy component in 1D speckle . . . . .	68
4.1.1 Phase formalism . . . . .	68
4.1.2 Transfer matrix calculations . . . . .	69

4.2	Expansion of a wave packet . . . . .	71
4.2.1	A typical ultra-cold atom experiment . . . . .	71
4.2.2	Theoretical model . . . . .	72
4.2.3	Fundamental quantities . . . . .	74
4.2.4	Numerical simulations . . . . .	77
<b>5</b>	<b>Transport and Anderson localization in anisotropic disorder</b>	<b>83</b>
5.1	Single-scattering . . . . .	86
5.1.1	Scattering mean-free time . . . . .	86
5.1.2	Anisotropic Gaussian speckle (2D) . . . . .	86
5.2	Boltzmann diffusion . . . . .	90
5.2.1	Solution of the Bethe-Salpeter equation . . . . .	90
5.2.2	Anisotropic Gaussian speckle (2D) . . . . .	92
5.3	Weak and strong localization . . . . .	96
5.3.1	Weak localization correction . . . . .	96
5.3.2	Strong localization . . . . .	98
5.3.3	Anisotropic Gaussian speckle (2D) . . . . .	99
<b>6</b>	<b>Localization in 3D disorder with structured correlations</b>	<b>103</b>
6.1	Speckle correlation functions in three dimensions . . . . .	105
6.1.1	Single speckle (3D) . . . . .	105
6.1.2	Orthogonally crossed speckles (3D) . . . . .	107
6.2	On-shell predictions . . . . .	107
6.2.1	Single-scattering . . . . .	108
6.2.2	Boltzmann diffusion . . . . .	111
6.2.3	Localization . . . . .	115
6.3	About the 3D mobility edge . . . . .	117
6.3.1	Method . . . . .	117
6.3.2	Three-dimensional isotropic speckle . . . . .	118
6.3.3	3D speckle with structured correlations . . . . .	119
<b>7</b>	<b>Matterwaves in 3D speckle potentials: experiment vs theory</b>	<b>123</b>
7.1	Urbana-Champaign experiment . . . . .	126
7.2	Palaiseau experiment . . . . .	128
7.2.1	Two-component density profiles . . . . .	129
7.2.2	Evidence of Anderson localization? . . . . .	134
<b>8</b>	<b>Tailoring Anderson localization by disorder correlations</b>	<b>139</b>
8.1	Tailoring correlations in speckle potentials . . . . .	142
8.2	One-dimensional speckle . . . . .	142
8.2.1	Tailored correlations in 1D speckle potentials . . . . .	142
8.2.2	Anderson localization in 1D tailored speckle potentials . . . . .	143
8.2.3	Observation schemes with ultracold atoms . . . . .	147
8.3	Higher dimensions . . . . .	151
	<b>Conclusion</b>	<b>155</b>

<b>A</b>	<b>Tools for Lyapunov exponents calculations in 1D</b>	<b>161</b>
A.1	Third order of the phase-formalism . . . . .	161
A.2	Transfer matrix calculations . . . . .	162
<b>B</b>	<b>Probability of quantum transport in 1D</b>	<b>165</b>
B.1	Introduction . . . . .	165
B.2	Diagrammatic technique and selection of diagrams . . . . .	166
B.3	Basic equations on the diagrams . . . . .	169
B.4	Solution of the equations . . . . .	172
<b>C</b>	<b>Quantum transport in <math>d \geq 2</math>: Tools and technical calculations</b>	<b>175</b>
C.1	Intensity kernel . . . . .	175
C.2	Isotropic disorder . . . . .	179
C.2.1	Two-dimensional case . . . . .	179
C.2.2	Three-dimensional case . . . . .	179
C.3	Conductivity . . . . .	180
C.3.1	Einstein relation . . . . .	180
C.3.2	Current vertex renormalization . . . . .	181
C.3.3	Weak-localization correction . . . . .	181
<b>D</b>	<b>Speckle potentials: 3D correlations in various configurations</b>	<b>183</b>
D.1	Single-speckle . . . . .	183
D.2	Orthogonally-crossed speckles . . . . .	185
D.2.1	Orthogonal incoherent-speckles . . . . .	185
D.2.2	Orthogonal coherent-speckles . . . . .	186
D.3	Parallel speckles . . . . .	187
D.3.1	Single shifted speckle . . . . .	187
D.3.2	Parallel incoherent-speckles . . . . .	188
D.3.3	Parallel coherent-speckles . . . . .	188
<b>E</b>	<b>Complementary models of 3D disorder correlations</b>	<b>191</b>
E.1	Three-dimensional isotropic speckle . . . . .	191
E.2	Anisotropic Gaussian correlation function (3D) . . . . .	192



# Introduction

'More is different'. By this concise statement [1], Philip W. Anderson pointed out that when confronted to a change of scale, the behaviour of a large and complex system might not always be simply extrapolated from the simple behaviour of its small scale components. When adding more complexity or more elements to a system, its behaviour might change in nature: it undergoes a phase transition.

In particular, in 1958 [2], Anderson has predicted that a large piece of disordered material can be an insulator, even when its elementary blocks have a metallic behaviour. The prediction of this effect, which is known as Anderson localization, started a new field of physics, which has attracted considerable attention. It started with the study of condensed matter systems [3,4], and later played an important role in classical waves physics, in particular in the field of optically-dense media [5,6]. However, Anderson localization of quantum waves has remained unobserved for a long time. The development of ultra-cold atoms revived those studies, and, following theoretical proposals [7,8], Anderson localization of ultra-cold matter waves has been finally observed in one dimension (1D) [9,10]. These results have actually opened a new field of research in disordered quantum systems [11–13]. It has stimulated numerous studies, with a view towards observing localization of matter waves in dimensions higher than one, studying its interplay with interactions, and its role in disordered spin systems for example. In this respect, quantum gases stimulate intensive experimental and theoretical research, and produced landmark results in the very last years. On one hand, they offer unprecedented control of their parameters, and novel measurement tools. On the other hand, they sustain original effects, which require special analysis in their own right.

In particular, among the specificities of disordered quantum gases, are the special statistical correlations of the disorder. In spite of the universal character of Anderson localization, disorder correlations can affect its macroscopic behaviour. This basic question is relevant for ultra-cold atomic systems, for their disorder correlations are well-characterized. Direct comparison between theory and experiment is then possible, and cannot be limited to a qualitative description. Indeed, correlations can have interesting effects. For instance they induce effective mobility edges in 1D [14,15], and they can lead to a divergence of the disorder power spectrum and the absence of a white-noise limit in three-dimensional (3D) isotropic models [16]. And yet, at the beginning of this thesis, the effects of correlations were largely unexplored. On one hand, correlations can be anisotropic in dimensions  $d > 1$ , for practical reasons [17–19]. On the other hand, structured correlations can be shaped (almost) at will, by simple optical means [13,20,21]. These are the topics addressed during this thesis.

In this manuscript, we present a theoretical study of quantum transport and Anderson localization of non-interacting matterwaves in correlated disorder in 1D, 2D and 3D. We focus on the microscopic details of the disorder, and on the effect of the statistical, possibly

anisotropic, correlations of a continuous disorder. While the theoretical developments are general, we apply them to speckle potentials, for the reasons explained above. My thesis may be somehow arbitrarily divided into three stages. First, stimulated by the recent observation of Anderson localization in Bose-Einstein condensates expanding in speckle potentials, Laurent and I first worked on one-dimensional Anderson localization and we developed a new model, which may explain some discrepancy between experimental data and a simplified model [22]. Second, we then turned to the study of quantum transport and Anderson localization in dimensions higher than one, with special emphasis on anisotropy effects, which are important in experiments with ultra-cold atoms. As Luca Pezzè had already worked on classical diffusion in 2D anisotropic speckle potentials [23], we worked together on this project. We eventually predicted interesting effects, such as the anisotropic suppression of the white-noise limit, reversed anisotropies between the scattering and transport times and inversion of the transport anisotropy with energy [24]. Our study turned out to come in very timely, as two experiments reported important evidence of Anderson localization in 3D [18, 19] where correlated disorder in different configurations is used. We collaborated with the experimental team of Vincent Josse and Alain Aspect at Institut d'Optique on Ref. [19]. This collaboration actually stimulated further theoretical work and we proposed a new method to compute the mobility edge, which on one hand is of clear physical meaning, and on the other hand is applicable in practice to disorder with structured correlations [25]. Third, we further studied the effect of disorder correlations, and predicted the enhancement of Anderson localization with the particle energy induced by tailored correlations in any dimension [26, 27].

The manuscript reviews these results, along the following lines:

Chapter 1: We start with an introductory chapter in which we present the concept of Anderson localization. We explain how it has spread from condensed matter to optics and many other fields, and recently to ultra-cold atoms. We introduce a few of the contemporary lines of research, such as the interplay between disorder and inter-particle interaction and the role of disorder correlations.

Chapter 2: In the second chapter we introduce the basics of quantum transport and Anderson localization of matterwaves in disordered media. We first present the general ideas in a simple picture. We then bring in formal tools that are necessary for such a study. The presentation is adapted to anisotropic disorder, which significantly complicates the theory as we will see. We however always discuss the physical meaning of the important quantities and make the connection with the simple picture.

Chapter 3: We then introduce speckle potentials, as a model of controlled disorder, which is used in ultra-cold atom experiments. We explain how speckle patterns are obtained, and compute their statistical properties, which are quite uncommon (they are non-Gaussian and non-symmetric). In particular their correlations are naturally anisotropic (in dimensions  $d > 1$ ), and can be easily modified, a property that we will use in the following.

Chapter 4: We study Anderson localization in one dimension. In 1D all single-particle states are predicted to be localized, however, it does not say it all, as is for example shown in Ref. [9]. Despite an overall agreement with the theoretical predictions of Ref. [8], in the experiments non-negligible deviations are observed [9, 28]. We have developed a new model for the localization of a wave-packet which includes ingredients that had been previously disregarded. Our results indicate that the deviations can be explained by a crossover towards a long-distance behaviour, which is different than the one predicted at short-distance.

Chapter 5: We then study quantum transport and Anderson localization in dimensions higher than one. We theoretically investigate the transport of a quantum wave in anisotropic, correlated disorder. We derive general expressions for scattering, Boltzmann diffusion and Anderson localization, whose properties are described by tensors. We then apply them to a model of 2D speckle with an anisotropic Gaussian correlation function, in which we find interesting and counter-intuitive anisotropy effects, such as a transport anisotropy different than that of the disorder, and a non-monotonous behaviour of the transport anisotropy with energy.

Chapter 6: We also study three-dimensional disorder with structured, anisotropic correlations. On one hand, in three specific models of speckle potentials we find rich transport properties, such as anisotropic suppression of the white-noise limit and inversion of the transport anisotropy. On the other hand, we focus on the localization energy threshold which separates the localized and the extended states in 3D, and we propose a new method to estimate its position, which includes a disorder-induced energy shift. It has the advantage of being easily interpretable and of being applicable to models of disorder with fine-structured correlations.

Chapter 7: The models of disorder studied in Chap. 6 are directly relevant to the experimental results reported in Refs. [18, 19]. We discuss those experiments in view of our theoretical predictions. Concerning Ref. [18] we focus on comparable quantities, which are the anisotropy of the localized profile, and the position of the mobility edge. As discussed herein, the discrepancy between experimental data and theoretical calculations opens questions, which should stimulate further experimental and theoretical work. Concerning Ref. [19] we detail the analysis of the experiment, in which we have been involved, where we found a semi-quantitative agreement. The comparison sheds new light on the problem, which on one hand stimulated our work reported in Chap. 6, and on the other hand opens new experimental perspectives.

Chapter 8: We further exploit the fact that speckle correlations are very well controlled and that they can be tailored in a broad range of configurations. We show that, due to disorder correlations, Anderson localization can be enhanced when the energy of the particle increases in continuous disorder. We illustrate this on specific examples in 1D, 2D and 3D, and argue that this effect could serve to discriminate quantum versus classical localization.

In the conclusion, we summarize the results obtained during this thesis, and give an outlook on how the methods exposed here could be extended.

## Version française

« More is different ». Par cette courte affirmation [1], Philip W. Anderson a mis en évidence que lors d'un changement d'échelle, le comportement d'un grand système complexe ne peut pas toujours être simplement déduit du comportement plus simple de ses composants à petite échelle. En rajoutant plus de complexité ou plus d'éléments à un système, son comportement peut changer de nature : il subit une transition de phase.

En particulier, en 1958 [2], Anderson a prédit qu'un grand morceau de matériau désordonné peut être isolant, même lorsque les blocs élémentaires qui le composent ont un comportement métallique. La prédiction de cet effet, connu sous le nom de localisation d'Anderson, a ouvert un nouveau domaine de la physique, qui a attiré une attention considérable. Cela a commencé par l'étude de systèmes pertinents pour la matière condensée [3, 4], et a plus tard joué un rôle important en physique des ondes classiques, en particulier dans le domaine des milieux optiques denses [5, 6]. Cependant, la localisation d'Anderson d'ondes quantiques est longtemps restée inobservée. Le développement des atomes ultrafroids a ravivé ces études, et, en suivant des propositions théoriques [7, 8], la localisation d'Anderson d'ondes de matière a finalement été observée à une dimension (1D) [9, 10]. Ces résultats ont en fait ouvert un nouveau champ de recherche concernant les systèmes quantiques désordonnés [11–13]. Cela a stimulé de nombreuses études, dans le but d'observer la localisation d'ondes de matière en dimensions supérieures à un, d'étudier comment elle se combine avec les interactions, et son rôle dans les systèmes de spins désordonnés par exemple. A cet égard, les gaz quantiques ont stimulé un intense travail de recherche expérimental et théorique, qui a conduit à des résultats marquants ces dernières années. D'une part, ils offrent un contrôle sans précédent des paramètres et de nouveaux outils de mesure. D'autre part, ils donnent lieu à des effets originaux, qui nécessitent une analyse particulière en eux-mêmes.

En particulier, parmi les spécificités des gaz quantiques désordonnés, il y a les propriétés de corrélations statistiques particulières du désordre. Malgré le caractère universel de la localisation d'Anderson, les corrélations du désordre peuvent avoir une influence sur son comportement macroscopique. Cette question fondamentale est pertinente pour les systèmes d'atomes ultrafroids, car leurs corrélations sont bien caractérisées. Une comparaison directe entre l'expérience et la théorie est alors possible, et ne peut pas se limiter à une comparaison qualitative. En effet, les corrélations peuvent avoir des effets très intéressants. Par exemple elles induisent des seuils de mobilité effectifs en 1D [14, 15], et elles peuvent mener à une divergence du spectre de puissance du désordre et à l'absence d'une limite de bruit-blanc dans des modèles isotropes à trois dimensions (3D) [16]. Et pourtant, au début de cette thèse, les effets des corrélations restaient encore largement inexplorés. D'une part, les corrélations peuvent être anisotropes en dimension  $d > 1$ , pour des raisons techniques [17–19]. D'autre part, des corrélations structurées peuvent être façonnées (presque) à souhait, par des méthodes optiques simples [13, 20, 21]. Tels sont les sujets qui ont été abordés au cours de cette thèse.

Dans ce manuscrit nous présentons une étude théorique du transport quantique et de la localisation d'Anderson d'ondes de matière sans interaction dans des modèles de désordre corrélés à 1D, 2D et 3D. Nous nous concentrons sur les détails microscopiques du désordre, et sur l'effet des corrélations statistiques, éventuellement anisotropes, d'un désordre continu. Alors que les développements théoriques sont généraux, nous les appliquons à des potentiels de speckle, pour les raisons soulignées ci-dessus. De façon un peu arbitraire, ma thèse peut être

séparée en trois étapes. Premièrement, stimulés par la récente observation de la localisation d'Anderson dans des condensats de Bose-Einstein en expansion dans des potentiels de speckle, Laurent et moi avons tout d'abord travaillé sur la localisation d'Anderson unidimensionnelle, et nous avons développé un nouveau modèle qui peut expliquer certains écarts entre les données expérimentales et un modèle plus simple [22]. Deuxièmement, nous nous sommes tournés vers l'étude du transport quantique et de la localisation d'Anderson en dimensions supérieures à un, en mettant particulièrement l'accent sur les effets d'anisotropie, qui sont importants pour les expériences avec des atomes ultrafroids. Comme Luca Pezzè avait déjà travaillé sur la diffusion classique dans des potentiels de speckle anisotropes 2D [23], nous avons travaillé ensemble sur ce projet. Nous avons finalement prédit des effets intéressants, tels que la suppression anisotrope de la limite de bruit blanc, des anisotropies des événements de diffusion et de transport opposées, et une inversion de l'anisotropie de transport avec l'énergie [24]. Notre étude s'est révélée être très opportune, car deux expériences apportaient justement des preuves de localisation d'Anderson à 3D [18, 19] pour lesquelles des désordres corrélés dans différentes configurations ont été utilisés. Nous avons collaboré avec l'équipe expérimentale de Vincent Josse et Alain Aspect à l'Institut d'Optique sur la Réf. [19]. Cette collaboration nous a stimulés à approfondir notre travail théorique et nous avons proposé une nouvelle méthode pour calculer le seuil de mobilité, qui, d'une part, a un sens physique clair, et d'autre part, est applicable en pratique aux modèles de désordre ayant des corrélations structurées [25]. Troisièmement, nous avons approfondi l'étude des effets des corrélations du désordre, et nous avons prédit l'accroissement de la localisation d'Anderson induit par des corrélations du désordre judicieusement adaptées, en toute dimensionnalité [26, 27].

Le manuscrit détaille ces résultats, selon le plan suivant :

Chapitre 1 : Nous commençons par un chapitre introductif dans lequel nous présentons le concept de la localisation d'Anderson. Nous expliquons comment il s'est répandu de la matière condensée à l'optique et de nombreux autres domaines, et récemment aux atomes ultrafroids. Nous introduisons quelques unes des lignes de recherches actuelles, telles que les effets combinés du désordre et des interactions inter-particules, ainsi que le rôle des corrélations du désordre.

Chapitre 2 : Dans le second chapitre nous introduisons les bases du transport quantique et de la localisation d'ondes de matière en milieu désordonné. Nous présentons d'abord les idées générales grâce à une image simple. Nous décrivons ensuite les outils formels qui sont nécessaires pour une telle étude. La présentation est adaptée aux désordres anisotropes, ce qui complique significativement la théorie comme nous allons le voir. Nous discutons cependant le sens physique des principales quantités et nous faisons le lien avec l'image simple.

Chapitre 3 : Nous introduisons ensuite les potentiels de tavelures optiques (« speckle »), comme un modèle de désordre contrôlé, qui est utilisé dans les expériences d'atomes ultrafroids. Nous expliquons comment on obtient des motifs de speckle, et nous calculons leurs principales propriétés statistiques, qui sont peu communes (ces potentiels sont non-gaussiens et non-symétriques). En particulier leurs corrélations sont naturellement anisotropes (en dimension  $d > 1$ ), et peuvent être facilement modifiées, une propriété que nous utiliserons dans la suite.

Chapitre 4 : Nous étudions la localisation d'Anderson à une dimension. A 1D tous les états à une particule doivent être localisés, cependant, comme cela est par exemple montré dans la Réf. [9], la localisation peut avoir un comportement complexe. Malgré un bon accord général

avec les prédictions théoriques de la Réf. [8], des déviations non-négligeables sont observées dans les expériences [9, 28]. Nous avons développé un nouveau modèle pour la localisation d'un paquet d'onde de matière qui inclut des ingrédients qui ont été négligés précédemment. Nos résultats indiquent que les déviations peuvent être expliquées par un crossover vers un comportement à longue-distance qui est différent de celui prédit à courte distance.

Chapitre 5 : Nous étudions ensuite le transport quantique et la localisation d'Anderson en dimensions supérieures à un. Nous examinons théoriquement le transport d'une onde quantique dans un désordre anisotrope et corrélé. Nous dérivons des expressions générales pour chaque événement de diffusion, la diffusion de Boltzmann et la localisation d'Anderson, dont les propriétés sont décrites par des tenseurs. Nous les appliquons ensuite à un modèle de speckle 2D ayant une fonction de corrélation gaussienne et anisotrope, pour lequel on trouve des effets d'anisotropie intéressants et contre-intuitifs, tels qu'une anisotropie de transport différente de celle du désordre, et un comportement non-monotone de l'anisotropie de transport avec l'énergie.

Chapitre 6 : Nous étudions aussi les désordres tridimensionnels ayant des corrélations structurées et anisotropes. D'une part, pour trois modèles particuliers de désordre nous trouvons de riches propriétés de transport, telles que la suppression anisotrope de la limite de bruit blanc et l'inversion de l'anisotropie de transport. D'autre part, nous nous concentrons sur le seuil de localisation qui sépare en énergie les états localisés et étendus à 3D, et nous proposons une nouvelle méthode pour estimer sa position, qui revient à une renormalisation auto-cohérente des énergies. Elle a l'avantage d'être facilement interprétable et d'être applicable à des modèles de désordre aux corrélations finement structurées.

Chapitre 7 : Les modèles de désordre étudiés dans le Chap. 6 sont directement pertinents pour les résultats expérimentaux présentés dans les Réfs. [18, 19]. Nous examinons ces expériences à la lumière de nos prédictions théoriques. En ce qui concerne la Réf. [18], nous nous focalisons sur les quantités comparables que sont l'anisotropie du profil localisé et la position du mobility edge. Comme cela est discuté dans ce chapitre, l'écart entre les données expérimentales et les calculs théoriques ouvre des questions qui devrait stimuler un approfondissement des travaux expérimentaux et théoriques. En ce qui concerne la Réf. [19], nous détaillons l'analyse de l'expérience, à laquelle nous avons pris part, et dans laquelle nous avons trouvé un accord semi-quantitatif. La comparaison donne un éclairage nouveau au problème, qui d'une part a stimulé le travail décrit dans le Chap. 6, et d'autre part ouvre de nouvelles perspectives expérimentales.

Chapitre 8 : Nous exploitons encore le fait que les corrélations des speckles sont très bien contrôlées et qu'elles peuvent être modifiées dans une large gamme de configurations. Nous montrons que, grâce aux corrélations du désordre, la localisation d'Anderson peut être accrue lorsque l'énergie de la particule augmente, dans un désordre continu. Nous illustrons cela grâce à des exemples précis à 1D, 2D et 3D, et nous argumentons que cet effet pourrait servir à distinguer localisation quantique et localisation classique.

Dans la conclusion nous résumons les résultats obtenus au cours de cette thèse, et nous donnons des perspectives visant à étendre les méthodes présentées ici.

# Chapter 1

## Waves in disorder: from condensed matter to ultra-cold atoms

### Abstract

The transport properties of a coherent wave in a disordered medium are inherently determined by interference of multiple scattering paths, which can lead to spatial localization and absence of diffusion. This effect, known as Anderson localization, was first predicted for electrons in disordered crystals and then extended to classical waves, which permitted its observation in a variety of systems. The most fundamental features of Anderson localization are therefore ubiquity and universality. However, observable features can depend on the details of the system. Here we make an introduction to weak and strong localization effects. We introduce background concepts, such as the scaling theory of localization, and briefly discuss interplay between disorder and interactions, and we show that correlated disorder can significantly alter usual features of Anderson localization. The recent advent of ultra-cold atomic systems, which are under great experimental control is reviewed. They offer new possibilities to study those problems.

### Résumé

Les propriétés de transport d'une onde cohérente en milieu désordonné sont déterminées par l'interférence des chemins de diffusion multiple, ce qui mène à la localisation spatiale et à l'absence de diffusion dans le milieu. Ce phénomène, connu sous le nom de localisation d'Anderson, a d'abord été prédit pour des électrons dans des cristaux désordonnés, avant d'être étendu au cas des ondes classiques, ce qui a permis son observation dans différents systèmes. Les caractéristiques les plus fondamentales de la localisation d'Anderson sont donc l'ubiquité et l'universalité. Cependant, ses caractéristiques observables peuvent dépendre des détails du système. Ici, nous présentons les effets de localisation faible et forte. Nous introduisons aussi des concepts de base, comme la théorie de scaling de la localisation, nous discutons brièvement comment désordre et interactions peuvent se combiner, et nous montrons que les corrélations du désordre peuvent modifier significativement les caractéristiques usuelles de la

localisation d'Anderson. L'avènement récent des systèmes d'atomes ultrafroids, qui sont très bien contrôlés expérimentalement, est passé en revue. Ils offrent de nouvelles possibilités pour étudier ces problèmes.

## Introduction

Disorder is always present at the microscopic scale in natural media, it is for example the result of inhomogeneities or impurities. Hence, by definition, each piece of matter is different, and should be modeled differently. Disorder is therefore usually viewed as non-desirable, and may be neglected in order to deal with generic models. This approach is often successful in describing macroscopic behaviour, and the microscopic disorder is then seen as a source of uncertainty in the results of physical measurements. However, it is now well-known that disorder can have dramatic effects at the macroscopic scale, in some cases. An emblematic and fascinating example is Anderson localization, in which weak disorder can turn a piece of metal into an insulator (at least in low dimension).

The concept of localization of particles by disorder has been introduced by Anderson in 1958 for electrons in solids [2]. It was later realized that it results from a subtle interference effect that concerns all types of coherent waves propagating in a random medium [11]. The concept has therefore spread to many other fields of physics: electromagnetic [29], optical [5,6], acoustic [30] and seismic [31] waves, but also disordered superconductors [32] and superfluid Helium in porous media [33], where it has been studied both theoretically and experimentally. As we will see, this problem is also very interesting to study with ultra-cold atoms, for the parameters of those systems are very well controlled. While the first examples concern classical waves, the three latter concern quantum waves (electrons, Helium atoms and ultracold atoms), which can be interacting. Depending on the situation, disorder and interactions can compete or cooperate for localization, and their interplay is a difficult and interesting problem. For studying localization, it is important to understand the non-interacting problem, which has been studied a lot in optics [5,6] and more recently in acoustics [30]. Then one has to consider the role of interactions. The recent development of ultracold atomic gases is a great asset to study both problems [12, 13, 21]: They make very manipulable matterwave systems with tunable interactions and to which controlled disorder can be applied.

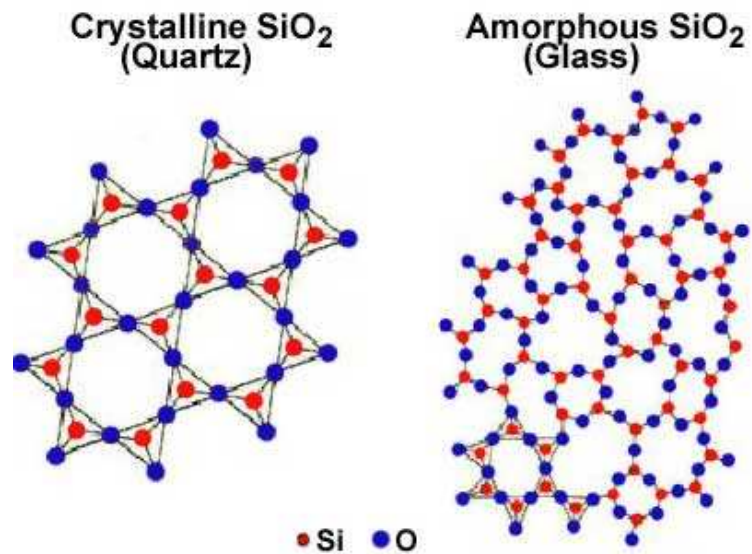
In this thesis, we focus on Anderson localization in noninteracting systems. The aim of this chapter is to review the above concepts, mainly about Anderson localization and briefly about the role of interactions. We first describe the link between disordered condensed matter systems and other types of waves in random media, in Sec. 1.1. We then give a few basic elements of coherent propagation of waves in random media, and an introduction to Anderson localization, in Sec. 1.2. Eventually, in Sec. 1.3, we describe ultracold atomic systems, and how they are useful for studying the effect of disorder in quantum systems.

## 1.1 From condensed matter systems to waves in disordered media

### 1.1.1 Disorder in solids

In molecules or solid state systems, atoms are strongly bound to each other as a result of the sharing of electrons. In usual solids, they are fixed in space and arranged in a regular structure (crystal), as is the case for water ice or quartz (see illustration on Fig. 1.1). This regular arrangement is then the background medium for the propagation of the 'shared' electrons. In the quantum theory of solids, the periodicity of the potential felt by the electrons is

Figure 1.1: Structures of crystalline  $\text{SiO}_2$  ('quartz'), and amorphous  $\text{SiO}_2$ , which is the standard glass. The structure of quartz is periodic, whereas the structure of glasses are disordered (i.e. they show no long-range order). Image from [36].



essential [34, 35]. Their eigenstates are then the so-called 'Bloch waves', which are extended over the whole system, and they are associated to an electronic band structure, which permitted to successfully understand the insulating or metallic behaviour of some materials, by the full or partial filling of the bands [34].

However such perfect layouts of atoms are idealized objects [37, 38], they hardly exist as such. In practice every arrangement of atoms is subject to localized defects: impurities (e.g. one atom is substituted by another species), vacancies or additional atoms, as well as dislocations of the crystalline structure. In addition, perfectly ordered lattice models are also inappropriate to describe another category of solid state systems: amorphous materials, in which the disorder is structural. In this class of systems the atoms are tightly bound in an irregular arrangement. It is the case of glasses for example, see Fig. 1.1.

Disorder seen by the conduction electrons in condensed matter can therefore have multiple origins [38], which are not always well-known, or at least not under experimental control. The goal of the physicist is then to describe those systems as generally as possible by looking for properties that are common to a number of disordered materials. To do so one needs to classify the systems by type and 'amount' of disorder, and proceed to statistical averaging.

### 1.1.2 Link with other waves

In solid-state systems, even at room temperature, the electrons are close to quantum degeneracy. It means that they cannot be described as a gas of classical particles, and one has to take into account their quantum nature. The study of a disordered material is then the study of the propagation of the electronic wave function in a random medium. For the sake of simplicity, let us consider a random potential  $V(\mathbf{r})$ , which will be the relevant case of the study of this thesis. This problem is therefore closely connected with the propagation of other types of waves in random media, and 'classical' waves in particular [39–41], as we discuss now on a simple example.

Consider first a particle of wave function  $\psi(\mathbf{r})$  whose eigenstate of energy  $E$  in a random

potential  $V(\mathbf{r})$  is described by the Schrödinger equation

$$\left[ -\frac{\hbar^2}{2m}\Delta + V(\mathbf{r}) \right] \psi(\mathbf{r}) = E\psi(\mathbf{r}), \quad (1.1)$$

where  $m$  is the mass of the particle. Consider now a scalar electromagnetic wave [of complex electric field  $e(\mathbf{r})$ ] of frequency  $\omega$  in a non-dissipative medium with random dielectric constant. It fulfills the Helmholtz equation [41]

$$\left[ -\frac{c^2}{\bar{n}^2}\Delta - \omega^2\mu(\mathbf{r}) \right] e(\mathbf{r}) = \omega^2e(\mathbf{r}), \quad (1.2)$$

where  $\mu(\mathbf{r})$  is the local relative fluctuation of the dielectric constant,  $\bar{n}$  is the average optical index of the medium and  $c$  the velocity of light. Those two wave equations have the same structure:  $-k_0^2\mu(\mathbf{r})$  in Eq. (1.1) plays an analogous role to that of the potential  $V(\mathbf{r})$  in Eq. (1.2) and  $k_0^2$  plays the role of the energy  $E$ . Therefore the picture presented in the following for a wave propagating coherently in a disordered medium, and in particular weak and strong (Anderson) localization effects, applies to both type of waves, with only slight modifications<sup>1</sup>.

One can however notice some differences between the two wave equations, that will change the details of the dynamics [39–41] but not the universal picture discussed below, in particular that obtained from the scaling theory of Anderson localization (see Sec. 1.2.2). First, those two equations are associated to different dispersion relations in the absence of disorder and to different conservation laws. The Schrödinger equation leads to  $E \sim p^2$  where  $p$  is the momentum and the total norm of the wavefunction is conserved. Conversely, the free Helmholtz equation [i.e. when  $\mu(\mathbf{r}) = 0$ ] gives  $\omega \sim p$  and it is the total electromagnetic energy which is conserved during the dynamics. Second, the analogous of the scattering potential in the Helmholtz equation is proportional to  $\omega^2$ , which means that the strength of the disorder depends on the energy, which is not the case in the Schrödinger equation. Finally, here we have neglected the vector nature of light, but it can also play an important role in the description of scattering.

### 1.1.3 Models of disordered systems

The sources of disorder in the wave equations of Sec. 1.1.2 can be very different. For the Schrödinger equation it is an external potential which is, for example, created by the Coulomb interaction of the electron with the ions of its environment which are not exactly ordered. For the Helmholtz equation it results from spatial modulations of the optical index of the medium. Usually, the details of the disorder are not precisely known in both cases. In order to reproduce the main physics of waves in such systems, one then resort to simple models. We will therefore compute the average values of the observables we are interested in. Then, the details of each realization of a disordered potential are not very useful, as they change from one realization to the next, and only the statistical properties of the disorder will intervene. Hereafter we present two founding models of disorder [37, 41, 42].

---

1. The same analogy can be made for many other wave equations which involve static disorder [41], such as acoustic or seismic wave, as well as superfluid bosons (e.g.  $^4\text{He}$  in porous media).

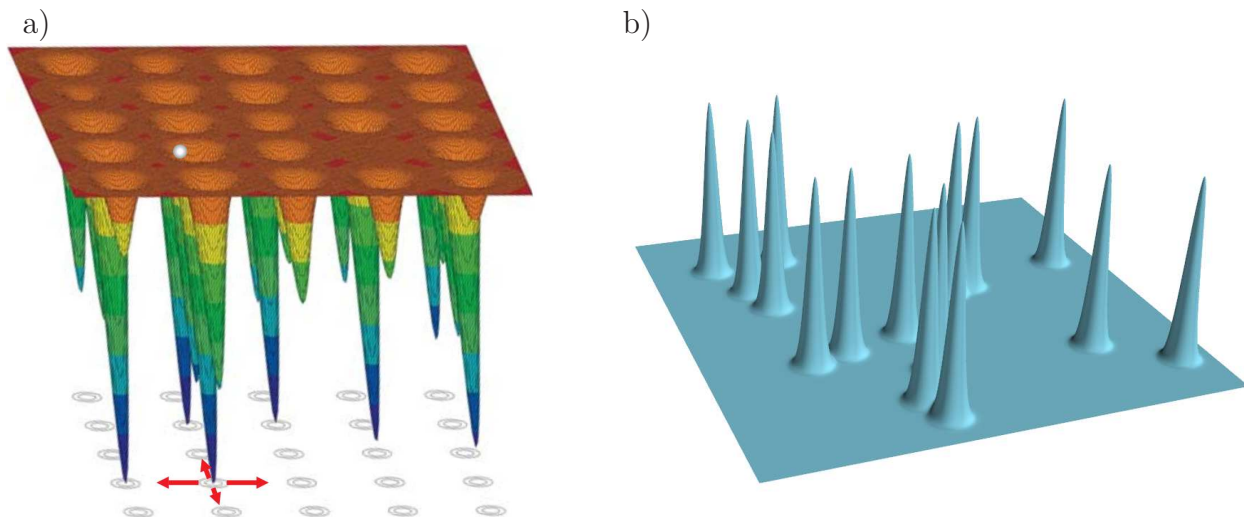


Figure 1.2: Two-dimensional views of two models of disorder: (a) The tight-binding model on a square lattice. An particle is hopping by quantum tunneling (represented by the arrows) on a two-dimensional lattice with random potential energies on each site. Figure reproduced from Ref. [11]. (b) The Edwards model. The particle probes the potential created by identical impurities randomly scattered in space.

**Tight-binding model** – Let us first consider that the underlying regular crystalline structure of the solid is preserved, which may be the case if the impurities are created by substitutional atoms that weakly affect the lattice order, and in alloys. In the tight-binding approximation, the electron is preferably bound to one ion of the lattice, and it has a certain probability to hop from one 'site' (ion) to the next by quantum tunneling. The different species are then modeled by different on-site potential energies for the electron, and/or different hopping probabilities [as is illustrated on Fig. 1.2(a)]. The simplest model that can describe this physics is the tight-binding Hamiltonian:

$$H = - \sum_{\langle i,j \rangle} t_{ij} (a_i^\dagger a_j + h.c.) + \sum_i \epsilon_i a_i^\dagger a_i, \quad (1.3)$$

where  $i$  and  $j$  index the lattice sites,  $a_i$  and  $a_i^\dagger$  are the annihilation and creation operators of the electron on site  $i$ ,  $t_{ij}$  is the hopping amplitude between sites  $i$  and  $j$ ,  $\langle i, j \rangle$  represents pairs of site that are usually restricted to neighbours, and  $\epsilon_i$  the on-site potential energy. It is the discrete limit of a continuous model of a deep periodic principal lattice, with small perturbations [37], and it is convenient to perform numerical simulations. As an example, a binary alloy may be modeled by an on-site energy  $\epsilon_i$  chosen randomly between two discrete values.

When this Hamiltonian is considered with nearest neighbour hopping that does not depend on the pair of sites,  $t$ , and random on-site energies uniformly distributed between  $-W/2$  and  $W/2$ , where  $W$  is the amplitude of the disorder, with no correlations between adjacent sites, this model is called the *Anderson model*. It is indeed with this model that Anderson demonstrated [43] the so-called Anderson localization, which will be introduced below. Anderson localization was later shown to be ubiquitous in wave physics and disorder.

**Edwards model** – If the crystalline structure is not preserved by the disorder, which is the case for amorphous media, it may be more convenient to resort to a continuous space model governed by Eq. (1.1) with randomness modeled by identical impurities scattered in space. The scattering potential that intervenes in the Schrödinger equation is then given by [44]

$$V(\mathbf{r}) = \sum_j U(\mathbf{r} - \mathbf{r}_j) \quad (1.4)$$

where  $U$  is the potential created by a single impurity (of typical strength  $U_0$ ), and the set of  $\{\mathbf{r}_j\}$  are the positions of the impurities [see e.g. Fig. 1.2(b)]. In this case the 'amount' of disorder is quantified by the density of impurities  $n_{\text{imp}} = N_{\text{imp}}/V$  in the medium, where  $N_{\text{imp}}$  is the total number of impurities and  $V$  the volume of the medium. This simple model is well-suited to study the effect of disorder correlations [which are given by the shape of  $U(\mathbf{r})$ , if the positions of the impurities are uncorrelated random values] on transport and localization. It bears two interesting limits:

- First,  $\delta$ -correlated impurities (also called 'white-noise' disorder) [ $U(\mathbf{r}) = \delta(\mathbf{r})$ , where  $\delta$  is the Dirac distribution] are often considered in the literature, because they lead to simple analytic expressions and scalings which bear part of the interesting physics. In many cases (but not all), in the low-energy limit, a continuous potential can be approximated by white-noise disorder, as we will see.
- Second, in the limit of an infinite density ( $n_{\text{imp}} \rightarrow \infty$ ) of weakly scattering impurities ( $U_0 \rightarrow 0$ ) we recover a continuous random potential. If  $n_{\text{imp}}U_0^2$  is kept constant, one can show by computing the correlation functions of the potential (1.4) that the disorder is Gaussian [41], i.e.  $V(\mathbf{r})$  is a Gaussian random variable and its correlation properties are uniquely determined by its two-point correlation function, through Wick's theorem.

These two relatively simple models for the study of waves propagating in disorder have enabled us to illustrate how the disorder can be described by its statistical properties. This will be important in the following. We will see for example that disorder correlations can modify the properties of Anderson localization not only quantitatively but also qualitatively (see Sec. 6.1 and Chaps. 5-8).

As discussed in this section, the physics of disorder was first introduced in the context of electrons in random lattices, more precisely in the tight-binding model [2]. The generalization to other kinds of waves was introduced later (see e.g. Ref. [29]). The latter is not only a simple extension to other domains of physics. It actually provides a different approach, complementary to the usual one of condensed matter. Both are useful for physical interpretations and in the following we will use both pictures and switch between the language of waves and particles.

## 1.2 Wave transport and Anderson localization

Let us now introduce basic ideas for the coherent propagation of waves in random media, and the concepts of weak and strong (Anderson) localization.

### 1.2.1 Waves, coherence and randomness

**Multiple scattering and phase coherence** – To set a physical picture of the effect of disorder on the propagation of a wave, one may start with a microscopic approach. Let us consider a wave, in one realization of an impurity disorder such as the one described by the Edwards model [see Fig. 1.2(b)]. This wave propagates in free space until it hits a first impurity. A part of the wave is then scattered by the impurity, giving rise to a diffuse wavelet. This wavelet and the main wave will propagate in the medium, and scatter on other impurities, giving rise to secondary wavelets that will in turn propagate in the disorder, etc... If the scattering is elastic, all those multiply-scattered wavelets have the same frequency/energy, and they can interfere.

In the particle picture, the density of the wave is the probability density of the particle. The scattered wavelet therefore represents the probability amplitude that the particle trajectory is deflected by the impurity. The motion of the quantum particle is then described by multiple-scattering paths realizing all the possible trajectories of the particle whose amplitudes should be added coherently. The interference between multiple-scattering paths depend on the disorder realization, and one could expect their effect to be smeared out as soon as we proceed to some averaging. It is not so because some interference effect survive disorder averaging, as we will discuss below.

Before proceeding, let us note that the coherence of the wavelets is fragile. If the particle is subjected to any dephasing or inelastic process (other than the dephasing introduced by scattering from the static potential) [3], e.g. phonons, magnetic impurities or couplings to the internal levels of the impurities for electrons and absorption for photons, the phase of the wave function can be randomized between scattering events or the modulus of its wavevector can be modified, which leads to decoherence and destruction of the interference. To understand the relevance of these interference for each problem, one has to compare different length scales [41]:

- The scattering length,  $l_s$ , which is the typical distance between two successive scattering events. It depends on the strength and the structure of the disorder and will be defined more precisely in Chap. 2.
- The coherence length,  $l_\phi$ , which is the typical length travelled by the particle before it undergoes a dephasing event. It determines the maximum length of the paths that are to be added coherently. It depends on the dephasing mechanisms that are at stake; in the case of inelastic scattering, it is the inelastic scattering length.
- The system size,  $L$ , if a system of finite size is considered. The length  $L$  determines the maximum extension of the multiple scattering paths.

If we are in a regime such that  $L < l_s$ , typically no scattering event occurs before the wave leaves the system, and the medium is irrelevant. If  $L \sim l_s$  there is typically one scattering event, so-called single-scattering regime. If  $l_\phi \lesssim l_s$ , each scattering event is independent from the previous one as regards interference: it is a regime of incoherent scattering. Finally, if  $l_s \ll l_\phi, L$ , the multiple-scattering paths are to be added coherently, and interference effects can occur<sup>2</sup>. In this thesis we will neglect decoherence, and we will study coherent multiple-scattering processes.

---

2. This simple argument is true in the case of isotropic scattering (for  $\delta$ -correlated scatterers). In the case of anisotropic scattering it is slightly more subtle: there is an additional length scale which is the transport mean free path  $l_B$  (see Chap. 2). The interference effects are then important for  $l_B \ll l_\phi$ .

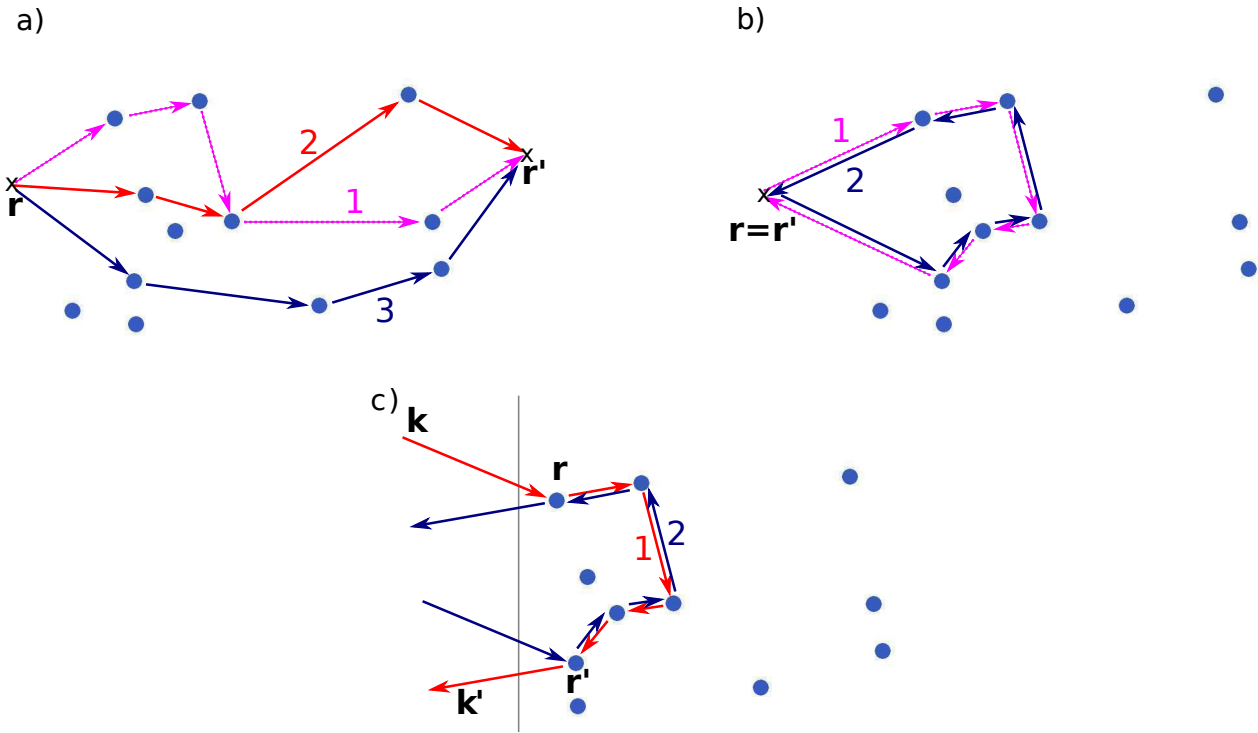


Figure 1.3: Typical multi-scattering trajectories of a particle in the disordered medium, whose amplitudes contribute in the summation (1.5). (a) Three paths for  $\mathbf{r} \neq \mathbf{r}'$ , that contribute to  $\overline{P_{incoh}}$ . (b) If  $\mathbf{r} = \mathbf{r}'$ , the paths form loops, which can be travelled in two directions. They contribute to both  $\overline{P_{incoh}}$  and  $\overline{P_{coh}}$ . (c) In a backscattering configuration, the reflected wave is enhanced if  $\mathbf{k} = \mathbf{k}'$ .

**Weak localization** – As pointed out above, interference effects can survive disorder averaging and induce important effects. Let us understand their origin qualitatively, along the lines of the enlightening introduction of Ref. [41]. In the other chapters, we will use more rigorous, and more elaborate, quantum transport theory tools.

Consider one realization of the same disordered medium as above. Each path represents a random walk in the disorder, as illustrated in Fig. 1.3(a). The probability for a particle to go from a point  $\mathbf{r}$  to a point  $\mathbf{r}'$  is given by the sum of the amplitudes of all the coherent multiple-scattering paths:

$$\begin{aligned}
 P(\mathbf{r}'|\mathbf{r}) &= \left| \sum_{\text{paths } i} A_i(\mathbf{r}, \mathbf{r}') \right|^2 \\
 &= \sum_{\text{paths } i} |A_i(\mathbf{r}, \mathbf{r}')|^2 + \sum_{\text{paths } i \neq j} A_i^*(\mathbf{r}, \mathbf{r}') A_j(\mathbf{r}, \mathbf{r}') \\
 &= P_{incoh} + P_{coh},
 \end{aligned} \tag{1.5}$$

where the  $A_i$  are the amplitudes of each path. It is therefore the sum of an incoherent and a coherent contribution. If there are dephasing processes, the phases of the paths of the coherent contribution is randomized in time, and the second term drops. In this case we see that the total probability to go from  $\mathbf{r}$  to  $\mathbf{r}'$  is simply given by the sum of the probability to travel along each individual path. This is therefore a classical description of transport which leads to diffusion in the medium (also called Drude or Boltzmann regime).

Let us now consider that there are no incoherent processes, and average over disorder realizations. If  $\mathbf{r} \neq \mathbf{r}'$ , as the paths involved are different for each realization of the disorder, the second term is a complex number with a different phase for each realization, and it is therefore averaged to zero, at least when  $|\mathbf{r} - \mathbf{r}'| \gtrsim l_s$ . However, if  $\mathbf{r} \simeq \mathbf{r}'$  some interference terms survive disorder averaging. In this case, all the paths considered in Eq. (1.5) are loops, which can be travelled in two different directions, as illustrated on Fig. 1.3(b). For the indices  $i$  and  $j$  in the second term of the right-hand side of Eq. (1.5) that correspond to the same loop but travelled in opposite directions, the phases of  $A_i$  and  $A_j$  are the same. We then find

$$\overline{P(\mathbf{r}|\mathbf{r})} = 2 \overline{\sum_{\text{paths } i} |A_i(\mathbf{r}, \mathbf{r})|^2} = 2\overline{P_{incoh}}, \quad (1.6)$$

where the overbar signifies disorder averaging. We see that in the case of coherent transport, the probability to come back to the starting point is twice the classical one. This interference effect is called *weak localization*.

Weak localization leads to an enhanced probability to return back to the origin. It therefore slows down transport, i.e. it reduces the diffusion constant and the conductivity compared to the Boltzmann/Drude incoherent contribution. This effect in condensed matter systems have been widely studied theoretically and experimentally, and signatures have been found in various systems (see the reviews [3, 45, 46]). For instance weak localization correction to the conductivity has been studied as a function of temperature (which activates sources of decoherence such as phonons) and magnetic field (which introduces spin-orbit couplings and additional phases to the paths). They have also been studied as a function of disorder parameters, such as impurity concentration for example. As an illustration, Fig. 1.4(a) (reproduced from Ref. [45]) presents the dependence of the resistance of a thin disordered Mg-film, with magnetic field for several values of the temperature. The term  $\overline{P_{incoh}}$  is independent of an external dephasing, and therefore the resistance should be independent of the magnetic field in the case of incoherent scattering. However, in the quantum description, a magnetic field [which dephases paths  $i$  and  $j$  with an opposite sign in Fig. 1.3(b)] should thwart the weak localization effect. It is what is observed on Fig. 1.4(a): For a given temperature the resistance decreases, i.e. the conductivity increases, with the amplitude of the magnetic field.

Weak localization has a counterpart in momentum space. Let us consider the configuration of Fig. 1.3(c), where we consider the reflection a beam of wavevector  $\mathbf{k}$  on a disordered medium. A treatment of this problem, very similar to the above one, yields for the average probability of angle-dependent reflection [41]

$$\overline{P(\mathbf{k}'|\mathbf{k})} = \overline{\sum_{\mathbf{r}, \mathbf{r}'} \sum_{\text{paths } i} |A_i(\mathbf{r}, \mathbf{r}')|^2 [1 + e^{i(\mathbf{k}+\mathbf{k}') \cdot (\mathbf{r}-\mathbf{r}')}]} \quad (1.7)$$

where  $\mathbf{k}'$  is the outgoing wavevector, and the summation over  $\mathbf{r}$  and  $\mathbf{r}'$  runs over all the scatterers that are hit by the incoming beam. Therefore, we see that for  $\mathbf{k} = \mathbf{k}'$  the same constructive interference occurs, and the intensity of the wave reflected from a disordered medium in the exact direction of the incoming beam, is enhanced by a factor of 2 compared to the intensity of the light reflected in the other directions. This effect is therefore called *coherent backscattering*. An enhanced reflected light beam with an enhancement factor smaller than two<sup>3</sup> for various experimental constraints was first observed experimentally on liquid suspensions of

---

3. The enhancement factors observed in those experiments in between 1.1 and 1.6.

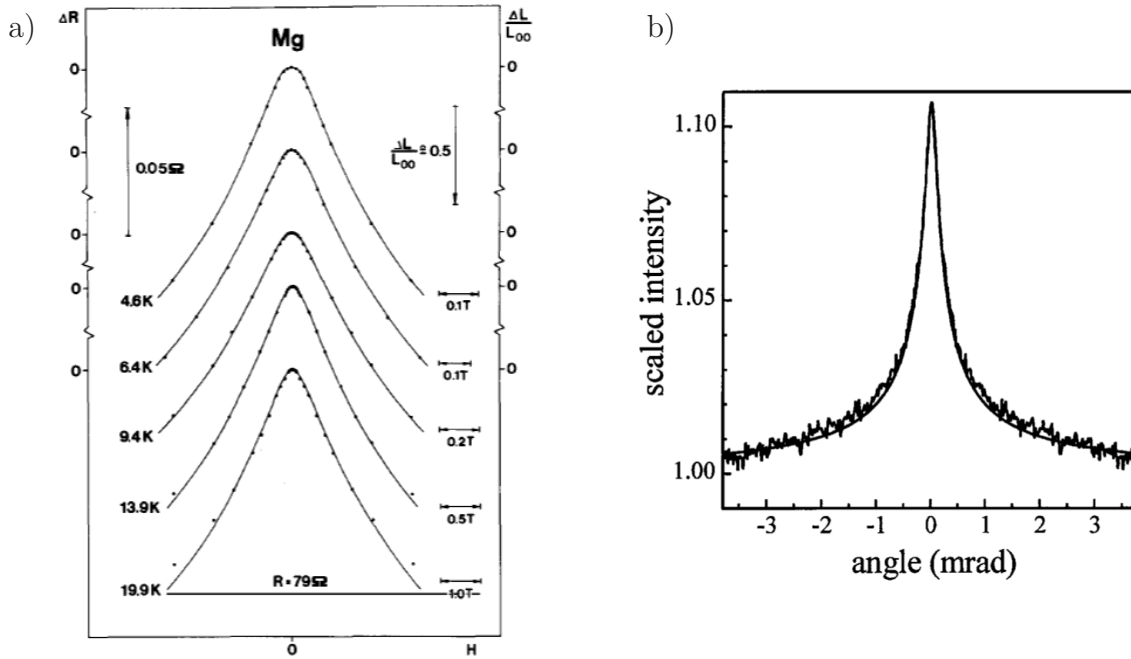


Figure 1.4: Evidence of weak localization. (a) The magneto-resistance of a thin Mg-film, induced by a transverse magnetic field applied to the film. Shown is the difference of the resistance of the film  $\Delta R = R(H) - R(0)$  as a function of the amplitude,  $H$ , of the magnetic field for different temperatures (indicated on the left-hand side of the plot). The decrease of  $\Delta R$  with  $H$  is a signature of weak localization. Reproduced from Ref. [45]. (b) Backscattered intensity of a light beam shone onto an atomic cloud, as a function of the scattering angle  $\theta$ . The peak at  $\theta = 0$  is a signature of coherent backscattering. Reproduced from Ref. [47].

colloidal particles in Refs. [48–50] in 1984–1985. A coherent backscattering peak twice as high as the background, as predicted by theory, was then obtained in Ref. [51] in powders of oxide materials. Coherent backscattering was also observed in many other situations, such as for light diffusing in cold atoms [47]. In all those experiments, the disordered medium is illuminated by a light beam, and the intensity of the reflection is measured as a function of the angle it makes with the incident beam. Figure 1.4(b) reproduces a figure from Ref. [47]. It shows the intensity of the light reflected by an atomic cloud as a function of the angle  $\theta$ . In the backscattering direction ( $\theta = 0$ ), the intensity is enhanced by a factor 1.1, hence demonstrating coherent backscattering<sup>4</sup>. Very recently, two experiments reported coherent backscattering of a Bose-Einstein condensate by a speckle potential [52, 53]. Note that the situation is then inverted: the light creates the potential on which the ultra-cold matter wave scatter.

**Strong localization** – In the weak localization regime, the transport is reduced by interference between multiple scattering paths, but particles can still propagate to infinity. However, in our simple model we only considered interference between loop paths that are travelled in one direction or the opposite, but interference effects are to be taken into account for many other pairs of paths, in principle all those which visit the same set of scatterers, and in

4. This enhancement factor lower than 2 can be explained by low-order scattering, and coupling of the light with the internal states of the atoms.

particular those which include loops inserted in loops etc... They can lead to the complete suppression of transport, an effect which is called Anderson (or strong) localization.

In his pioneering work [43], Anderson considered Hamiltonian (1.3) with the so-called Anderson model (random on-site energies  $\epsilon_i \in [-W/2, W/2]$  and uniform hopping parameter  $t$ ) [see illustration on Fig. 1.2(a)]. By analyzing the spectrum, he showed that, in three dimensions and for sufficiently strong disorder (i.e. large enough  $W/t$ ), a particle of energy  $E$  initially located on site  $i$ , has a probability to diffuse away that decreases exponentially with distance. The particle then remains localized around its initial position, and it leads to a total suppression of transport, i.e. diffusion is stopped and conductivity strictly vanishes.

The onset of Anderson localization has various consequences on the properties of the system. Consider the case of the Anderson model, Hamiltonian (1.3). For weak disorder the eigenstates close to the band edges are localized, while close to the center of the band they are extended. The two regimes are separated by a phase transition as can be simply explained along the lines of Mott's *reductio ad absurdum* argument [54]. Extended and localized states cannot coexist in the spectrum: If a localized and an extended state coexist with infinitely close energy, for a given configuration of the disorder, any infinitesimal change in the disorder would hybridize them, leading to two extended states. Therefore, at a given energy, all states are either extended or localized. The localized and extended regions of the spectrum are separated by critical energies: the mobility edges. When the parameters of a system vary in such a way that its energy changes from an extended to a localized region of the spectrum, it undergoes a metal-insulator phase transition. For stronger disorder all states are localized. In the continuous case [see Eq. (1.4) for example], the picture is essentially the same, except that in general there is a single mobility edge, the low-energy states are localized, whereas the high-energy states are extended.

In the preceding paragraphs, we have introduced Anderson localization as a further consequence of the interference effects that lead to weak localization; and weak localization can thus be seen as a precursor of strong localization. Even if it did not enable us to understand the complete suppression of transport, this semi-classical wave approach permits to enlighten some basic qualitative features of weak and strong localization.

- First, the arguments we developed do not depend on any particular property of the scattering disorder, and weak localization is therefore ubiquitous to wave physics in disorder, as is Anderson localization.
- Second, we saw that the weak localization correction is dominated by loop-paths. One can show that any random walk path returns to its origin after a finite time in 1D, and asymptotically in 2D. Hence, every random walk path is a loop in one and two dimensions, and we thus understand that all quantum states are localized in 1D and 2D infinite systems (2D being the marginal dimension). Conversely, in 3D, many paths do not loop back to the origin, and a transition between a localized and a diffusive regime occurs. However, if the size of the system is smaller than the localization length (the typical length of decay of the localized states), a 1D and 2D disordered system might not always show an insulating behaviour.
- Finally, the underlying interference effect enables us to find a general criterion to discriminate 'weak' and 'strong' disorder in 3D. The typical characteristic length for interference effects is the wavelength ( $\lambda = 2\pi/k$ ). In the description of transport developed above, we have implicitly assumed that this wavelength was small compared to the scattering length  $l_s$ , i.e. that the wave propagated as a plane wave between each scatter-

ing event. This is true in 'weak' disorder (i.e. when the scattering length is large), and we indeed found that in this regime transport is reduced, but not cancelled. However, this semi-classical picture breaks down when  $kl_s$  becomes of the order of unity, and we enter a regime in which transport has to be described by a fully coherent approach. This criterion, which was first introduced by Ioffe and Regel [55], gives an approximate boundary for Anderson localization in 3D. However it is not a universal criterion, i.e. one should understand it as  $kl_s \sim C$  where  $C$  is a constant which depends on the model.

### 1.2.2 Scaling theory of localization

Beyond the simple interference picture described above, various theoretical approaches have been developed to study different aspects of Anderson localization, and we do not aim at giving a full picture here. Using a different approach, an important development was made in 1979 by the so-called 'gang of four' (Abrahams, Anderson, Licciardello and Ramakrishnan) when they formulated the scaling theory of localization [56]. This discussion is enlightening, because it permits to put the picture worked out in the preceding section in a more robust and universal fashion. Let us briefly redraw it here.

A scaling theory attempts at describing the macroscopic behaviour of the system by looking at how its properties evolve when increasing the system size, without describing into too much details the microscopic scale. In Ref. [56] the authors make the assumption that only one scaling variable [the dimensionless conductance  $g(L)$ ] permits to describe the behaviour of the material in the metallic and the insulating regimes. For a system of size  $L^d$ , where  $d$  is the dimension, the dimensionless conductance<sup>5</sup> is given by

$$g(L) = L^{d-2} \sigma(L) \hbar / e^2, \quad (1.8)$$

where  $\sigma$  is the conductivity of the sample, and  $e$  the electronic charge. The one parameter scaling hypothesis [57] states that, if  $n^d$  cubes of size  $L^d$  with the same disorder properties are assembled to form a cube of size  $(nL)^d$ , the conductance of the large cube,  $g(nL)$ , is only a function of that of the  $L^d$  cube, and it depends neither on the microscopic details, nor on  $L$ . The scaling function

$$\beta(g) = \frac{d \ln g}{d \ln L} \quad (1.9)$$

is also found to be only a function of  $g$  [58]. This function, which permits to analyze how the conductance changes with the system size, is shown in figure 1.5 as a function of  $\ln g$ .

Let us first explain the limiting cases. On the metallic side (i.e. for large  $g$ ), transport can be described by the classical regime (see Sec. 1.2.1), and the dimensionless conductance is then given by  $g(L) = \sigma_B L^{d-2} \hbar / e^2$  where  $\sigma_B$  is the Drude conductivity, and thus

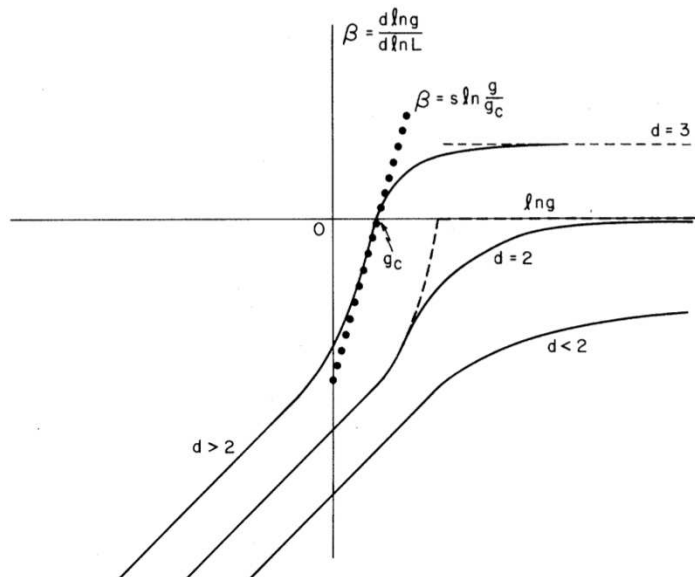
$$\beta(g) = d - 2. \quad (1.10)$$

One can also show perturbatively that the first correction is given by  $\beta(g) = d - 2 - a_d/g$ , where  $a_d > 0$  is a constant. This correction shows that the curves approach their asymptotes from below in Fig. 1.5, which is very relevant for the 2D case, as we will see. In the localized

---

5. The conductance is the inverse of the resistance.

Figure 1.5: The scaling function  $\beta(g)$  [see Eq. (1.9)] as a function of the logarithm of the dimensionless conductance  $\ln g$ , in dimension 1, 2 and 3. In 3D the scaling function crosses the horizontal axis, denoting a phase transition between a conducting and an insulating phase. Conversely in 1D and 2D, a disordered system is always an insulator. This figure is extracted from the original paper [56].



regime, conduction can only be realized by electrons hopping from localized states to localized states. The hopping probability is roughly given by the overlap integral, which is exponentially small, and one finds  $g(L) \sim e^{-L/L_{\text{loc}}}$ , where  $L_{\text{loc}}$  is the localization length. Therefore we have

$$\beta(g) = \ln g + c_d \quad (1.11)$$

where  $c_d$  is a constant that may depend on the model of disorder. Those limiting behaviours at low and high  $g$  give the asymptotic behaviours on Fig. 1.5, and the overall curve is assumed to be monotoneous. Note that this picture for the scaling function  $\beta$  is universal, i.e. it does not depend on the material. It however depends on the global symmetries and does not hold if time-reversal invariance is broken (for example by a magnetic field) [59, 60].

We now analyze the behaviour that is predicted by Fig. 1.5 with dimensionality. In 3D, we see that the curve of  $\beta(g)$  cuts the axis at a critical point  $\ln g_c$  given by  $\beta(g_c) = 0$ . If the disorder is weak such that one can find a mesoscopic<sup>6</sup> scale  $L$  at which  $g(L) > g_c$ , we have  $\beta[g(L)] > 0$  and when the size of the system increases, the dimensionless conductance  $g$  increases (the point moves right on the curve), and reaches the asymptotic behaviour  $\beta(g) = 1$ , i.e.  $g \propto L$ . The system is therefore metallic at large scales. On the other hand, if the disorder is strong enough, we may find a scale such that  $g(L) < g_c$ . Then, we have  $\beta(g) < 0$  at the starting point, and the point moves to the left when  $L$  increases, and  $g \rightarrow 0$ . The system has an insulating behaviour. The critical point  $g_c$  is therefore an unstable fixed point, and the metallic and insulating phases are stable. It is found that the scaling theory predicts a metal-insulator phase transition in 3D [56]. It also gives some predictions about the critical behaviour. Near the critical mobility edge  $E_c$ , whose value depend on the microscopic details of the system, one finds [61]

$$L_{\text{loc}} \propto (E_c - E)^{-\nu} \quad \text{and} \quad \sigma \propto (E - E_c)^s \quad (1.12)$$

with the scaling relation  $s = (d - 2)\nu$ . For  $d = 3$ , it gives  $s = \nu$ . The exact value of the critical exponents are not predicted by the scaling theory. It was evaluated as  $s = \nu = 1.58$  in numerical simulations of the Anderson model [61]

6. By mesoscopic we mean an intermediate scale larger than  $l_s$ .

In 1D and 2D,  $\beta(g)$  is always negative and therefore the conductance always flows to  $g = 0$  when the size of the system increases. It always reaches the localized regime in the thermodynamic limit. We also see on Fig. 1.5 that 2D is the marginal dimension.

Finally note that in principle, in order to describe an ensemble of disordered systems, not only the average conductance should be considered in the scaling theory, but its full probability distribution [62, 63]. However, the one-parameter scaling hypothesis for the average conductance has been confirmed by renormalization group calculations [64], perturbation theory [3] and self-consistent theory [65], which will be introduced later in this thesis (see Chap. 5). Let us only mention other fundamental approaches to study localization in non-interacting disordered systems, such as random matrix theory [66], other field theoretical methods such as supersymmetry [67] and multifractal analysis [68] etc..., which are complementary to the ideas exposed here. For a review, see Refs. [3, 68, 69].

### 1.2.3 Anderson localization in correlated disorder

With the scaling theory, we have outlined the main features of Anderson localization in its most universal picture, which ignores the details of the system, in particular the disorder statistical correlations. However, in this thesis we will study the effects of disorder correlations, and we will see that they can change the quantum transport and localization properties quantitatively and have very interesting effects. For a long-time, study of Anderson localization has mostly been done for white-noise disorder, and very few studies considered statistical correlations of impurities in Edwards-like models [70, 71]. This lack of interest for correlated disorder was due to the apparent absence of physical applications: The disorder was not well-characterized in solids. However, in 1980, the study of quasi-periodic potentials revealed the existence of a metal-insulator transition in 1D when the strength of quasi-disorder increases [72, 73]. This is in apparent contradiction with the fact that all single-particle states should be localized in 1D disorder. However, this result relies on the scaling argument, which does not hold anymore if the disorder possesses some kind of long-range correlations, which is the case for quasi-periodic potentials.

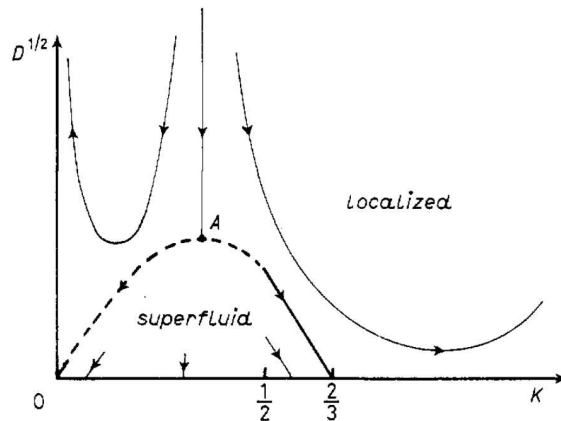
'True'<sup>7</sup> statistically correlated disorder was then studied in the tight-binding model and for continuous models, mostly in 1D. For example, the dependence of the localization length on the correlations of the potential, by comparison to white-noise disorder, has been examined theoretically [74] and observed in semiconductor structures [75], and microwaves [76]. For very specific correlations [77], such as the random-dimer model [78] a discrete set of extended state was found numerically, which do not couple to the localized states, and raised the question of the possibility of coexistence. This model was found to be relevant to model the disorder in conducting polymers [79, 80]. For some correlations, the inverse localization length was then found to vanish in a given window of the spectrum in first-order perturbative approaches [81], leading to effective mobility edges. The same occurs in 1D speckle potentials [82].

Finally, only recently, long-range correlations were considered. In this case, the scaling hypothesis does not hold. In 1D, it was shown in Ref. [83, 84] (see also Ref. [85]) that if the spectral density of the disorder is  $C(k) \propto 1/k^\alpha$  with  $\alpha > 2$ , the system exhibits a metal-insulator transition, even for  $L \rightarrow \infty$ . The same result was also found in 2D [86, 87].

---

7. By true disorder we mean disorder with a dense spectra, in opposition to quasi-periodic potentials.

Figure 1.6: Phase diagram for 1D interacting bosons in continuous disorder. On the abscissa is the Luttinger parameter  $K$ , which increases with the strength of repulsive interactions, and on the ordinate  $D^{1/2}$  represents the amplitude of the uncorrelated disordered potential. A superfluid phase is predicted for low disorder and moderate interaction strength, and a Bose glass phase 'localized' is predicted everywhere else. Reproduced from Ref. [97].



### 1.2.4 Disorder and interactions

In both models we have introduced to study localization, interaction effects, which are very strong in solid-state systems, have been neglected. Indeed, the Anderson model does not bear any interaction term. And in the continuous case, to derive the Schrödinger equation (1.1) for one electron in a solid-state system, we have left aside the presence of the other electrons. We have therefore neglected the inter-electron Coulomb interaction, as well as the fact that they are identical Fermi particles near quantum degeneracy (i.e. one should take into account the Pauli exclusion principle).

Interactions and quantum statistics in condensed matter systems can change the behaviour, not only quantitatively, but also qualitatively. In the absence of disorder, they can induce many-body effects such as the Mott transition on a lattice (metal-insulator transition induced by repulsive interactions) [88, 89], or superfluidity [90] and superconductivity [91]. Several difficult and broad questions arise: What happens to the disorder-induced single-particle effects (such as Anderson localization) in the presence of interactions? What about the many-body effects (such as superconductivity) in the presence of disorder? Are those transitions destroyed, or only quantitatively modified? The interplay between interactions and disorder is a very important question of condensed matter physics.

Study of disorder in many-body systems is a very active field of research, and the questions raised above have already been partially addressed, giving rise to the study of a variety of new phenomena and quantum phases. Let us illustrate this with a few examples.

In the Schrödinger equation (1.1), weak interactions can often be modeled by a non-linear term [92, 93]. A non-linear term can also arise in the Helmholtz equation (1.2) in the presence of a non-linearity in the propagation medium [94]. Therefore the role of weak interactions is related to the competition between non-linearities and disorder in the wave equation [95, 96]. However, such an effective single-particle description does not hold in strongly interacting systems, and one has to deal with a full many-body problem.

The phase diagram for 1D repulsively interacting bosons in a continuous disordered potential is shown in Fig. 1.6. Let us first scan it for an intermediate value of the disorder amplitude. At zero interaction all bosons occupy the same single-particle ground state; when interactions slightly increase a few other isolated localized states are populated, and a localized phase, which is called Bose glass is stabilized. When interactions further increase, more and more states are populated and at some point they merge, and a superfluid phase is predicted. It is destroyed again at stronger interactions, where again a Bose glass phase is predicted. For

this particular example, the strong interaction transition has been characterized by Luttinger liquid theory and renormalization techniques [97]. The weak interaction limit is more difficult because the effective Luttinger theory breaks down, due to strong spatial modulations of the density. In this regime, the superfluid transition is expected to occur close to the fragmentation point [98], as supported by numerical calculations in the Bogoliubov approach [99]. The effect of possible density-assisted tunneling between fragments remains open. In addition, the different picture of the superfluid transition for weak and strong interactions suggest the possible existence of a critical point (A in Fig. 1.6), and thus of two distinct Bose glass phases. This question is completely open however.

Another interesting problem is the study of many-body localization. In Ref. [100], it was shown that for fermions, at  $T = 0$ , all states should remain localized under the effect of weak repulsive interactions. But a finite-temperature metal-insulator transition is expected. For bosons in 1D, a finite-temperature transition can occur between a localized phase and a normal fluid [101]. Many-body Anderson localization in weakly interacting systems has also been studied within the Bogoliubov approach [102–104]. It was for instance shown that Bogoliubov quasi-particles undergo genuine Anderson localization in 1D.

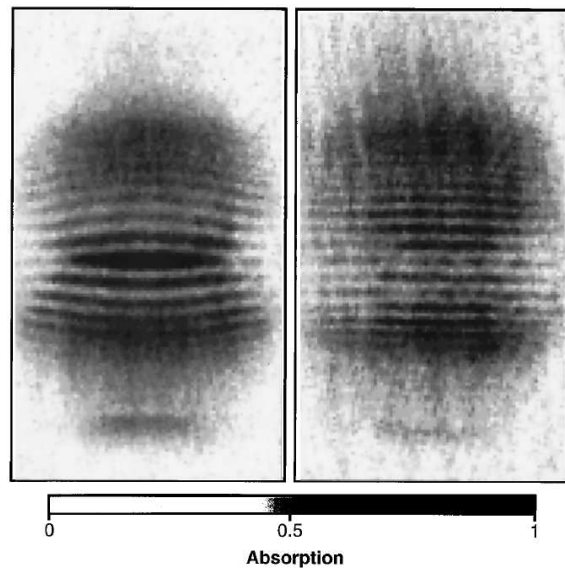
Finally, the study of the interplay between superfluidity, superconductivity and disorder is also a major field of research. Superfluidity and superconductivity both originate from the presence of interactions [90] and therefore they can also be destroyed by disorder. In particular, weak disorder can modify the normal to superconductor transition temperature [105], but this dependence is rather weak in general [3]. Strong disorder can even suppress the transition towards the superconducting state [32] by different mechanisms which may depend on the type of disorder.

In this section we have first introduced weak and strong localization as a wave interference effect at the microscopic scale. We then presented the result obtained by Anderson in 3D and the scaling theory, which gives the behaviour of localization with dimensionality. It provided us with a good general understanding, in particular of the dimensionality effects, however it does not give any theoretical predictions for the critical behaviour. Up to now, the determination of the critical exponents and the prediction of the position of the mobility edge remains a challenge. As disorder is present almost everywhere in natural media, the study of Anderson localization has spread far beyond its initial context. It is now studied in many other fields than condensed matter, and it has opened various branches of research such as disorder in many-body systems, and Anderson localization in correlated random potentials, which are very active.

### 1.3 Ultra-cold atoms in disorder

Experiments on Anderson localization in condensed matter systems are rendered difficult by the presence of interactions and phonons, which create decoherence. Some evidence of a metal-insulator transition were found in condensed matter system [106, 107], however, in these experiments the value of the critical exponent may be modified by the interactions and a quantitative analysis is complicated (for a review see Refs. [3, 4]).

Figure 1.7: Interference pattern of expanding condensates. Two independent Bose-Einstein condensates are let to expand; in the area where they overlap, interference fringes are observed, hence demonstrating that each condensate is a spatially coherent matter-wave. The two images are for different initial conditions. Reproduced from [112].



Anderson localization has also been studied outside of its original context, in non-interacting classical waves where it has found many experimental applications. Following a proposal by S. John [29], the first experiments were made with electromagnetic waves: micro-waves [108] and light waves [5]. However, their interpretation is controversial, because it is difficult to discriminate between Anderson localization and absorption (which also induces exponential decrease of the intensity in the medium) [109, 110]. With the study of the fluctuations of the transmission it however became possible to show non-ambiguous evidence of Anderson localization [111]. More recently, Anderson localization has been studied with seismic [31] and sound [30] waves, and in photonic crystals [94] where the intensity profile can be monitored. For a short review, see Ref. [11].

Ultracold atoms are atomic vapors of bosonic or fermionic particles, cooled by laser and evaporative cooling near the absolute zero temperature. Temperatures such as a few nK can be reached. At those temperatures the de Broglie wavelength of the particles becomes of the order of the  $\mu\text{m}$ , which can be larger than the interparticle distance. They are thus genuine quantum particles. The phase space density is then high, and quantum gases are spatially coherent atomic matter waves. This was illustrated by one of the first experiments of manipulation of Bose-Einstein condensates after their experimental obtention in 1995: In W. Ketterle's group [112], two condensates were let to expand and interference fringes were observed in their overlapping area, as illustrated on Fig 1.7. Since the first experiments with Bose-Einstein condensates and, more recently, the obtention of quantum degenerated fermionic gases [113, 114], the experimental techniques have improved very fast. The control is now such that ultracold atomic gases are another system in which the effect of disorder can be investigated [12, 13].

### 1.3.1 Quantum simulators/ assets

Ultracold matterwaves are very controllable systems from an experimental point of view. First of all, one can choose to work with species of bosons, fermions, or mixtures. Second, the atoms can be manipulated by electromagnetic fields. In the case of a magnetic field, they can form a harmonic trap for the atoms. The latter can be done also with the dipole force induced

by laser light (see Chap. 3). This dipole force is particularly well-suited because it can be tailored rather easily to create wells and barriers. For instance, using two counter propagating laser beams, one creates a periodic potential. Atoms launched in such lattice mimic the physics of electrons in a crystal. It permits to experimentally realize lattice Hamiltonians [see e.g. the first term of Eq. (1.3)] in which the coupling parameter between sites can be tuned by the depth of the lattice [115, 116]. Optical lattices can also be used to control the effective dimensionality of ultra-cold atomic gases from 0D to 3D. For example, a one-dimensional standing wave (created by two counter-propagating laser beams) can be used to make a series of 2D planes in which the atoms are trapped [117]. Third, the possibility to manipulate the internal state of the atoms permits to polarize them and study spin physics [118, 119]. Finally, the inter-atomic interactions can be tuned by controlling the density of the atomic gas or using Feshbach resonances. One can then continuously change from no interactions to strongly-correlated systems.

Another great asset of ultracold quantum gases is that they are relatively well isolated systems, which means that they do not suffer from one of the great limitations of condensed matter systems: the coupling to the environment, such as phonons for example, which induces decoherence. In addition, their spatial profile can be probed directly by absorption or fluorescence imaging, and their momentum distribution is also measurable.

This makes ultracold atomic gases ideal systems to realize model Hamiltonians in which each term is under experimental control, and the parameters can be varied continuously. It then enables quantitative comparison with theoretical predictions, and permits to investigate further the physics of systems for which numerical simulations are limited, such as many-body systems. It also permits to explore regimes which are not accessible in traditional condensed matter systems, such as weak interactions. Those quantum simulators could then help to answer open questions [120, 121].

### 1.3.2 Controlled Disorder

In particular, ultracold atoms are very interesting to investigate the issue of this thesis: the physics of disordered systems [7, 11–13]. Several proposals have been made to apply disorder to ultra-cold atomic systems:

- An impurity disorder can be realized for one atomic species by using a second species in a static configuration. The second species can for example be trapped on random sites of an optical lattice while the first species is insensitive to the lattice [122–125]. The atoms of the second species create a random pattern of impurities, like in the Edwards model, on which the first species scatter.
- A disorder can be created in a tight-binding configuration [see Eq. (1.3)] by adding a weak spatially-varying light pattern to a deep main optical lattice. If the weak light pattern is an optical lattice with a frequency which is non-commensurate with that of the main one, it creates a quasi-periodic potential [see illustration in Fig. 1.8(a)]. In 1D this configuration realizes the Aubry-Andre model [72]. Using optical phase modulators, which allow to engineer any light pattern, it is also possible to implement the Anderson model for ultracold matterwaves, as well [126, 127].
- One could also use the disorder that is naturally introduced by the roughness of the wires, for potentials created by atom chips, and which can be partially controlled during the realization of the chip [128].

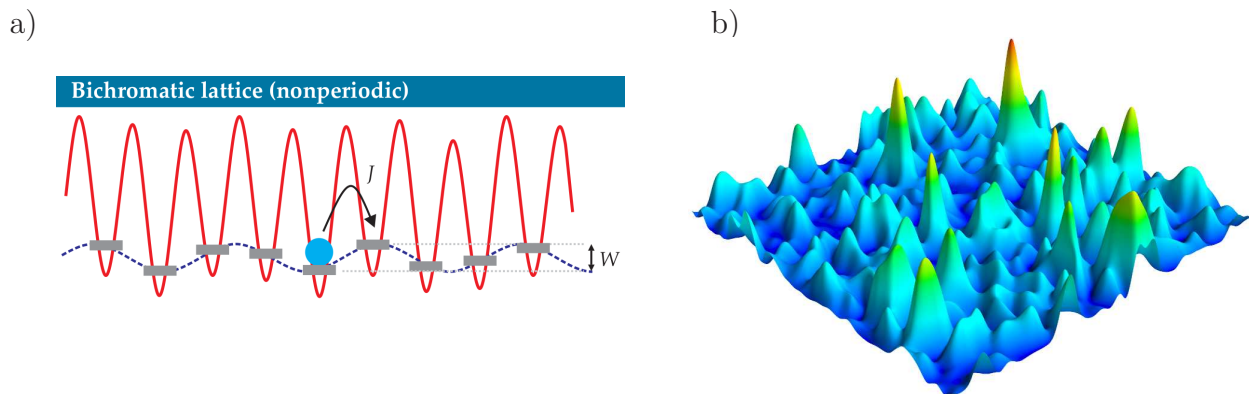


Figure 1.8: Disordered potentials for cold atoms. (a) One-dimensional quasi-periodic potential, obtained by the superposition of two optical lattices with incommensurate frequencies. It creates a tight-binding model to an effective on-site energy shift which is pseudo-periodic. Illustration from Ref. [12]. (b) A two-dimensional speckle potential (see details in Chap. 3). The spatially-random light-pattern depicted here acts as a continuous potential for the atoms.

– Finally, speckle patterns which are spatially-random light patterns can be imaged onto the atoms, thus realizing a continuous disorder [see Fig. 1.8(b) and details in Chap. 3]. Quasi-periodic [10, 129–131], speckle potentials [9, 17–20, 53, 127, 132–139] and impurity potentials [140] have been implemented in experiments up to now. Speckle potentials are correlated disorder and have anisotropic features in  $d > 1$ , which will allow us to investigate Anderson localization in correlated and anisotropic disorder.

### 1.3.3 State of the art

Let us finally summarize the experimental quest for Anderson localization with ultracold atoms, which is the result of a great interplay between theory and experiments.

The first experiments with 1D ultra-cold atoms in speckle disorder were carried out simultaneously in the group of M. Inguscio, in Florence [133, 134], in the group of A. Aspect, in Palaiseau [20, 135] and in the group of W. Ertmer, in Hannover [132]. They observed suppression of transport, which was due to large atomic interactions and strong reflections from high peaks of the disordered potential [82]. Following the theoretical proposal [8], in 2008 Anderson localization of non-interacting ultra-cold atoms was finally observed experimentally in speckle potentials, in Palaiseau [9]. In this experiment, which is described in more details in Sec. 4.2.1, a good quantitative agreement was found with theoretical predictions [14]. At the same time, the disorder-induced transition predicted in one dimensional quasi-periodic systems by Aubry and André [72], was observed in Florence [10]. These observations have opened many perspectives [13] and triggered experiments on the effect of interactions and also in higher dimensions.

As outlined above, the interplay between interactions and disorder is a very challenging and open question. Ultra-cold atomic systems have been used to investigate this question, thanks to Feshbach resonances. In Florence [129–131], the regime of weak interactions is studied in a 1D quasi-periodic potential, where they have observed delocalization and subdiffusion. Signatures of a Bose glass phase has also been observed with bosons in a 1D lattice with impurity disorder in D. Schneble group in Stony Brook [140]. And interacting bosons in

1D speckle potentials have been investigated in the group of R. Hulet, in Houston [137], where they have analyzed the damping of the motion of a condensate in the disorder, and its fragmentation. In the group of B. DeMarco, in Urbana-Champaign [127], strongly-interacting bosons in an 3D optical lattice superimposed with a speckle pattern have been studied, and they have measured the effect of disorder on the condensate fraction. And recently, the influence of disorder on the Berezinskii-Kosterlitz-Thouless transition has been analyzed in Palaiseau [138], and in the group of S. Rolston in NIST [139], and a shift of the transition temperature was observed.

Finally, a great quest at the beginning of my thesis, was the observation of Anderson localization of matter waves in dimension higher than one. Two-dimensional motion of atoms in speckle potential had been investigated in Palaiseau, in the classical regime [17, 23], yet, as we will see, observation of Anderson localization in 2D remains a great challenge, as it is the marginal dimension. In three dimension, several theoretical proposals had been made for isotropic disorder [16, 141]. However, the effect of the specific anisotropic correlations of speckle potentials on transport properties, had not been investigated yet. We collaborated with the experimental group in Palaiseau, which permitted to show the first evidence of 3D Anderson localization, in real space, with ultra-cold atoms in speckle potentials, with a Bose-Einstein condensate [19]; almost at the same time as it was shown in a fermionic gas, in Urbana-Champaign [18]. Those experiments, which are directly relevant for this thesis, are described and analyzed in view of our theoretical results in Sec. 7.

Cold atomic systems have also been used to investigate the 3D Anderson transition in a kicked-rotor setup [142]. This system can be mapped onto an Anderson Hamiltonian [143], and localization is then observed in momentum space. It recently permitted to measure the universal critical exponents of the transition [144], and the results are in agreement with numerical predictions [61].

Therefore many experiments with cold atoms in disorder are currently carried out. It shows that, apart from the 'grail quest' which is direct observation of Anderson localization of matter waves in real space, ultra-cold atoms will permit to address many other challenges in the field, where a number of questions are still debated. They also present specific features that are to be addressed theoretically, as is done in this thesis. We will study transport and localization of non-interacting matterwaves in disorder with a special emphasis on anisotropy and statistical correlations of the disorder.

## Conclusion

Waves and disorder are everywhere. It is therefore very important to understand the effect of disorder in many fields, ranging from condensed matter systems (where interactions are also important) to classical waves. Disorder has now also invested ultra-cold atoms: The observation of 1D Anderson localization of ultra-cold atoms in 2008 [9, 10] triggered the field to address many other challenges by adding interactions and investigating higher dimensionalities. Cold atoms are model systems, whose parameters are under great experimental control, but they also have their own specificities. In particular, the effect of correlations (which can be anisotropic and structured) had not been investigated a lot. It is the subject of this thesis, and in the following, we will mainly focus on the study of quantum transport with the specificities of ultra-cold atoms.



## Chapter 2

# Quantum transport theory: Matter waves in disordered media

### Abstract

After presenting a simple physical picture of transport and localization of waves in disordered media, we review the basics of quantum transport theory in a form adapted to matter waves. We introduce the general formalism to describe single-scattering as well as multiple-scattering of a quantum particle in a disordered medium. To characterize transport, we define the Green function which follows from the Dyson equation, the density propagator, which is determined by the Bethe-Salpeter equation, and a conductivity for our system. We discuss the physical meaning of those quantities, how they can be computed diagrammatically, and how to proceed to disorder averaging. We also discuss how these quantities, which are energy-dependent, can be used to describe the transport and localization of wave packets with broad energy distributions. This chapter is a toolbox for Chaps. 4 to 8.

### Résumé

Après avoir présenté une image physique simple du transport et de la localisation d'ondes en milieu désordonné, nous présentons les bases de la théorie de transport quantique, dans un cadre adapté aux ondes de matière. Nous introduisons le formalisme général permettant de décrire un événement de diffusion unique ainsi que la diffusion multiple d'une particule quantique dans le milieu désordonné. Afin de caractériser le transport, nous définissons la fonction de Green, régie par l'équation de Dyson, le propagateur de densité, déterminé par l'équation de Bethe-Salpeter, et une conductivité pour notre système. Nous discutons le sens physique de ces quantités, comment elles peuvent être calculées par des méthodes diagrammatiques, et comment procéder au moyennage sur les configurations du désordre. Nous discutons aussi comment ces quantités, qui dépendent de l'énergie, peuvent être utilisées pour décrire le transport et la localisation de paquets d'onde ayant une large distribution d'énergie. Ce chapitre est une boîte à outils pour les Chaps. 4 à 8.



## Introduction: Basics of quantum transport

Before turning to a more formal description in this chapter and the next ones, it is worth recalling the basic picture of coherent transport in a disordered medium. The basic ingredients are genuinely understood in a microscopic approach [42, 58]. Consider a wave of momentum  $\mathbf{k}$  (and velocity  $\mathbf{v} = \hbar\mathbf{k}/m$ ) propagating in a disordered medium<sup>1</sup>. The anisotropy of the disordered medium will be an important ingredient of the following, but let us assume, for the moment, that the medium is isotropic. We will then drop this assumption in the rest of the manuscript, and we will see that it doesn't change the physical picture presented here.

The wave propagation is governed by scattering from the random impurities. Three typical energy-dependent length scales can be identified<sup>2</sup>, which characterize three basic effects induced by the disorder (see Fig. 2.1). First, single scattering from impurities depletes the  $\mathbf{k}$ -wave states, which can be seen as quasiparticles in the disordered medium, with a finite life-time  $\tau_s(k)$ . Single scattering hence defines the first length scale, namely the *scattering mean-free path*,  $l_s = v\tau_s$ , which characterizes the typical length travelled by the wave before it loses the memory of its initial state.

Then, multiple scattering defines the second length scale, namely the *transport (Boltzmann) mean-free path*,  $l_B$ , which characterizes the typical length travelled by the wave before it loses the memory of its initial direction. In general, several scattering events are necessary to significantly deflect the trajectories so that  $l_B \geq l_s$ . The two length scales are found to be equal only in the white-noise limit (if it exists), where the wavelength is smaller than the typical size of the impurities. The disorder is then equivalent to a set of randomly distributed Dirac peaks and the scattering is isotropic. In this case the wave loses the memory of its initial state and initial propagation direction at the same time. In the general case, within the distance  $l_B$ , the transport crosses over from ballistic to diffusive. The average squared size of the wavepacket increases linearly in time,  $\overline{\mathbf{r}^2} \sim 2dD_B t$ , with  $D_B = vl_B/d$  (where  $d$  is the space dimension) the Boltzmann diffusion constant [34, 54].

Finally, diffusive transport allows the wave to return to its initial position via loop paths, and interference effects enter the game. Each loop can be travelled in one way or the other, which generates two multiple-scattering paths along which exactly the same phase is accumulated during the successive scattering events. This coherent effect holds for any specific realization of the disordered potential and thus survives disorder averaging. Moreover, since these two paths are in phase, this gives rise to a constructive interference of the matter wave, which significantly enhances its return probability. This effect induces coherent back-scattering and weak localization (see Sec. 1.2.1), which leads to diffusive transport with a reduced diffusion coefficient,  $D_* < D_B$  [41]. For strong-enough disorder, the diffusion can completely cancel, an effect known as strong, or Anderson, localization [145]. Then, the probability distribution of the wave decays exponentially in space, hence defining the third characteristic length,  $L_{\text{loc}}$ , the so-called *localization length*. The picture above shows that localization relies on two characteristics of the medium: coherence along the multiple-scattering paths and return probability to the origin. One then understands that the strength of localization should be governed by the interference parameter  $kl_B$  [55] (since the more the coherence length exceeds the typical

---

1. Here we assume for simplicity the dispersion relation  $\epsilon(\mathbf{k}) = \hbar^2\mathbf{k}^2/2m$  which holds for studies reported in the next chapter. The discussion can be generalized to any dispersion relation  $\epsilon(\mathbf{k})$ , such that  $\mathbf{v} = \nabla_{\mathbf{k}}\epsilon/\hbar$ .

2. Alternatively, one can identify three typical time scales  $\tau$ , which are straightforwardly associated to the length scales  $l$  by the relation  $\tau = l/v$ .

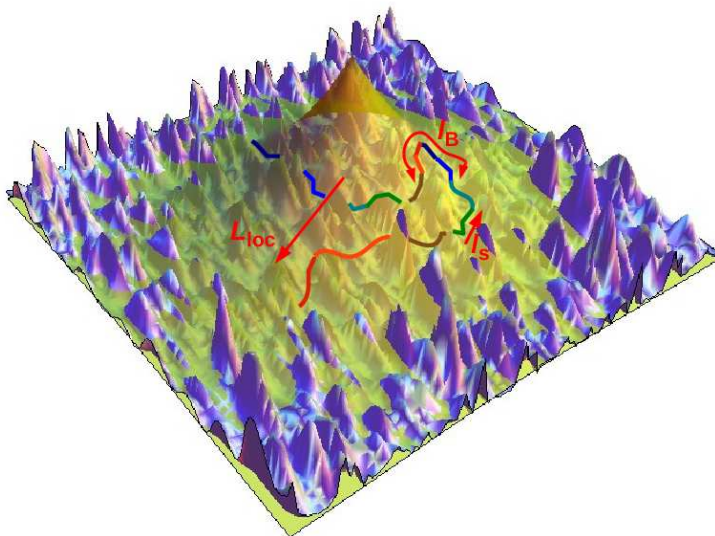


Figure 2.1: Schematic view of the coherent transport of a matter wave in a disordered medium, with special emphasis on the characteristic length scales. The figure shows a trajectory of a particle (solid multicolor line) in a two-dimensional disordered landscape (blue surface). Along its trajectory, the wave loses the memory of its phase (encoded in the various colors along the trajectory) on the characteristic length  $l_s$  (scattering mean-free path). Multiple scattering then deflects the trajectory and the wave loses the memory of its direction on the characteristic length  $l_B$  (transport mean-free path). Interference between the multiple-scattering paths can finally cancel diffusion (strong or Anderson localization). The wave then acquires an exponentially decaying probability profile (orange-green surface) of characteristic length  $L_{loc}$  (localization length).

length of a loop path, the more significant interference terms are), and by the dimension of space  $d$  (since the return probability decreases when  $d$  increases).

As a matter of fact, the above outlined picture, where diffusion is a precursor of localization, is not strictly valid in 1D, where diffusion is absent<sup>3</sup>, and the return probability is very high. It should be remembered that, in 1D and 2D, any state is localized [56]. In 2D one finds  $l_B < L_{loc}$  and diffusion shows up at intermediate distances and times. In 3D, where the return probability is weak, and becomes weaker and weaker as the energy increases, localization is found only at sufficiently low energy. In this case, a mobility edge shows up, which separates localized states (for  $kl_B \lesssim 1$ ) from diffusive states (for  $kl_B \gtrsim 1$ ) [56, 146, 147].

The microscopic description outlined above offers a comprehensive picture of transport and localization effects for coherent waves in disordered media. In the next sections we will give mathematical support to this picture. The formalism is rather involved, in particular for the anisotropic models of disorder we are interested in. The interpretation of this formalism will however drive us back to this picture, as we will see.

---

3. For instance, when calculating the Boltzmann mean-free path in 1D, one finds that it is of the same order as the localization length.

## 2.1 Green functions

Let us turn to a more formal description. Consider a quantum particle in a given homogeneous underlying medium and subjected to some static randomness. We are first interested in calculating its wave function  $\psi(t)$ , which contains all the information about the dynamics of the system. It is governed by the Schrödinger equation

$$i\hbar \frac{\partial}{\partial t} |\psi(t)\rangle = H |\psi(t)\rangle \quad (2.1)$$

with the single-particle Hamiltonian

$$H = H_0 + V(\mathbf{r}), \quad (2.2)$$

where  $H_0$  is the disorder-free, translation-invariant, Hamiltonian of the underlying medium, and  $V(\mathbf{r})$  is the time-independent (conservative) disordered potential. For a particle in free space, which we will mainly consider below, the underlying medium is the vacuum, and  $H_0 = -\frac{\hbar^2}{2m} \nabla^2$ . Without loss of generality, the disordered potential can be assumed to be of zero mean value<sup>4</sup>  $\overline{V} = 0$ . The evolution of the wave function between times  $t_0$  and  $t > t_0$  is determined by the retarded single-particle propagator  $G(t, t_0)$ , such that

$$|\psi(t)\rangle = G(t, t_0) |\psi(t_0)\rangle \quad (2.3)$$

with

$$G(t, t_0) \equiv e^{-iH(t-t_0)/\hbar} \Theta(t - t_0), \quad (2.4)$$

where the Heaviside step function  $\Theta(t - t_0)$  accounts for temporal ordering. In the energy domain<sup>5</sup>,  $G$  is the retarded Green operator

$$G(E) = (E - H + i0^+)^{-1}, \quad (2.5)$$

where  $E$  is the particle energy. It is the solution of the equation

$$G(E) = G_0(E) + G_0(E) V G(E), \quad (2.6)$$

where  $G_0 = (E - H_0 + i0^+)^{-1}$  is the disorder-free retarded Green function associated to the unperturbed Hamiltonian  $H_0$ .

The disorder-free retarded Green function, which is a translation-invariant operator, is conveniently written in momentum representation<sup>6</sup>, where it is diagonal. It reads

$$\begin{aligned} \langle \mathbf{k} | G_0(E) | \mathbf{k}' \rangle &\equiv (2\pi)^d \delta(\mathbf{k} - \mathbf{k}') G_0(E, \mathbf{k}) \\ &= \frac{(2\pi)^d \delta(\mathbf{k} - \mathbf{k}')}{E - \epsilon(\mathbf{k}) + i0^+}, \end{aligned} \quad (2.7)$$

---

4. For any other choice of the energy reference all energies appearing below should be shifted by  $\overline{V}$ , i.e. replace  $E$  by  $E - \overline{V}$ .

5. Here, we use the convention for Fourier transform  $G(E) \equiv \frac{-i}{\hbar} \int d\tau G(\tau) \exp[iE\tau/\hbar]$ .

6. The states  $|\mathbf{k}\rangle$  represent the plane waves, normalized by the relation  $\int \frac{d\mathbf{k}}{(2\pi)^d} |\mathbf{k}\rangle \langle \mathbf{k}| = 1$ .

where  $\epsilon(\mathbf{k})$  [here equal to  $\hbar^2\mathbf{k}^2/2m$ ] is the dispersion relation associated to  $H_0$  [ $\langle\mathbf{k}|H_0|\mathbf{k}'\rangle \equiv (2\pi)^d\delta(\mathbf{k}-\mathbf{k}')\epsilon(\mathbf{k})$ ] and  $d$  the space dimension. For an isotropic underlying medium,  $\epsilon(\mathbf{k})$  and the Green function  $G_0(E, \mathbf{k})$  depend only on the modulus of  $\mathbf{k}$ ,  $k \equiv |\mathbf{k}|$ .

The Green function  $G(E)$  contains all the information about the dynamics of the particle for any realization of the disordered potential. It is not translation invariant for each realization of the disorder. As we will see below, its average  $\overline{G}(E)$  over the disorder realizations is translation invariant. It contains some but not all the information about the average dynamics of the system, and some quantities depend on higher moments of the distribution of  $G(E)$ .

## 2.2 Properties of the disordered medium

The calculation of any observable quantity is specific to the particular realization of the disorder. Therefore, meaningful quantities correspond to statistical averages over realizations of disordered potentials. When averaging over disorder realizations, some quantities can be written in terms of the average Green function  $\overline{G}(E)$ , for instance the spectral function (see below).

**Dyson equation** – In order to compute  $\overline{G}(E)$ , one can use the Born series of Eq. (2.6), averaged over the disorder, which reads

$$\overline{G} = G_0 + G_0\overline{V}G_0\overline{V}G_0 + G_0\overline{V}G_0\overline{V}G_0\overline{V}G_0 + \dots \quad (2.8)$$

where the first order term  $G_0\overline{V}G_0$  drops owing to our choice of energy reference,  $\overline{V} = 0$ . It is convenient to represent this equation diagrammatically:



$$\text{thick black arrow} = \text{grey arrow} + \text{grey arrow with two dots and dashed arc} + \text{grey arrow with two dots, dashed arc, and vertical dashed line} + \dots \quad (2.9)$$

where a plain line is a Green function (grey for  $G_0$  and black for  $\overline{G}$ ), the vertices (black dots) are scattering events and the dashed lines recall that they are correlated. One can also write the Dyson equation [90]

$$\overline{G} = G_0 + G_0\Sigma\overline{G}, \quad (2.10)$$

which is formally solved by

$$\overline{G} = (G_0^{-1} - \Sigma)^{-1}. \quad (2.11)$$

The self energy  $\Sigma(E)$  can be developed in powers of  $V$  by identifying terms of increasing power in  $\Sigma$  or  $V$  in the developments of Eqs. (2.8) and (2.10). The self energy is then the sum of all the diagrams that cannot be generated by chaining two, or more, lower-order diagrams which are already in the self energy. Those basic diagrams, which cannot be split in two by cutting only one free Green function line, are called 'irreducible'.

**Translation-invariance** – As already said, for a given realization of the disorder,  $G(E)$  is not a translation-invariant operator. However, for all the cases we will be interested in, the disorder is homogeneous, i.e. its statistical properties are translation-invariant [37]. The invariance by translation is then restored *after* ensemble-averaging. The disorder-averaged Green function is then diagonal in  $\mathbf{k}$ -space, and it reads [see Eqs. (2.7) and (2.11)]:

$$\begin{aligned} \langle \mathbf{k} | \overline{G}(E) | \mathbf{k}' \rangle &\equiv (2\pi)^d \delta(\mathbf{k} - \mathbf{k}') \overline{G}(E, \mathbf{k}) \\ &= \frac{(2\pi)^d \delta(\mathbf{k} - \mathbf{k}')}{E - \epsilon(\mathbf{k}) - \Sigma(E, \mathbf{k}) + i0^+}. \end{aligned} \quad (2.12)$$

In addition, if the statistical properties of the disorder are isotropic, then  $\overline{G}(E, \mathbf{k}) \equiv \overline{G}(E, k)$ .

**Spectral function** – As mentioned above, the knowledge of the average Green function  $\overline{G}$  is sufficient to calculate certain quantities. It is the case of the spectral function  $A(E, \mathbf{k})$  defined by [58]:

$$2\pi \langle \mathbf{k} | \overline{\delta(E - H)} | \mathbf{k}' \rangle \equiv (2\pi)^d \delta(\mathbf{k} - \mathbf{k}') A(E, \mathbf{k}). \quad (2.13)$$

It contains all the information about the spectrum of the disordered medium. For example, the average density of states (per unit volume) reads

$$N(E) = \int \frac{d\mathbf{k}}{(2\pi)^d} \frac{A(E, \mathbf{k})}{2\pi}. \quad (2.14)$$

Using Eq. (2.5), it yields

$$A(E, \mathbf{k}) = -2\Im \left[ \overline{G}(E, \mathbf{k}) \right]. \quad (2.15)$$

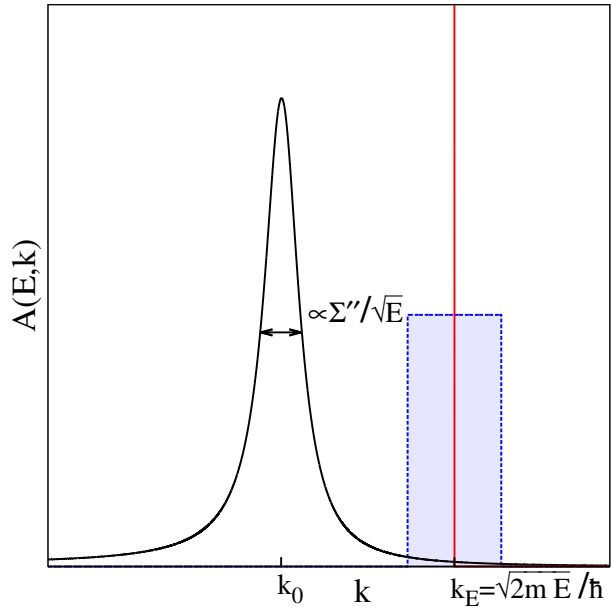
The spectral function can be interpreted (up to a numerical factor) as the (normalized) probability density for an excitation of momentum  $\mathbf{k}$  to have energy  $E$  and  $\int \frac{dE}{2\pi} A(E, \mathbf{k}) = 1$ . It is also the unnormalized probability, per unit energy, to find a particle of energy  $E$  with momentum  $\mathbf{k}$ , as  $\int \frac{d\mathbf{k}}{(2\pi)^d} A(E, \mathbf{k}) = 2\pi N(E)$  [see Eq. (2.14)]. For a particle in disorder-free space, it is given by  $A_0(E, \mathbf{k}) = 2\pi \delta[E - \epsilon(\mathbf{k})]$ . In the presence of disorder, Eqs. (2.12) and (2.15) yield

$$A(E, \mathbf{k}) = \frac{-2\Sigma''(E, \mathbf{k})}{\left(E - \epsilon(\mathbf{k}) - \Sigma'(E, \mathbf{k})\right)^2 + \Sigma''(E, \mathbf{k})^2}, \quad (2.16)$$

with  $\Sigma'$  and  $\Sigma''$  the real and imaginary parts of  $\Sigma$ , respectively. As represented schematically in Fig. 2.2, for a particle in free space [ $\epsilon(\mathbf{k}) = \hbar^2 k^2 / 2m$ ] with a weak disordered potential [ $\Sigma(E, \mathbf{k})$  weakly depends on the momentum], the spectral function has a Lorentzian-like shape as a function of  $\mathbf{k}^2$ . It is centered in  $\mathbf{k}_0$ , solution of  $E - \epsilon(\mathbf{k}_0) - \Sigma'(E, \mathbf{k}_0) = 0$ . The quantity  $\Sigma'(E, \mathbf{k}_0)$  thus describes the shift in energy of the free-particle modes when they are dressed by the disorder. The quantity  $\Sigma''(E, \mathbf{k})$  is the energy width of the spectral function, which defines the scattering mean free time

$$\tau_s(E, \mathbf{k}) = -\frac{\hbar}{2\Sigma''(E, \mathbf{k})}, \quad (2.17)$$

Figure 2.2: Schematic representation of the spectral function  $A(E, \mathbf{k})$  of a particle of energy  $E$ , as a function of the particle momentum  $\mathbf{k}$ . The vertical red line is the spectral function for the disorder free particle  $A_0(E, \mathbf{k}) = 2\pi\delta[E - \epsilon(\mathbf{k})]$  with  $\epsilon(\mathbf{k}) = \hbar^2 k^2/2m$ . In the presence of disorder the spectral function is shifted and broadened (black line). The standard on-shell approximation consists in neglecting the energy shift related to the real part of the particle self energy and the structure of the spectral function [(schematic) dashed blue line].



or equivalently the scattering mean free path  $l_s(E, \mathbf{k}) = |\mathbf{v}| \tau_s(E, \mathbf{k})$ . It accounts for the depletion of the free particle mode at  $E = \epsilon(\mathbf{k})$  due to scattering from the disordered medium. Therefore the spectral function contains all the information about the relative weight, the energy, and the lifetime of the quasi-particles, i.e. the particles dressed by the disordered medium, which on average define an effective medium.

**Energy distribution** – In ultracold-atom experiments (see chapters 4 and 7), a broad range of energies are involved, but only the momentum distribution is usually measured by time-of-flight techniques. The spectral function permits to relate the energy distribution ( $\mathcal{D}_E$ ) and the momentum distribution ( $\mathcal{D}_k$ ) of the stationary particles in the disorder via

$$\mathcal{D}_E(E) = \int \frac{d\mathbf{k}}{(2\pi)^d} A(E, \mathbf{k}) \mathcal{D}_k(\mathbf{k}), \quad (2.18)$$

which is normalized by  $\int \frac{dE}{2\pi} \mathcal{D}_E(E) = 1$ . The calculation of the energy distribution therefore requires the knowledge of the full spectral function, i.e. of the real and imaginary parts of the self energy  $\Sigma$  [see Eq. (2.16)]. This is, in general, a complicated task, especially in dimensions larger than one and for anisotropic disorder. In Sec. 5.1 we will compute the spectral function by employing a perturbation theory and retaining only the first order in the self energy (Born approximation) in Eq. (2.8) or (2.9). In Sec. 7.2, we will compute the spectral function numerically by direct diagonalization of the disordered Hamiltonian and an average over disorder realizations, according to Eq. (2.13).

**On-shell approximation** – The spectral function will be a key element at each step of the following calculations, where we will compute quantities that depend on the energy  $E$ . In the framework of the usual on-shell approximation [42, 90, 148, 149], when spectral functions, or combinations of spectral and Green functions, appear in the calculation, one usually neglects the real part of the self-energy  $\Sigma'(E, \mathbf{k})$  and the structure of the spectral function

(see schematic dashed blue line in Fig. 2.2). It permits to drop some integrals over  $\mathbf{k}$ , and therefore lead the analytic calculations. It is justified for weak disorder, in which the self energy is small. We make use of this approximation in Chap. 5 (see also appendix C.1), and we will see that it is well supported in weak disorder, in particular in 1D (see Chap. 4) but also for the diffusive regime in 3D (see Chap. 7). We will however discuss its relevance and show how to extend it for calculating the 3D mobility edge.

## 2.3 Propagation of the Wigner function

Some observables are not simply related to the average Green function  $\overline{G}$  and require a more elaborate treatment. It is for instance the case of the spatial density and the momentum distribution, which are the main observables in ultra-cold atom experiments, and which we will consider to characterize transport.

**Density propagator** – Consider the time evolution of the one-body density matrix  $\rho(t)$  [58] or equivalently of the Wigner function [150]

$$W(\mathbf{r}, \mathbf{k}, t) \equiv \int \frac{d\mathbf{q}}{(2\pi)^d} e^{i\mathbf{q}\cdot\mathbf{r}} \left\langle \mathbf{k} + \frac{\mathbf{q}}{2} \left| \rho(t) \right| \mathbf{k} - \frac{\mathbf{q}}{2} \right\rangle. \quad (2.19)$$

Its knowledge allows us to determine both the spatial density probability, given by  $n(\mathbf{r}, t) = \int \frac{d\mathbf{k}}{(2\pi)^d} W(\mathbf{r}, \mathbf{k}, t)$ , and the momentum distribution, given by  $\mathcal{D}_{\mathbf{k}}(\mathbf{k}, t) = \int d\mathbf{r} W(\mathbf{r}, \mathbf{k}, t)$ . It is fruitful to rewrite Eq. (2.19) in a form explicitly indicating the initial conditions, making use of the relation  $\rho(t) = \Theta(t - t_0) e^{-iH(t-t_0)/\hbar} \rho(t_0) e^{+iH(t-t_0)/\hbar}$ . When averaging over disorder, if there is no correlations between the initial state and the disorder<sup>7</sup>, one finds [151]

$$\overline{W}(\mathbf{r}, \mathbf{k}, t) = \int d\mathbf{r}' \int \frac{d\mathbf{k}'}{(2\pi)^d} W_0(\mathbf{r}', \mathbf{k}') F_{\mathbf{k}, \mathbf{k}'}(\mathbf{r} - \mathbf{r}'; t - t_0), \quad (2.20)$$

where  $W_0(\mathbf{r}, \mathbf{k}) \equiv W(\mathbf{r}, \mathbf{k}, t_0)$  is the initial Wigner function and  $F_{\mathbf{k}, \mathbf{k}'}(\mathbf{R}; t)$  is the phase-space propagation kernel, defined by (if  $t > 0$ )

$$F_{\mathbf{k}, \mathbf{k}'}(\mathbf{R}; t) \equiv \int \frac{dE}{2\pi} \int \frac{d\mathbf{q}}{(2\pi)^d} \int \frac{d\hbar\omega}{2\pi} e^{i\mathbf{q}\cdot\mathbf{R}} e^{-i\omega t} \Phi_{\mathbf{k}, \mathbf{k}'}(\mathbf{q}, \omega, E), \quad (2.21)$$

and

$$\overline{\langle \mathbf{k}_+ | G(E_+) | \mathbf{k}'_+ \rangle \langle \mathbf{k}'_- | G^\dagger(E_-) | \mathbf{k}_- \rangle} \equiv (2\pi)^d \delta(\mathbf{q} - \mathbf{q}') \Phi_{\mathbf{k}, \mathbf{k}'}(\mathbf{q}, \omega, E), \quad (2.22)$$

with  $\mathbf{k}_\pm \equiv \mathbf{k} \pm \mathbf{q}/2$ ,  $\mathbf{k}'_\pm \equiv \mathbf{k}' \pm \mathbf{q}'/2$ ,  $E_\pm \equiv E \pm \hbar\omega/2$ , and  $(\mathbf{q}, \omega)$  the Fourier conjugates of the space and time variables<sup>8</sup>. As discussed above, disorder averaging features a translation invariance in space and introduces an effective medium for the expanding wave. As a direct consequence, Eq. (2.21) depends only on the difference  $\mathbf{R} = \mathbf{r} - \mathbf{r}'$ , which expresses the equivalence of all points in space. For the same reason, translation invariance, or equivalently momentum conservation, imposes that the sum of the in-going wavevectors ( $\mathbf{k}_+$  and  $\mathbf{k}'_-$ ) on one hand, and out-going wavevectors ( $\mathbf{k}'_+$  and  $\mathbf{k}_-$ ) on the other hand, are equal. It leads to the condition on momentum transfer:  $\mathbf{q} = \mathbf{q}'$  in Eq. (2.22).

7. This holds if the disorder is abruptly turned on at time  $t_0$ , but not if it is already present initially.

8. We use the Fourier transform  $\tilde{f}(\mathbf{q}, \omega) \equiv \int d\mathbf{r} dt f(\mathbf{r}, t) \exp[-i(\mathbf{q} \cdot \mathbf{r} - \omega t)]$ .

**Bethe-Salpeter equation** – As we have just seen, the building block to describe wave propagation in random media is the density propagator  $\Phi$ , which can be represented as a four-point vertex with  $\mathbf{k}_\pm$  and  $\mathbf{k}'_\pm$  the left and right entries [see left-hand side of Eq. (2.24)]. The skeleton of this vertex is made by a retarded and an advanced Green functions (respectively  $G$ , represented by the top line, and  $G^\dagger$ , represented by the bottom line). It contains all possible correlations between the scattering events of these Green functions. Following the same approach as used for the average field propagator  $\overline{G}$  [leading to the Dyson equation (2.10)], the vertex  $\Phi = \overline{G} \otimes \overline{G}^\dagger$  is formally constructed from the uncorrelated-average vertex  $\overline{G} \otimes \overline{G}^\dagger$ . The operator  $\Phi$  is then governed by the so-called Bethe-Salpeter equation [58]

$$\Phi = \overline{G} \otimes \overline{G}^\dagger + \overline{G} \otimes \overline{G}^\dagger U \Phi. \quad (2.23)$$

It can be represented diagrammatically by

$$\begin{array}{c} \mathbf{k}_+ \quad \mathbf{k}'_+ \\ \square \\ \Phi \\ \mathbf{k}_- \quad \mathbf{k}'_- \end{array} = \begin{array}{c} \mathbf{k}_+ \\ \longrightarrow \\ \mathbf{k}_- \\ \longleftarrow \end{array} + \begin{array}{c} \mathbf{k}_+ \quad \mathbf{k}'_+ \\ \square \quad \square \\ U \quad \Phi \\ \mathbf{k}_- \quad \mathbf{k}'_- \end{array} \quad (2.24)$$

where  $U$  is the vertex function including all irreducible four-point scattering diagrams:

$$\square \quad U = \begin{array}{c} \bullet \\ \vdots \\ \bullet \end{array} + \begin{array}{c} \bullet \quad \bullet \\ \longrightarrow \quad \longrightarrow \\ \bullet \quad \bullet \\ \longleftarrow \quad \longleftarrow \end{array} + \begin{array}{c} \bullet \quad \bullet \\ \longrightarrow \quad \longrightarrow \\ \bullet \quad \bullet \\ \longleftarrow \quad \longleftarrow \end{array} + \dots \quad (2.25)$$

The first term in the Bethe-Salpeter equation [Eq. (2.23) or (2.24)] describes uncorrelated propagation of the field and its conjugate in the effective medium. The second term accounts for all correlations in the density propagation. The Bethe-Salpeter equation is the basis of the following calculations for deriving transport properties in the disordered medium. Note that the Bethe-Salpeter equation (2.23) does not comprise any approximation. In the next chapters we will use perturbative approaches, and select some diagrams in Eq. (2.25).

**Formal solution** – Analogously to Eq. (2.11), the solution of the Bethe-Salpeter equation (2.23)-(2.24) can be formally obtained from the inverse, if it exists [152], of the four-point operator  $\Lambda \equiv 1 - \overline{G} \otimes \overline{G}^\dagger U$ :

$$\Phi = \Lambda^{-1} \overline{G} \otimes \overline{G}^\dagger. \quad (2.26)$$

We have already expressed the elements of  $\overline{G}$  [see Eq. (2.12)] (therefore we also know those of  $\overline{G}^\dagger \equiv \overline{G}^\dagger$ ), and we are left with calculating  $\Lambda$ . Explicitly, the  $(\mathbf{k}, \mathbf{k}')$  component of a four-point vertex  $\Lambda$  which fulfills momentum conservation is  $\Lambda_{\mathbf{k}, \mathbf{k}'}(\mathbf{q}, \omega, E)$ , such that  $\langle \mathbf{k}_+, \mathbf{k}'_- | \Lambda | \mathbf{k}'_+, \mathbf{k}_- \rangle \equiv (2\pi)^d \delta(\mathbf{q} - \mathbf{q}') \Lambda_{\mathbf{k}, \mathbf{k}'}(\mathbf{q}, \omega, E)$ , and<sup>9</sup>

$$\Lambda_{\mathbf{k}, \mathbf{k}'}(\mathbf{q}, \omega, E) = (2\pi)^d \delta(\mathbf{k} - \mathbf{k}') - f_{\mathbf{k}}(\mathbf{q}, \omega, E) U_{\mathbf{k}, \mathbf{k}'}(\mathbf{q}, \omega, E), \quad (2.27)$$

9. The product of two four-point operators is defined by  $\langle \mathbf{k}_+, \mathbf{k}'_- | AB | \mathbf{k}'_+, \mathbf{k}_- \rangle \equiv \int \frac{d\mathbf{k}''_+}{(2\pi)^d} \int \frac{d\mathbf{k}''_-}{(2\pi)^d} \langle \mathbf{k}_+, \mathbf{k}''_+ | A | \mathbf{k}''_+, \mathbf{k}_- \rangle \langle \mathbf{k}''_+, \mathbf{k}'_- | B | \mathbf{k}'_+, \mathbf{k}''_- \rangle$ , and the tensor product of two Green operators reads  $\langle \mathbf{k}_+, \mathbf{k}'_- | G \otimes G^\dagger | \mathbf{k}'_+, \mathbf{k}_- \rangle \equiv \langle \mathbf{k}_+ | G | \mathbf{k}'_+ \rangle \langle \mathbf{k}'_- | G^\dagger | \mathbf{k}_- \rangle$ .

and

$$f_{\mathbf{k}}(\mathbf{q}, \omega, E) \equiv \overline{G}(E_+, \mathbf{k}_+) \overline{G}^\dagger(E_-, \mathbf{k}_-). \quad (2.28)$$

Therefore Eq. (2.26) reads<sup>10</sup>

$$\Phi_{\mathbf{k}, \mathbf{k}'}(\mathbf{q}, \omega, E) = \Lambda_{\mathbf{k}, \mathbf{k}'}^{-1}(\mathbf{q}, \omega, E) f_{\mathbf{k}'}(\mathbf{q}, \omega, E). \quad (2.29)$$

Note that the operator  $\Lambda^{-1}(\omega, E)$  can be expressed in terms of the eigenvectors and associated eigenvalues of the operator  $\Lambda(\omega, E)$ .

The calculation of the eigenvectors of the operator  $\Lambda(\omega, E)$  is the basic idea followed in Refs. [153, 154] and in Chap. 5 to solve the Bethe-Salpeter equation. It then gives access, via  $\Phi$  which is the quantity of interest, to the time dependence of the Wigner function [see Eqs. (2.19) to (2.21)], and of the spatial density in particular.

**Diffusion pole** – In order to describe the physical meaning of the vertex  $\Phi$ , it is worth discussing its usual form. In the following we will see that  $\Lambda$  is not invertible when  $(\mathbf{q} = 0, \omega = 0)$ . However, it can be inverted in the limit of small (but non-zero)  $(\mathbf{q}, \omega)$ , i.e. in the long-time and large-distance limit (see Chap. 5 and appendix C.1). The intensity kernel  $\Phi$  then has a *diffusion pole*, which takes the form

$$\Phi_{\mathbf{k}, \mathbf{k}'}(\mathbf{q}, \omega, E) = \frac{1}{2\pi N(E)} \frac{A(E, \mathbf{k})A(E, \mathbf{k}')}{i\hbar\omega - \hbar\mathbf{q} \cdot \mathbf{D}(\omega, E) \cdot \mathbf{q}} \quad (2.30)$$

where  $\mathbf{D}$  is a  $d$ -dimensional tensor, so called dynamic diffusion tensor.

The average spatial density distribution is then given by [see Eqs. (2.20) and (2.21)]

$$\begin{aligned} \overline{n}(\mathbf{r}, t) &= \int \frac{d\mathbf{k}}{(2\pi)^d} \overline{W}(\mathbf{r}, \mathbf{k}, t) \\ &= \int \frac{dE}{2\pi} \int d\mathbf{r}' \mathcal{D}_0(\mathbf{r}', E) P(\mathbf{r} - \mathbf{r}', t - t_0 | E) \end{aligned} \quad (2.31)$$

where  $\mathcal{D}_0(\mathbf{r}', E) = \int \frac{d\mathbf{k}'}{(2\pi)^d} A(E, \mathbf{k}') W_0(\mathbf{r}', \mathbf{k}')$  represents the initial joint position-energy density and  $P(\mathbf{r} - \mathbf{r}', t - t_0 | E)$  is the probability of quantum transport, i.e. the probability for a particle of energy  $E$  originating from point  $\mathbf{r}'$  at time  $t_0$  to be in  $\mathbf{r}$  at  $t$ . It can be expressed thanks to Eqs. (2.20), (2.21) and (2.30) as the space-time Fourier Transform of the diffusion pole:

$$P(\mathbf{R}, t | E) = \int \frac{d\mathbf{q}}{(2\pi)^d} \int \frac{d\hbar\omega}{2\pi} \frac{e^{i\mathbf{q} \cdot \mathbf{R}} e^{-i\omega t}}{i\hbar\omega - \hbar\mathbf{q} \cdot \mathbf{D}(\omega, E) \cdot \mathbf{q}}. \quad (2.32)$$

**Propagation kernel** – In the long-time limit, we will encounter two different situations. First, if  $\lim_{\omega \rightarrow 0} \mathbf{D}(\omega, E) = \mathbf{D}(E)$  is a real definite positive tensor, the probability of quantum transport [see Eq. (2.32)] reads

$$P(\mathbf{R}, t \rightarrow \infty | E) = \frac{e^{-\mathbf{R} \cdot \mathbf{D}^{-1}(E) \cdot \mathbf{R} / 4t}}{\sqrt{(4\pi t)^d \det \{\mathbf{D}(E)\}}} \Theta(t), \quad (2.33)$$

---

10. The inverse of an operator  $\Lambda$  is defined by  $\int \frac{d\mathbf{k}_1}{(2\pi)^d} \Lambda_{\mathbf{k}, \mathbf{k}_1}(\mathbf{q}, \omega, E) \Lambda_{\mathbf{k}_1, \mathbf{k}'}^{-1}(\mathbf{q}, \omega, E) = (2\pi)^d \delta(\mathbf{k} - \mathbf{k}')$ .

where  $\Theta(t) \equiv 1$  if  $t > 0$  and 0 otherwise. For example, in the orthonormal basis  $\{\mathbf{e}_i\}$  in dimension  $d$  where  $\mathbf{D}(E)$  is diagonal, we find  $P(\mathbf{R}, t \rightarrow \infty | E) = \prod_{i=1}^d \exp[-R_i^2/4D^i(E)t] / [4\pi D^i(E)t]^{d/2}$ . The diffusion pole of the intensity kernel (2.30) therefore describes a diffusive behaviour with the anisotropic diffusion tensor  $\mathbf{D}(E)$  (hence its name!).

Second, we will encounter situations where normal diffusion vanishes. We will then find  $\mathbf{D}(\omega, E) \sim 0^+ - i\omega \mathbf{L}_{\text{loc}}^2(E)$  in the limit  $\omega \rightarrow 0^+$  with  $\mathbf{L}_{\text{loc}}(E)$  a real positive definite tensor. In this case the pole in Eq. (2.30) describes localization. In 2D, it leads to,

$$P(\mathbf{R}, t \rightarrow \infty | E) = \frac{K_0 \left( \sqrt{\mathbf{R} \cdot \mathbf{L}_{\text{loc}}^{-2}(E) \cdot \mathbf{R}} \right)}{2\pi \det\{\mathbf{L}_{\text{loc}}(E)\}} \Theta(t) \quad (2.34)$$

where  $K_0$  is the modified Bessel function. In the large distance limit ( $x \gg 1/4$ ), one finds  $K_0(x) \sim e^{-x} \sqrt{\pi/2x}$ , and therefore, in each eigen-direction of the tensor  $\mathbf{L}_{\text{loc}}(E)$ , the density decreases as  $\exp[-|R_i|/L_{\text{loc}}^i(E)] / \sqrt{|R_i|}$  at large distance. In 3D, we find,

$$P(\mathbf{R}, t \rightarrow \infty | E) = \frac{e^{-\sqrt{\mathbf{R} \cdot \mathbf{L}_{\text{loc}}^{-2}(E) \cdot \mathbf{R}}}}{4\pi \det\{\mathbf{L}_{\text{loc}}(E)\} \sqrt{\mathbf{R} \cdot \mathbf{L}_{\text{loc}}^{-2}(E) \cdot \mathbf{R}}} \Theta(t), \quad (2.35)$$

which behaves as  $\exp[-|R_i|/L_{\text{loc}}^i(E)] / |R_i|$  at large distance in the eigen-directions. In both 2D and 3D, we find exponentially localized probability of quantum transport at long distance, with algebraic corrections, the anisotropic localization tensor being  $\mathbf{L}_{\text{loc}}(E)$ .

In 1D, as every state is localized, we always encounter the second situation. Thanks to a perturbative approach developed by Berezinskii [155], the long-time limit of the propagation kernel can be computed at any distances in weak disorder [we recall that Eqs. (2.30) to (2.35) are valid at large distances]. For correlated disorder, the calculation is due to Gogolin *et al.* [70, 71] and is detailed in appendix B. The final expression for the propagation kernel [see Eq. (B.48)] shows that it is asymptotically exponentially-localized at any energy (see also Chap. 4).

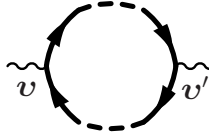
## 2.4 Conductivity and Einstein relation

**Definition** – Finally, another quantity of great interest for our problem – in parallel of those studied in sections 2.2 and 2.3 – is the conductivity. Although not usual in the context of ultra-cold atoms, it is the main quantity measured in condensed matter physics. The particles we consider do not bear any electric charge, however, in complete analogy to the usual electric conductivity in condensed matter systems [90], we here define the conductivity tensor  $\boldsymbol{\sigma}$  as proportional to the current-current correlation function, via the Kubo formula<sup>11</sup> [41]:

$$\sigma^{i,j}(\omega, E) = \int \frac{d\mathbf{k}}{(2\pi)^d} \frac{d\mathbf{k}'}{(2\pi)^d} \Re \left[ \overline{v_i \langle \mathbf{k} | G(E_+) | \mathbf{k}' \rangle v_j' \langle \mathbf{k}' | G^\dagger(E_-) | \mathbf{k} \rangle} \right], \quad (2.36)$$

11. This definition corresponds to the more general definition  $\sigma^{i,j}(\omega, E) = \int_0^\infty dt e^{i\omega t} \text{Tr}\{\delta(E - H) j_i(x, t) j_j(x)\}$  ( $j$  is the current operator) where the correlations between  $G$  and  $G^\dagger$  have been dropped (see for example Ref. [41]).

where  $v_i = \hbar k_i/m$  is the velocity along axis  $i$ . As the structure of Eq. (2.36) is reminiscent of the definition of the four-point vertex  $\Phi$  [see Eq. (2.22)], calculations of the conductivity tensor can also be represented diagrammatically. The skeleton diagram, shown in Eq. (2.37), consists of the in and out-going velocities  $\mathbf{v}$  and  $\mathbf{v}'$  and of a *bubble* made of a retarded (top line) and an advanced (bottom line) Green function. As for  $\Phi$ , the scattering events of the top and bottom lines can be correlated [see for example Eqs. (2.24) and (2.25)].


(2.37)

**Einstein relation** – Einstein pointed out that, at thermal equilibrium, for a classical gas submitted to a force, the diffusion and drift currents have to be equal. This relation holds in general for quantum systems in the linear response regime (see e.g. Ref. [58]). In particular, here we expect the DC conductivity and diffusion tensors to be proportional :  $\sigma(\omega = 0) \propto \mathbf{D}$ . More precisely, computing  $\sigma_{\text{B}}(\omega = 0)$  in the Boltzmann and Born approximations for anisotropic disorder permits to find the proportionality factor (see details in appendix C.3.1). In our system, we have

$$\sigma = \frac{2\pi N_0(E)}{\hbar} \mathbf{D} \quad (2.38)$$

where  $N_0(E)$  is the disorder-free density of states.

## Conclusion

In this chapter we presented a basic picture of quantum transport in disorder in any dimension through its different characteristic length scales: the scattering and transport mean-free paths and the localization length. We introduced basic theoretical tools for calculating those quantities in the case of disorder with anisotropic correlations. They appear in the calculations of the average Green function  $\overline{G}$  and the spectral function  $A(E, \mathbf{k})$ , which give properties of the disordered medium, and in the density propagator  $\Phi$  and the conductivity  $\sigma$ , which characterize transport. In Chaps. 4 and 5 and appendix B we will use perturbative approaches to calculate those quantities: We will select the most relevant diagrams and series of diagrams in Eqs. (2.9) and (2.25) for our problem. In particular we will proceed to the Born approximation and retain only diagrams with second order correlators, which is valid for weak disorder<sup>12</sup>.

In one dimension, the probability of quantum transport can then be computed exactly [70, 71, 155]. It is therefore exact for models of Gaussian disorder, and approximate, but valid in the weak disorder limit, for non-Gaussian disorder as speckle potentials. This technique, which consists in ordering the diagrams in real-space (see appendix B), is specific to one

---

<sup>12</sup>. This approximation is valid if the weight of the diagrams that we have neglected is negligible, i.e. if the series of scattering events that they represent is unlikely to occur. In particular, diagrams containing  $n > 2$ -correlators are significant only when the  $n$  scattering events occur within a typical volume  $\sim \sigma_{\text{R}}^d$ : They are negligible when  $l_{\text{s}} \gg \sigma_{\text{R}}$ , i.e. for weak-enough disorder.

dimension. In higher dimensions, one has to proceed with further approximations: select further the diagrams and to take the long-time and large-distance limits.

## Chapter 3

# Speckle Potentials: A model of controlled disorder

### Abstract

We describe speckle potentials, which result from spatially-random light patterns. We explain how they are obtained and controlled, and show how they can serve as correlated disordered potentials for ultra-cold atomic gases in 1D, 2D and 3D. We discuss their quite unusual statistical features, which can be anisotropic and of complex structure. In standard cases, we explicitly compute the properties that are relevant for the following, such as the intensity distribution and the two-point correlation function. We also explain how, and to what extent, the correlation properties of a speckle pattern can be tailored by simple optical means. We will take advantage of this particularity in this thesis (see in particular Chap. 8).

### Résumé

Nous décrivons les potentiels de taverlures (« speckle »), qui sont créés par des motifs de lumière aléatoires dans l'espace. Nous expliquons comment ces motifs sont obtenus et contrôlés, et nous montrons qu'ils peuvent servir de potentiels désordonnés pour des gaz d'atomes ultrafroids à 1D, 2D et 3D. Nous présentons leurs propriétés statistiques plutôt inhabituelles, qui peuvent être anisotropes et présenter des structures complexes. Pour des configurations usuelles, nous calculons explicitement les propriétés qui sont pertinentes pour la suite, telles que la distribution d'intensité et la fonction de corrélation à deux points. Nous discutons aussi comment, et dans quelle mesure, les propriétés de corrélation d'un motif de speckle peuvent être adaptées par des méthodes optiques simples. Nous utiliserons cette particularité dans ce manuscrit (en particulier dans le Chap. 8).



## Introduction: A disorder for cold atoms

Even though the approach of this manuscript (see Chaps. 2 and 5), and a number of results, do not make any assumption on the model of disorder, we have applied them to particular models of disorder, namely speckle potentials. Indeed, to study matterwaves in a disordered potential with ultracold atoms, one needs to find a way to apply a disordered potential on the atoms, whom statistical properties are well-characterized. Different ideas have been proposed in the litterature (see Sec. 1.3.2), among which are speckle potentials.

Speckle patterns (e.g. see Fig. 3.1) are spatially-random light patterns which appear in many optical devices (for example, it can be a limitation in holographic imaging or medical ultrasonography) [156]. As a non-trivial consequence of optical coherence they are a very interesting subject of research and have been extensively studied in optics [156–160]. For our concern, they act on the atoms through the dipolar force (see below) and they form a disordered medium whose statistical properties are well-characterized, somewhat unusual and quite controllable. We will see in the next chapters that they induce rich transport and localization properties. They have been widely used experimentally to create disordered potentials for cold atoms [12, 13, 20, 21] in 1D [9, 133–135, 161, 162], 2D [17, 138, 139] and 3D [18, 19] which came along with numerous theoretical proposals and studies [16, 22, 23, 25, 26, 82, 98, 103, 151, 163–170].

**The dipolar potential** – When submitted to an electromagnetic field, an atom experiences a force which is composed of a conservative and a dissipative part which results from the coupling of the atomic dipole and the electric field. The radiation pressure force (dissipative part) permits to transfer energy to the internal state of the atoms, a property which is used in laser cooling for example via the Doppler and Sisyphus processes [171]. The dipolar force (conservative part) results from the coupling of the atomic dipole with the electric field and mainly produces a position-dependent atomic energy, which can be used to trap or manipulate the atoms [172, 173]. As those two components of the same interaction scale differently with the detuning  $\delta = \omega_L - \omega_0$  of the electromagnetic field (of frequency  $\omega_L = 2\pi c/\lambda_L$  where  $c$  is the speed of light and  $\lambda_L$  the wavelength of the field) with respect to the atomic transition (of frequency  $\omega_0$ ), the radiation pressure force can experimentally be made negligible<sup>1</sup>. In the following we will consider only the dipolar potential

$$V_{\text{opt}}(\mathbf{r}) = \frac{3\pi c^2 \Gamma \mathcal{I}(\mathbf{r})}{2\omega_0^3 \delta} \quad (3.1)$$

where  $\Gamma$  is the decay rate of the excited state and  $\mathcal{I}$  is the intensity of the field. Therefore the potential experienced by the atom is directly proportional to the intensity pattern and its sign is determined by  $\delta$ : if  $\delta > 0$  (blue-detuning of the field with respect to the transition) the potential is repulsive  $V_{\text{opt}}(\mathbf{r}) \propto +\mathcal{I}(\mathbf{r})$  and if  $\delta < 0$  (red-detuning) the potential is attractive  $V_{\text{opt}}(\mathbf{r}) \propto -\mathcal{I}(\mathbf{r})$ .

We are therefore interested in the intensity pattern  $\mathcal{I}(\mathbf{r})$ . In this chapter we recall the properties of speckle patterns that are relevant for this thesis, with a particular emphasis on their spatial correlations. As an illustration, we explicitly compute them for a few standard cases.

---

1. The radiation pressure force scales as  $\Gamma/\delta^2$  ( $\Gamma$  is defined below), whereas the dipolar force scales as  $1/\delta$ . Therefore at high-enough detuning ( $\delta \gg \Gamma$ ) one can neglect the radiation pressure force.

Figure 3.1: A typical realization of a two dimensional speckle pattern (cut in the focal plane, at  $z = 0$ ), obtained numerically for an isotropic Gaussian beam [see Sec. 3.2.2 and 3.3 for details, the intensity is colour-coded from dark-blue (minimum) to red (maximum)].

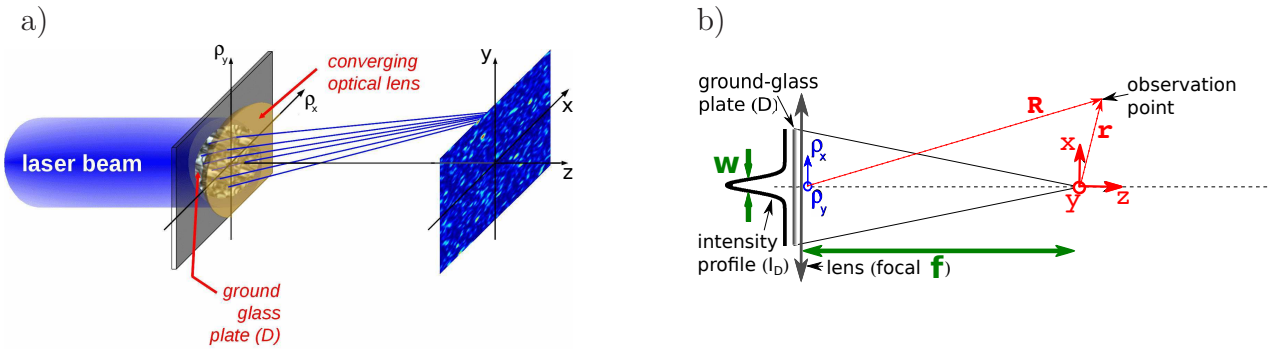
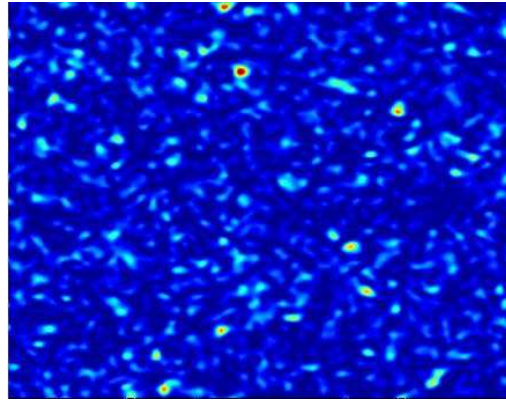


Figure 3.2: Setup considered for the obtention of the speckle pattern. (a) Optical apparatus: A laser beam is diffracted by a ground-glass plate diffuser (D) of pupil function  $I_D(\boldsymbol{\rho})$ , where  $\boldsymbol{\rho} \equiv (\rho_x, \rho_y)$  spans the diffuser, which imprints a random phase on the various light paths. The intensity of the field,  $\mathcal{I}(\mathbf{r})$ , observed in the focal plane of a converging lens (e.g. see Fig. 3.1), is a speckle pattern, which creates a disordered potential  $V_{\text{opt}}(\mathbf{r})$  for the atoms. (b) Horizontal cut of the apparatus with the notations used in this chapter.

## 3.1 Introduction to speckle theory

### 3.1.1 Realization of a speckle pattern

In an experiment, a speckle pattern is obtained when a coherent beam is reflected on a rough surface or transmitted through a diffusive plate [156]. In Huygens' principle, the coherent partial waves emitted at each point of the diffusing surface have random phases. They will interfere at the observation point, leading to a characteristic random pattern (see Fig. 3.1). In the following we will consider the setup presented in figure 3.2 in which a ground-glass diffusive plate is lit by a coherent laser beam linearly polarized. The results of this section essentially follow Refs. [20] and [156].

The electric field is considered as being scalar<sup>2</sup> and its complex amplitude in a plane right after the diffusive plate is written  $\epsilon(\boldsymbol{\rho}) = \epsilon(\rho_x, \rho_y)$ . Its square modulus is the pupil function  $I_D(\boldsymbol{\rho}) = |\epsilon(\boldsymbol{\rho})|^2$  (which is therefore the intensity distribution of the light leaving the diffusive plate<sup>3</sup>), whereas we assume that its phase is spatially randomized (uniformly distributed

2. This is justified in the paraxial approximation ( $|\rho_x|, |\rho_y| \ll f$ ), if the diffusive plate does not modify the polarization of the incoming beam.

3. The actual intensity (in  $W.m^{-2}$ ) is  $\mathcal{I} = \epsilon_0 c |\mathcal{E}|^2 / 2$  where  $\epsilon_0$  is the vacuum permittivity, but here we choose units such that  $\epsilon_0 c / 2 = 1$ .

between 0 and  $2\pi$ ) at each point<sup>4</sup>  $\boldsymbol{\rho}$  after passing through the diffusive plate. The plate is therefore considered as a collection of many spatially-incoherent point-like sources.

The beam is then focused by a converging lens, of focal distance  $f$  and we observe the intensity  $\mathcal{I}$  of the field at a point  $\mathbf{r} = \{x, y, z\}$  near the focal point, where the speckle is fully developed. The complex amplitude of the field  $\mathcal{E}$  is given by the Rayleigh-Sommerfeld formula [158]

$$\mathcal{E}(\mathbf{r}) = \frac{1}{i\lambda_L} \int d^2\boldsymbol{\rho} \epsilon(\boldsymbol{\rho}) \frac{R_z}{|\mathbf{R} - \boldsymbol{\rho}|^2} e^{i\frac{2\pi}{\lambda_L}|\mathbf{R} - \boldsymbol{\rho}|}, \quad (3.2)$$

in which we have only assumed that the observation point is far from the diffusive plate, i.e.  $|\mathbf{R}| \gg \lambda_L$  [see notations on Fig. 3.2(b)].

In the following we will use the paraxial approximation: If  $D \ll f$  (where  $D$  is the size of the diffusive plate) and if  $|x|, |y|$  and  $|z| \ll f$  we find the Fresnel formula

$$\mathcal{E}(\mathbf{r}) \simeq \frac{e^{i\frac{2\pi f}{\lambda_L}}}{i\lambda_L f} e^{i\frac{\pi}{\lambda_L f}(x^2 + y^2)} \int d^2\boldsymbol{\rho} \epsilon(\boldsymbol{\rho}) e^{i\frac{\pi}{\lambda_L f}(\rho_x^2 + \rho_y^2)} e^{-i\frac{2\pi}{\lambda_L f}(x\rho_x + y\rho_y)}. \quad (3.3)$$

As the phase of  $\epsilon(\boldsymbol{\rho})$  is a random variable at each point  $\boldsymbol{\rho}$ , we see in Eq. (3.3) that the field in  $\mathbf{r}$  results from the summation of many independent and identically distributed complex random variables<sup>5</sup>, and one can apply the central limit theorem. The electric field  $\mathcal{E}(\mathbf{r})$  is then a complex Gaussian random variable, i.e. its real and imaginary parts are two independent Gaussian random variables. The intensity of the field, which intervenes in Eq. (3.1), is given by<sup>3</sup>

$$\mathcal{I}(\mathbf{r}) = |\mathcal{E}(\mathbf{r})|^2. \quad (3.4)$$

The distribution of the random variable  $\mathcal{I}$  – and of the associated disordered potential thus created – is therefore not Gaussian. In particular, this implies that the disorder correlations are not uniquely determined by the two-point correlation function. However, we will be able to calculate the speckle statistical properties thanks to the underlying Gaussian distribution of the electric field, and we will find non usual properties [see e.g. Eqs. (3.10) and (3.12)].

### 3.1.2 Statistical properties

We have described a way to create spatially disordered potentials for the atoms; we now want to characterize them.

A model of disorder is determined by its statistical properties, which are common to all realizations of the disorder. The latter are completely described by all the correlation functions of any number of points  $n$

$$C_n^{\mathcal{I}}(\mathbf{r}_1, \mathbf{r}_2, \dots, \mathbf{r}_n) = \overline{\mathcal{I}(\mathbf{r}_1)\mathcal{I}(\mathbf{r}_2)\dots\mathcal{I}(\mathbf{r}_n)} \quad (3.5)$$

---

4. In reality the phase of the electric field right after the diffusive plate is correlated over a length  $\sigma_D$  which is typically the size of the cross section of the scatterers composing the diffusive plate. But very often we have  $\sigma_D \ll D$  where  $D$  is the size of the plate and the application of the central limit theorem (see below) still holds. The finite size of the scatterers then only influences the angle of the diffraction cone creating the speckle, i.e. the spatial extension of the pattern.

5. Their amplitude distribution is given by the distribution of  $\epsilon(\boldsymbol{\rho})$ . It is therefore of finite variance, as, in realistic cases, the pupil function  $I_D \propto |\epsilon|^2$  is of finite support.

where the overbar means ensemble averaging over the different realizations of the disordered potential. The disorder is considered homogenous, i.e. its statistical properties are translation-invariant, which means that they do not depend on the spatial reference that is chosen. In particular, for the above correlation functions we have, for any vector  $\mathbf{a}$ ,  $C_n^{\mathcal{I}}(\mathbf{r}_1 + \mathbf{a}, \mathbf{r}_2 + \mathbf{a}, \dots, \mathbf{r}_n + \mathbf{a}) = C_n^{\mathcal{I}}(\mathbf{r}_1, \mathbf{r}_2, \dots, \mathbf{r}_n)$ , therefore  $C_n^{\mathcal{I}}$  depends only on  $n - 1$  independent variables: for instance  $\mathbf{r}_2 - \mathbf{r}_1, \dots, \mathbf{r}_n - \mathbf{r}_1$ . The potential is also assumed to have vanishing statistical correlations at infinity<sup>6</sup>, i.e.  $\lim_{|\mathbf{a}| \rightarrow \infty} \overline{\mathcal{I}(\mathbf{r}_1 + \mathbf{a}) \dots \mathcal{I}(\mathbf{r}_n + \mathbf{a}) \mathcal{I}(\mathbf{r}_{n+1}) \dots \mathcal{I}(\mathbf{r}_m)} = \overline{\mathcal{I}(\mathbf{r}_1) \dots \mathcal{I}(\mathbf{r}_n)} \overline{\mathcal{I}(\mathbf{r}_{n+1}) \dots \mathcal{I}(\mathbf{r}_m)}$ . In such a disorder the statistical properties are ergodic [37]: the calculations of a property by spatial averaging in a system of size  $L \rightarrow \infty$  with a given realization of the potential and by ensemble averaging give the same result.

In the following we will mostly be interested in the single-point properties of the disorder, which give the 'typical' shape of the potential, and in the two-point correlations, which govern transport and localization properties, as we will see. Let us define

- the mean value of the intensity :

$$\overline{\mathcal{I}} = \lim_{L \rightarrow \infty} \frac{1}{L^d} \int_{-L/2}^{L/2} d^d \mathbf{r} \mathcal{I}(\mathbf{r}) \quad (3.6)$$

- its standard deviation :

$$\mathcal{I}_R \equiv \left[ \overline{(\mathcal{I} - \overline{\mathcal{I}})^2} \right]^{1/2} = \left[ \lim_{L \rightarrow \infty} \frac{1}{L^d} \int_{-L/2}^{L/2} d^d \mathbf{r} (\mathcal{I}(\mathbf{r}) - \overline{\mathcal{I}})^2 \right]^{1/2} \quad (3.7)$$

- its correlation length  $\sigma_R$ , as the typical length over which the two-point correlation function  $C_2^{\mathcal{I}}(\delta \mathbf{r})$  decays :

$$C_2^{\mathcal{I}}(\mathbf{r}, \mathbf{r} + \delta \mathbf{r}) = \overline{\mathcal{I}(\mathbf{r}) \mathcal{I}(\mathbf{r} + \delta \mathbf{r})}. \quad (3.8)$$

The definition of  $\sigma_R$  will be specified for each type of pupil function.

Figure 3.3 presents a 1D cut of a typical realization of a speckle pattern, with its main statistical properties. As can be seen, a speckle pattern is made of 'grains' of light of various sizes and amplitudes. The grain size is proportional to the correlation length  $\sigma_R$  and the typical amplitude to the intensity standard deviation  $\mathcal{I}_R$ . Note that, as the light intensity is always positive ( $\mathcal{I} > 0$ ), the potential is bounded from below in the blue-detuned case, but it can take any arbitrary high value. Conversely, in the red-detuned case, the potential is bounded from above. The intensity distribution is therefore very asymmetric, as we will see below.

**Intensity distribution** – Let us first consider the simplest statistical property: the intensity distribution of the speckle pattern  $\mathcal{I}(\mathbf{r})$ . It is a one-point statistical property, and therefore it can be calculated from the knowledge of the probability distribution of  $\mathcal{E}$  [see Eq. (3.4)], which is a complex Gaussian random variable. The joint probability distribution of  $\Re(\mathcal{E})$  and  $\Im(\mathcal{E})$  (the real and imaginary parts of  $\mathcal{E}$ ) reads

$$P[\Re(\mathcal{E}), \Im(\mathcal{E})] = \frac{1}{2\pi\sigma_{\mathcal{E}}^2} \exp\left(-\frac{\Re(\mathcal{E})^2 + \Im(\mathcal{E})^2}{2\sigma_{\mathcal{E}}^2}\right), \quad (3.9)$$

---

6. This property is verified for all the models of speckle presented in this thesis.

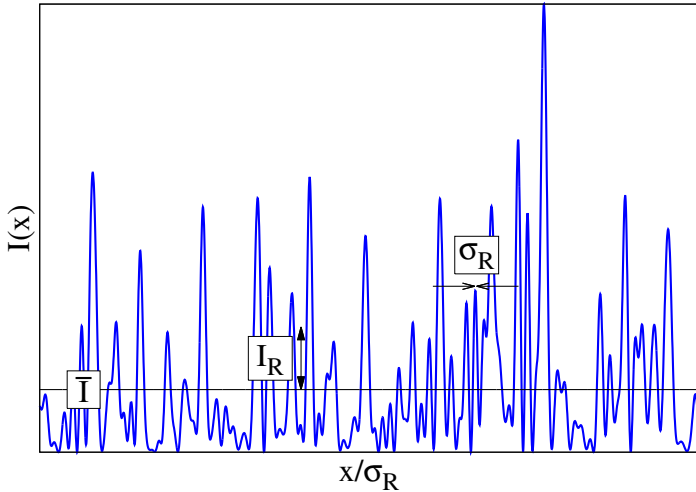


Figure 3.3: Illustration of the main statistical properties of a blue-detuned speckle pattern: a typical realization of a one dimensional speckle potential (cut along axis  $x$ , at  $y, z = 0$ ), obtained numerically for a square aperture (see Secs. 3.2.1 and 3.3 for details) with its mean value  $\bar{\mathcal{I}}$ , its standard deviation  $\mathcal{I}_R$  and its correlation length  $\sigma_R$ . A typical red-detuned speckle pattern is obtained by a vertical flip of this figure.

where  $\sigma_{\mathcal{E}}^2$  is the variance of  $\Re(\mathcal{E})$  and  $\Im(\mathcal{E})$ . Transforming into the set of variables  $(\Re(\mathcal{E}), \Im(\mathcal{E})) = (\sqrt{\mathcal{I}} \cos \phi, \sqrt{\mathcal{I}} \sin \phi)$ , one finds the joint probability distribution for the intensity  $\mathcal{I}$  and the phase  $\phi$ ,  $P(\mathcal{I}, \phi) = \exp(-\mathcal{I}/2\sigma_{\mathcal{E}}^2)/4\pi\sigma_{\mathcal{E}}^2$  and finally the Rayleigh intensity probability distribution

$$P(\mathcal{I}) \equiv \int_0^{2\pi} d\phi P(\mathcal{I}, \phi) = \frac{1}{\bar{\mathcal{I}}} \exp\left(-\frac{\mathcal{I}}{\bar{\mathcal{I}}}\right), \quad (3.10)$$

with  $\bar{\mathcal{I}} = 2\sigma_{\mathcal{E}}^2$ . The intensity distribution is thus very asymmetric around the mean value [as already noticed in Fig. 3.3]. Finally, one finds the particular property

$$\mathcal{I}_R = \bar{\mathcal{I}}. \quad (3.11)$$

Note that those single-point properties apply for any speckle patterns, as soon as the central limit theorem can be applied [see below Eq. (3.3)], independently of the shape of the pupil function and of the dimension in which the speckle is considered.

**Spatial correlations (1D and 2D)** – A second important characteristics of the disorder is its two-point correlation function. In particular, we will see in Chaps. 4 to 8 that it determines transport properties. If the atoms are confined in a 1D (resp. 2D) geometry by a strong trapping potential in the  $y$  and  $z$  directions (resp. in the  $z$  direction) centered on  $y = z = 0$  (resp.  $z = 0$ ), they experience the potential along the line  $x$  or in the focal plane  $(x, y)$  [see Fig. 3.2(b)]. We then want to calculate  $C_2^{\mathcal{I}}(\mathbf{r}, \mathbf{r}') = \overline{\mathcal{I}(\mathbf{r})\mathcal{I}(\mathbf{r}')} = \overline{\mathcal{E}(\mathbf{r})\mathcal{E}^*(\mathbf{r})\mathcal{E}(\mathbf{r}')\mathcal{E}^*(\mathbf{r}')}$ , with  $z = z' = 0$ . As explained in Sec. 3.1.1,  $\mathcal{E}(\mathbf{r})$  is a complex Gaussian random variable. We can therefore apply Wick's theorem and obtain :

$$C_2^{\mathcal{I}}(\mathbf{r}, \mathbf{r}') = \overline{|\mathcal{E}(\mathbf{r})\mathcal{E}^*(\mathbf{r}')|^2} + \bar{\mathcal{I}}^2 \quad (3.12)$$

Using the model of Sec. 3.1.1, where we assumed that the phase of the electric field exiting the diffusive plate is spatially randomized, we can write  $\overline{\epsilon(\boldsymbol{\rho})\epsilon^*(\boldsymbol{\rho}')} = \mathcal{A}|\epsilon(\boldsymbol{\rho})|^2\delta(\boldsymbol{\rho} - \boldsymbol{\rho}')$  where  $\mathcal{A}$  has the dimension of a length squared, and we get [from Eq. (3.2)]

$$\overline{\mathcal{E}(\mathbf{r})\mathcal{E}^*(\mathbf{r}')} = \mathcal{A} \frac{f^2}{\lambda_L^2} \int d^2\boldsymbol{\rho} I_D(\boldsymbol{\rho}) \frac{e^{ik(|\mathbf{R}-\boldsymbol{\rho}|-|\mathbf{R}'-\boldsymbol{\rho}|)}}{|\mathbf{R}-\boldsymbol{\rho}|^2|\mathbf{R}'-\boldsymbol{\rho}|^2}, \quad (3.13)$$

which becomes in the paraxial approximation [see Eq. (3.3)]

$$\overline{\mathcal{E}(\mathbf{r})\mathcal{E}^*(\mathbf{r}')} = \frac{\mathcal{A}}{\lambda_L^2 f^2} e^{i\frac{\pi}{\lambda_L f}(x^2+y^2-x'^2-y'^2)} \int d^2\boldsymbol{\rho} I_D(\boldsymbol{\rho}) e^{-i\frac{2\pi}{\lambda_L f}\boldsymbol{\rho}\cdot(\mathbf{r}-\mathbf{r}')}. \quad (3.14)$$

Using Eq. (3.12), one finally obtains the two-point correlation function

$$\begin{aligned} C_2^{\mathcal{I}}(\mathbf{r}-\mathbf{r}') &= \overline{\mathcal{I}}^2 + \frac{\mathcal{A}^2}{\lambda_L^4 f^4} \left| \int d^2\boldsymbol{\rho} I_D(\boldsymbol{\rho}) e^{-i\frac{2\pi}{\lambda_L f}\boldsymbol{\rho}\cdot(\mathbf{r}-\mathbf{r}')} \right|^2 \\ &= \overline{\mathcal{I}}^2 \left[ 1 + \left| \frac{\int d^2\boldsymbol{\rho} I_D(\boldsymbol{\rho}) e^{-i\frac{2\pi}{\lambda_L f}\boldsymbol{\rho}\cdot(\mathbf{r}-\mathbf{r}')}}{\int d^2\boldsymbol{\rho} I_D(\boldsymbol{\rho})} \right|^2 \right]. \end{aligned} \quad (3.15)$$

Equation (3.15) is equivalent to the van Cittert-Zernike theorem [156]. In the following, we will often use the power spectrum, which is the Fourier transform<sup>7</sup> of  $C_2^{\mathcal{I}}$ . In 2D it reads

$$\tilde{C}_2^{\mathcal{I}}(\mathbf{k}) = \overline{\mathcal{I}}^2 \left[ (2\pi)^2 \delta(\mathbf{k}) + (\lambda_L f)^2 \frac{\int d^2\boldsymbol{\rho} I_D(\boldsymbol{\rho}) I_D\left(\boldsymbol{\rho} + \frac{\lambda_L f}{2\pi} \mathbf{k}\right)}{[\int d^2\boldsymbol{\rho} I_D(\boldsymbol{\rho})]^2} \right]. \quad (3.16)$$

If the speckle is considered in 1D [take  $y-y'=0$  in Eq. (3.15)], and if  $I_D(\boldsymbol{\rho})$  is separable<sup>8</sup>, we have<sup>9</sup>

$$\tilde{C}_2^{\mathcal{I}}(k_x) = \overline{\mathcal{I}}^2 \left[ 2\pi \delta(k_x) + \lambda_L f \frac{\int d\rho_x I_D(\rho_x) I_D\left(\rho_x + \frac{\lambda_L f}{2\pi} k_x\right)}{[\int d\rho_x I_D(\rho_x)]^2} \right]. \quad (3.17)$$

Therefore the Fourier transform of the two-point correlation function of a speckle pattern considered in 1D or 2D is the autoconvolution of the pupil function  $I_D$ . It is a property that we will often use in the manuscript.

The higher order correlation functions of the speckle ( $C_n^{\mathcal{I}}$  with  $n > 2$ ), which are for instance useful to compute perturbative expansions of some transport properties, can be calculated in the same way, using Wick's theorem. They are then expressed as a sum of  $n!$  terms, each consisting of a product of  $n$  pair correlation functions of the field. In 1D, we will use the three-point correlations in Chap. 8. This calculation has been made up to  $n = 4$  in Refs. [14, 174], for a 1D speckle pattern obtained by a square aperture.

## 3.2 Standard examples

We now apply the above theory to usual configurations used to obtain speckle patterns. In a standard manner, the pupil function is either given by the aperture of the diffusive plate, if it is uniformly illuminated, or by the profile of the beam illuminating the plate, if the latter can be considered infinite.

7. In all the manuscript, we use the convention  $\tilde{f}(\mathbf{k}) = \int d^d\mathbf{r} f(\mathbf{r}) e^{-i\mathbf{k}\cdot\mathbf{r}}$  for the Fourier transform.

8. i.e. if we can write  $I_D(\boldsymbol{\rho}) = I_1(\rho_x) \times I_2(\rho_y)$

9. Note that, in 1D (e.g. along axis  $x$ ), it is strictly equivalent to consider:

- the speckle pattern created by a 2D aperture with separable pupil function [e.g.  $I_D(\boldsymbol{\rho}) = I_1(\rho_x) \times I_2(\rho_y)$ ], as done here
- or the speckle pattern created with a slit of pupil function  $I_1(\rho_x)$  [i.e.  $I_D(\boldsymbol{\rho}) = I_1(\rho_x) \times \delta(\rho_y)$ ], in which case the light pattern is homogeneous in  $y$ .

In the following we will often consider that 1D speckle patterns are created by slit apertures.

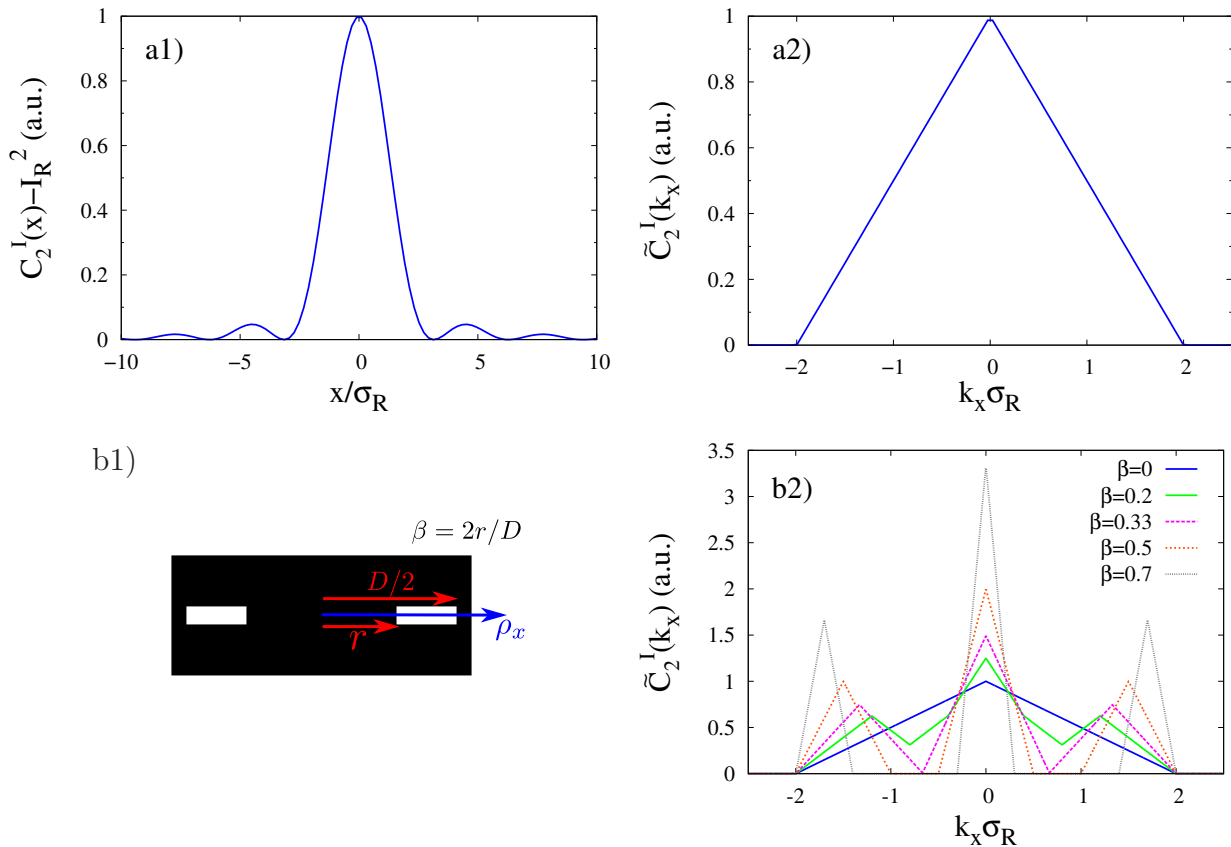


Figure 3.4: Correlation functions in two standard 1D cases: (a) One-dimensional speckle obtained by a square aperture [see Eqs. (3.18) and (3.19)]. (b) One-dimensional speckle obtained by a square aperture with a mask for various values of  $\beta$ : (b1) sketch of  $I_D(\rho_x)$ , (b2) function  $\tilde{C}_2^I(k_x)$  [see Eq. (3.20)].

### 3.2.1 Uniformly illuminated apertures

Let us first consider situations in which an aperture with straight borders is uniformly lit. The pupil function  $I_D$  is then given by the shape of this aperture.

**One-dimensional square aperture** – In Ref. [9] a 1D speckle potential obtained by a slit of length  $D$  is used: It corresponds to the pupil function  $I_D(\rho_x) = I_0\Theta(D/2 - |\rho_x|)$ . Using Eqs. (3.15) and (3.17), we have in this case

$$C_2^I(x) = \mathcal{I}_R^2 \left\{ 1 + \left[ \frac{\sin(x/\sigma_R)}{x/\sigma_R} \right]^2 \right\} \quad (3.18)$$

and

$$\frac{\tilde{C}_2^I(k_x)}{\sigma_R} = \mathcal{I}_R^2 \left\{ 2\pi \frac{\delta(k_x)}{\sigma_R} + \pi \left[ 1 - \frac{|k_x|\sigma_R}{2} \right]_{\oplus} \right\}, \quad (3.19)$$

where  $\sigma_R = \lambda_L f / \pi D$  and  $[g(x)]_{\oplus} = g(x)$  if  $g(x) > 0$  and 0 otherwise. As an illustration,  $C_2^I(x) - \mathcal{I}_R^2$  and  $\tilde{C}_2^I(k_x)$  are plotted in Fig. 3.4(a1) and (a2). Note that  $\tilde{C}_2^I(k_x)$  exhibits a

cut-off: we have  $\tilde{C}_2^{\mathcal{I}}(k_x) = 0$  for any  $|k_x| > 2/\sigma_R$ . This absence of Fourier components in the disorder for  $|k_x| > 2/\sigma_R$  has been shown to induce an effective mobility edge in 1D (see Refs. [8] and also Chap. 4).

**One-dimensional square aperture with a mask** – Equation (3.17) shows that the correlations of a 1D speckle pattern can very simply be modified by changing the shape of the pupil function. We will exploit this property in the following (see Sec. 8), in particular to induce non-monotoneous behaviour of the localization length with particle energy. To illustrate this, one can for example look at the correlations that are obtained when putting a mask of width  $2r$  at the center of the slit [see illustration in Fig. 3.4(b1)]. When doing so, a gap is created in the pupil function:  $I_D(\rho_x) = I_0\Theta(|\rho_x| - r)\Theta(D/2 - |\rho_x|)$ ; leading to an increase of the integral (3.17) on a certain interval of  $k_x$ :

$$\frac{\tilde{C}_2^{\mathcal{I}}(k_x)}{\sigma_R} = 2\pi\mathcal{I}_R^2\frac{\delta(k_x)}{\sigma_R} + \frac{\pi\mathcal{I}_R^2}{(1-\beta)^2} \left\{ \left[ 1 - \beta - |k_x|\sigma_R \right]_{\oplus} + \frac{1}{2} \left[ 1 - \beta - \left| |k_x|\sigma_R - (\beta + 1) \right| \right]_{\oplus} \right\}, \quad (3.20)$$

with  $\beta = 2r/D$ . This correlation function is shown in Fig. 3.4(b2) for various values of  $\beta$ . We see that  $\tilde{C}_2^{\mathcal{I}}$  bears the same cut-off as previously. The non-monotoneous behaviour with  $k_x$  is all the more marked that  $\beta$  is large, and for  $\beta > 1/3$  a gap in the Fourier components is opened around  $|k_x| \sim 2/3\sigma_R$ , which broadens with  $\beta$ .

**Two-dimensional circular aperture** – In two dimensions, the natural extension is to use a circular aperture of diameter  $D$ , so that  $I_D(\boldsymbol{\rho}) = I_0\Theta(D/2 - |\boldsymbol{\rho}|)$ . Using Eqs. (3.15) and (3.16), it yields

$$C_2^{\mathcal{I}}(\mathbf{r}) = \mathcal{I}_R^2 \left\{ 1 + \left[ \frac{2J_1(|\mathbf{r}|/\sigma_R)}{|\mathbf{r}|/\sigma_R} \right]^2 \right\}, \quad (3.21)$$

where  $J_n$  is the Bessel function of the first kind. In Fourier space, it corresponds to

$$\frac{\tilde{C}_2^{\mathcal{I}}(\mathbf{k})}{\sigma_R^2} = (2\pi)^2\mathcal{I}_R^2\frac{\delta(\mathbf{k})}{\sigma_R^2} + 8\mathcal{I}_R^2 \left[ \arccos\left(\frac{|\mathbf{k}|\sigma_R}{2}\right) - \frac{|\mathbf{k}|\sigma_R}{2} \sqrt{1 - \left(\frac{|\mathbf{k}|\sigma_R}{2}\right)^2} \right] \Theta\left(1 - \frac{|\mathbf{k}|\sigma_R}{2}\right), \quad (3.22)$$

with  $\sigma_R = \lambda_L f / \pi D$  and  $\Theta(x)$  is the Heaviside function [ $\Theta(x) = 1$  if  $x > 0$  and 0 otherwise]. Those functions [ $C_2^{\mathcal{I}}(\mathbf{r}) - \mathcal{I}_R^2$  and  $\tilde{C}_2^{\mathcal{I}}(\mathbf{k})$ ] are plotted in Fig. 3.5(a1) and (a2).

**Two-dimensional ring-shaped aperture** – In 2D also, one can very simply modify the correlation function. A simple possibility is to put a circular mask of radius  $r$  at the center of the circular aperture [see illustration in Fig. 3.5(b1)],  $I_D(\boldsymbol{\rho}) = I_0\Theta(|\boldsymbol{\rho}| - r)\Theta(D/2 - |\boldsymbol{\rho}|)$ . In this case Eq. (3.16) amounts to compute the area of the intersection of two such rings shifted

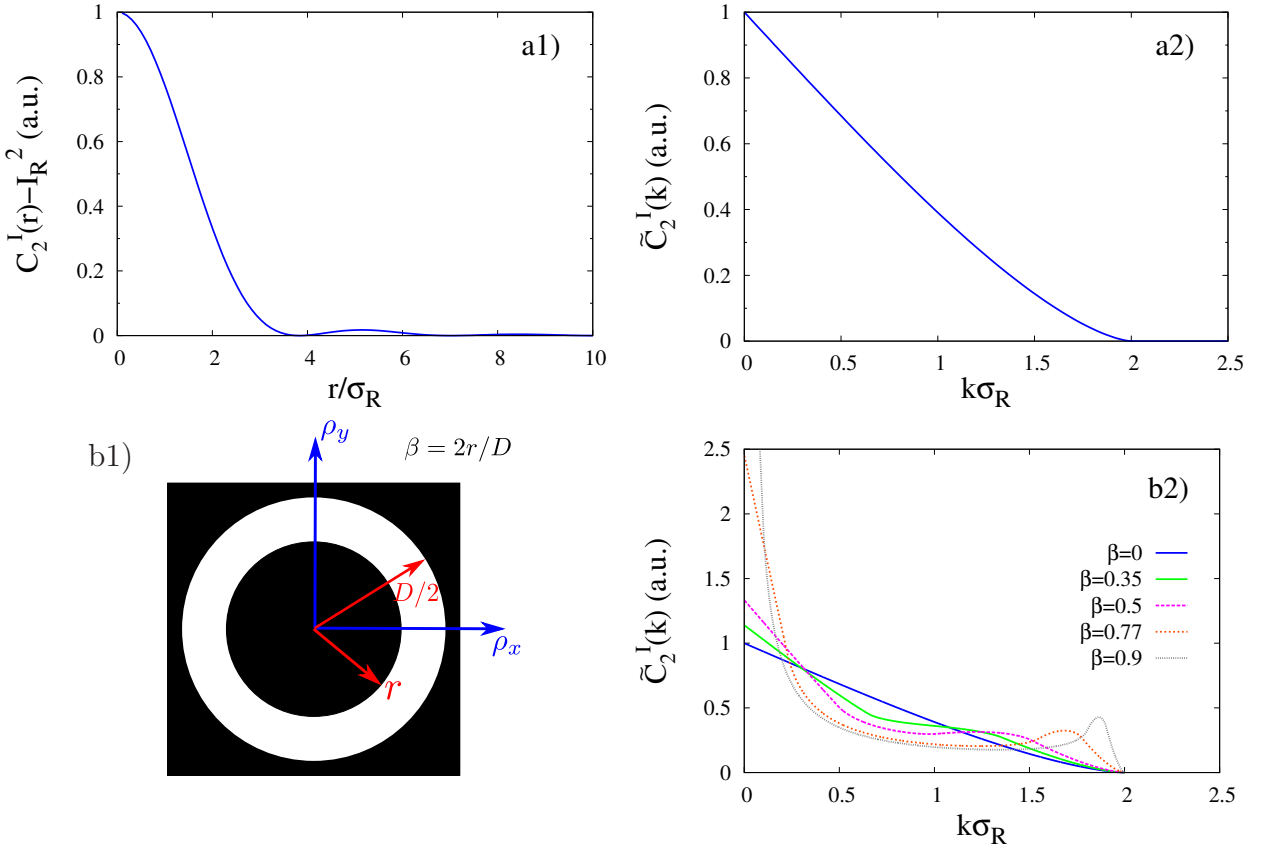


Figure 3.5: Radial behaviour of the correlation functions in two standard 2D cases: (a) Two-dimensional speckle obtained by a circular aperture [see Eqs. (3.21) and (3.22)]. (b) Two-dimensional speckle obtained by a circular aperture with a mask for various values of  $\beta$ : (b1) sketch of  $I_D(|\boldsymbol{\rho}|)$ , (b2) function  $\tilde{C}_2^I(|\mathbf{k}|)$  [see Eq. (3.20)].

by a certain distance, and we obtain

$$\begin{aligned}
\frac{\tilde{C}_2^I(k_x, k_y)}{\sigma_R^2} &= \frac{4\mathcal{I}_R^2}{(1-\beta^2)^2} \left( \left\{ 2 \arccos\left(\frac{|\mathbf{k}|\sigma_R}{2}\right) - \sin\left[2 \arccos\left(\frac{|\mathbf{k}|\sigma_R}{2}\right)\right] \right\} \Theta(2 - |\mathbf{k}|\sigma_R) \right. \\
&\quad + \beta^2 \left\{ 2 \arccos\left(\frac{|\mathbf{k}|\sigma_R}{2\beta}\right) - \sin\left[2 \arccos\left(\frac{|\mathbf{k}|\sigma_R}{2\beta}\right)\right] \right\} \Theta(2\beta - |\mathbf{k}|\sigma_R) \quad (3.23) \\
&\quad \left. - \left\{ \beta^2 [\alpha_1 - \sin(\alpha_1)] + \alpha_2 - \sin(\alpha_2) \right\} \Theta(1 + \beta - |\mathbf{k}|\sigma_R) \right) + (2\pi)^2 \mathcal{I}_R^2 \frac{\delta(\mathbf{k})}{\sigma_R^2}
\end{aligned}$$

with  $\beta = 2r/D$ ,  $\alpha_1 = 2 \arccos\left\{\left[ (|\mathbf{k}|\sigma_R)^2 + \beta^2 - 1 \right] / 2\beta|\mathbf{k}|\sigma_R\right\}$  and  $\alpha_2 = 2 \arccos\left\{\left[ (|\mathbf{k}|\sigma_R)^2 + 1 - \beta^2 \right] / 2|\mathbf{k}|\sigma_R\right\}$ , and where we extend the function  $\arccos$  with  $\arccos(x) = \pi$  if  $x < -1$  and  $\arccos(x) = 0$  if  $x > 1$ . This correlation function is shown in Fig. 3.5(b2) for various values of  $\beta$ .

### 3.2.2 Gaussian laser beam shone onto infinite plate

**Anisotropic Gaussian speckle (2D, and 1D)** – We now consider the case where the diffusive plate is illuminated by a Gaussian laser beam. If the size of the diffusive plate is large compared to the extension of the beam, the pupil function is given by the (possibly anisotropic) Gaussian profile of the beam of waists  $w_x$  and  $w_y$ , i.e.  $I_D(\boldsymbol{\rho}) = I_0 e^{-2(\rho_x^2/w_x^2 + \rho_y^2/w_y^2)}$ . Inserting this pupil function into Eq. (3.15), we get

$$C_2^{\mathcal{I}}(\mathbf{r}) = \mathcal{I}_R^2 \left\{ 1 + \exp \left[ -\frac{1}{\sigma_R^2} (x^2 + \xi^2 y^2) \right] \right\}, \quad (3.24)$$

with  $\sigma_{R,x,y} = \lambda_L f / \pi w_{x,y}$ ,  $\sigma_R \equiv \sigma_{R,x}$  and  $\xi \equiv \sigma_{R,x} / \sigma_{R,y}$  the configuration anisotropy factor<sup>10</sup>. The Fourier transform of Eq. (3.24) gives the speckle power spectrum

$$\frac{\tilde{C}_2^{\mathcal{I}}(k_x, k_y)}{\sigma_R^2} = \mathcal{I}_R^2 (2\pi)^2 \frac{\delta(\mathbf{k})}{\sigma_R^2} + \mathcal{I}_R^2 \frac{\pi}{\xi} \exp \left[ -\frac{\sigma_R^2}{4} \left( k_x^2 + \frac{k_y^2}{\xi^2} \right) \right]. \quad (3.25)$$

The correlation functions of the disorder reflect the anisotropy of the laser beam used to create the speckle  $\xi = w_y/w_x$ . When  $|\mathbf{k}| \ll \sigma_{R,x}^{-1}, \sigma_{R,y}^{-1}$ , we get  $\tilde{C}_2^{\mathcal{I}}(\mathbf{k}) \simeq \mathcal{I}_R^2 (2\pi)^2 \delta(\mathbf{k}) + \mathcal{I}_R^2 \pi \frac{\sigma_R^2}{\xi}$  and we recover the power spectrum of a white noise disorder of mean value  $\mathcal{I}_R$ , the only relevant parameter being  $\mathcal{I}_R^2 \sigma_{R,x} \sigma_{R,y}$ .

The correlation function (3.24) is obtained by shining an anisotropic Gaussian beam on the diffusive plate. It also approximately holds in the case of Ref. [17] where a quasi-2D Bose gas of width  $l_z$  is subjected to a speckle created by an *isotropic* Gaussian laser beam shone with an angle  $\theta$  with respect to the plane of atoms, if  $l_z \ll \sigma_R \ll 4\sigma_R f/w$  [see Eq. (D.5) of App. D.1]. In this case  $\xi \simeq 1/\sin \theta$  ( $\theta \simeq \pi/6$  for the experiment of Ref. [17]).

As the pupil function,  $I_D(\boldsymbol{\rho})$ , is separable, the 1D case is trivially obtained by taking  $y = 0$  in Eq. (3.24), and its Fourier transform is a one-dimensional Gaussian.

### 3.2.3 Further considerations

**Correlations in 3D** – In all previous examples (Secs. 3.2.1 and 3.2.2), the light pattern is also disordered along the  $z$  axis, but with correlations very different than in the transverse plane, and which are usually characterized by a larger correlation length. Therefore 3D disorder can be obtained with a single laser creating the speckle, the correlations of which are anisotropic (even when  $w_x = w_y$ ). The calculation of the 3D correlations of a speckle pattern obtained with one Gaussian beam, near the focal point, is treated in appendix D.1. For experimental realizations of a 3D speckle with one Gaussian beam see e.g. Refs. [18, 53, 127, 136]. In appendix D.1 we also present 3D speckle patterns obtained with more involved configurations of Gaussian beams, which are useful throughout the manuscript, and which are relevant for the experiments at Institut d'Optique [19].

**Beyond the paraxial approximation** – Note that the light pattern is disordered in the whole half-space beyond the diffusive plate ( $R_z > 0$ ). We have calculated its properties in

---

10. If the trap is not centered on the focal plane (i.e. if it is centered on  $z \neq 0$ ), the equations below still hold but the values of  $\mathcal{I}_R$  and  $\sigma_R$  are modified according to Eq. (3.15).

the paraxial approximation (i.e. far from the diffusive plate), where the Fresnel formula (3.3) holds and the speckle is fully developed (i.e. the secondary sources from all the diffusive plate contribute to  $\mathcal{I}(\mathbf{r})$  and one can apply the central-limit theorem safely). The previous approach is however not valid if the observation point is too close to the diffusive plate (typically for  $|\mathbf{R}| \lesssim \sigma_D D / \lambda_L$  with  $\sigma_D$  the cross section of the scatterers composing the diffusive plate), where the speckle is not fully developed and one has to take into account the angle of emission of the secondary sources of the plate, as well as the polarization. In this regime other approximations can be made (see for example Refs. [159, 160]), and the correlation properties of the speckle are different. The previous approach also does not hold if the focal distance of the lens is of the order or smaller than the size of the diffusive plate  $f \lesssim D$ . In this case Eq. (3.3) is not valid and one has to use the full Rayleigh-Sommerfeld formula (3.2). The expressions for the correlation function and its Fourier transform are then much more involved.

**From the intensity to potential correlation functions** – Let us finally specify some notations for the remainder of the manuscript. As shown in Eq. (3.1) the potential felt by the atoms is  $V_{\text{opt}}(\mathbf{r}) \propto \pm \mathcal{I}(\mathbf{r})$ . In the following, as in Chap. 2, we will always choose the energy reference in the Hamiltonian describing the atoms so that the potential is of zero mean value. Therefore let us define

$$V(\mathbf{r}) \equiv V_{\text{opt}}(\mathbf{r}) - \overline{V_{\text{opt}}} = V_R \left[ \frac{\mathcal{I}(\mathbf{r})}{\overline{\mathcal{I}}} - 1 \right], \quad (3.26)$$

such that  $\overline{V} = 0$ , and where  $V_R$  can be positive (blue-detuned case) or negative (red-detuned case). We also define the  $n$ -point correlation function of this potential:

$$C_n(\mathbf{r}_2 - \mathbf{r}_1, \dots, \mathbf{r}_n - \mathbf{r}_1) = \overline{V(\mathbf{r}_1)V(\mathbf{r}_2)\dots V(\mathbf{r}_n)}, \quad (3.27)$$

which can easily be related to the function  $C_n^{\mathcal{I}}$  via Eq. (3.26). In particular, for the two-point correlations, we find<sup>11</sup>

$$C(\mathbf{r}) \equiv C_2(\mathbf{r}) = V_R^2 [C_2^{\mathcal{I}}(\mathbf{r}) - 1] / \overline{\mathcal{I}}^2 \quad (3.28)$$

and the disorder power spectrum reads

$$\tilde{C}(\mathbf{k}) \equiv \tilde{C}_2(\mathbf{k}) = V_R^2 [\tilde{C}_2^{\mathcal{I}}(\mathbf{k}) - (2\pi)^d \delta(\mathbf{k})] / \overline{\mathcal{I}}^2, \quad (3.29)$$

where  $C_2^{\mathcal{I}}$  and  $\tilde{C}_2^{\mathcal{I}}$  have been calculated in Sec. 3.2.

### 3.3 Numerical implementation

In order to study quantum transport in speckle potentials, we have carried out numerical simulations of the Gross-Pitaevski equation (see Chap. 4), transfer-matrix calculations (see Chap. 8 and App. A.2) or direct diagonalization of the Hamiltonian (see Chap. 6). To do so we had to generate numerically different realizations of speckle patterns in 1D, 2D and 3D, with the appropriate correlation properties.

---

11. We also have  $C_3(\mathbf{r}, \mathbf{r}') = V_R^3 C_3^{\mathcal{I}}(\mathbf{r}, \mathbf{r}') / \overline{\mathcal{I}}^3 - V_R^3 [C_2^{\mathcal{I}}(\mathbf{r}) + C_2^{\mathcal{I}}(\mathbf{r}') + C_2^{\mathcal{I}}(\mathbf{r} - \mathbf{r}')] / \overline{\mathcal{I}}^2 + 2V_R^3$ .

In 1D and 2D, we see in the Fresnel formula (3.3) that the amplitude of the complex electric field  $\mathcal{E}$  is given by the amplitude of the Fourier Transform of the electric field right after the diffusive plate  $\epsilon(\boldsymbol{\rho})$ . One can therefore efficiently draw realizations of a speckle field by using the Fast Fourier Transform (FFT) algorithm to compute the Fourier Transform of a field  $\epsilon(\boldsymbol{\rho}) = \sqrt{I_D(\boldsymbol{\rho})}e^{i\phi(\boldsymbol{\rho})}$ , where  $\phi$  is a random phase at each point and  $I_D$  is given by the particular configuration we are considering. Taking the modulus squared of this field, we then obtain a speckle pattern such as those presented in Fig. 3.3 (1D) and in Fig. 3.1 (2D). As we use the FFT algorithm, the numerical discretization in  $\boldsymbol{\rho}$  ( $\delta\rho$ ) has to be properly chosen so as to describe the diffuser properly and to meet the FFT criterion  $\delta\rho = \lambda_L f / (N_{points} \delta r)$  where  $\delta r$  are the spatial discretization in  $\mathbf{r}$  and  $N_{points}$  is the number of numerical points. In 1D this scheme enabled us to draw realizations of speckle patterns of typically  $10^6$  points. We have checked that the statistical properties (intensity distribution and two-point correlation function) of the patterns generated numerically agree with the theory. For applications of this scheme in 2D refer to Ref. [23].

In 3D, i.e. if we consider the  $z$  dependence of the speckle pattern, the field cannot be expressed as a simple Fourier Transform anymore, and one has to use the full Rayleigh-Sommerfeld formula (3.2) to generate numerical speckle. In this case a 2-dimensional integral on  $\boldsymbol{\rho}$  has to be performed for each spatial point  $\mathbf{r}$ . This scheme is therefore considerably heavier than the previous one, but we have performed it when necessary (see Chap. 6 Sec. 7).

## Conclusion

In this chapter we have presented some basic aspects of speckle patterns and how they can serve as disordered potentials for neutral atoms. We have introduced how they are obtained, and their main statistical properties. We have mainly focused on the disorder power spectrum, which will be a major ingredient for computing quantum transport properties in the remainder of the manuscript. We have computed those correlation functions for some examples in 1D and 2D that are relevant for the following, and showed that they can be non-monotoneous and anisotropic. We will see that this has important consequences on quantum transport and Anderson localization of ultra-cold atoms in those potentials (see Chaps.5-8). Three-dimensional cases are presented in appendix D. The principle of the calculation is the same, but the expressions are heavier. In practical cases, the disorder power spectrum can be very complicated and show different dependencies in different directions. Finally, we have explained how speckle patterns can be generated numerically, which we used for the numerical determination of the energy distribution in the analysis of Ref. [19] for instance and for numerical simulations in 1D.

## Chapter 4

# Localization in one-dimensional speckle potentials

### Abstract

We theoretically study Anderson localization of matterwaves in a one-dimensional disordered potential. We first study the paradigmatic signature of localization, which is obtained from the transmission of a wave through a disordered medium. We compute the Lyapunov exponent using the phase formalism, which allows for perturbative expansions, and compare the results with numerical calculations using a transfer matrix approach. For realistic parameters for ultracold atoms in speckle potentials, we find that the correction to the Born approximation is small but non-negligible. We then study the expansion of a matter wave packet in a standard 1D speckle potential. We develop an analytical model which includes the initial phase-space density of the matter wave and the spectral broadening induced by the disorder. Our approach predicts a behavior of the localized density profile significantly more complex than a simple exponential decay. These results are confirmed by large-scale and long-time numerical calculations. They shed new light on experiments with ultracold atoms and may impact their analysis.

### Résumé

Nous menons une étude théorique de la localisation d'Anderson d'ondes de matière dans un potentiel désordonné unidimensionnel. Nous étudions dans un premier temps la signature paradigmatique de la localisation, qui est obtenue au moyen de la transmission d'une onde à travers un milieu désordonné. Nous calculons l'exposant de Lyapunov grâce au formalisme de phase, qui permet des expansions perturbatives, et nous comparons les résultats à des calculs numériques par matrices de transfert. En utilisant des paramètres réalistes pour des atomes ultrafroids dans des potentiels de speckle, nous trouvons que la correction à l'approximation de Born est faible, mais non négligeable. Nous étudions ensuite l'expansion d'un paquet d'onde de matière dans un potentiel de speckle usuel à 1D. Nous développons un modèle analytique qui inclut la densité initiale de l'onde de matière dans l'espace des phases et l'élargissement

spectral induit par le désordre. Notre approche prédit un comportement du profil localisé significativement plus complexe qu'une simple décroissance exponentielle. Ces résultats sont confirmés par des calculs numériques à grandes échelles de temps et d'espace. Ils donnent un éclairage nouveau sur les expériences avec des atomes ultrafroids et peuvent permettre de revoir leur analyse.

## Introduction: Localization in one dimension

Anderson localization is present in all dimensions, however, its features strongly differ (see Chaps. 1 and 2). In one dimension all single-particle states are strongly localized, and exact calculations can be carried out in the weak disorder limit. The paradigmatic signature of Anderson localization in 1D is obtained from the transmission of a wave of energy  $E$  through a disordered region of finite length  $x$ . The logarithm of the transmission  $\ln |\phi_E(x)|^2$  is then a self-averaging quantity, which means that for very large systems it converges to its statistical average  $\overline{\ln |\phi_E(x)|^2}$  [37]. It is characterized by the typical decay  $\overline{\ln |\phi_E(x)|^2} \simeq -2\gamma(E)|x|$ , with  $\gamma(E)$  the Lyapunov exponent (inverse localization length) [37].

Here, we study Anderson localization in 1D speckle potentials. In the first part of this chapter, we consider the genuine approach of the transmission of a wave through a disordered medium, and we compute the Lyapunov exponent both analytically (by the so-called phase formalism) and numerically (with transfer matrices). This approach allows us in particular to compute corrections, due to higher-order terms in the perturbative expansions, to the localization length usually calculated in the Born approximation. The correction appears to be small but non-negligible for realistic parameters of present-day experiments with ultra-cold atoms.

The localization of a wave packet is a more complicated issue as it is determined by the superposition of many energy components. Since the latter cannot be separated from each other, the relevant quantity is rather the average of the localized density profile,  $\overline{n(x)} = \overline{|\psi(x)|^2}$ , which is not self-averaging [37]. Moreover, each energy component localizes exponentially with its own localization length, and the superposition of all their contributions can lead to non-exponentially decaying density profiles [8, 141]. Localization of wave packets is for instance relevant to experiments where a Bose-Einstein condensate (BEC) propagates in a disordered potential [9]. The situation is modeled by the following scenario [8, 82, 175]: A non-disordered, interacting BEC (with initial healing length  $\xi_{\text{in}}$ ) is first released from a trap. It expands in free space and its initial interaction energy is converted into kinetic energy. At a given time  $t_0$ , a speckle potential (with correlation length  $\sigma_{\text{R}}$ ) is switched on and the interactions off. This creates a wave packet with a broad energy distribution. The energy components are then independent and eventually localize exponentially in the disordered potential, which results in the localization of the matter wave. For  $\xi_{\text{in}} > \sigma_{\text{R}}$ , recent experiments report an exponential decay of the density profile, in fair agreement with the prediction of the above scenario [9, 28]. The data however suggest deviations from exponential decay in the wings, and a discrepancy between theory and experiment at high amplitude of the disorder. The origin of those differences remains to be elucidated.

In the second part of this chapter, we revisit the theoretical model for Anderson localization of matter wave packets in 1D disorder presented in Refs. [9, 14]. Beyond previous models, our approach allows us to include (i) the phase-space density of the matter wave at time  $t_0$ , and (ii) the spectral broadening induced by the disorder. We show that these new ingredients significantly affect the predicted density profile of the localized matter wave at both short and long distances. It predicts a complex behavior of the density profile, which significantly deviate from pure exponential decay. Our results are confirmed by large-scale and long-time numerical calculations. They shed new light on the Anderson localization of matter wave packets, in particular on the experiments of Refs. [9, 28], and may explain experimental discrepancies. This chapter is adapted from Ref. [22].

## 4.1 Anderson localization of a single energy component in one-dimensional speckle

### 4.1.1 Phase formalism

We first study one-dimensional Anderson localization of a single particle in a disordered potentials using the phase formalism [37], which allows for efficient perturbative expansions [14]. For a detailed description of this formalism, refer to Pierre Lukan's PhD thesis [174].

Let us consider a particle of mass  $m$  and given energy  $E$  in the disordered potential. The corresponding eigenstate  $\phi_E(x)$  is governed by the 1D Schrödinger equation

$$-\frac{\hbar^2}{2m} \frac{\partial^2}{\partial x^2} \phi_E(x) + V(x) \phi_E(x) = E \phi_E(x), \quad (4.1)$$

where  $V(x)$  is the disordered potential. As in the remainder of this thesis, the latter is assumed to be stationary with a null ensemble average ( $\overline{V} = 0$ ) and is characterized by its statistical properties, in particular by its  $n$ -point correlation functions  $C_n(x_1, \dots, x_{n-1})$ .

Then, let us write the (real-valued) eigenfunction  $\phi_E(x) = r(x) \sin[\theta(x)]$  and its spatial derivative  $\partial_x \phi_E(x) = k_E r(x) \cos[\theta(x)]$  where  $k_E = \sqrt{2mE}/\hbar$  is the free-particle wavevector associated to energy  $E$ . In this representation, Eq. (4.1) transforms into the set of equations

$$\partial_x \theta(x) = k_E \left( 1 - \frac{V(x)}{E} \sin^2[\theta(x)] \right) \quad (4.2a)$$

$$\ln \left[ \frac{r(x)}{r(0)} \right] = k_E \int_0^x dx' \frac{V(x')}{2E} \sin[2\theta(x')]. \quad (4.2b)$$

Equation (4.2a) can be solved in the form of a Born-like perturbative series for the phase  $\theta$  in powers of the external potential  $V$ . Then, the Lyapunov exponent  $\gamma(E) \equiv L_{\text{loc}}(E)^{-1} \equiv \lim_{|x-x_0| \rightarrow \infty} \overline{\ln[r(x)/r(x_0)]}/|x-x_0|$  can be calculated at each order in  $V$  by inserting the result of Eq. (4.2a) into Eq. (4.2b). It yields<sup>1</sup>  $\gamma(E) = \sum_{n \geq 2} \gamma^{(n)}(E)$  with

$$\gamma^{(n)}(E) = \frac{1}{\sigma_R} \left( \frac{V_R}{\sqrt{E}} \sqrt{\frac{2m\sigma_R^2}{\hbar^2}} \right)^n f_n(k_E \sigma_R), \quad (4.3)$$

where each function  $f_n$  depends on the  $n$ -point correlation function of the disorder,  $C_n(x_1, \dots, x_{n-1})$  [14]. The quantities  $V_R$  and  $\sigma_R$  denote the amplitude and correlation length of the disorder (see below for precise definitions). In particular, the leading term of the series (Born approximation) is

$$f_2(\kappa) = \frac{1}{8} \frac{\tilde{C}_2(2\kappa/\sigma_R)}{V_R^2 \sigma_R}. \quad (4.4)$$

This term, which leads to

$$\gamma^{(2)}(E) = \frac{m^2}{2\hbar^4 k_E^2} \tilde{C}_2(2k_E), \quad (4.5)$$

---

1. Note that the first-order term vanishes because  $\overline{V} = 0$ .

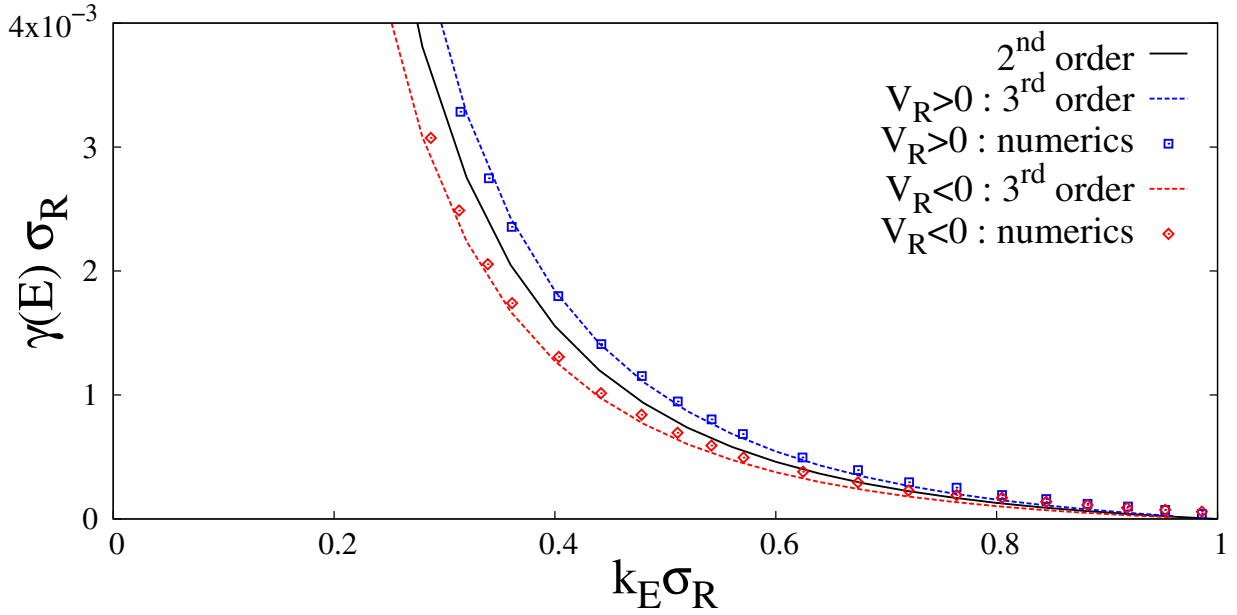


Figure 4.1: Lyapunov exponent for both blue- and red-detuned speckles with the standard correlation function (4.7) and  $V_R = \pm 0.01625(\hbar^2/m\sigma_R^2)$ . Shown are the numerical results extracted from a transfer matrix method (space step of  $\Delta x = 0.1\sigma_R$  and total system size of  $L_{tot} = 411775\sigma_R$  with random initial conditions) averaged over 5000 disorder realizations (blue squares:  $V_R > 0$ , red diamonds:  $V_R < 0$ ), and analytical results obtained from the phase formalism up to order 2 (solid black line) and up to order 3 (dotted blue and red lines).

generally captures most localization properties in 1D disorder. However, we will encounter some discrepancies between analytic calculations in the Born approximation and numerical calculations in the following. Therefore we will also include the next-order term [14]

$$f_3(\kappa) = \frac{-1}{4} \int_{-\infty}^0 du \int_{-\infty}^u dv \frac{C_3(u\sigma_R, v\sigma_R)}{V_R^3} \sin(2\kappa v). \quad (4.6)$$

The function  $f_3(\kappa)$  for the configuration of speckle considered here are given in appendix A.1 [take  $\beta = 0$  in Eq. (A.2)]. The fourth order term, that we will not use here, can be found in Refs. [14, 174].

### 4.1.2 Transfer matrix calculations

To check the validity of the phase formalism, we have performed numerical calculations for the transmission through the disorder of a particle governed by Eq. (4.1), using a transfer matrix technique (which are described in appendix A.2) [14, 176].

As in the experiments [9, 28], we consider a 1D speckle potential created with a square aperture (see Sec. 3.2.1). The correlation function of the intensity pattern in Fourier space is given by Eq. (3.19). The potential, which is related to the light intensity by Eq. (3.26), has the power spectrum

$$\tilde{C}_2(k) = \pi V_R^2 \sigma_R \left[ 1 - \frac{|k|\sigma_R}{2} \right]_{\oplus}. \quad (4.7)$$

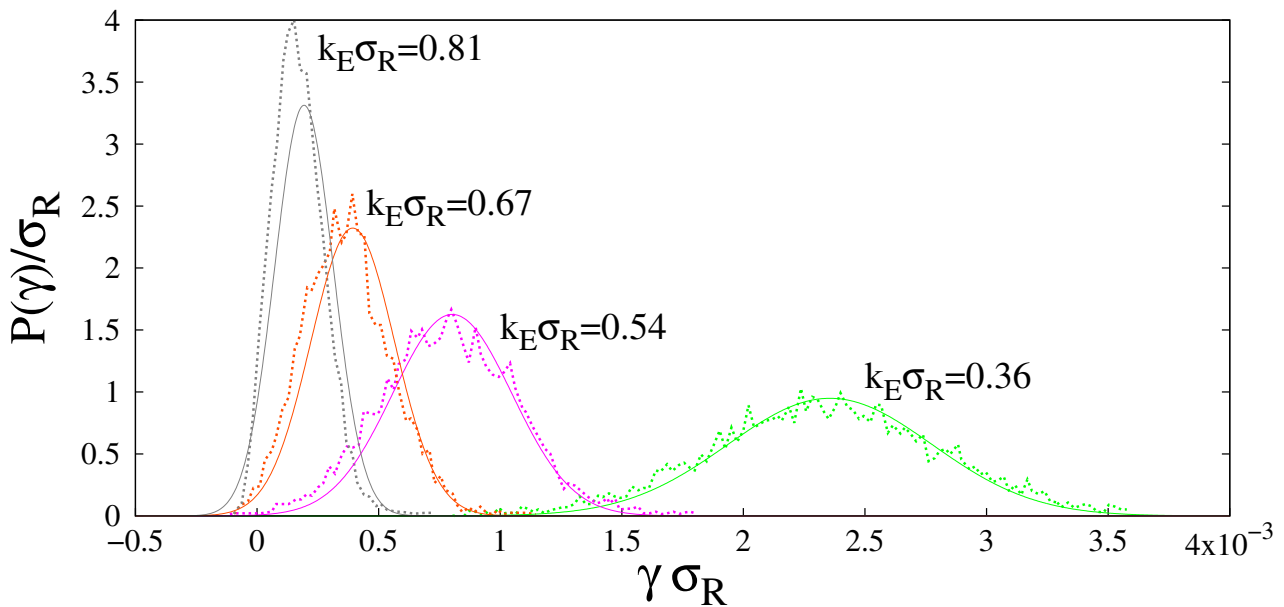


Figure 4.2: Probability distributions of the Lyapunov exponents obtained by transfer matrix calculations (dotted lines) with the disorder parameters of Fig. 4.1,  $V_R > 0$  (space step of  $\Delta z = 0.1\sigma_R$  and total system size of  $L_{tot} = 13333\sigma_R$  with random initial conditions), and various energies (indicated on the figure). The solid lines are the corresponding theoretical distributions (4.8).

**Average Lyapunov exponent** – Figure 4.1 shows the Lyapunov exponent obtained by transfer matrix calculations in this configuration, for both blue- and red-detuned speckle potentials ( $V_R > 0$  and  $V_R < 0$  respectively), with parameters relevant for current 1D experiments [9]. The numerical data (blue squares and red diamonds) are averaged over 5000 speckle realizations for each value of  $k_E$ . The analytic calculations of the Lyapunov exponent in the Born approximation [ $\gamma^{(2)}(E)$  given by Eq. (4.5)], which do not depend on the sign of  $V_R$ , fairly reproduce the numerical data (see solid black line in Fig 4.1). In this standard configuration, both numerics and analytic calculation in the Born approximation shows that the Lyapunov exponent, i.e. the localization strength, decreases with increasing particle energy. It corresponds to weaker localization at higher energy, which is an intuitive behavior.

We however find a significant discrepancy, which depends on the sign of  $V_R$  between, the numerics and the analytics up to order two. This leading term does not depend on the sign of  $V_R$ , whereas the sign of  $\gamma^{(3)}$ , which is proportional to  $V_R^3$ , does. As is seen on Fig. 4.1 (dotted blue and red lines), the discrepancy is very well accounted for by analytic calculations to the next order in the perturbative series,  $\gamma^{(2)}(E) + \gamma^{(3)}(E)$ , where  $\gamma^{(3)}(E)$  is given by Eq. (4.3) with  $n = 3$  and Eq. (A.1). Those results are in agreement with those of Ref. [14] and are obtained for similar parameters.

**Distribution of  $\gamma(E)$**  – Figure 4.1 shows the average values of the Lyapunov exponent, which we write  $\bar{\gamma}(E)$  in this paragraph. We now study its full distribution  $P(\gamma)$ . In Fig. 4.2 we show some distributions of the Lyapunov exponents  $\gamma(E)$  obtained for different realizations

of the potential at four values of the energy, together with the Gaussian distribution

$$P(\gamma) = \frac{1}{\sqrt{2\pi}\Delta_\gamma} \exp\left[-\frac{(\gamma - \bar{\gamma})^2}{2\Delta_\gamma^2}\right] \quad (4.8)$$

with  $\Delta_\gamma = \sqrt{\bar{\gamma}/L_{tot}}$  and  $L_{tot}$  the system size, which is expected for  $\delta$ -correlated disorder when  $L_{tot} \gg 1/\bar{\gamma}$  (see appendix A.2). For low energy, we find a good agreement in Fig. 4.2. At high energy ( $k_E\sigma_R \gtrsim 0.8$ ) the numerical distributions differ from Eq. (4.8). This is expected because for  $k_E\sigma_R = 0.81$ , we find  $1/\bar{\gamma} \sim 5000\sigma_R$ , which is of the order of magnitude of  $L_{tot} = 13333\sigma_R$ , and Eq. (4.8) doesn't hold anymore.

When  $L_{tot}/\bar{\gamma} \rightarrow \infty$ , Eq. (4.8) converges to a Dirac distribution centered on  $\bar{\gamma}$ , thus confirming that the Lyapunov exponent is a self-averaging quantity. Since  $\gamma(E) = -\ln(T)/2L_{tot}$ , where  $T$  is the transmission probability of the wave through a sample of finite length  $L_{tot}$ ,  $T$  follows a log-normal distribution, whose relative width increases with system size (see details in appendix A.2). The transmission coefficient  $T$  is therefore not a self-averaging quantity.

In this section we have studied analytically and numerically the Lyapunov exponent for a one-dimensional speckle potential obtained by a square aperture. It is a quantity which can be calculated exactly in weak disorder thanks to the phase formalism expansion. Comparison with numerical transfer matrices calculations, which simulate the transmission of a wave through a disordered medium, gave a very good agreement. For typical experimental parameters, we found that the Born approximation is in fair agreement with numerical data. However, there remains a discrepancy, which depends on the sign of  $V_R$ . It is very well accounted for by the third order of the phase formalism.

## 4.2 Expansion of a wave packet

We now study Anderson localization in the second typical situation that we introduced: the expansion of a matterwave packet in disorder, which is in particular relevant to the ultra-cold atom experiments performed so far.

### 4.2.1 A typical ultra-cold atom experiment

To start with, let us recall the main features of a typical experiment with ultra-cold atoms in a disordered potential, by taking the particular example of the scheme proposed in Ref. [8] and realized experimentally in Ref. [9]. In this experiment, a one-dimensional Bose-Einstein condensate of  $^{87}\text{Rb}$  atoms is initially trapped in a harmonic trap in Thomas-Fermi regime [as presented schematically in Fig. 4.3(a)]. The longitudinal confinement is switched off at time  $t_i = 0$ , and the atoms are let to expand in a one-dimensional wave-guide superimposed with a 1D blue-detuned speckle pattern [see Fig. 4.3(b)]. The evolution of the density profile  $n(x, t)$  of the expanding condensate can be imaged by absorption imaging.

At the beginning, the expansion of the atoms is driven by their interaction energy, and the disorder can be neglected. The initial interaction energy is converted into kinetic energy, and the atoms acquire a broad momentum distribution which extends from  $k = 0$  to  $k_m$ . Afterwards, as the density lowers, the interactions become less important, and at some point

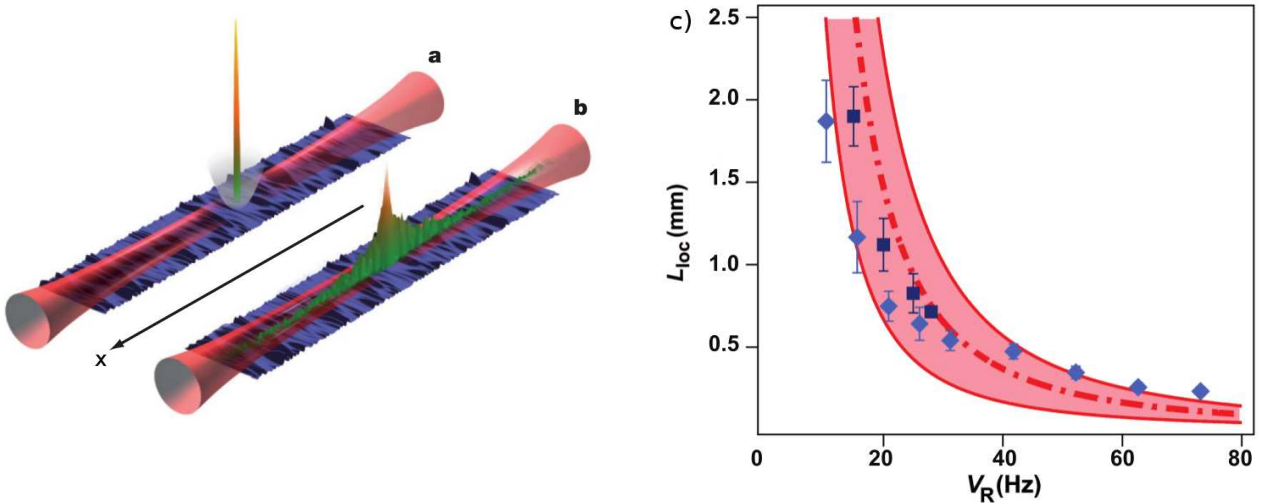


Figure 4.3: (a-b) Schematic representation of the experimental setup: the atoms, initially tightly trapped (a), are then let to expand in a 1D wave-guide superimposed with a transversally invariant speckle potential (b). This figure is extracted from Ref. [9]. (c) Experimental localization lengths extracted by exponential fits of the localized density profiles  $n(x) \propto e^{-2|x|/L_{\text{loc}}}$  for  $k_{\text{m}}\sigma_{\text{R}} = 0.65$  and different values of the disorder amplitude  $V_{\text{R}}$  (blue dots). The diamonds are data from Ref. [9], and the squares are more recent data from Ref. [177]. The red curve is the theoretical prediction in the Born approximation [Eq. (4.18)]. This figure is extracted from Ref. [177].

their effect can be neglected compared to the disorder. The profiles then become stationary, and the shape of the localized wings can be analyzed to extract quantitative information about localization in the disorder.

Let us consider here that the effect of the disorder on the density of states is negligible, i.e. that we have  $E \simeq \hbar^2 k^2 / 2m$ , even in the disorder, as was done in Refs. [8, 9, 14]. Two situations can then be distinguished:

- If the initial parameters are such that  $k_{\text{m}} < \sigma_{\text{R}}^{-1}$ , all the energy components are localized in the Born approximation (which will be explicated below) with an energy-dependent localization length  $L_{\text{loc}}(E)$ , and the density profile is dominated by the largest localization length, i.e.  $L_{\text{loc}}(E_{\text{m}})$ . In Fig. 4.3(c) we show this localization length extracted by fits of the density profiles (blue dots), for  $k_{\text{m}}\sigma_{\text{R}} = 0.65$  and various amplitudes of the disorder  $V_{\text{R}}$ . Also shown is the theoretical prediction of the Born approximation (red line) [see below, Eq. (4.18)].
- If the initial parameters are such that  $k_{\text{m}} > \sigma_{\text{R}}^{-1}$ , some energy components are not localized in the Born approximation. The profiles are then found to decrease algebraically, as predicted in Ref. [8].

The data presented in figure 4.3(c) and Ref. [9] show a fair quantitative agreement with the Born approximation, which is a great evidence for Anderson localization. However, one observes that the fitted localized lengths show deviations with the theory at high values of  $V_{\text{R}}$ , which indicate that the analysis might be pushed further.

## 4.2.2 Theoretical model

Let us now revisit the theoretical model of Refs. [8, 9, 14]. We want to compute the evolution of the average density  $\bar{n}(x, t)$ , which is the relevant quantity for typical experiments

with ultra-cold atoms. The approach of Sec. 4.1.1, which computes  $\overline{\ln|\phi_E(x)|^2}$ , is not useful here. In order to calculate  $\overline{n(x)}$ , we rather need to compute  $\overline{|\phi_E(x)|^2}$  and superimpose all energy components.

We consider a 1D matter wave subjected to a harmonic trap and a disordered potential, with repulsive short-range interactions. In the weakly-interacting regime (i.e. for large enough 1D density,  $n \gg mg/\hbar^2$ , where  $m$  is the atomic mass and  $g$  is the coupling parameter, which is verified experimentally), its dynamics is governed by

$$i\hbar\frac{\partial}{\partial t}\psi = \left[ -\frac{\hbar^2}{2m}\frac{\partial^2}{\partial x^2} + V_{\text{ho}}(x) + V(x) + g|\psi|^2 - \mu \right] \psi, \quad (4.9)$$

where  $\mu$  is the chemical potential, the wavefunction is normalized to the total number of atoms ( $\int dx|\psi|^2 = N$ ),  $V_{\text{ho}}(x) = m\omega^2 x^2/2$  is the trapping potential, and we define the healing length of the trapped BEC by<sup>2</sup>  $\xi_{\text{in}} \equiv \hbar/\sqrt{4m\mu}$ , which is the typical scale of variation of the wavefunction.

**Two-stage scenario** – Following the scenario of Refs. [8, 175], an interacting BEC is first produced in the harmonic trap and in the absence of disorder ( $V \equiv 0$  and  $V_{\text{ho}} \neq 0$ ). For interactions strong enough that  $n \gg \hbar\omega/g$  (Thomas-Fermi regime), one can neglect the kinetic term in Eq. (4.9), the phase is then uniform and the density profile is a truncated inverted parabola,

$$n_i(x) = \frac{\mu}{g} \left[ 1 - \left( \frac{x}{L_{\text{TF}}} \right)^2 \right]_{\oplus}, \quad (4.10)$$

where<sup>3</sup>  $L_{\text{TF}} = \sqrt{2\mu/m\omega^2}$ . Then, an expanding matter wave is produced by switching off the trap ( $V_{\text{ho}} \rightarrow 0$ ) at time  $t_i = 0$ . We assume that, in the first expansion stage ( $t_i = 0 \leq t \leq t_0$ ), the disordered potential is still off; the density matrix at time  $t_0$  is then the pure state:  $\rho(t_0) = |\psi_0\rangle\langle\psi_0|$ , where  $\psi_0(x) = e^{i\theta_0(x)}\sqrt{n_0(x)}$  is determined by the integration of Eq. (4.9) with  $V \equiv 0$ . The solution reads [178, 179]:

$$n_0(x) = \frac{n_i(x/b(t_0))}{b(t_0)} \quad \text{and} \quad \theta_0(x) = \frac{mx^2\dot{b}(t_0)}{2\hbar b(t_0)}, \quad (4.11)$$

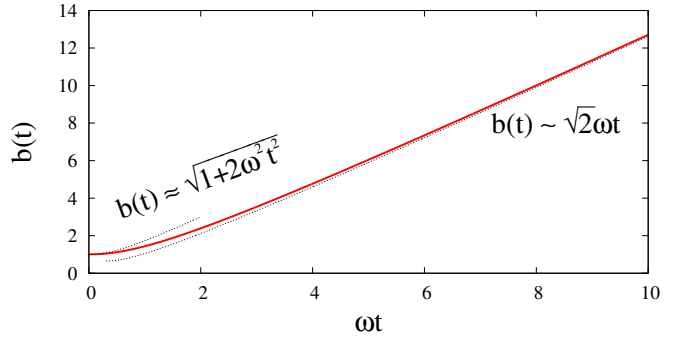
where the scaling parameter  $b(t)$  is the unique solution of  $\sqrt{b(t)[b(t) - 1]} + \ln[\sqrt{b(t)} + \sqrt{b(t) - 1}] = \sqrt{2}\omega t$  [135]. It characterizes a self-similar expansion of the initial density profile  $n_i(x)$  which is an inverted parabola [Eq. (4.10)]. Therefore for  $0 < t < t_0$ , the density profile is still an inverted parabola of half-width  $b(t)L_{\text{TF}}$ . The scaling parameter  $b(t)$  is shown as a function of time in Fig. 4.4. For  $t \ll 1/\omega$ , one finds an accelerating expansion with  $b(t) \simeq \sqrt{1 + 2(\omega t)^2}$ . And for longer times ( $t \gg 1/\omega$ ), we have  $b(t) \simeq \sqrt{2}\omega t + (1/2)[1 - \ln(4\sqrt{2}\omega t)] \sim \sqrt{2}\omega t$ ; the expansion becomes ballistic.

The second expansion stage ( $t > t_0$ ) starts when the disorder is suddenly switched on and the interactions off ( $V \neq 0$  and  $g \rightarrow 0$ ). Then, Eq. (4.9) reduces to the linear Schrödinger

2. This definition is that of Ref. [8]. It is not the usual one (by a factor  $\sqrt{2}$ ), but it permits to avoid a number of  $\sqrt{2}$  in the following equations.

3. We define, as in Chap. 3,  $[f(x)]_{\oplus} = f(x)$  for  $f(x) > 0$  and 0 otherwise.

Figure 4.4: Evolution of the scaling parameter  $b(t)$  (solid red line) and its two asymptotic behaviours (dashed black lines):  $b(t) \simeq \sqrt{1+2(\omega t)^2}$  when  $\omega t \ll 1$  and  $b(t) \simeq \sqrt{2}\omega t + (1/2)[1 - \ln(4\sqrt{2}\omega t)]$  when  $\omega t \gg 1$ . For  $\omega t = 10$ , the approximation  $b(t) \simeq \sqrt{2}\omega t$  is very good.



equation of Hamiltonian  $H = -\hbar^2\partial_x^2/2m + V(x)$ , and we can use the formalism introduced in Chap. 2 with the initial state given by Eq. (4.11) at time  $t_0$ . The evolution of the average density (see Eq. (2.31), see also Ref. [141]) is then given by

$$\bar{n}(x, t) = \int \frac{dE}{2\pi} \int dx_0 \int \frac{dk}{2\pi} W_0(x_0, k) A(k, E) P(x - x_0, t - t_0 | E) \quad (4.12)$$

where  $W_0(x_0, k)$  is the initial Wigner function at time  $t_0$ ,  $A(k, E)$  is the spectral function, and the quantity  $P(x - x_0, t - t_0 | E)$  is the probability of quantum diffusion, which is interpreted as the density probability to find in  $x$  at time  $t$ , a particle of energy  $E$  that was located in  $x_0$  at time  $t_0$ .

This two-stage scenario is approximately realized in experiments such as that of Ref. [9] (described in Sec. 4.2.1), if the parameters are such that the disorder is felt by the atoms around a time  $t_0 \gg 1/\omega$ . We have verified this in numerical simulations of the Gross-Pitaevskii equation (4.9) for typical parameters of Ref. [9].

### 4.2.3 Fundamental quantities

In order to compute the average density profile of the atoms in the disorder, we now have to compute the quantities appearing in Eq. (4.12).

**Semi-classical approach** – If  $t_0 \gg 1/\omega$ , the expansion at the end of the first stage is ballistic. The initial state (4.11) is then characterized by the velocity field  $v_0(x) \equiv (\hbar/m)\partial_x\theta_0 = x\dot{b}(t_0)/b(t_0)$ , associated to the local de Broglie wavelength  $\lambda_{\text{dB}}(x) \equiv \hbar/mv_0(x) \sim \hbar t_0/mx$ . We find  $\lambda_{\text{dB}}(x) \ll n_0/|\partial_x n_0|$ , except in a small region of width  $\Delta x \sim \xi_{\text{in}}$  near the edges of the BEC, and where  $n_0/|\partial_x n_0|$  represents the typical variation scale of the density of the atoms. We can consider that the velocity of each atom is given by its position in the condensate and use the semi-classical phase-space distribution  $W_0(x, k) \simeq n_0(x) \times 2\pi\delta[k - mv_0(x)/\hbar]$ . It can be rewritten

$$W_0(x, k) \simeq \mathcal{D}_{k,0}(k) \times \delta\left(x - \left[b(t_0)/m\dot{b}(t_0)\right]\hbar k\right) \quad (4.13)$$

where  $\mathcal{D}_{k,0}(k) = 2\pi\left(3N/4k_m(t_0)\right) [1 - (k/k_m(t_0))^2]_{\oplus}$  is the momentum distribution. It is also an inverted parabola, truncated at  $k_m(t_0) \equiv (1/\xi_{\text{in}})(\dot{b}(t_0)/\sqrt{2}\omega)$ . In the long-time limit ( $t_0 \rightarrow \infty$ ), we find that the cut-off of the momentum distribution is simply given by  $k_m \rightarrow 1/\xi_{\text{in}}$ . The full Wigner function at the end of the first stage, computed [see Eq. (2.19)] from the wavefunction obtained by numerical integration of Eq. (4.9) between  $t = 0$  and  $t_0$ , is shown

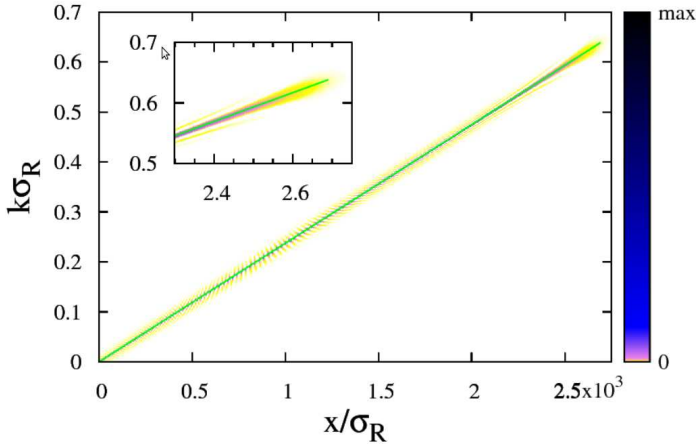


Figure 4.5: Wigner function computed at time  $t_0 = 10/\omega$ , after the first expansion stage (the value  $W_0(x, k)$  is color-coded from white to black, with a color scale enhancing low values). We have integrated numerically Eq. (4.9) in the conditions described in Sec. 4.2.2 and for  $\omega = 2 \times 10^{-2} \mu/\hbar$  and  $\xi_{\text{in}} = 1.5\sigma_{\text{R}}$  [parameters of Fig. 4.7(a1)]. It is well approximated by Eq. (4.13), which is represented by the solid green line. The inset shows a zoom on  $x \in [2.3, 2.75] \times 10^3 \sigma_{\text{R}}$ .

in Fig. 4.5. It sits on a line and is indeed well approximated by Eq. (4.13). When looking into details, we see that there is a discrepancy on the edges of the condensate. Just after the application of the disorder, the initial state can be characterized by a position-energy distribution in Eq. (4.12)

$$\begin{aligned} \mathcal{D}_0(x, E) &\equiv \int \frac{dk}{2\pi} W_0(x, k) A(k, E) \\ &\simeq \frac{A(x/\zeta, E)}{2\pi\zeta} \mathcal{D}_{k,0}(x/\zeta) \end{aligned} \quad (4.14)$$

where<sup>4</sup>  $\zeta = \hbar b(t_0)/mb\dot{b}(t_0)$ . In particular, the energy distribution of the atoms, which is given by  $\mathcal{D}_{\text{E}}(E) = \int \frac{d\mathbf{k}}{(2\pi)^d} A(E, \mathbf{k}) \mathcal{D}_{\mathbf{k}}(\mathbf{k})$  [see Eq. (2.18)], extends, in weak disorder [i.e. if  $A(k, E) \rightarrow 2\pi\delta(E - \hbar^2 k^2/2m)$ ], from  $E = 0$  to  $E_{\text{m}} = \hbar^2 k_{\text{m}}^2/2m \simeq 2\mu$ .

**Spectral function** – In order to calculate the average spectral function [see Eq. (2.16)],

$$A(k, E) = \frac{-2\Sigma''(E, k)}{\left(E - \hbar^2 k^2/2m - \Sigma'(E, k)\right)^2 + \Sigma''(E, k)^2}, \quad (4.15)$$

we evaluate the self-energy  $\Sigma(E, k)$  in the Born approximation in which only the first two terms of Eqs. (2.8)-(2.9) are retained [58]:  $\langle k | \overline{V G_0(E) V} | k' \rangle = 2\pi\delta(k - k')\Sigma(E, k)$ . For  $V_{\text{R}}^2 \ll E^{3/2} E_{\sigma_{\text{R}}}^{1/2}$  where  $E_{\sigma_{\text{R}}} \equiv \hbar^2/m\sigma_{\text{R}}^2$  is the correlation energy of the disorder [i.e.  $\gamma(E) \ll p_E/\hbar$ ], we get the explicit formula

$$\Sigma''(E, k) \simeq -\frac{m}{2\hbar^2 k_E} \left\{ \tilde{C}_2(k_E - k) + \tilde{C}_2(k_E + k) \right\} \quad (4.16)$$

where  $k_E \equiv \sqrt{2mE}/\hbar$  is the momentum associated to energy  $E$  in free space. The real-part of the self-energy,  $\Sigma'(E, k) = \int \frac{dk'}{2\pi} \tilde{C}_2(k' - k) \times \text{PV} \left( \frac{1}{E - \hbar^2 k'^2/2m} \right)$  with PV the Cauchy principal value, turns out to be negligible for the parameters used here and we disregard it in the remainder of this chapter. Note that this will not be true for the 3D cases discussed in this manuscript, where we will take the real part of the self energy into account.

4. Note that  $\zeta$  has the dimension of a length squared.

**Probability of quantum transport** – In order to calculate the probability of quantum diffusion, we rely on the one-dimensional diagrammatic method developed in Refs. [70,71,155] in the Born approximation, which is detailed in appendix B. In the weak disorder limit [ $\gamma(E) \ll \sigma_R^{-1}, k_E$ ], it provides the infinite-time limit<sup>5</sup>

$$\begin{aligned} P_\infty(x|E) &\equiv P(x, t \rightarrow \infty | E) \\ &= \frac{\pi^2 \gamma(E)}{8} \int_0^\infty du u \sinh(\pi u) \left[ \frac{1+u^2}{1+\cosh(\pi u)} \right]^2 \exp \left\{ -(1+u^2) \frac{\gamma(E)|x|}{2} \right\}, \end{aligned} \quad (4.17)$$

with

$$\gamma(E) \equiv L_{\text{loc}}^{-1}(E) \simeq \frac{m^2}{2\hbar^4 k_E^2} \tilde{C}_2(2k_E). \quad (4.18)$$

This quantity, which characterizes the typical decay of the probability of quantum diffusion (4.17), is the same as the Lyapunov exponent found with the phase formalism in the Born approximation [see Eq. (4.5)]; therefore we will also call it 'Lyapunov exponent' in the following. Equation (4.17) is shown on Fig. 4.6(a) (solid black line). When  $|x| \ll [2\gamma(E)]^{-1}$  we find

$$P_\infty(x|E) \simeq \gamma(E) e^{-2\gamma(E)|x|}, \quad (4.19)$$

which is the dashed red line. For  $|x| \gg [2\gamma(E)]^{-1}$  we find

$$P_\infty(x|E) \simeq \frac{\pi^{7/2} 2^{1/2}}{64 \sqrt{\gamma(E)} |x|^{3/2}} e^{-\gamma(E)|x|/2} \quad (4.20)$$

(see dotted cyan line), which gives

$$\ln[P_\infty(x|E)] \sim -\frac{\gamma(E)|x|}{2} \quad (4.21)$$

at very large distances. Therefore Eq. (4.17) interpolates between two exponential decreases with typical length  $L_{\text{loc}}(E)/2$  at small distance and  $2L_{\text{loc}}(E)$  at large distance, as shown in Fig. 4.6(b).

Equation (4.12) allows us to determine the density profile of the matter wave packet. We recover the formulation of Ref. [8] – where the initial width of the condensate and the spectral broadening have been neglected – by using the substitutions  $W_0(x_0, k) \rightarrow \mathcal{D}_{k,0}(k) \times \delta(x_0)$ , which holds at distances exceeding the initial size of the gas and  $A(k, E) \rightarrow 2\pi\delta(E - \hbar^2 k^2 / 2m)$ , which is the free spectral function. Our approach here goes beyond that of Ref. [8]: It allows us to take into account (i) the initial position distribution via  $W_0(x_0, k)$  and (ii) the spectral broadening  $A(k, E)$  of a particle of momentum  $k$  in the disordered potential. We will show below that both play a significant role in the localization process.

---

5. In Ref. [8] the term inside the exponential function in  $P_\infty(x|E)$  was mistakenly written (see erratum of Ref. [8]). The present Eq. (4.17) is the correct formula.

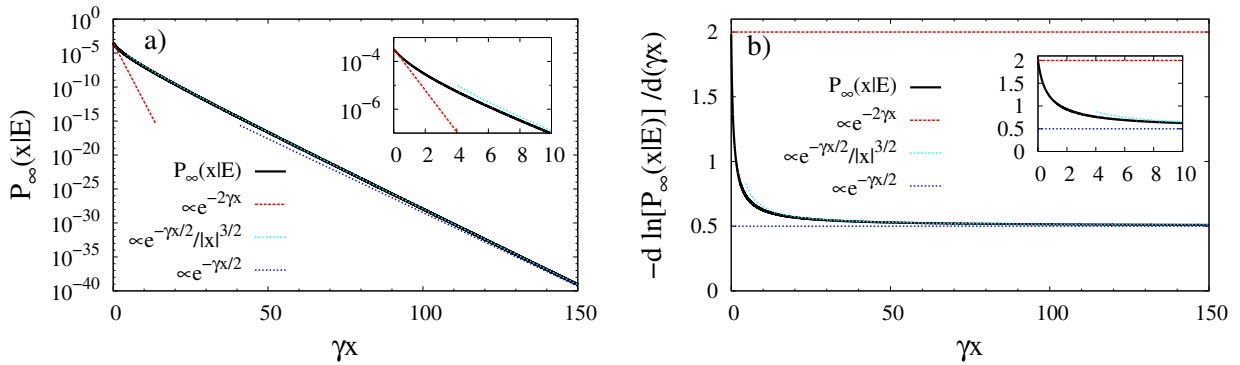


Figure 4.6: Probability of quantum diffusion  $P_\infty(x|E)$ . (a) Equation (4.17) as a function of  $\gamma(E)x$  (solid black line), and limiting regimes: Eq. (4.19) valid for  $\gamma(E)x \lesssim 1/2$  (dashed red line), Eq. (4.21) valid for  $\gamma(E)x \gtrsim 20$  (dotted cyan line), and the Eq. (4.20) valid for  $\gamma(E)x \gtrsim 100$  (dotted blue line). (b) Logarithmic derivative  $d \ln[P_\infty(x|E)]/d[\gamma(E)x]$  (solid black line), and the same limiting regimes. It interpolates between 2 (dashed red line) and 1/2 (dotted blue line).

#### 4.2.4 Numerical simulations

We now perform numerical calculations to test the predictions of our analytical model. In order to integrate Eq. (4.9), we use a Crank-Nicolson algorithm [180], with space step  $\Delta x = 0.1\sigma_R$  (we will take  $\xi_{\text{in}}$  of the order of  $\sigma_R$  in the following, and this will be the smallest characteristic length in the system), and time step  $\Delta t = 0.1\hbar/E_{\sigma_R}$ , in a box with Dirichlet boundary conditions [ $\psi(-L_{\text{tot}}/2) = \psi(L_{\text{tot}}/2) = 0$ ], where  $L_{\text{tot}}$  is the size of the box]. Only the central half of the box used in the numerics is plotted in Fig. 4.7. We have checked that the boundary conditions do not significantly alter the results in the represented space window by using boxes of different sizes.

The disorder is also a 1D speckle potential created with a square aperture, whose power spectrum is given in Eq. (4.7). We use parameters close to those of Ref. [9] and both blue and red detunings [ $V_R = \pm 0.01625E_{\sigma_R}$ , which corresponds to  $V_R/h \sim 33$  Hz in the units of Ref. [9] and Fig. 4.3(c)]. Our numerical calculations differ from those of Ref. [8] in that we use significantly larger boxes and longer times. Moreover, we consider here exactly the above scenario where the disorder is switched on and the interactions off at a time  $t_0 \gg 1/\omega$ , while in the numerics of Ref. [8], both disorder and interactions were on during the whole expansion, as in the experiment. Due to the cut-offs of  $\tilde{C}_2(k)$  at  $k = \pm 2/\sigma_R$ , the quantities  $\gamma(E)$  and  $P_\infty(x|E)$  vanish for  $E > E_{\sigma_R}/2$  and, as in the description of the experiment in Sec. 4.2.1, it is useful to distinguish two cases for the analysis of the density profiles.

**Case  $2\mu < E_{\sigma_R}/2$  (i.e.  $\xi_{\text{in}} > \sigma_R$ )** – When  $\xi_{\text{in}} > \sigma_R$ , we have  $E_m \simeq 2\mu < E_{\sigma_R}/2$ , and, under the assumptions of Refs. [8, 9] (i.e. when neglecting the spectral broadening), all the energy components are expected to be localized in the Born approximation. The left panel of Fig. 4.7 shows the time evolution of the density profile in semi-log scale for  $\xi_{\text{in}} = 1.5\sigma_R$ . The different rows represent different times [(a1):  $t = 0$  and  $t = t_0$ , (a2):  $t = 26.7/\omega$  and (a3):  $t = 133.3/\omega$ ]. For  $t < t_0 \equiv 10/\omega$  [Fig. 4.7(a1)], the matter wave expands in free space, with the shape of a truncated inverted parabola of increasing size, according to Eq. (4.11). At  $t = t_0$ , when the disorder is switched on and the interactions off, the matter wave continues expanding and develops long wings [Fig. 4.7(a2)]. In the long-time limit [Fig. 4.7(a3)], the density profile

converges to a stationary shape, hence demonstrating Anderson localization. The localized density profile is in fair agreement with the theoretical prediction based on Eq. (4.12), using Eqs. (4.13), (4.15) and (4.17) for the correlation function (4.7), with a global multiplying factor as the only fitting parameter [see solid black line in Fig. 4.7(a3)]. This holds over the full space, except very close to the center. There, for the chosen parameters, Eq. (4.12) predicts a non-physical dip due to the over-estimation of the Lyapunov exponents and the spectral broadenings<sup>6</sup> at low energies in the lowest-order perturbation theory used to derive Eqs. (4.15) and (4.17). This dip affects the balance between the center and the wings in the normalization of the wavefunction, which justifies the multiplying factor to correctly fit the wings. These results validate the localization model of the matter wave.

Let us now discuss the density profile in more detail, and accordingly examine the impact of the various terms in Eq. (4.12). For  $|x| \lesssim b(t_0)L_{\text{TF}}$  [where  $b(t_0)L_{\text{TF}}$  is the width of the initial density distribution], the stationary density profile is mainly determined by particles originating from the BEC at time  $t_0$  that propagate over very short distances in the disordered potential. Using the full phase-space distribution  $W_0(x, k)$  is then necessary to account for the central feature of the density profile. For  $|x| \gtrsim b(t_0)L_{\text{TF}}$  only, we can neglect the initial density distribution and rely on the approximation  $W_0(x, k) \rightarrow \mathcal{D}_{k,0}(k) \times \delta(x)$  in Eq. (4.12), which was used in Ref. [8]. For  $b(t_0)L_{\text{TF}} \lesssim |x| \lesssim 1/2\gamma(2\mu)$ , we find that the density profile shows an essentially exponential decay of rate approximately equal to  $2\gamma(2\mu)$  [see dashed green line in Fig. 4.7(a3)]. This is consistent with experimental observations [9], where the profiles are fitted by the pure exponential  $n(x) \propto e^{-2|x|/L_{\text{loc}}}$ , and the results are compared to  $L_{\text{loc}}(2\mu)$  in the Born approximation [see Fig. 4.3(c)]. For longer distances however, the logarithmic derivative of the density continuously decreases in modulus. Neglecting the spectral broadening induced by the disorder [8, 175],  $A(k, E) \rightarrow 2\pi\delta(E - \hbar^2 k^2/2m)$ , we are able to reproduce the numerical results over about five decades [see dotted black line in Fig. 4.7(a3)]. This approximation cuts all components with  $E > 2\mu$ , as explained above, and predicts a long-distance exponential decay of rate<sup>5</sup>  $\gamma(2\mu)/2$  [8]. This behavior can be understood on the basis of the probability of quantum diffusion (4.17), which continuously interpolates from  $d \ln P_\infty(x|E)/dx \simeq -2\gamma(E)$  for  $|x| \ll 1/2\gamma(E)$  to  $d \ln P_\infty(x|E)/dx \simeq -\gamma(E)/2$  for  $|x| \gg 2/\gamma(E)$  (see Fig. 4.6(b)) [71]. For  $|x| \gg 2/\gamma(2\mu)$ , the numerics show significant deviation from exponential decay, owing to the Lorentzian-like form of the spectral function (4.15) which does populate components with  $E > 2\mu$ . Then, taking into account the full spectral function, Eq. (4.12) fits well the numerics [see solid black line in Fig. 4.7(a3)]. Finally, note that our model relies on the Born approximation which is not sufficient to account for components with  $E > E_{\sigma_R}/2$  [see Eq. (4.18)] [14, 15]. To do so, it would be necessary to include arbitrary high-order terms at arbitrary large distances. It however appears irrelevant in the space window used for the numerics.

A discrepancy between blue and red detuned realizations appears on Fig. 4.7(a3), which cannot be accounted for in the Born approximation either [Eq. (4.18) does not depend on the sign of  $V_R$ ]. However, the deviations are consistent in sign with those found with the third order of the phase formalism (see Fig. 4.2).

---

6. The over-estimation of the self energy at low energies in the Born approximation leads to an over-estimation of the spectral broadening at low energy. Low energies mostly determine the density profile at the center, and as  $\gamma(E)$  is a decreasing function of  $E$ , the 'local' localization lengths can therefore be over-estimated at the center, leading to the dip observed in Fig. 4.7(a3).

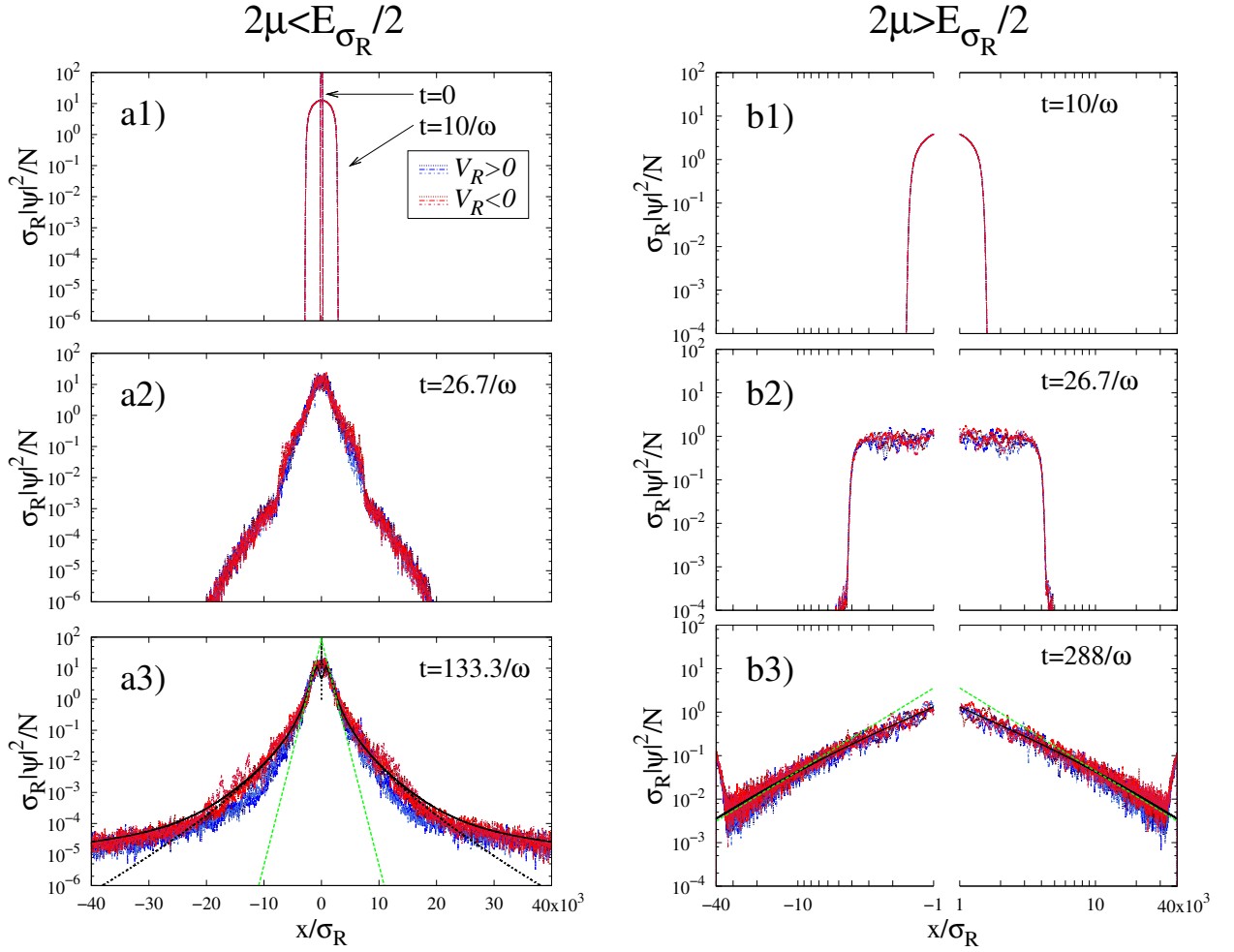


Figure 4.7: Time evolution of the density profile of a matter wave expanding in 1D speckle potentials for  $2\mu < E_{\sigma_R}/2$  (left panel) and  $2\mu > E_{\sigma_R}/2$  (right panel). Shown are the running averages,  $\tilde{n}(x) = \int_{-l/2}^{+l/2} \frac{dx}{l} n(x+x)$  with  $l = 100\sigma_R$ , of numerical data, for blue- and red-detuned speckle potentials (three realizations each). Here, we use  $\omega = 2 \times 10^{-2} \mu/\hbar$  and  $V_R = \pm 0.01625 E_{\sigma_R}$ . Left panel (a1-a3): semi-log scale for  $\xi_{in} = 1.5\sigma_R$  ( $2\mu \simeq 0.22 E_{\sigma_R}$ ). The solid black line shows a fit of the full Eq. (4.12) and the dotted black line to Eq. (4.12) with  $A(p, E) \rightarrow 2\pi\delta(E - p^2/2m)$ , both with a multiplying factor as the only fitting parameter. The dashed green line is a fit of  $\ln[n(x)] = A - 2\gamma(2\mu)|x|$ , with  $A$  as the fitting parameter. Right panel (b1-b3): log-log scale for  $\xi_{in} = 0.83\sigma_R$  ( $2\mu \simeq 0.72 E_{\sigma_R}$ ). The solid black line shows the full Eq. (4.12) and the dashed green line is a fit of  $n(x) = A/|x|^\beta$  with  $A$  and  $\beta$  as the fitting parameters.

**Case  $2\mu > E_{\sigma_R}/2$  (i.e.  $\xi_{in} < \sigma_R$ )** – When  $\xi_{in} < \sigma_R$ , we have  $E_m \simeq 2\mu > E_{\sigma_R}/2$ , and some energy components are not localized in the Born approximation, which led to algebraically-localized density profiles under the assumptions of Refs. [8, 9]. The right panel of Fig. 4.7 shows the counterpart of the left panel for  $\xi_{in} = 0.83\sigma_R$  and in log-log scale. In this regime too, the complete model of Eq. (4.12) reproduces well the numerical results over the full space (except very close to the center), with a multiplying factor as the only fitting parameter [see solid black line in Fig. 4.7(b3)]. In 1D speckle potentials, the correlation function provides a high-momentum cut-off which strongly suppresses back-scattering of matter waves with

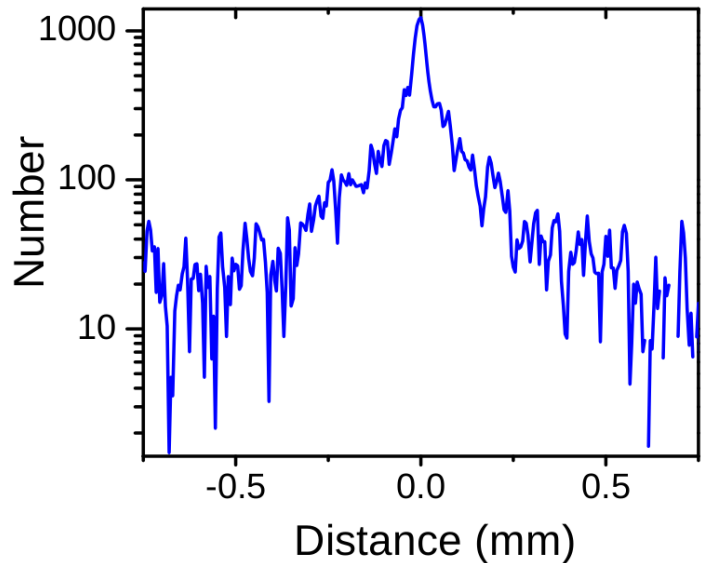


Figure 4.8: Experimental density profile from the group of R. Hulet, obtained in a similar scheme as Ref. [9], for  ${}^7\text{Li}$  atoms, and  $\xi_{\text{in}} = 2.86\sigma_{\text{R}}$ . Data presented during the BEC 2009 conference in Sant Feliu [28].

momentum  $k > 1/\sigma_{\text{R}}$  [8, 14, 15]. For  $E > E_{\sigma_{\text{R}}}/2$ , the Lyapunov exponent, calculated in the Born approximation then vanishes [see Eq. (4.18)], and the determination of  $P_{\infty}(x|E)$  would require an extension of the formalism of Refs. [70, 155] by at least two orders in perturbation theory. Using the results of Refs. [14, 15] based on the phase-formalism approach, we estimate that, for our parameters, the Lyapunov exponent drops by about two orders of magnitude around  $E \simeq E_{\sigma_{\text{R}}}/2$  and we neglect localization of waves with  $E > E_{\sigma_{\text{R}}}/2$ . Since  $E_{\sigma_{\text{R}}}/2 < 2\mu$ , the spectral broadening has little importance here and we can safely rely on the approximation  $A(k, E) \rightarrow 2\pi\delta(E - \hbar^2 k^2/2m)$ . The above model then predicts algebraic localization<sup>7</sup>,  $n(x) \propto 1/|x|^2$  [8]. Fitting an algebraic function,  $A/|x|^{\beta}$  with  $A$  and  $\beta$  as fitting parameters, to the numerical data of three different realizations of blue- and red-detuned speckle potentials in the intervals  $[-30, -10] \times 10^3\sigma_{\text{R}}$  and  $[+10, +30] \times 10^3\sigma_{\text{R}}$  independently, we find  $\beta \simeq 1.91 \pm 0.22$ . This is in fair agreement with the analytical prediction (within the error bars) and was observed in Ref. [9].

**Discussion of experiments** – Let us now compare the predictions of our full model, to the experimental results available. In Ref. [9], the experimentally-accessible window was such that only the short-distance exponential decay of the density profiles was observed. Then exponential fits agree well with the theoretical prediction  $\gamma(2\mu)$  as shown in Fig. 4.3(c). However, at large distance, a slight broadening of the density profiles compared to pure exponential decay is observed in Ref. [9], and the fitted localization length are over-estimated at high  $V_{\text{R}}$ , i.e. the Lyapunov exponents are found smaller than expected when localization is the strongest. Both deviations cannot be explained in the framework of the approximations of Refs. [8, 9]; but they are consistent with the deviations from a pure exponential decay found here, due to the behaviour of the probability of quantum transport: If the experiment is sensitive to the crossover between the exponential decays  $\ln[n(x)] \sim -2|x|/L_{\text{loc}}$  and  $\ln[n(x)] \sim -|x|/2L_{\text{loc}}$ , it will primarily show up for small localization lengths, and lead to an overestimation of  $L_{\text{loc}}$  by the fits. A similar experiment with  ${}^7\text{Li}$  atoms in 1D speckle disorder was carried out in the team of R. Hulet [28]. Deviations from a pure exponential decay were also reported, as

<sup>7</sup>. The power of this algebraic decay depends on which is the first non-vanishing derivative of  $\tilde{C}_2(k)$  at the cut-off.

shown for example in Fig. 4.8, which may be ascribed to the same effects as above.

## Conclusion

In summary, we have studied Anderson localization of ultra-cold atoms in 1D speckle potentials. First, we have considered a transmission scheme for a wave with a single energy component through a one-dimensional speckle potential with correlation length  $\sigma_R$ . It enabled us to compute the Lyapunov exponent in a perturbative series using the so-called phase formalism. It permitted to show that corrections to the Born approximation are non-negligible for typical experimental parameters. More precisely, including the third order allows us to reproduce accurately exact numerical results and in particular accounts for the difference between blue- and red-detunings.

Second, we have developed a theoretical model for the Anderson localization of a matter wave packet (with initial chemical potential  $\mu$ ) expanding in the same 1D speckle potential (with correlation length  $\sigma_R$ ). It extends previous approaches [8] by including (i) the initial phase-space density of the matter wave, and (ii) the spectral broadening induced by the disorder. We have shown that these new ingredients affect the localized density profiles, which significantly deviate from a pure exponential decay, and the predictions of the model agree with our large scale numerical calculations. For  $2\mu < E_{\sigma_R}/2$  (where  $E_{\sigma_R} = \hbar^2/m\sigma_R^2$ ), we found that  $\bar{n}(x)$  essentially shows an exponential decay of rate  $2\gamma(2\mu)$  at short distance, in accordance with experimental observations [9]. For larger distance, however,  $\bar{n}(x)$  crosses over to an exponential decay of rate  $\gamma(2\mu)/2$  and then deviates from exponential decay due to the disorder-induced spectral broadening. This may explain the very large distance behavior of experimental data [9, 28], where signs of a deviation from a pure exponential decay are observed, and the large disorder localization lengths are systematically over-estimated. For  $2\mu > E_{\sigma_R}/2$ , we found algebraic localization,  $\bar{n}(x) \propto 1/|x|^2$ , as observed in Ref. [9] in accordance with the prediction of Ref. [8].

In the future, it would be interesting to extend the present approach towards two directions. First, our analysis relies on the calculation of the probability of quantum diffusion,  $P_\infty(x|E)$ , to lowest order, which is valid only below the effective mobility edge at  $E = E_{\sigma_R}/2$  [14, 15]. In addition, it may explain the slight difference in the localized density profiles found for blue- and red-detuned speckle potentials [see Fig. 4.7(a3)], which was expected from the above findings. Extending the diagrammatic method of Refs. [70, 155] to higher orders would allow one to incorporate the components of energy  $E > E_{\sigma_R}/2$ . Second, although ultracold atoms allow for an exact realization of the above scenario using time-dependent control of optical disorder and of interactions via Feshbach resonance techniques, recent experiments have followed a slightly different scheme where the BEC is created already in the presence of the disorder and the interactions are not switched off [9, 28]. Extending our model to this case would require to include (i) the effect of the disorder at  $t \lesssim 1/\omega$ , which can significantly modify the relevant phase-space density  $W_0(x, k)$  and (ii) the effect of interactions in the probability of quantum diffusion  $P_\infty(x|E)$ . Whether and how interactions destroy localization in this scheme is still a very debated subject [95, 96, 181–183].



## Chapter 5

# Quantum transport and Anderson localization in dimension $d > 1$ : Theory and application to anisotropic two-dimensional disorder

### Abstract

The macroscopic transport properties of a coherent wave in a disordered medium, namely diffusion and weak/strong localization, closely depend on the microscopic and statistical properties of the disorder itself. In this chapter we study quantum transport of matterwaves in disordered potentials with anisotropic correlations in dimension  $d > 1$ . The presentation of the theoretical developments, which include single-scattering, Boltzmann diffusion and Anderson localization (with the self-consistent theory) is intended to be as pedagogical as possible. We illustrate the theoretical findings with a 2D anisotropic example which is relevant for current experiments on ultra-cold atoms in speckle disorder. This chapter represents a guideline for future experiments aimed at studying anisotropic diffusion and localization effects in 2D. The counterpart to the discussed physics in 3D is presented in the next chapter.

### Résumé

Les propriétés macroscopiques de transport d'une onde cohérente en milieu désordonné, à savoir la diffusion et les localisations faible et forte dépendent fortement des propriétés microscopiques et statistiques du désordre lui-même. Dans ce chapitre nous étudions le transport quantique d'ondes de matière dans des potentiels désordonnés ayant des corrélations anisotropes, en dimension  $d > 1$ . La présentation des développements théoriques, qui incluent l'étude d'un événement de diffusion unique, de la diffusion de Boltzmann et de la localisation d'Anderson (grâce à la théorie « self-consistent ») a une vocation pédagogique. Nous illustrons les résultats théoriques avec un exemple anisotrope à 2D qui est pertinent pour les expériences actuelles d'atomes ultrafroids dans des désordres de speckle. Ce chapitre représente un guide

pour les expériences à venir sur les effets de diffusion et de localisation anisotropes en 2D. La contrepartie de cette physique à 3D est présentée dans le chapitre suivant.

## Introduction: Transport in anisotropic media

Presently, a major challenge of the theory of localization is the study of quantum transport in dimensions higher than one. While localization is the dominant effect in one dimension [146, 184], higher dimensions show a richer phenomenology where all regimes of diffusion, weak localization and Anderson localization can appear [56]. Recent experiments reported the observation of an Anderson transition in momentum space using cold-atom kick-rotor setups [142–144], study of classical diffusion in two-dimensional (2D) speckle potentials [17, 23], coherent back-scattering [19, 52] and evidence of Anderson localization in noninteracting Fermi [18] and Bose [19] gases in three-dimensional (3D) speckle potentials. The latter is particularly interesting because correlations in speckle potentials are non-standard and can be tailored.

So far, diffusion and localization of noninteracting matter waves have been thoroughly studied for disordered potentials with zero-range correlations [141, 175] and isotropic correlation functions [16, 151, 163, 165, 169, 185]. However, transport experiments with ultra-cold atoms in dimensions higher than one are most often done in speckle potentials which are anisotropic, either effectively in 2D setups [17, 23], or for fundamental optical constraints in 3D [18, 19]. Moreover, the possibility of tailoring correlations in speckle potentials in a broad range of configurations [20], offers scope for investigation of localization in nonstandard models of disorder (see Refs. [26, 186] and Chap. 8). Taking into account anisotropic effects is of fundamental importance because they can strongly affect coherent transport and localization properties.

Having reviewed the general theory of quantum transport in disordered media in Chap. 2, we now specify the framework of our study in dimensions higher than one. We present here a detailed description of the theoretical framework pioneered in Refs. [42, 153, 154], which intends to be pedagogical (technical details are presented in the appendix C). We study single-scattering (Sec. 5.1), Boltzmann diffusion (Sec. 5.2), and localization (Sec. 5.3), as a function of the particle energy, and discuss in particular the different anisotropies of these quantities. From a technical viewpoint, while the scattering allows for analytic expressions as for isotropic models of disorder [16], diffusion and localization are more involved and require in general numerical diagonalization of a certain operator.

In the following, we will consider ultracold matter waves as realized in several experiments [9, 10, 17–19, 23, 127, 132–136, 161, 162]. In our case, the underlying (disorder-free) medium is the vacuum, and  $\epsilon(\mathbf{k}) = \hbar^2 \mathbf{k}^2 / 2m$ . The disorder has anisotropic correlations, and is characterized by its amplitude  $V_R$  and its two-point correlation function  $C(\mathbf{r}) = \overline{V(\mathbf{r}_0)V(\mathbf{r}_0 + \mathbf{r})}$  with the choice of the zero of energies such that  $\overline{V} = 0$  (see Chap. 3).

As an illustration, we focus in this chapter on the 2D case, which contains most of the anisotropy effects and we will discuss 3D cases in Chap. 6. We consider here the anisotropic two dimensional speckle presented in Sec. 3.2.2, which is relevant to current 2D experiments [17]. The two-point correlations of the light intensity pattern are given by Eq. (3.24) and its Fourier transform by Eq. (3.25). The power spectrum of the disordered potential [see Eq. (3.29)] is then

$$\tilde{C}(\mathbf{k}) = V_R^2 \pi \frac{\sigma_R^2}{\xi} \exp \left[ -\frac{\sigma_R^2}{4} \left( k_x^2 + \frac{k_y^2}{\xi^2} \right) \right], \quad (5.1)$$

with typical correlation lengths  $\sigma_R$  in the  $x$  direction, and  $\sigma_R/\xi$  in the  $y$  direction. Without loss of generality, we assume in this chapter that the geometrical anisotropy factor is  $\xi \geq 1$ .

## 5.1 Single-scattering

Let us start with the first time scale introduced in Sec. 2: The scattering mean free time.

### 5.1.1 Scattering mean-free time

In order to calculate the scattering mean free time, defined previously in Eq. (2.17), we retain only the lowest order contribution to the self-energy (Born approximation). Within this approximation, the Born series of Eqs. (2.8)-(2.9) is truncated after the first two terms, which, according to Eq. (2.11), yields

$$\Sigma(E) = \overline{VG_0(E)V}. \quad (5.2)$$

For homogeneous disorder, we have  $\langle \mathbf{k} | \Sigma(E) | \mathbf{k}' \rangle = (2\pi)^d \delta(\mathbf{k} - \mathbf{k}') \Sigma(E, \mathbf{k})$  with

$$\Sigma(E, \mathbf{k}) = \int \frac{d\mathbf{k}''}{(2\pi)^d} \tilde{C}(\mathbf{k} - \mathbf{k}'') G_0(E, \mathbf{k}''). \quad (5.3)$$

Using Eq. (2.17) and the disorder-free Green function, Eq. (2.7), we thus have

$$\tau_s(E, \mathbf{k}) = \frac{\hbar}{2\pi} \frac{1}{\langle \tilde{C}(\mathbf{k} - \mathbf{k}') \rangle_{\mathbf{k}'|E}}, \quad (5.4)$$

where

$$\langle \dots \rangle_{\mathbf{k}'|E} = \int \frac{d\mathbf{k}'}{(2\pi)^d} \dots \delta[E - \epsilon(\mathbf{k}')] \quad (5.5)$$

represents integration over the  $\mathbf{k}$ -space shell defined by  $\epsilon(\mathbf{k}) = E$ . Equation (5.4) allows one to determine the scattering time from the two-point correlation function of the disorder. In the following we discuss anisotropic properties of the scattering time for the 2D case (the 3D cases are presented in Sec. 6.2.1).

In the case of isotropic disorder (i.e. isotropic disorder correlations), we have  $\tilde{C}(\mathbf{k} - \mathbf{k}') = \tilde{C}(|\mathbf{k} - \mathbf{k}'|)$ , and the scattering time does not depend on the direction of the incoming wave vector  $\mathbf{k}$  [ $\tau_s(E, \mathbf{k}) = \tau_s(E, k)$ ]. In general (even with isotropic correlations), the scattering is however anisotropic:  $\tilde{C}(|\mathbf{k} - \mathbf{k}'|) \neq \tilde{C}(|\mathbf{k} - \mathbf{k}''|)$  and the probability that the particle acquires a direction  $\mathbf{k}'$  or  $\mathbf{k}''$  after the single-scattering event are different. Isotropic scattering is found for a  $\delta$ -correlated (or 'white-noise') disorder [with  $\tilde{C}(\mathbf{k}) = \text{cst}$ ], which is a key model of disordered metals. In this case, each scattering event contributes to the complete loss of the initial momentum direction  $\mathbf{k}$ . In the case of anisotropic disorder we are interested in, not only the scattering is anisotropic, but it also depends on the direction of the incoming wave  $\mathbf{k}$ .

### 5.1.2 Anisotropic Gaussian speckle (2D)

Let us now consider the 2D anisotropic speckle potential of geometrical anisotropy factor  $\xi$  introduced in Sec. 3.2.2. Replacing  $\tilde{C}(\mathbf{k})$  by Eq. (5.1) in Eq. (5.4) and using the disorder-free

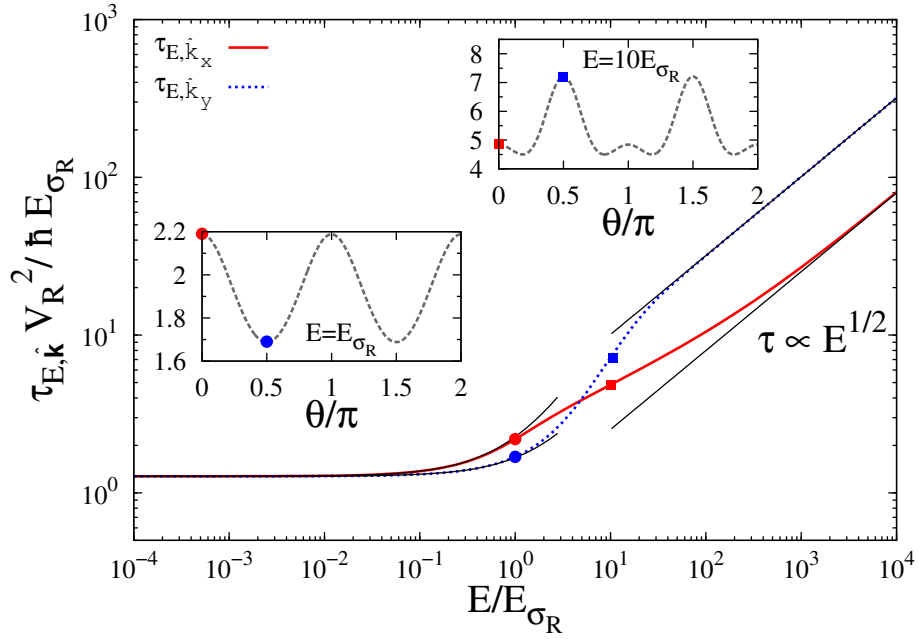


Figure 5.1: On-shell scattering mean free time  $\tau_{E,\hat{\mathbf{k}}} \equiv \tau_s(E, k_E \hat{\mathbf{k}})$  [Eq. (5.6) for  $|\mathbf{k}| = k_E$ ] along the  $\hat{\mathbf{k}}_x$  (solid red line) and  $\hat{\mathbf{k}}_y$  directions (dotted blue line) for the 2D speckle potential defined in Sec. 3.2.2 [power spectrum given by Eq. (5.1)] with  $\xi = 4$ . The solid black lines are the isotropic low-energy limit obtained for  $k_E \sigma_R \ll 1$  [Eq. (5.7)] and the high-energy limit obtained for  $k_E \sigma_R \gg \xi$  [Eq. (5.8)]. The insets show the angular dependance of  $\tau_{E,\hat{\mathbf{k}}}$  at two different energies [with the parametrization  $\hat{\mathbf{k}} \equiv (\cos \theta, \sin \theta)$ ]. The points on the lines are color- and shape-coded to match those in the insets.

dispersion relation of the vacuum in Eq. (5.5), we obtain the scattering mean free time

$$\tau_s(E, \mathbf{k}) = \frac{\hbar E \sigma_R}{V_R^2} \frac{2\xi}{\int d\Omega_{\hat{\mathbf{k}}'} \exp\left[-\frac{\sigma_R^2}{4}(k_E \hat{k}'_x - k_x)^2\right] \exp\left[-\frac{\sigma_R^2}{4\xi^2}(k_E \hat{k}'_y - k_y)^2\right]}, \quad (5.6)$$

where  $\hat{\mathbf{k}} \equiv \mathbf{k}/|\mathbf{k}|$  is the unit vector pointing in the direction of  $\mathbf{k}$ ,  $\Omega_{\hat{\mathbf{k}}}$  is the  $\mathbf{k}$ -space solid angle,  $k_E \equiv \sqrt{2mE}/\hbar$  is the momentum associated to energy  $E$  in free space and  $E_{\sigma_R} \equiv \hbar^2/m\sigma_R^2$  is the correlation energy of the disorder. The scattering time (5.6) is plotted in Fig. 5.1 as a function of energy along the two main axes and for a fixed geometrical anisotropy  $\xi = 4$ . In the figure, we actually plot the on-shell (i.e. taken at  $|\mathbf{k}| = k_E$ ) scattering mean free time  $\tau_{E,\hat{\mathbf{k}}} \equiv \tau_s(E, k_E \hat{\mathbf{k}})$ . Let us discuss some limiting cases.

**Low-energy limit** – In the low-energy limit,  $k_E \sigma_R \ll 1$ , we have

$$\tau_{E,\hat{\mathbf{k}}} = \frac{\hbar E \sigma_R}{V_R^2} \frac{\xi}{\pi} + \frac{\hbar E}{4\pi V_R^2} \left[ \xi + \frac{2}{\xi} + 2 \left( \xi \hat{k}_x^2 + \frac{\hat{k}_y^2}{\xi} \right) + O\left(\frac{E^2}{\xi^4 E_{\sigma_R}^2}\right) \right], \quad (5.7)$$

which is displayed in Fig. 5.1 (left-hand side black lines). In this limit the de Broglie wavelength of the particle ( $2\pi/k_E$ ) exceeds the correlation lengths of the disorder ( $\sigma_{Rx}$  and  $\sigma_{Ry}$ ) and the speckle can be approximated by a white-noise (uncorrelated) disordered potential. More

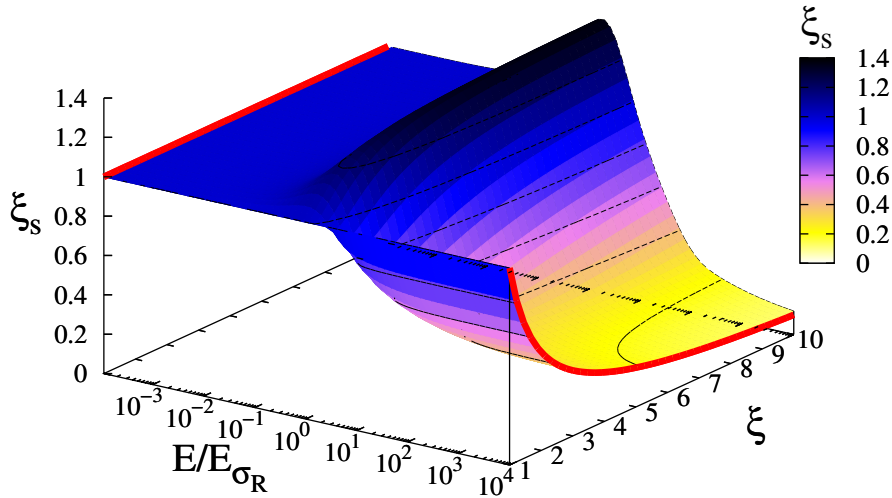


Figure 5.2: Anisotropy factor,  $\xi_s = \tau_{E, \hat{\mathbf{k}}_x} / \tau_{E, \hat{\mathbf{k}}_y}$ , of the scattering time as a function of  $E/E_{\sigma_R}$  and  $\xi$ , for the 2D power spectrum (5.1). The red lines are the low ( $\xi_s \rightarrow 1$ ) and high energy limits ( $\xi_s \rightarrow \frac{1}{\xi}$ ) [see Eqs. (5.7) and (5.11)].

precisely, Eq. (5.1) becomes  $\tilde{C}(\mathbf{k}) \simeq V_R^2 \pi \frac{\sigma_R^2}{\xi}$  (see Sec. 3.2.2) and  $\tau_{E, \hat{\mathbf{k}}}$  is isotropic, constant, and it only depends on the product  $V_R^2 \sigma_{R,x} \sigma_{R,y}$  (up to corrections of relative order  $E/E_{\sigma_R}$ ).

**High-energy limit** – In the opposite, high-energy limit,  $k_E \sigma_R \gg \xi$ , the de Broglie wavelength of the particle is much smaller than the smallest correlation length of the disorder. The particle then behaves ‘classically’. Since  $\tilde{C}(\mathbf{k})$  has a wider extension in the  $\hat{\mathbf{k}}_y$  direction than in the  $\hat{\mathbf{k}}_x$  direction (for  $\xi > 1$ ), there are more scattering channels for particles travelling along  $x$  so that we can expect  $\tau_{E, \hat{\mathbf{k}}_x} < \tau_{E, \hat{\mathbf{k}}_y}$ . More precisely, we find

$$\tau_{E, \hat{\mathbf{k}}} \simeq \frac{\hbar E_{\sigma_R}}{V_R^2} \frac{k_E \sigma_R}{\sqrt{\pi}} \sqrt{\hat{k}_x^2 + \xi^2 \hat{k}_y^2}, \quad (5.8)$$

which is shown in Fig. 5.1 (right-hand side black lines). Equation (5.8) confirms that  $\tau_{E, \hat{\mathbf{k}}_x} \leq \tau_{E, \hat{\mathbf{k}}_y}$  for  $\xi \geq 1$ . In addition, we find that in the high-energy limit  $\tau_{E, \hat{\mathbf{k}}} \propto \sqrt{E}$ .

**Anisotropy** – It is also interesting to study the anisotropy factor of the scattering time

$$\xi_s \equiv \frac{\tau_{E, \hat{\mathbf{k}}_x}}{\tau_{E, \hat{\mathbf{k}}_y}}, \quad (5.9)$$

which is shown in Fig. 5.2 as a function of  $E/E_{\sigma_R}$  and  $\xi$ . As already mentioned  $\tau_{E, \hat{\mathbf{k}}}$  is isotropic in the white-noise limit, so that  $\xi_s \simeq 1$  for  $k_E \sigma_R \ll 1$  (left-hand side red line in Fig. 5.2). When increasing the energy, the scattering time first increases along the direction with the largest correlation length, i.e. the direction in which  $\tilde{C}(\mathbf{k})$  is narrower ( $x$  for  $\xi > 1$ ).

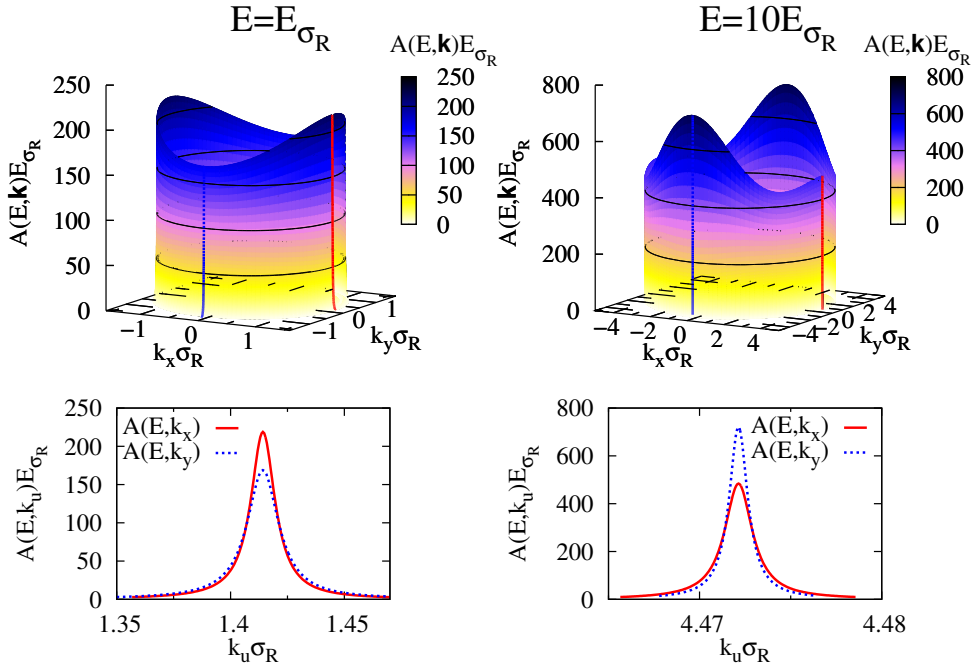


Figure 5.3: On-shell spectral function as a function of  $\mathbf{k}$  for the 2D power spectrum (5.1),  $V_R = 0.2E_{\sigma_R}$ , and  $\xi = 4$ . The top row shows the full spectral function. The bottom row shows cuts along the  $k_x$  (solid red lines) and  $k_y$  axis (dotted blue lines). The two columns refer to different energies:  $E = E_{\sigma_R}$  (left) and  $E = 10E_{\sigma_R}$  (right), which correspond to the dots and the squares in Fig 5.1, respectively.

Therefore,  $\xi_s$  increases with  $E$ , for sufficiently small values of  $E/E_{\sigma_R}$ , and we have  $\xi_s > 1$ . Using Eq. (5.7), an explicit calculation yields

$$\xi_s \simeq 1 + \frac{E}{E_{\sigma_R}} \frac{\xi^2 - 1}{2\xi^2} + \mathcal{O}\left(\frac{E^2}{\xi^4 E_{\sigma_R}^2}\right). \quad (5.10)$$

For  $k_E \sigma_R \gg \xi$ , using Eq. (5.8), we obtain

$$\xi_s \simeq \frac{1}{\xi}, \quad (5.11)$$

which shows that the anisotropy factor of scattering is proportional to the inverse of the geometrical anisotropy (right-hand side red line in Fig. 5.2). Note that the classical limit relation (5.11) is universal provided that the configuration anisotropy factor is well defined i.e. that the disorder correlation function can be obtained by the anisotropic homothety of an isotropic one,  $C(x, y) = C_{\text{iso}}(x, \xi y)$ . In this high-energy limit,  $\xi_s < 1$  (contrary to the low-energy limit case). Therefore, for any value of  $\xi$ ,  $\tau_{E, \hat{\mathbf{k}}}$  exhibits an inversion of anisotropy when the energy increases, typically at  $E \sim E_{\sigma_R}$ .

**Spectral function** – As described in section 2.2 the scattering time is the width of the spectral function. It can be measured in a 2D experiment such as that of Ref. [17] by monitoring the momentum distribution of an almost energy-resolved wavepacket [185]. To illustrate

this, a plot of the spectral function as a function of momentum and at fixed energy is shown in Fig. 5.3. In this plot the scattering time is calculated in the Born approximation (as above), and we have neglected the real part of the self-energy  $\Sigma'(E, \mathbf{k})$  in Eq. (2.16). In each direction  $\hat{\mathbf{k}}$  the spectral function peaks to  $4\tau_{E, \hat{\mathbf{k}}}/\hbar$  and has a width proportional to  $1/\tau_{E, \hat{\mathbf{k}}}$ . The anisotropy of the scattering time is revealed in the angle-dependence of both these quantities. It is more apparent in the angular dependence of the amplitude, which shows marked peaks. At low energy, the maxima are located on the  $k_x$  axis, while at high energy, they are located on the  $k_y$  axis, which signals inversion of the scattering anisotropy.

## 5.2 Boltzmann diffusion

We now turn to the behaviour of the spatial density in the incoherent diffusive regime, which is characterized by the Boltzmann diffusion tensor  $\mathbf{D}_B(E)$ . This regime is relevant in the presence of strong decoherence processes (such that  $l_\phi \lesssim l_s$ , see Sec. 1.2.1). In 2D and in 3D, in the regime where localization is expected, incoherent diffusion is also relevant at finite distances (and times) such that  $l_B < |\mathbf{r}| < L_{loc}$ . In the diffusive regime in 3D, it is relevant between  $l_B < |\mathbf{r}| < l_*$ , where  $l_*$  is the transport mean free path associated to the diffusion tensor corrected by quantum interference. We first give an explicit formula for the Boltzmann diffusion tensor and then apply it to 2D disorder (3D cases are discussed in Sec. 6.2.2).

### 5.2.1 Solution of the Bethe-Salpeter equation

**Boltzmann approximation** – In the independent scattering (Boltzmann) and weak disorder (Born) approximation, only the first term in Eq. (2.25) is retained, which means that all correlations between successive scattering events and interferences between different multiple-scattering paths are neglected. The irreducible vertex function  $U$  then equals the disorder structure factor [58]:  $U \simeq U_B = \overline{V \otimes V}$  and

$$U_{\mathbf{k}, \mathbf{k}'}(\mathbf{q}, \omega, E) \simeq U_{B\mathbf{k}, \mathbf{k}'} = \tilde{C}(\mathbf{k} - \mathbf{k}'), \tag{5.12}$$

or equivalently

$$\boxed{U_B} = \begin{array}{c} \bullet \\ \vdots \\ \bullet \end{array} . \tag{5.13}$$

Then, incorporating Eq. (5.12)-(5.13) into the BSE (2.23)-(2.24) and expanding it in series of  $U$ , one finds

$$\begin{array}{ccc} \begin{array}{c} \mathbf{k}_+ \quad \mathbf{k}'_+ \\ \boxed{\Phi} \\ \mathbf{k}_- \quad \mathbf{k}'_- \end{array} & = & \begin{array}{c} \mathbf{k}_+ \\ \longrightarrow \\ \mathbf{k}_- \\ \longleftarrow \end{array} + \begin{array}{c} \mathbf{k}_+ \quad \mathbf{k}'_+ \\ \longrightarrow \quad \longrightarrow \\ \Gamma \\ \longleftarrow \quad \longleftarrow \\ \mathbf{k}_- \quad \mathbf{k}'_- \end{array} \end{array} \tag{5.14}$$

where the diffuson  $\Gamma$  reduces to ladder diagrams:

$$\boxed{\Gamma} = \begin{array}{c} \bullet \\ \vdots \\ \bullet \end{array} + \begin{array}{c} \bullet \longrightarrow \bullet \\ \vdots \\ \bullet \longleftarrow \bullet \end{array} + \begin{array}{c} \bullet \longrightarrow \bullet \longrightarrow \bullet \\ \vdots \\ \bullet \longleftarrow \bullet \longleftarrow \bullet \end{array} + \dots \tag{5.15}$$

It describes an infinite series of independent scattering events, which leads to Drude-like diffusion, as we will see below.

**Density propagator and diffusion tensor** – In appendix C.1, explicit calculations are detailed. In brief, in the long-time ( $\omega \rightarrow 0$ ) and large-distance ( $|\mathbf{q}| \rightarrow 0$ ) limit the vertex  $\Phi$  is the sum of a regular term and a singular term [153, 154]:

$$\Phi_{\mathbf{k},\mathbf{k}'}(\mathbf{q}, \omega, E) = \Phi_{\mathbf{k},\mathbf{k}'}^{\text{sing}}(\mathbf{q}, \omega, E) + \Phi_{\mathbf{k},\mathbf{k}'}^{\text{reg}}(0, 0, E). \quad (5.16)$$

The regular part is given by

$$\Phi_{\mathbf{k},\mathbf{k}'}^{\text{reg}}(0, 0, E) = \sum_{\lambda_E^n \neq 1} \frac{1}{1 - \lambda_E^n} f_{E,\mathbf{k}} \phi_{E,\mathbf{k}}^n \phi_{E,\mathbf{k}'}^n f_{E,\mathbf{k}'}, \quad (5.17)$$

where  $f_{E,\mathbf{k}} \equiv f_{\mathbf{k}}(\mathbf{q} = 0, \omega = 0, E)$  [see Eq. (2.28)] and  $\phi_{E,\mathbf{k}}^n$  ( $\lambda_E^n$ ) are the eigenvectors (eigenvalues) of an integral operator involving the disorder correlation function and  $f_{E,\mathbf{k}}$ <sup>1</sup>:

$$\int \frac{d\mathbf{k}'}{(2\pi)^d} \tilde{C}(\mathbf{k} - \mathbf{k}') f_{E,\mathbf{k}'} \phi_{E,\mathbf{k}'}^n = \lambda_E^n \phi_{E,\mathbf{k}}^n. \quad (5.18)$$

The regular part contributes to the finite time and finite distance propagation of the density, which we hence disregard here. The singular part is more interesting. Its existence is a direct consequence of the Ward identity [149] which expresses the conservation of particle number, and which guarantees that one of the eigenvalues of Eq. (5.18) is equal to one  $\lambda_E^{n=1} = 1$  (see appendix C.1). In the following we will consider the on-shell approximation such that  $\epsilon(\mathbf{k}) = \epsilon(\mathbf{k}') = E$ . In the long time and large distance limit ( $|\mathbf{q}|, \omega \rightarrow 0$ ), the vertex  $\Phi$  is given by

$$\Phi_{\mathbf{k},\mathbf{k}'}^{\text{sing}}(\mathbf{q}, \omega, E) = \frac{2\pi}{\hbar N_0(E)} \frac{\gamma_{\mathbf{k}}(\mathbf{q}, E) \gamma_{\mathbf{k}'}(\mathbf{q}, E)}{-i\omega + \mathbf{q} \cdot \mathbf{D}_B(E) \cdot \mathbf{q}} \quad (5.19)$$

with  $N_0(E)$  the disorder-free density of states, and

$$\gamma_{\mathbf{k}}(\mathbf{q}, E) = \frac{A_0(E, \mathbf{k})}{2\pi} \left\{ 1 - \frac{2\pi i}{\hbar} \sum_{\lambda_E^n \neq 1} \frac{\lambda_E^n}{1 - \lambda_E^n} \tau_{E,\hat{\mathbf{k}}} \phi_{E,\hat{\mathbf{k}}}^n \langle \mathbf{q} \cdot \mathbf{v}' \tau_{E,\hat{\mathbf{k}}'} \phi_{E,\hat{\mathbf{k}}'}^n \rangle_{\mathbf{k}'|E} \right\}, \quad (5.20)$$

where  $A_0(E, \mathbf{k}) = 2\pi\delta[E - \epsilon(\mathbf{k})]$  is the disorder-free spectral function. Equation (5.19) shows that the vertex  $\Phi$  is dominated by the diffusion pole  $(i\hbar\omega - \hbar\mathbf{q} \cdot \mathbf{D}_B(E) \cdot \mathbf{q})^{-1}$  whose physical meaning has been discussed in Sec. 2.3. The Boltzmann diffusion tensor  $\mathbf{D}_B(E)$  has components [153]

$$D_B^{i,j}(E) = \frac{1}{N_0(E)} \left\{ \left\langle \tau_{E,\hat{\mathbf{k}}} v_i v_j \right\rangle_{\mathbf{k}|E} + \frac{2\pi}{\hbar} \sum_{\lambda_E^n \neq 1} \frac{\lambda_E^n}{1 - \lambda_E^n} \left\langle \tau_{E,\hat{\mathbf{k}}} v_i \phi_{E,\hat{\mathbf{k}}}^n \right\rangle_{\mathbf{k}|E} \left\langle \tau_{E,\hat{\mathbf{k}}} v_j \phi_{E,\hat{\mathbf{k}}}^n \right\rangle_{\mathbf{k}|E} \right\}, \quad (5.21)$$

where  $v_i = \hbar k_i/m$ ,  $\tau_{E,\hat{\mathbf{k}}} \equiv \tau_s(E, k_E \hat{\mathbf{k}}) = \hbar/2\pi \langle \tilde{C}(k_E \hat{\mathbf{k}} - \mathbf{k}') \rangle_{\mathbf{k}'|E}$  is the on-shell scattering mean free time [see Eq. (5.4)], and  $\langle \dots \rangle_{\mathbf{k}|E}$  represents integration over the  $\mathbf{k}$ -space shell defined by  $\epsilon(\mathbf{k}) = E$  [see Eq. (5.5)]. The functions  $\phi_{E,\hat{\mathbf{k}}}^n$  and the real-valued positive numbers  $\lambda_E^n$  are the

---

1. This operator is  $1 - \Lambda$ , taken in the Born and Boltzmann approximations, where  $\Lambda$  has been introduced in paragraph 2.3.

solutions of the integral eigenproblem (5.18), which becomes, in the on-shell approximation (see appendix C.1),

$$\frac{2\pi}{\hbar} \left\langle \tau_{E,\hat{\mathbf{k}}} \tilde{C}(k_E \hat{\mathbf{k}} - \mathbf{k}') \phi_{E,\hat{\mathbf{k}}}^n \right\rangle_{\mathbf{k}'|E} = \lambda_E^n \phi_{E,\hat{\mathbf{k}}}^n, \quad (5.22)$$

normalized by  $\frac{2\pi}{\hbar} \left\langle \tau_{E,\hat{\mathbf{k}}} \phi_{E,\hat{\mathbf{k}}}^n \phi_{E,\hat{\mathbf{k}}}^m \right\rangle_{\mathbf{k}|E} = \delta_{n,m}$  [153]. It follows from Eq. (5.21) that the incoherent (Boltzmann) diffusion tensor  $\mathbf{D}_B(E)$  is obtained from the two-point disorder correlation function  $C(\mathbf{r})$ , which determines  $\tau_{E,\hat{\mathbf{k}}}$  [see Eq. (5.4)] as well as  $\phi_{E,\hat{\mathbf{k}}}^n$  and  $\lambda_E^n$  [see Eq. (5.22)]. The diffusion tensor then gives the probability of quantum transport via Eq. (2.32).

**Isotropic limit** – In the isotropic case (for details see appendix C.2), Eq. (5.22) is solved by the cylindrical (2D) or spherical (3D) harmonics  $Y_l^m$ , the same level harmonics [i.e. with the same  $l$ ] being degenerate in  $\lambda_E^n$ . Then, it follows from the symmetries of the cylindrical/spherical harmonics that only the first term in Eq. (5.21) plus the  $p$ -level harmonics ( $Z_1^{\pm 1}$  in 2D and  $Y_1^m$  with  $m = -1, 0, 1$  in 3D; the cylindrical harmonics  $Z_l^{\pm 1}$  are defined in appendix C.2) couple to  $v$  and contribute to  $D_B(E)$ . Incorporating the explicit formulas for  $\phi_{E,\hat{\mathbf{k}}}^n$  and  $\lambda_E^n$  [see Eqs. (C.18) to (C.24)], we then recover well-known expressions for isotropic disorder (see Eqs. (C.21) and (C.24) and Refs. [16, 151, 163, 165]).

Note also that for white-noise disorder, we find that for any  $n \neq 1$ ,  $\lambda_E^n = 0$ , and only the first term in the right-hand side of Eq. (5.21) contributes to diffusion: It gives an isotropic diffusion coefficient.

**Anisotropic case** – For anisotropic disorder, the harmonics couple, and the  $\phi_{E,\hat{\mathbf{k}}}^n$  are no longer cylindrical/spherical harmonics. Then the calculation of the diffusion tensor requires first the diagonalization of the integral operator (5.22) whose solutions are then incorporated in Eq. (5.21). In the following, this is done numerically for an anisotropy factor relevant to current matter-wave experiments.

### 5.2.2 Anisotropic Gaussian speckle (2D)

Consider again the 2D anisotropic speckle potential of Sec. 3.2.2. The first step in the calculation of  $\mathbf{D}_B$  is to determine the eigenfunctions  $\phi_{E,\hat{\mathbf{k}}}^n$  and the associated eigenvalues  $\lambda_E^n$  of Eq. (5.22). We solve Eq. (5.22) numerically, by a standard algorithm of diagonalization, with  $2^9 = 512$  points, regularly spaced on the  $\mathbf{k}$ -space shell  $|\mathbf{k}| = k_E$ . The diffusion tensor is diagonal in the basis made by the symmetry axes of the correlation function (5.1):  $\{\hat{\mathbf{u}}_x, \hat{\mathbf{u}}_y\}$ .

**Eigenfunctions** – The eigenvalues and some eigenfunctions obtained numerically are shown in Fig. 5.4 for various values of  $E/E_{\sigma_R}$ . As discussed above, we find  $\lambda_E^{n=1} = 1$ . For  $E \ll E_{\sigma_R}$ , only the first term in the right-hand side of Eq. (5.21) contributes to the diffusion tensor since all  $\lambda_E^{n>1}$  are vanishingly small. When the energy increases, the values of the coefficients  $\lambda_E^{n>1}$  increase. It corresponds to an increase of the weight of the terms associated to the orbitals with  $n > 1$  in Eq. (5.21), and a priori all the orbitals with  $n > 1$  might have an increasing contribution. However, we find that, the symmetry properties of the functions  $\phi_{E,\hat{\mathbf{k}}}^n$  cancel the contributions of most of them, and only the orbitals with  $n = 2$  and 3 do contribute (see below).

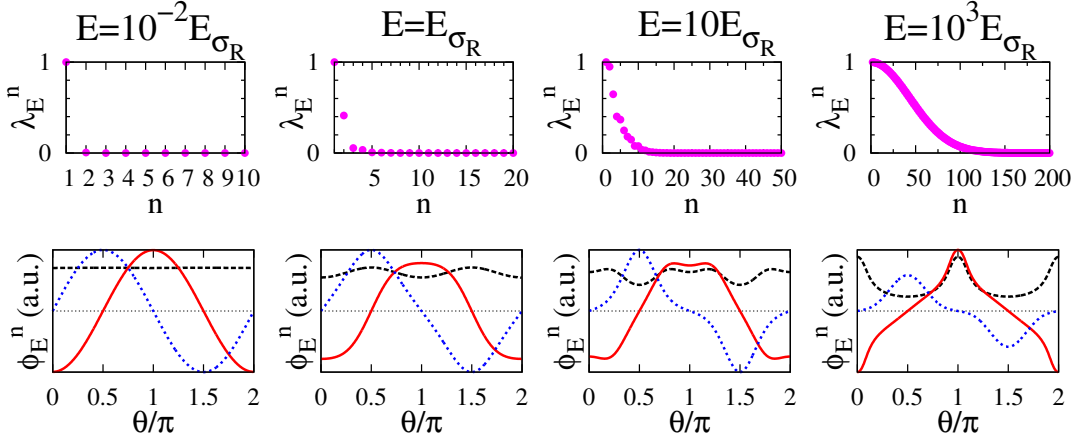


Figure 5.4: Top row: Eigenvalues of Eq. (5.22). Bottom row: Angular dependence of the eigenfunctions  $\phi_{E,\hat{\mathbf{k}}}^n$  for  $n = 1$  (dashed black line), 2 (solid red line) and 3 (dotted blue line). We use the parametrization  $\hat{\mathbf{k}} \equiv (\cos \theta, \sin \theta)$  for the 2D power spectrum (5.1) with  $\xi = 4$ . The different columns refer to different energies (indicated on top of the figure).

In the low energy limit, one can develop Eq. (5.1) in powers of  $|\mathbf{k}|$ . Up to order  $O(E^2/\xi^4 E_{\sigma_R}^2)$ , the first three eigenfunctions are given by:

$$\phi_{E,\hat{\mathbf{k}}}^1 = 1 - \frac{E}{2\xi^2 E_{\sigma_R}} \left[ 1 + (\xi^2 - 1)\hat{k}_x^2 \right] + O\left(\frac{E^2}{\xi^4 E_{\sigma_R}^2}\right), \quad (5.23)$$

with eigenvalue  $\lambda_E^1 = 1$ ;

$$\phi_{E,\hat{\mathbf{k}}}^2 = \hat{k}_x \left[ \sqrt{2} + B_2 \frac{E}{\xi^2 E_{\sigma_R}} \right] + O\left(\frac{E^2}{\xi^4 E_{\sigma_R}^2}\right) \quad (5.24)$$

with eigenvalue  $\lambda_E^2 = E/2E_{\sigma_R}$ , and

$$\phi_{E,\hat{\mathbf{k}}}^3 = \hat{k}_y \left[ \sqrt{2} + B_3 \frac{E}{\xi^2 E_{\sigma_R}} \right] + O\left(\frac{E^2}{\xi^4 E_{\sigma_R}^2}\right) \quad (5.25)$$

with eigenvalue  $\lambda_E^3 = E/2\xi^2 E_{\sigma_R}$ , where  $B_2$  and  $B_3$  are constant values that do not intervene in the following. In this limit the numerical results agree very well with the analytical findings (which are not shown on Fig. 5.4 for clarity). In the very low energy limit, the disorder power spectrum becomes isotropic and constant,  $\tilde{C}(\mathbf{k}) \simeq V_R^2 \pi \sigma_R^2 / \xi$ , [see Sec. 3.2.2 and Eq. (5.1)]. The orbitals  $\phi_{E,\hat{\mathbf{k}}}^n$  are thus proportional to the cylindrical harmonics, which are exact solutions of Eq. (5.22) in the isotropic case (see appendix C.2, and use the parametrization  $\hat{k}_x = \cos \theta$  and  $\hat{k}_y = \sin \theta$ ). In this white-noise limit, we also find  $\lambda_E^{n>1} = 0$ . For non-zero energy, in contrast to the isotropic case where the values of  $\lambda_E^n$  are degenerated in a given  $l$ -level, here we find that the degeneracy inside a  $l$  level is lifted for any anisotropy  $\xi \neq 1$  [see the values of  $\lambda_E^{2,3}$  below Eqs. (5.24) and (5.25)]. When the energy further increases, the anisotropy plays a more important role and the harmonics are more and more distorted (see Fig. 5.4). However their topology remains the same, and in particular the number of nodal points and their positions are unchanged: for example  $\phi_{E,\hat{\mathbf{k}}}^2$  (respectively  $\phi_{E,\hat{\mathbf{k}}}^3$ ) is a  $2\pi$ -periodic and even (resp. odd) function of  $\theta$ , as  $Z_1^{+1}$  (resp.  $Z_1^{-1}$ ). In the following, we thus refer to  $Z_l^{\pm 1}$ -like orbitals.

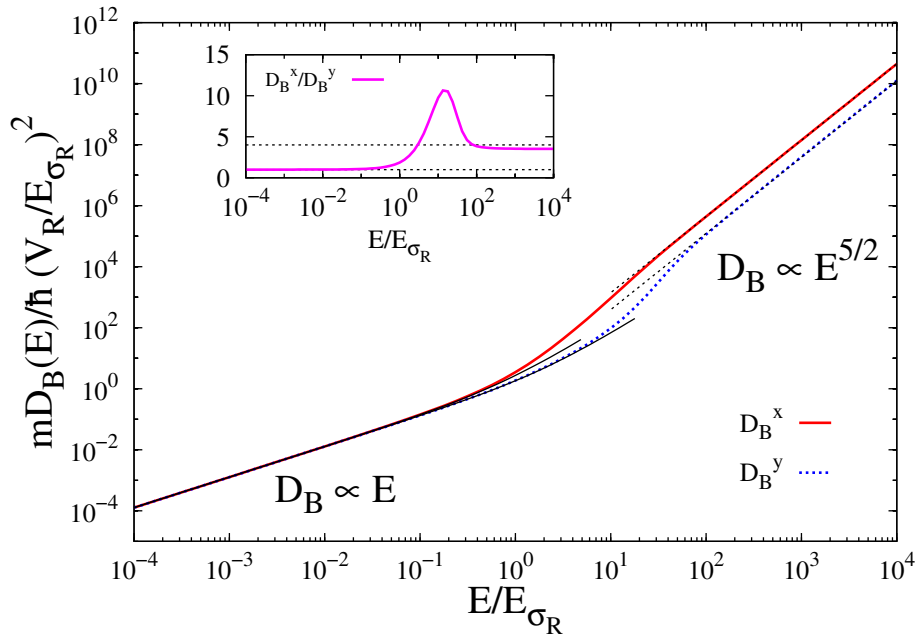


Figure 5.5: Components of the diffusion tensor:  $D_B^x$  (solid red line) and  $D_B^y$  (dotted blue line) for the 2D power spectrum (5.1) and  $\xi = 4$ . Solid black lines are limit values at small  $E/E_{\sigma_R}$  [Eqs. (5.26) and (5.27)], with the isotropic white-noise limit  $D_B^x(E) = D_B^y(E) \sim \hbar\xi EE_{\sigma_R}/m\pi V_R^2$ . For large  $E/E_{\sigma_R}$  we find  $D_B(E) \sim E^{5/2}$  (see text); a fit of the numerical data gives the prefactors  $D_B^x = 4.43 E^{5/2}/V_R^2 E_{\sigma_R}^{1/2}$  and  $D_B^y = 1.24 E^{5/2}/V_R^2 E_{\sigma_R}^{1/2}$  (see dotted black lines). The inset shows the transport anisotropy factor  $\xi_B = D_B^x/D_B^y$ .

**Boltzmann diffusion tensor** – Incorporating the values of  $\lambda_E^n$ ,  $\phi_{E,\hat{\mathbf{k}}}^n$  and  $\tau_{E,\hat{\mathbf{k}}}$  in Eq. (5.21), we can now determine the Boltzmann diffusion tensor. Figure 5.5 shows the resulting eigen-components of the diffusion tensor. In the low energy limit ( $E \ll E_{\sigma_R}$ ), using Eqs. (5.7), (5.24) and (5.25), we find that the first term in the right-hand side of Eq. (5.21) gives the leading contribution to  $\mathbf{D}_B(E)$  (of order  $E/E_{\sigma_R}$ ). This contribution is isotropic owing to the isotropy of  $\tau_{E,\hat{\mathbf{k}}}$  at low energy and of the underlying medium. At very low energy, in the white-noise limit, we recover an isotropic diffusion tensor  $D_B^x(E) = D_B^y(E) \sim \hbar\xi EE_{\sigma_R}/m\pi V_R^2$ . The scaling  $D_B^u(E) \propto E$  is universal for 2D disorder in the white-noise limit (when it exists). The  $Z_1^{+1}$ -like orbital  $\phi_{E,\hat{\mathbf{k}}}^2$  contributes to the next order of  $D_B^x$  and the  $Z_1^{-1}$ -like orbital  $\phi_{E,\hat{\mathbf{k}}}^3$  to  $D_B^y$ . Up to order  $O(E^3/\xi^6 E_{\sigma_R}^3)$ , we obtain

$$D_B^x(E) = \frac{\hbar E_{\sigma_R}^2}{m V_R^2} \left[ \frac{\xi E}{\pi E_{\sigma_R}} + \frac{E^2}{\pi E_{\sigma_R}^2} \frac{9\xi^2 + 3}{8\xi} + O\left(\frac{E^3}{\xi^6 E_{\sigma_R}^3}\right) \right], \quad (5.26)$$

and

$$D_B^y(E) = \frac{\hbar E_{\sigma_R}^2}{m V_R^2} \left[ \frac{\xi E}{\pi E_{\sigma_R}} + \frac{E^2}{\pi E_{\sigma_R}^2} \frac{3\xi^2 + 9}{8\xi} + O\left(\frac{E^3}{\xi^6 E_{\sigma_R}^3}\right) \right], \quad (5.27)$$

which are displayed on Fig. 5.5 (left-hand side solid lines). When the energy increases, the anisotropy first comes from the anisotropic contribution of the scattering time  $\tau_{E,\hat{\mathbf{k}}}$ , and from the lift of the degeneracy between  $\lambda_E^2$  and  $\lambda_E^3$ . When the energy further increases, the harmonics are distorted, – but their symmetries (i.e. periodicity and parity) are preserved (see

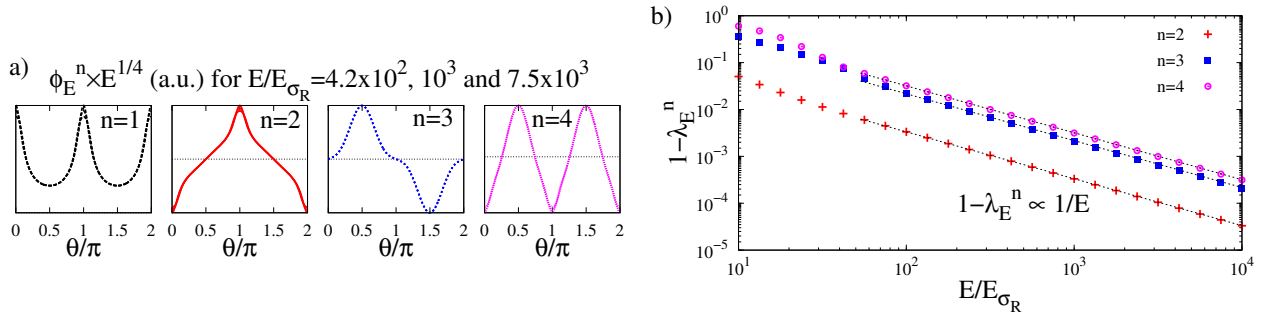


Figure 5.6: High-energy scalings: (a) Angular dependence of  $\phi_{E,\hat{\mathbf{k}}}^n \times E^{1/4}$  found numerically for  $n = 1$  (dashed black line), 2 (solid red line), 3 (dotted blue line) and 4 (stippled pink line). Three different energies are superimposed:  $E/E_{\sigma_R} = 4.2 \times 10^2$ ,  $10^3$  and  $7.5 \times 10^3$ . We use the parametrization  $\hat{\mathbf{k}} \equiv (\cos \theta, \sin \theta)$  for the 2D power spectrum (5.1) with  $\xi = 4$ . (b) Energy dependence of  $1 - \lambda_E^n$  for  $n = 2$  (red crosses), 3 (blue squares) and 4 (pink dots). The solid black lines are fits to the numerical data by  $A/E$ , with  $A$  as fitting parameter.

Fig. 5.4). Hence, for the same reasons as in the isotropic case (see appendix C.2) only the  $Z_1^{\pm 1}$ -like orbitals couple to  $\mathbf{v}$  in Eq. (5.21) and contribute to  $D_B$  while the others don't. The associated  $\lambda_E^n$  increase (see Fig. 5.4), the weight of the second term in Eq. (5.21) increases, and the components of the diffusion tensor show a very different behavior in the large- $E$  limit. For  $k_E \sigma_R \gg \xi$ , we found  $\tau_{E,\hat{\mathbf{k}}} \propto k_E$  (see Sec. 5.1.2). In addition, we find numerically a weak topological change of the orbitals with energy for  $E/E_{\sigma_R} \gtrsim 10^2$  [see Fig. 5.6(a)]. Therefore the evaluation of  $\mathbf{D}_B$  with  $E$  is mainly determined by the normalization condition [see formula below Eq. (5.21)], which yields  $\phi_{E,\hat{\mathbf{k}}}^n \propto 1/\sqrt{k_E}$ . Then, assuming the scaling  $1 - \lambda_E^n \propto 1/E$ , also verified numerically [see Fig. 5.6(b)], we obtain  $D_B^u(E) \propto E^{5/2}$ , which matches the numerical results (see dotted black lines in Fig. 5.5). This scaling is similar to that found for isotropic disorder [16]. As shown in Fig. 5.5, the change of slope between the low- and high-energy regimes is different in the two directions. For this reason, the anisotropy factor of the diffusion tensor,  $\xi_B = D_B^x/D_B^y$  shows a nonmonotonous behaviour versus  $E$ , with a marked peak (see inset of Fig. 5.5).

**Anisotropy** – The Boltzmann transport anisotropy factor  $\xi_B$  is shown in Fig. 5.7 for various geometrical anisotropies  $\xi$ . As it is well-known, the scattering and transport mean free times are different quantities in correlated disorder, due to angle-dependent scattering [58,187,188]. In particular, in the 2D speckle we consider, we do not find any inversion of the anisotropy of the diffusion, contrary to the scattering time, i.e. the component  $D_B^x(E)$  of the diffusion tensor is always larger than the component  $D_B^y(E)$ . For large values of  $E/E_{\sigma_R}$ , the Boltzmann transport anisotropy  $\xi_B$  reaches a constant value (see the inset of Fig. 5.5 for a cut at  $\xi = 4$ ), which increases with the geometrical anisotropy  $\xi$ , see inset of Fig. 5.7. This asymptotic value is larger than  $\xi$  for small  $\xi$  and smaller for larger values of  $\xi$ . Therefore the anisotropy of the diffusion in the classical regime is not simply related to the spatial anisotropy.

In this simple model of 2D anisotropic disorder, we found two distinct regimes in the behaviour of  $\mathbf{D}_B$ :  $D_B^u(E) \propto E$  at low energy, and  $D_B^u(E) \propto E^{5/2}$  at high energy. We also found a non-trivial behaviour of the anisotropy factor:  $\xi_B$  is non-monotonous with energy for

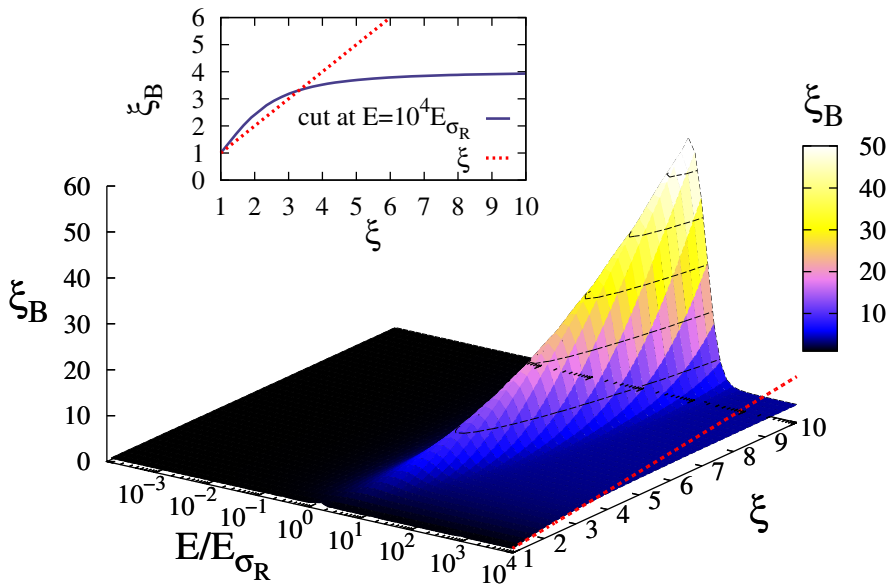


Figure 5.7: Boltzmann transport anisotropy factor  $\xi_B = D_B^x/D_B^y$  as a function of  $E/E_{\sigma_R}$  and  $\xi$  for the 2D speckle potential of Sec. 3.2.2. The inset shows the high energy asymptotic value (cut at  $E = 10^4 E_{\sigma_R}$ ). The dotted red line in both the figure and the inset is  $\xi$ .

any geometrical anisotropy factor  $\xi$ . Both properties make the Boltzmann diffusion regime in anisotropic 2D potentials very interesting for future experiments. Those properties could be probed by controlling the width of the atomic energy distribution and imaging directly the atoms in the 2D speckle (as in Ref. [17]).

## 5.3 Weak and strong localization

Having discussed the incoherent (Boltzmann) transport properties, we now consider interference effects, which lead to weak and strong localization. We first describe the quantum corrections (Sec. 5.3.1), then the self-consistent theory (Sec. 5.3.2), and apply it to the 2D speckle potential (Sec. 5.3.3). The 3D cases, which follow the same route, are discussed in Sec. 6.2.3.

### 5.3.1 Weak localization correction

We calculate corrections to Boltzmann diffusion by taking into account quantum interference terms between the multiple-scattering paths. Those interferences appear when the correlated scattering events do not occur in the same order in the propagation of the field and its conjugate. This is diagrammatically translated into crossing correlation lines as in the second term of Eq. (2.25) for example. In the weak scattering regime only the two-point correlations are retained in the scattering diagrams (Born approximation) and the leading scale-dependent corrections to the classical conductivity are given by the maximally crossed diagrams [41, 153, 154, 189]: the cooperon [Eq. (5.28)], which is the standard maximally crossed diagram, and the first two Hikami boxes [Eqs. (5.29) and (5.30)], which have to be included

in the case of anisotropic scattering to ensure that the Ward identity<sup>2</sup> is verified. We have

$$\Delta\sigma_{(X)} = \text{Diagram (5.28)} \quad (5.28)$$

$$\Delta\sigma_{(H_1)} = \text{Diagram (5.29)} \quad (5.29)$$

$$\Delta\sigma_{(H_2)} = \text{Diagram (5.30)} \quad (5.30)$$

where the cooperon  $X$  is the sum of maximally crossed diagrams

$$X = \text{Diagram (5.31)} + \dots \quad (5.31)$$

and

$$\text{Diagram (5.32)} \quad (5.32)$$

is the renormalized vertex function (see appendix C.3.2).

Using time-reversal invariance<sup>3</sup> [56, 58, 148, 149], the cooperon  $X$  can be expressed in terms of the diffuson  $\Gamma$  [defined in Eq. (5.15)]

$$X_{\mathbf{k}, \mathbf{k}'}(\mathbf{q}, \omega, E) = \Gamma_{\frac{\mathbf{k}-\mathbf{k}'+\mathbf{q}}{2}, \frac{\mathbf{k}'-\mathbf{k}+\mathbf{q}}{2}}(\mathbf{k} + \mathbf{k}', \omega, E). \quad (5.33)$$

The diffusion pole carried by  $\Gamma$  in the limit  $(\omega, \mathbf{q}) \rightarrow 0$  leads to a divergence of  $X$  when  $\omega, \mathbf{k} + \mathbf{k}' \rightarrow 0$ . In appendix C.3.3 we translate diagrams (5.28) to (5.30) into equations, and show that

$$\Delta\sigma(\omega, E) \equiv \Delta\sigma_{(X+H_1+H_2)}(\omega, E) = -\frac{\sigma_B(E)}{\pi N_0(E)} \int \frac{d\mathbf{Q}}{(2\pi)^d} \frac{1}{-i\hbar\omega + \hbar\mathbf{Q} \cdot \mathbf{D}_B(E) \cdot \mathbf{Q}}. \quad (5.34)$$

2. The Ward identity, which is given in Eq. (C.9), traduces the conservation of particle number [149].

3. In a time-reversal invariant system, the single particle states  $\mathbf{k}$  and  $-\mathbf{k}$  are equivalent, which permits to relate some diagrams or sets of diagrams with their 'twisted' counterparts. Eq. (5.33) is proven by:

$$\text{Diagram (5.35)} = \text{Diagram (5.36)} = \text{Diagram (5.37)}.$$

Using Einstein's relation (2.38) we then obtain the dynamic diffusion tensor  $\mathbf{D}_*(\omega, E) = \mathbf{D}_B(E) + \Delta\mathbf{D}(\omega, E)$ , with [153]

$$\frac{\Delta\mathbf{D}(\omega, E)}{\mathbf{D}_B(E)} = -\frac{1}{\pi N_0(E)} \int \frac{d\mathbf{Q}}{(2\pi)^d} \frac{1}{-i\hbar\omega + \hbar\mathbf{Q} \cdot \mathbf{D}_B(E) \cdot \mathbf{Q}}. \quad (5.35)$$

Note that the quantum corrections  $\Delta\mathbf{D}(\omega, E)$  do not explicitly depend on the disorder [i.e. on  $\tilde{C}(\mathbf{k})$ ], but only on the Boltzmann diffusion tensor  $\mathbf{D}_B(E)$  [153]. In other words, in this approach, Boltzmann incoherent diffusion sets a diffusing medium, which contains all necessary information to compute coherent terms<sup>4</sup>. In particular, it follows from Eq. (5.35) that the weak localization quantum correction tensor  $\Delta\mathbf{D}(\omega, E)$  has the same eigenaxes and anisotropies as the Boltzmann diffusion tensor  $\mathbf{D}_B(E)$ . Thus the anisotropy can be removed by rescaling distances along the transport eigenaxes  $u$  by  $\sqrt{D_B^u/D_B^{\text{av}}}$  (i.e. momenta are rescaled by  $\sqrt{D_B^{\text{av}}/D_B^u}$ ) with  $D_B^{\text{av}} \equiv \det\{\mathbf{D}_B\}^{1/d}$  the geometric average of the Boltzmann diffusion constants. Since  $\Delta\mathbf{D}$  is always negative in the limit  $\omega \rightarrow 0^+$ , the weak localization correction determines slower diffusion than the one obtained from incoherent diffusion. Equivalently, as long as the correction (5.35) is small, one can write

$$\frac{\mathbf{D}_B(E)}{\mathbf{D}_*(\omega, E)} = 1 + \frac{1}{\pi N_0(E)} \int \frac{d\mathbf{Q}}{(2\pi)^d} \frac{1}{-i\hbar\omega + \hbar\mathbf{Q} \cdot \mathbf{D}_B(E) \cdot \mathbf{Q}}, \quad (5.36)$$

which is the lowest-order term of a perturbative expansion of  $1/\mathbf{D}_*(\omega, E)$ .

### 5.3.2 Strong localization

The quantum interference correction (5.35) has been derived perturbatively and is therefore valid as long as the correction itself is small, i.e. for  $\mathbf{D}_B(E) - \mathbf{D}_*(\omega, E) \ll \mathbf{D}_B(E)$ . In order to extend this approach and eventually describe the localization regime where  $\mathbf{D}_*$  vanishes, Vollhardt and Wölfle [148, 149] proposed to self-consistently replace  $\mathbf{D}_B(E)$  by the dynamic diffusion tensor  $\mathbf{D}_*(\omega, E)$  in the right-hand side of Eq. (5.36). For isotropic scattering this procedure amounts to resumming more divergent diagrams than the cooperon (which contain a square of a diffusion pole), thus contributing to localization [42, 149]. Generalizing this standard approach to anisotropic disorder yields

$$\frac{\mathbf{D}_B}{\mathbf{D}_*(\omega)} = 1 + \frac{1}{\pi N_0(E)} \int \frac{d\mathbf{Q}}{(2\pi)^d} \frac{1}{-i\hbar\omega + \hbar\mathbf{Q} \cdot \mathbf{D}_*(\omega) \cdot \mathbf{Q}}. \quad (5.37)$$

In dimension  $d \geq 2$  the integral in the right-hand side of Eq. (5.37) features ultraviolet divergence, i.e. in the limit  $|\mathbf{Q}| \rightarrow +\infty$ . Since the diffusive dynamics is relevant only on length scales larger than the Boltzmann mean free path  $l_B^u(E) \equiv d\sqrt{m/2E} D_B^u(E)$  along each transport eigenaxis, we regularize this divergence by setting an upper ellipsoidal cut-off of radii  $1/l_B^u$  in the integral domain. It corresponds to an isotropic cut-off in the space rescaled according to the anisotropy factors of  $\mathbf{D}_B$  as described above.

---

4. This property is found within the on-shell approximation, and does not hold in general, where  $\Delta\mathbf{D}(\omega, E)$  can also depend on the scattering medium [i.e. on  $\tilde{C}(\mathbf{k})$  in the Born approximation].

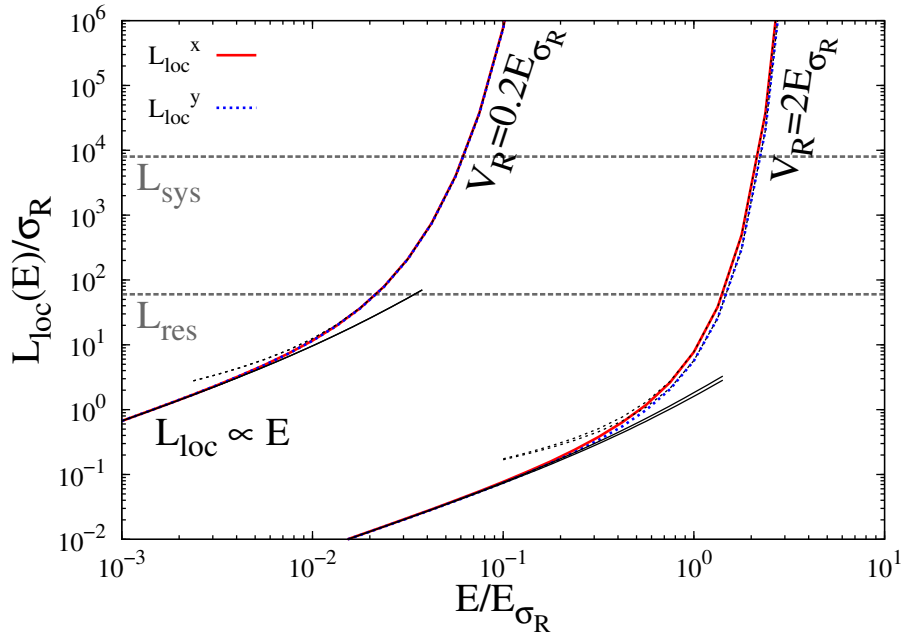


Figure 5.8: Components of the localization tensor  $L_{\text{loc}}^x$  (solid red line) and  $L_{\text{loc}}^y$  (dotted blue line) for the 2D power spectrum (5.1), with  $\xi = 4$  and  $V_{\text{R}} = 0.2E_{\sigma_{\text{R}}}$  and  $2E_{\sigma_{\text{R}}}$ . The solid black lines are the limiting behaviour for small values of  $E/E_{\sigma_{\text{R}}}$  [Eq. (5.39)] and the dotted ones for high values of  $E/E_{\sigma_{\text{R}}}$  [Eq. (5.40)]. The dashed grey lines indicate typical values of the imaging resolution ( $L_{\text{res}}$ ) and the system size ( $L_{\text{sys}}$ ) in ultracold-atom experiments, see text at the end of Sec. 5.3.3.

### 5.3.3 Anisotropic Gaussian speckle (2D)

**Self-consistent theory: 2D case** – We now solve the self-consistent equation (5.37) for the inverse dynamic diffusion tensor in the 2D case [148, 149]. In the long time limit  $\omega \rightarrow 0^+$ , the unique solution of Eq. (5.37) is of the form  $\mathbf{D}_*(\omega, E) \sim 0^+ - i\omega \mathbf{L}_{\text{loc}}^2(E)$ , where  $\mathbf{L}_{\text{loc}}(E)$  is a real positive definite tensor. The normal quantum-corrected diffusion coefficient vanishes, and there is localization for any energy  $E$ , as predicted by the scaling theory of localization (see Sec. 1.2.2). As described in Sec. 2.3, it leads to the exponentially decreasing propagation kernel (2.34). Solving Eq. (5.37) then yields the anisotropic localization tensor,

$$\mathbf{L}_{\text{loc}}(E) = l_{\text{B}}^{\text{av}}(E) \sqrt{\frac{\mathbf{D}_{\text{B}}(E)}{D_{\text{B}}^{\text{av}}(E)}} \left( e^{\pi k_E l_{\text{B}}^{\text{av}}(E)} - 1 \right)^{1/2} \quad (5.38)$$

where  $l_{\text{B}}^{\text{av}}(E) \equiv d\sqrt{m/2E} D_{\text{B}}^{\text{av}}(E)$ . The eigenaxes of the localization tensor are thus the same as those of the Boltzmann diffusion tensor and its anisotropy factors are the square root of those of  $\mathbf{D}_{\text{B}}(E)$ , i.e.  $\xi_{\text{loc}} \equiv L_{\text{loc}}^x/L_{\text{loc}}^y = \sqrt{\xi_{\text{B}}}$ .

**Anisotropic Gaussian speckle** – We now apply the self-consistent theory to our running example: the 2D anisotropic speckle potential with correlation function given by Eq. (5.1). Including the results for the Boltzmann diffusion tensor  $\mathbf{D}_{\text{B}}(E)$  obtained in Sec. 5.2.2 into Eq. (5.38), we find the localization tensor  $\mathbf{L}_{\text{loc}}(E)$ . Figure 5.8 presents the eigencomponents of  $\mathbf{L}_{\text{loc}}$  in its eigenbasis  $\{\hat{\mathbf{u}}_x, \hat{\mathbf{u}}_y\}$  as a function of energy, for a geometrical anisotropy of

$\xi = 4$  and two different amplitudes of the disorder  $V_{\text{R}}/E_{\sigma_{\text{R}}} = 0.2$  and  $2$ . At low energy ( $E \ll E_{\sigma_{\text{R}}}, V_{\text{R}}, V_{\text{R}}^2/E_{\sigma_{\text{R}}}$ ), using Eqs. (5.26) and (5.27), we find

$$L_{\text{loc}}^{x,y}(E) = \sigma_{\text{R}} \frac{E_{\sigma_{\text{R}}}^3}{V_{\text{R}}^3} \frac{\xi^{3/2}}{\pi} \frac{2E}{E_{\sigma_{\text{R}}}} \left[ 1 + \frac{\xi E E_{\sigma_{\text{R}}}}{2V_{\text{R}}^2} + \frac{E}{E_{\sigma_{\text{R}}}} \frac{(18 \pm 3)\xi^2 + (18 \mp 3)}{16\xi^2} + \text{O} \left( \frac{E^2}{\xi^4 E_{\sigma_{\text{R}}}^2}, \frac{E^2}{\xi^2 V_{\text{R}}^2}, \frac{E^2 E_{\sigma_{\text{R}}}^2}{V_{\text{R}}^4} \right) \right], \quad (5.39)$$

where the upper sign holds for direction  $x$ , and the lower sign for direction  $y$ . Equation (5.39) corresponds to the solid black lines in Fig. 5.8. As  $\mathbf{D}_{\text{B}}$  is almost isotropic for  $E/E_{\sigma_{\text{R}}} \lesssim 1$  (see Fig. 5.5),  $\mathbf{L}_{\text{loc}}$  is also almost isotropic in the whole range presented in Fig. 5.8. Equation (5.39) describes an isotropic localization tensor with an anisotropic correction which is significant only if  $V_{\text{R}}/E_{\sigma_{\text{R}}} \gtrsim \xi^{3/2}/\sqrt{\xi^2 - 1}$  ( $\simeq 2$  for  $\xi = 4$ ). At higher energy, when  $k_{\text{E}} l_{\text{B}}^{\text{av}}(E) = 2mD_{\text{B}}^{\text{av}}(E)/\hbar \gtrsim 1$ , we expect

$$L_{\text{loc}}^u(E) \simeq \sigma_{\text{R}} \frac{2}{k_{\text{E}} \sigma_{\text{R}}} \frac{m \sqrt{D_{\text{B}}^{\text{av}}(E) D_{\text{B}}^u(E)}}{\hbar} e^{\pi m D_{\text{B}}^{\text{av}}(E)/\hbar}, \quad (5.40)$$

which is plotted as dotted black lines in Fig. 5.5. According to Eqs. (5.26) and (5.27), (retaining only the lowest-energy term), this regime appears for  $E/E_{\sigma_{\text{R}}} \gtrsim (\pi/2\xi)(V_{\text{R}}/E_{\sigma_{\text{R}}})^2$ . When  $\xi = 4$  (as in Fig. 5.8), it gives  $E/E_{\sigma_{\text{R}}} \gtrsim 0.015$  for  $V_{\text{R}}/E_{\sigma_{\text{R}}} = 0.2$  and  $E/E_{\sigma_{\text{R}}} \gtrsim 1.5$  for  $V_{\text{R}}/E_{\sigma_{\text{R}}} = 2$ . As predicted by the scaling theory of Anderson Localization [56] and explicitly seen in Eq. (5.40), the 2D localization length increases exponentially at large energy (hence the limited energy range in Fig. 5.8). Therefore measuring it experimentally with ultracold atoms [23, 138, 190] is very challenging and can be done in a rather narrow energy window, in which  $L_{\text{loc}}$  is larger than the resolution of the imaging system ( $L_{\text{res}}$ ) but smaller than the size of the sample ( $L_{\text{sys}}$ ). This is illustrated for  $\sigma_{\text{R}} = 0.25 \mu\text{m}$  on Fig. 5.8 by the grey dashed lines  $L_{\text{res}} \sim 15 \mu\text{m}$  and  $L_{\text{sys}} \sim 2 \text{mm}$ , which are typical values extracted from Refs. [17, 19].

## Conclusion

We have presented a general quantum transport theory for calculating general expressions for the transport properties of a matter wave in an anisotropic disordered potential: scattering length, diffusion tensor and localization tensor. We have computed them for anisotropic Gaussian 2D speckles, which illustrates the effects of anisotropy.

In weak disorder, we found that scattering and Boltzmann diffusion properties are both determined by the disorder power spectrum. In correlated and anisotropic disorder, the structure of the disorder power spectrum can lead to very rich transport properties. For example, in our 2D example, we found that the anisotropy of transport is not that of the disorder, that the scattering time and Boltzmann diffusion tensor anisotropies are both non-monotonous functions of energy, and the scattering time even shows an inversion of anisotropy with energy.

In the framework of the standard on-shell self-consistent approximation, we found that the localization properties are uniquely determined by the properties of the diffusing medium. In particular, the anisotropy of the corrected diffusion tensor is that of the Boltzmann tensor, and the anisotropy of the localization length, is the square root of that of Boltzmann diffusion. We found that for typical parameters, the localization length diverges exponentially with energy,

and the anisotropy expected in the observable regime is very small, as opposed to what was found in the classical regime [17, 23].

The counter part of these properties in three dimensions are discussed in the next chapter, where we recover the same type of effects. In contrast to two dimensions, it is almost impossible to produce isotropic 3D speckles, and they usually have complex, structured correlations, which can induce new effects as we will see.



## Chapter 6

# Quantum transport and Anderson localization: Three-dimensional disorder with structured correlations

### Abstract

In the preceding chapter we saw that the macroscopic behavior of Anderson localization is intimately related to the microscopic properties of single scattering from the asperities of the disorder. Here, we study quantum transport of matter waves in anisotropic three-dimensional disorder with three models of disorder showing fine structured, anisotropic correlations. First, we show that structured correlations can induce rich effects, such as anisotropic suppression of the white-noise limit and inversion of the transport anisotropy. Second, we propose a new method to estimate the 3D localization threshold (mobility edge), which includes a disorder-induced shift of the energy states: The latter is shown to be very important for the estimate of the mobility edge. Our method not only sheds new light on previous results but also is applicable to models of disorder with structured correlations. After validating the method by comparison with other ones applicable to isotropic disorder, we apply it to anisotropic speckle potentials. This work is directly relevant for current experiments as regards 3D mobility edge and study of diffusion and localization effects in 3D optical speckle, which are discussed in the next chapter.

### Résumé

Dans les chapitres précédents nous avons vu que le comportement macroscopique de la localisation d'Anderson est intimement lié aux propriétés microscopiques des événements de diffusion sur les aspérités du désordre. Ici, nous étudions le transport quantique d'ondes de matière dans un désordre anisotrope tri-dimensionnel, à travers trois modèles de désordre aux corrélations comportant des structures fines et anisotropes. Dans un premier temps, nous montrons que des corrélations structurées peuvent induire de nombreux effets, tels que la suppression anisotrope de la limite de bruit blanc et l'inversion de l'anisotropie de transport.

Dans un second temps, nous proposons une nouvelle méthode pour estimer la position du seuil de localisation à 3D (seuil de mobilité), en incluant un décalage de l'énergie des états propres induit par le désordre : nous montrons que ce dernier est très important lors de l'estimation du seuil de mobilité. Non seulement notre méthode apporte un éclairage nouveau sur des résultats précédents, mais elle est aussi applicable à des modèles de désordre avec des corrélations structurées. Après avoir validé la méthode en la comparant avec d'autres approches applicables à un désordre isotrope, nous l'appliquons aux potentiels de speckle anisotropes. Ce travail est directement pertinent pour les expériences actuelles en ce qui concerne le seuil de mobilité à 3D et l'étude des effets de diffusion et de localisation dans un speckle optique 3D, qui sont examinées dans le chapitre suivant.

## Introduction: Structured, anisotropic correlations

As shown in the previous chapter, coherent transport in disordered media is strongly affected by anisotropy effects. So far, theoretical analyses mainly focused on models of disorder made of isotropic impurities imbedded in anisotropic media [153, 191] or stretched scatterers in isotropic media [192, 193]. In the example developed in Chap. 5 the correlation function is an anisotropic homothety of an isotropic function and the geometrical anisotropy ratio  $\xi$  is well-defined. Rich anisotropic transport properties, such as non-monotonous behaviour of the diffusion anisotropy with energy, were already found in this case. The recent advent of systems where the disorder correlations can be controlled, e.g. tunable arrangements of scatterers for microwaves [76, 194], engineered optical materials [195] or ultracold atoms in optical disorder [13, 20], opens new perspectives, and it becomes increasingly important to better understand transport in disordered media with more complex correlations.

Speckle potentials considered in 3D 'naturally' offer situations in which the type of correlations depends on the direction. For example, as explained in Chap. 3, due to the laws of optics, the two-point correlation function of a speckle pattern created by a single Gaussian beam is Lorentzian in the direction of the beam, while it is Gaussian in the transverse plane (see appendix D.1). In more involved speckle configurations, the correlation function can be even more complicated (see also examples in appendix D). The disorder can then have multiple characteristic lengths, the geometrical anisotropy of the disorder being ill-defined.

In this chapter, we study quantum transport and Anderson localization of matter waves in three-dimensional disorder with structured, anisotropic correlations. We will first determine the diffusion and localization tensors using the self-consistent approach introduced in Chap. 5. We will show that structured correlations can lead to rich transport properties, such as anisotropic suppression of the white-noise limit and inversion of the transport anisotropy with energy. Then, going beyond the standard on-shell approximation of Vollhardt and Wölfle [153] (see Chap. 5), we include the real part of the particle self energy. While the latter affects the above results only quantitatively, we show that it strongly modifies the behavior of the mobility edge. Our results have direct implications to recent experiments with ultracold atoms in optical disorder [18, 19], which will be discussed in Chap. 8. They can also be extended to waves with different dispersion relations and other models of disorder, where counterpart effects can be expected. This chapter can be considered as a detailed version of Ref. [25]

## 6.1 Speckle correlation functions in three dimensions

Speckle patterns and their transverse 1D and 2D correlation properties are described in the introductory chapter 3. Here we will consider the 3D correlations of speckle patterns obtained with isotropic Gaussian laser beams of waists  $w$  and plates with homogeneous transmission, so that the pupil function reads  $I_D(\boldsymbol{\rho}) = I_0 e^{-2|\boldsymbol{\rho}|^2/w^2}$ .

### 6.1.1 Single speckle (3D)

The simplest configuration is obtained for one laser beam illuminating an infinite diffusive plate (see Fig. 3.2). For this *single-speckle* configuration, the calculations are detailed in

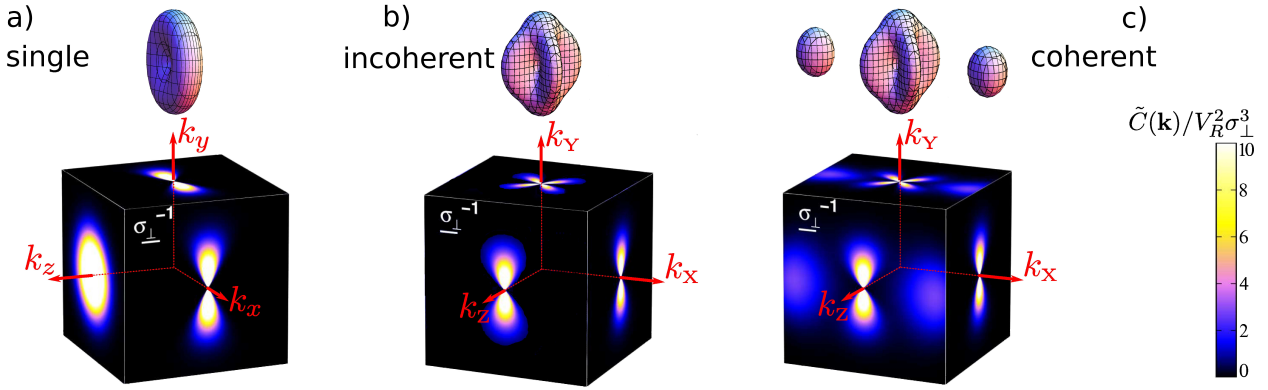


Figure 6.1: Disorder power spectrum  $\tilde{C}(\mathbf{k})$  for the (a) single-speckle, (b) incoherent-speckles, and (c) coherent-speckles cases [Eqs. (6.3), (6.5), and (6.6)] with the parameters of Refs. [18, 19] ( $\sigma_{\parallel}/\sigma_{\perp} \simeq 5.8$ , and for (c)  $\lambda_L/\sigma_{\perp} \simeq 2.16$ ). The functions  $\tilde{C}(\mathbf{k})$  are represented as iso-value surfaces (at  $2V_R^2\sigma_{\perp}^3$ ) and cuts in the planes defined by the symmetry axes:  $\{\hat{\mathbf{u}}_x, \hat{\mathbf{u}}_y, \hat{\mathbf{u}}_z\}$  for (a) and  $\{\hat{\mathbf{u}}_X \equiv (\hat{\mathbf{u}}_x - \hat{\mathbf{u}}_z)/\sqrt{2}, \hat{\mathbf{u}}_Y \equiv \hat{\mathbf{u}}_y, \hat{\mathbf{u}}_Z \equiv (\hat{\mathbf{u}}_x + \hat{\mathbf{u}}_z)/\sqrt{2}\}$  for (b) and (c).

appendix D.1. In the paraxial approximation we find

$$C(\mathbf{r}) = V_R^2 c_{1\text{sp}}(x, y, z) \quad (6.1)$$

with

$$c_{1\text{sp}}(x, y, z) = \frac{1}{1 + 4z^2/\sigma_{\parallel}^2} e^{-\frac{1}{\sigma_{\perp}^2} \frac{x^2+y^2}{1+4z^2/\sigma_{\parallel}^2}}, \quad (6.2)$$

$\sigma_{\parallel} = 4\lambda_L f^2/\pi w^2$  and  $\sigma_{\perp} = \lambda_L f/\pi w$ . Here, as in Chap. 3,  $x$  and  $y$  are the coordinates orthogonal to the propagation axis  $z$ , and  $z = 0$  corresponds to the focal plane. We have also chosen  $V_R \equiv \sqrt{C(\mathbf{r} = 0)}$  as definition of the amplitude of the disorder [see Eq. (3.26)].

It is the configuration used in Ref. [18] for instance. The resulting speckle pattern is significantly anisotropic. It has correlation lengths  $\sigma_{\parallel}$  in the propagation axis ( $z$ ) and  $\sigma_{\perp}$  in the orthogonal plane ( $x, y$ ). In general  $4f > w$ , and  $C(\mathbf{r})$  is elongated along  $z$  (for instance  $\sigma_{\parallel}/\sigma_{\perp} \simeq 5.8$  in Ref. [18]). The corresponding disorder power spectrum reads (see appendix D.1)

$$\tilde{C}(\mathbf{k}) = V_R^2 \tilde{c}_{1\text{sp}}(\mathbf{k}) \quad (6.3)$$

with

$$\tilde{c}_{1\text{sp}}(\mathbf{k}) = \pi^{3/2} \frac{\sigma_{\perp} \sigma_{\parallel}}{\sqrt{k_x^2 + k_y^2}} e^{-\frac{\sigma_{\perp}^2}{4}(k_x^2 + k_y^2)} e^{-\frac{1}{4} \left(\frac{\sigma_{\parallel}}{\sigma_{\perp}}\right)^2 \frac{k_z^2}{k_x^2 + k_y^2}}. \quad (6.4)$$

It is isotropic in the  $(k_x, k_y)$  plane but has a significantly different shape along the  $k_z$  axis. This can be seen in Fig. 6.1(a): A typical iso-value surface of  $\tilde{C}(\mathbf{k})$  is wheel-shaped, and its cuts in planes containing  $\hat{\mathbf{k}}_z$  are shaped like "8" figures. It also shows a strong algebraic divergence when  $k_z = 0$  and  $k_x^2 + k_y^2 \rightarrow 0$ . It features absence of white-noise limit, which reflects the long-range correlations of the potential. The consequences of this property, obtained in the paraxial approximation, will be further discussed in the following.

### 6.1.2 Orthogonally crossed speckles (3D)

A way to decrease the effective anisotropy in speckle potentials is to use two orthogonally-crossed speckle fields, propagating along the  $z$  and  $x$  axes, respectively. It is the configuration used in Ref. [19]. The polarizations and the frequencies of the two lasers can be chosen such that the two beams are fully incoherent (so-called *incoherent-speckles* configuration in the following) or mutually coherent (so-called *coherent-speckles* configuration, case of Ref. [19]).

**Fully incoherent case** – In the incoherent-speckles case (see details in appendix D.2.1) the 3D-correlation function in real space and the corresponding power spectrum  $\tilde{C}(\mathbf{k})$  are given by the sum of two orthogonally-oriented spectra, similar to that of the single-speckle case, so that

$$\tilde{C}(\mathbf{k}) = (V_R/2)^2 [\tilde{c}_{\text{1sp}}(k_x, k_y, k_z) + \tilde{c}_{\text{1sp}}(k_z, k_y, k_x)], \quad (6.5)$$

where  $\tilde{c}_{\text{1sp}}(k_x, k_y, k_z)$  is given by Eq. (6.4). Therefore, as shown in figure 6.1(b), a typical iso-value surface of  $\tilde{C}(\mathbf{k})$  is the superposition of two crossed wheel-shaped spectra.

**Fully coherent case** – In the coherent-speckles case (see appendix D.2.2) the 3D-correlation function in real space and the corresponding power spectrum  $\tilde{C}(\mathbf{k})$  are the same as for the incoherent-speckles case, plus a coherence term, which results from the interference of the two speckle patterns. We then have

$$\tilde{C}(\mathbf{k}) = (V_R/2)^2 [\tilde{c}_{\text{1sp}}(k_x, k_y, k_z) + \tilde{c}_{\text{1sp}}(k_z, k_y, k_x) + 2\tilde{c}_{\text{coh}}(k_x, k_y, k_z)] \quad (6.6)$$

where  $\tilde{c}_{\text{1sp}}(\mathbf{k})$  is given by Eq. (6.4),  $\tilde{c}_{\text{coh}}(\mathbf{k})$  is the Fourier transform of

$$c_{\text{coh}}(\mathbf{r}) = \sqrt{c_{\text{1sp}}(x, y, z) \times c_{\text{1sp}}(z, y, x)} \frac{(1 + 4\frac{xz}{\sigma_{\parallel}^2}) \cos[\phi(\mathbf{r})] + 2\frac{x-z}{\sigma_{\parallel}} \sin[\phi(\mathbf{r})]}{\sqrt{1 + 4z^2/\sigma_{\parallel}^2} \sqrt{1 + 4x^2/\sigma_{\parallel}^2}}$$

and  $\phi(\mathbf{r}) = \frac{2\pi}{\lambda_L}(x-z) - \frac{z}{\sigma_{\perp}^2 \sigma_{\parallel}} \frac{x^2+y^2}{1+4z^2/\sigma_{\parallel}^2} - \frac{x}{\sigma_{\perp}^2 \sigma_{\parallel}} \frac{z^2+y^2}{1+4x^2/\sigma_{\parallel}^2}$ , where  $c_{\text{1sp}}(x, y, z)$  is given by Eq. (6.2). The latter term mainly creates two broad structures (*bumps*), centered on the  $\hat{\mathbf{k}}_X \equiv (\hat{\mathbf{k}}_x - \hat{\mathbf{k}}_z)/\sqrt{2}$  axis [see Fig. 6.1(c)]. For the parameters of Ref. [19],  $\sigma_{\parallel}/\sigma_{\perp} \simeq 5.8$  and  $\lambda_L/\sigma_{\perp} \simeq 2.16$ , these bumps are located at  $k_X \simeq \pm 3.8\sigma_{\perp}^{-1}$ .

## 6.2 On-shell predictions

In this section we apply the formalism introduced in Secs. 5.1 to 5.3 to the 3D speckle potentials of Secs. 6.1.1 and 6.1.2. We discuss single-scattering (Sec. 6.2.1), Boltzmann diffusion (Sec. 6.2.2) and localization (Sec. 6.2.3) properties, successively for the single-speckle and orthogonally-crossed-speckles configurations. We recall that those systems are relevant for ultracold atoms experiments, in particular our configurations apply to Ref. [18] (single-speckle) and Ref. [19] (coherent orthogonally-crossed speckles), respectively. This section can be viewed as a detailed version of Ref. [26].

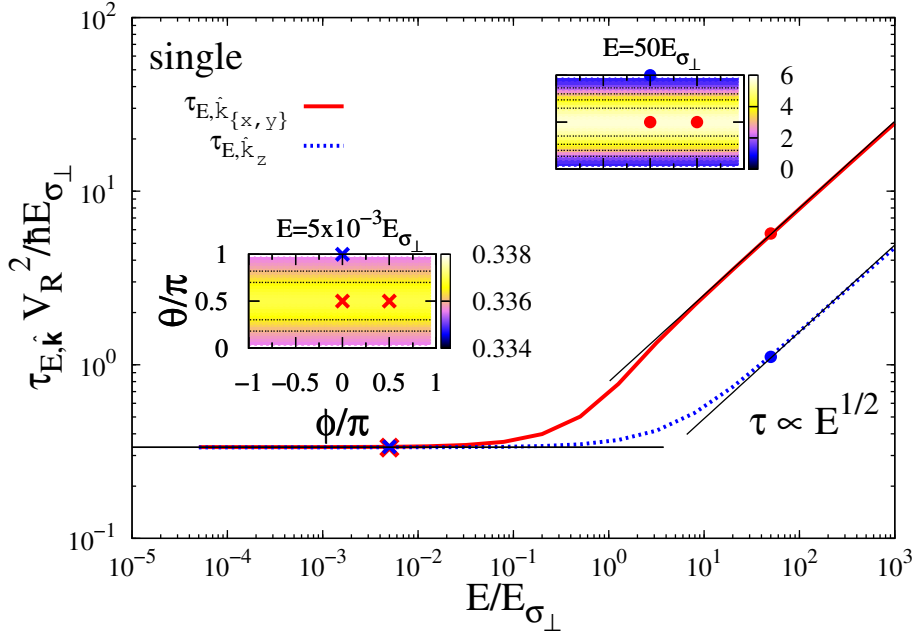


Figure 6.2: Scattering mean free time  $\tau_{E,\hat{\mathbf{k}}}$  in the 3D *single-speckle* case [Eq. (6.7)] with  $|\mathbf{k}| = k_E$  for the parameters of Fig. 6.1, in the  $(\hat{\mathbf{k}}_x, \hat{\mathbf{k}}_y)$  plane (solid red line) and along the  $\hat{\mathbf{k}}_z$  direction (dotted blue line). The black lines are the low-energy [ $k_E\sigma_\perp \ll 1$ , see Eq. (6.9)] and the high energy [ $k_E\sigma_\perp \gg 1$ , see Eq. (6.10)] limits. Note that in both limits  $\tau_{E,\hat{\mathbf{k}}}$  is anisotropic, although for  $k_E\sigma_\perp \ll 1$ , the anisotropy is very small,  $\xi_s \simeq 1.002$ . The insets show the angular dependence of  $\tau_{E,\hat{\mathbf{k}}}$  at different energies [with the parametrization  $\hat{\mathbf{k}} = (\hat{\mathbf{k}}_x, \hat{\mathbf{k}}_y, \hat{\mathbf{k}}_z) \equiv (\sin\theta \cos\phi, \sin\theta \sin\phi, \cos\theta)$ ]. The points on the lines are color- and shape-coded to match those in the insets.

### 6.2.1 Single-scattering

**Single-speckle configuration** – For the *single-speckle* case, inserting Eqs. (6.3) and (6.4) into Eq. (5.4), we find the scattering mean free time

$$\tau_s(E, \mathbf{k}) = \frac{\hbar E \sigma_\perp}{V_R^2} \frac{(2\pi)^2 / k_E \sigma_\perp}{\int d\Omega_{\hat{\mathbf{k}}} \tilde{c}_{1\text{sp}}(k_E \hat{\mathbf{k}}' - \mathbf{k}) / \sigma_\perp^3}, \quad (6.7)$$

which is shown in Fig. 6.2 for  $|\mathbf{k}| = k_E$  [as for the 2D case of Sec. 5.1.2 we define the on-shell scattering mean free time  $\tau_{E,\hat{\mathbf{k}}} \equiv \tau_s(E, k_E \hat{\mathbf{k}})$ ]. Since  $\tilde{C}(\mathbf{k})$  is isotropic in the  $(k_x, k_y)$  plane,  $\tau_{E,\hat{\mathbf{k}}}$  only depends on the polar angle  $\theta$  between  $\mathbf{k}$  and  $\hat{\mathbf{k}}_z$  and not on the azimuthal angle  $\phi$ . We find that the scattering time is an increasing function of energy. It is also shorter for particles travelling along the  $z$  direction ( $\tau_{E,\hat{\mathbf{k}}_z} < \tau_{E,\hat{\mathbf{k}}_{\{x,y\}}}$ ) for all values of  $E$ . As for the 2D case, analyzed in Sec. 5.1.2, this is due to the wider extension of  $\tilde{C}(\mathbf{k})$  in the plane  $(k_x, k_y)$ , which offers more scattering channels to particles travelling along  $z$ . In contrast to the 2D speckle case, however,  $\tau_{E,\hat{\mathbf{k}}}$  shows no inversion of anisotropy.

In the low energy limit ( $k_E\sigma_\perp \ll 1$ ),  $\tau_{E,\hat{\mathbf{k}}}$  converges to a constant value. In contrast to the 2D case, it signals the absence of a 3D white-noise limit<sup>1</sup>. This can be attributed to the

1. In the case of a white-noise limit in 3D, the scattering time is isotropic with the scaling  $\tau_{E,\hat{\mathbf{k}}} \propto 1/\sqrt{E}$  (i.e.  $l_{sE,\hat{\mathbf{k}}}$  is constant). This can be found by inserting  $\tilde{C}(\mathbf{k}) = \text{cst}$  in Eq. (5.4).

strong anisotropic divergence of  $\tilde{C}(\mathbf{k})$  when  $|\mathbf{k}| \rightarrow 0$  which reflects the long-range correlations of the disorder (see Sec. 6.1.1). More precisely, for  $|\mathbf{k}|\sigma_\perp \ll 1$ , we have

$$\tilde{c}_{\text{1sp}}(\mathbf{k}) \simeq \pi^{3/2} \frac{\sigma_\perp \sigma_\parallel}{|\mathbf{k}|} g(\hat{\mathbf{k}}) = \pi^{3/2} \frac{\sigma_\perp \sigma_\parallel}{|\mathbf{k}|} e^{-\frac{1}{4} \left( \frac{\sigma_\parallel}{\sigma_\perp} \right)^2 \frac{k_z^2}{k_x^2 + k_y^2}}. \quad (6.8)$$

Replacing  $\tilde{c}_{\text{1sp}}$  in Eq. (6.7) we then find

$$\tau_{E,\hat{\mathbf{k}}} = \frac{\hbar E_{\sigma_\perp}}{V_R^2} \frac{4\sqrt{\pi}}{\int d\Omega_{\hat{\mathbf{k}}}' g(\hat{\mathbf{k}}' - \hat{\mathbf{k}})}, \quad (6.9)$$

which is independent of  $E$ . Equation (6.9) is plotted as solid black lines on the left-hand side of Fig. 6.2. Note that  $\tau_{E,\hat{\mathbf{k}}}$  does not become strictly isotropic in this limit. However, the residual anisotropy of the scattering time, found from Eq. (6.9) and from the anisotropy of  $\tilde{c}(\hat{\mathbf{k}})$  in Eq. (6.8), is very small, and practically unobservable ( $\tau_{E,\hat{\mathbf{k}}_{\{x,y\}}}/\tau_{E,\hat{\mathbf{k}}_z} \simeq 1.002$ ). When the energy increases, the scattering time in the  $(x, y)$  plane is the first to deviate significantly from the low-energy behaviour at  $E \sim E_{\sigma_\parallel} (= 3 \times 10^{-2} E_{\sigma_\perp})$  for the parameters of Fig. 6.2), while the scattering time in the  $z$  direction increases only at  $E \sim E_{\sigma_\perp}$ . This can be understood again by the narrower width of the power spectrum  $\tilde{C}(\mathbf{k})$  in the  $k_z$  direction.

In the high-energy limit ( $k_E \sigma_\perp \gg 1$ ) the  $\mathbf{k}$ -space shell integral of Eq. (6.7), which is done on a sphere of radius  $k_E$  containing the origin, can be reduced to integrating  $\tilde{c}_{\text{1sp}}$  on the plane which is tangent to the sphere at the origin. We then find

$$\tau_{E,\hat{\mathbf{k}}} \simeq \frac{\hbar E_{\sigma_\perp}}{V_R^2} \frac{\sigma_\perp}{\sigma_\parallel} \frac{4\sqrt{\pi} k_E \sigma_\perp}{\int d\kappa d\kappa' \frac{e^{-\frac{\kappa^2 k_z^2 + \kappa'^2}{4}} e^{-\frac{1}{4} \left( \frac{\sigma_\parallel}{\sigma_\perp} \right)^2 \frac{\kappa^2 (k_x^2 + k_y^2)}{\kappa^2 k_z^2 + \kappa'^2}}}{\sqrt{\kappa^2 k_z^2 + \kappa'^2}}}. \quad (6.10)$$

In particular, we find  $\tau_{E,\hat{\mathbf{k}}_{\{x,y\}}} = \hbar E_{\sigma_\perp} k_E \sigma_\perp / 2V_R^2 \sqrt{\pi}$ ,  $\tau_{E,\hat{\mathbf{k}}_z} = \hbar E_{\sigma_\perp} k_E \sigma_\perp^2 / V_R^2 \pi \sigma_\parallel$  (both shown as the right-hand side solid black lines in Fig. 6.2). The anisotropy of the scattering then becomes significant for the parameters of Fig. 6.2,  $\tau_{E,\hat{\mathbf{k}}_{\{x,y\}}}/\tau_{E,\hat{\mathbf{k}}_z} = \sqrt{\pi} \sigma_\parallel / 2\sigma_\perp$  in this limit. The high-energy scaling  $\tau_{E,\hat{\mathbf{k}}} \propto k_E$ , which was also found in our 2D speckle, is quite universal: as long as the power spectrum is of finite integral in all the planes (lines in 2D) crossing the origin, the procedure described above can be applied to Eq. (5.4). Then  $\tau_{E,\hat{\mathbf{k}}}$  only depends on the dispersion relation  $\epsilon(\mathbf{k})$  and, in particular, it is independent of the space dimension.

**Orthogonally-crossed speckles** – We now consider the case of two orthogonally crossed speckle fields, that can be either mutually incoherent or coherent, and whose power spectrum are given by Eqs. (6.5) and (6.6) respectively. The 3D on-shell scattering mean free time [Eq. (5.4) with  $|\mathbf{k}| = k_E$ ] is presented in Fig. 6.3 in both configurations.

The power spectrum of the *incoherent-speckles* case is made of two orthogonally-oriented spectra, similar to that of the single-speckle case. As a consequence, its scattering time [see Fig. 6.3(a)] is qualitatively similar to the single-speckle one. It shows two distinct regimes:  $\tau_{E,\hat{\mathbf{k}}}$  constant at low energy and  $\tau_{E,\hat{\mathbf{k}}} \propto \sqrt{E}$  at high energy. Note that even though the directions  $X$  and  $Z$  are equivalent,  $\tau_{E,\hat{\mathbf{k}}}$  has a dependence in  $\Theta = (\hat{\mathbf{k}}, \hat{\mathbf{k}}_Z)$  and in  $\varphi$  (the

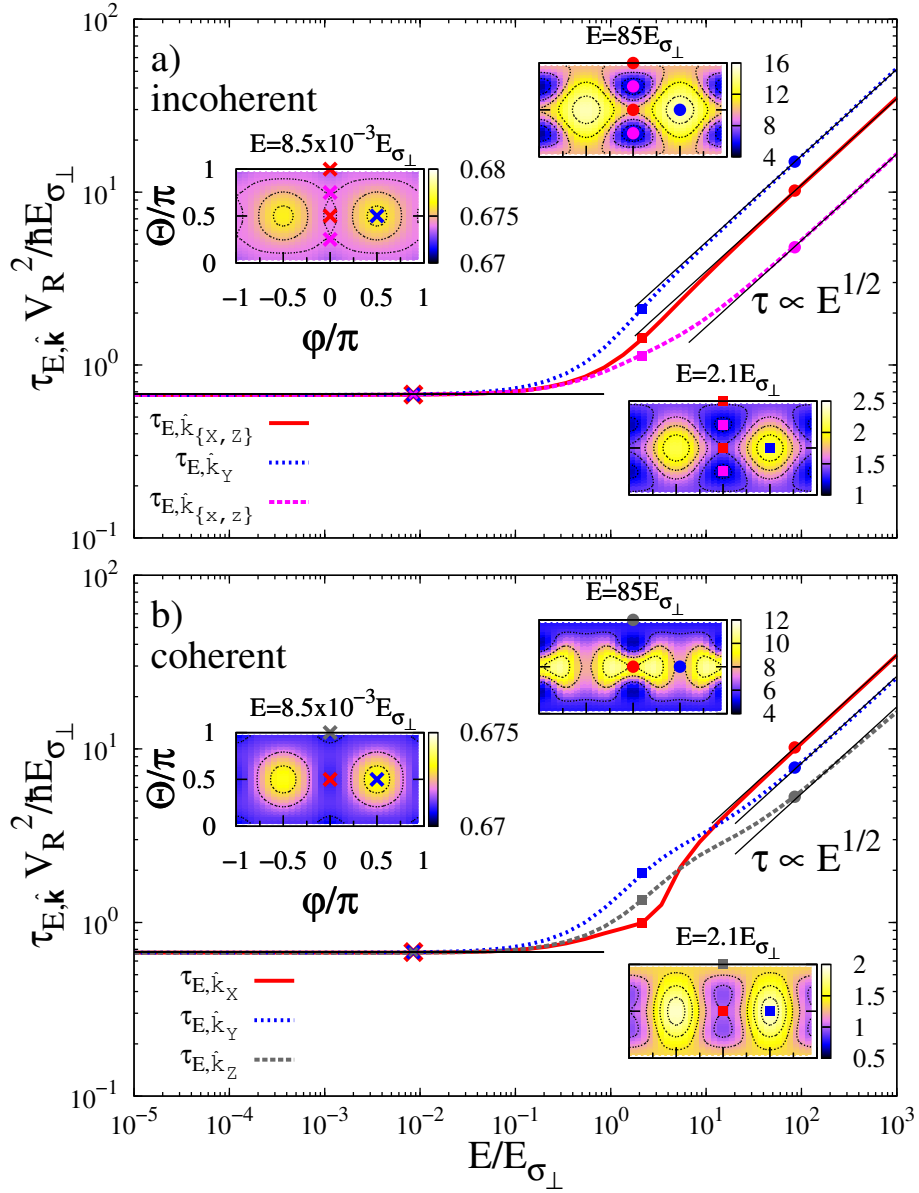


Figure 6.3: Scattering mean free time  $\tau_{E,\hat{\mathbf{k}}}$  in the 3D *incoherent*- (top) and *coherent*- (bottom) *speckles* cases for the parameters of Fig. 6.1, along the symmetry axes of the correlation functions (see Fig. 6.1),  $\hat{\mathbf{k}}_X \equiv (\hat{\mathbf{k}}_x - \hat{\mathbf{k}}_z)/\sqrt{2}$  (solid red line),  $\hat{\mathbf{k}}_Y \equiv \hat{\mathbf{k}}_y$  (dotted blue line), and  $\hat{\mathbf{k}}_Z \equiv (\hat{\mathbf{k}}_x + \hat{\mathbf{k}}_z)/\sqrt{2}$  (dashed gray line) directions. The solid black lines are the low-energy limits obtained for  $k_E \sigma_\perp \ll 1$  and the high energy limits obtained for  $k_E \sigma_\perp \gg 1$  [see Eq. (6.11)]. The insets show the angular dependance of  $\tau_{E,\hat{\mathbf{k}}}$  at different energies [with the parametrization  $\hat{\mathbf{k}} = (\hat{\mathbf{k}}_X, \hat{\mathbf{k}}_Y, \hat{\mathbf{k}}_Z) \equiv (\sin \Theta \cos \varphi, \sin \Theta \sin \varphi, \cos \Theta)$ ]. Note that this parametrization differs from that of Fig. 6.2 because the symmetry axes of  $\tilde{C}(\mathbf{k})$  are different. The points on the lines are color- and shape-coded to match those in the insets.

azimuthal angle in the  $(k_X, k_Y)$  plane) because the correlation function does not show rotation invariance around any axis. As an example  $\tau_{E,\hat{\mathbf{k}}_{\{x,z\}}}$  is also presented on Fig. 6.3(a). Note also that the anisotropy between the directions of minimal ( $\hat{\mathbf{k}}_{\{x,z\}}$ ) and maximal ( $\hat{\mathbf{k}}_Y$ ) scattering times is reduced compared to the single-speckle case.

In the *coherent-speckles* case, the power spectrum is the incoherent one plus a coherence term that creates two additional bumps centered on the  $\hat{\mathbf{k}}_X$  axis [at  $k_X \simeq \pm 3.8\sigma_\perp^{-1}$  for our parameters, see Fig. 6.1]. As already mentioned, the scattering time (taken on-shell) in the Born approximation samples  $\tilde{C}(\mathbf{k})$  on a  $\mathbf{k}$ -space shell of radius  $k_E$  centered in  $k_E\hat{\mathbf{k}}$  [see Eq. (5.4)]. Therefore we recover the incoherent-speckles case at low energy. The bumps play a role for  $2k_E\sigma_\perp \gtrsim 3.8$ , i.e. for  $E \gtrsim 1.8E_{\sigma_\perp}$ . They offer more scattering channels to the particle travelling along  $Y$  and  $Z$ , making the corresponding scattering times drop below the values obtained in the coherent case [see Fig. 6.3(b)]. This leads to an inversion of the anisotropy of the scattering time with energy:  $\tau_{E,\hat{\mathbf{k}}_X} < \tau_{E,\hat{\mathbf{k}}_Y}, \tau_{E,\hat{\mathbf{k}}_Z}$  at low energy and  $\tau_{E,\hat{\mathbf{k}}_X} > \tau_{E,\hat{\mathbf{k}}_Y}, \tau_{E,\hat{\mathbf{k}}_Z}$  at high energy.

At low energy ( $k_E\sigma_\perp \ll 1$ ) the absence of white-noise limit and the scaling of  $\tilde{c}_{\text{isp}}(\mathbf{k})$  presented in Eq. (6.8) gives, as for the single-speckle configuration, a constant anisotropic scattering time in both cases (the term  $\tilde{c}_{\text{coh}}(\mathbf{k})$  present in the coherent case being negligible), with a very small anisotropy. When  $E$  increases, the scattering time in all directions deviates from the low-energy behaviour around  $E \sim E_{\sigma_\parallel}$  ( $= 3 \times 10^{-2} E_{\sigma_\perp}$  for the parameters of Fig. 6.3). In the high-energy regime ( $k_E\sigma_\perp \gg 1$  for the incoherent and  $k_E\sigma_\perp \gg 3.8$  for the coherent case) we have

$$\tau_{E,\hat{\mathbf{k}}} = \frac{\hbar E_{\sigma_\perp}}{V_R^2} \frac{(2\pi)^2 k_E \sigma_\perp}{\int d\kappa d\kappa' \tilde{C} \left( \kappa \hat{k}_z, \kappa', \kappa \sqrt{\hat{k}_x^2 + \hat{k}_y^2} \right) / V_R^2 \sigma_\perp}, \quad (6.11)$$

which is displayed as the solid black lines on the right-hand side of Fig. 6.3.

## 6.2.2 Boltzmann diffusion

Let us now analyze Boltzmann diffusion in our 3D speckle potentials. It is obtained, as in the 2D case analyzed previously in Sec. 5.2, by solving Eq. (5.22) numerically and incorporating the results in Eq. (5.21). For the diagonalization of the integral operator (5.22) we use  $2^7 \times 2^7 = 128 \times 128$  points regularly spaced on the  $\mathbf{k}$ -space shell  $|\mathbf{k}| = k_E^2$ .

**Single-speckle** – The eigenvalues  $\lambda_E^n$  of Eq. (5.22) for different energies, as well as the topography of the eigenvectors of Eq. (5.22) that dominate  $D_B^x$  (bottom row),  $D_B^y$  (2<sup>nd</sup> row), and  $D_B^z$  (3<sup>rd</sup> row) are shown in Fig. 6.4. We find (similarly as for the 2D speckle potential) that the  $\phi_{E,\hat{\mathbf{k}}}^n$  are topologically similar to the spherical harmonics at all energies, i.e. they show similar nodal surfaces, but the associated  $\lambda_E^n$  are not degenerated in a given  $l$ -like level. More precisely, due to the cylindrical symmetry of the power spectrum [see Fig. 6.1(a)], the values of  $\lambda_E^n$  associated to the  $Y_l^{+m}$ -like and  $Y_l^{-m}$ -like orbitals are the same for a given  $m$ , but the degeneracy between the different values of  $|m|$  is lifted.

Figure 6.5 shows the resulting eigencomponents of the diffusion tensor in the *single-speckle* case. It is isotropic in the  $(x, y)$  plane, because of the rotation-invariance of the correlation function  $\tilde{C}(\mathbf{k})$  around the axis  $\hat{\mathbf{k}}_z$ . For the same symmetry reasons as in the isotropic case (see appendix C.2) and as in the 2D case, only the  $p$ -level-like orbitals couple to  $\mathbf{v}$ . For  $k_E\sigma_\perp \ll 1$ , we find that  $D_B^{x,y}$  is dominated by the first term in Eq. (5.21) and  $D_B^z$  by the

---

2. Comparison to calculations with  $2^6 \times 2^6$  points show that the results are converged. In addition, test in the case of an isotropic 3D speckle [16], the power spectrum of which show similar infrared ( $k \rightarrow 0$ ) divergence to our anisotropic speckle, gave very good agreement with analytical formulas (see appendix C.2 and Fig. E.2 in particular).

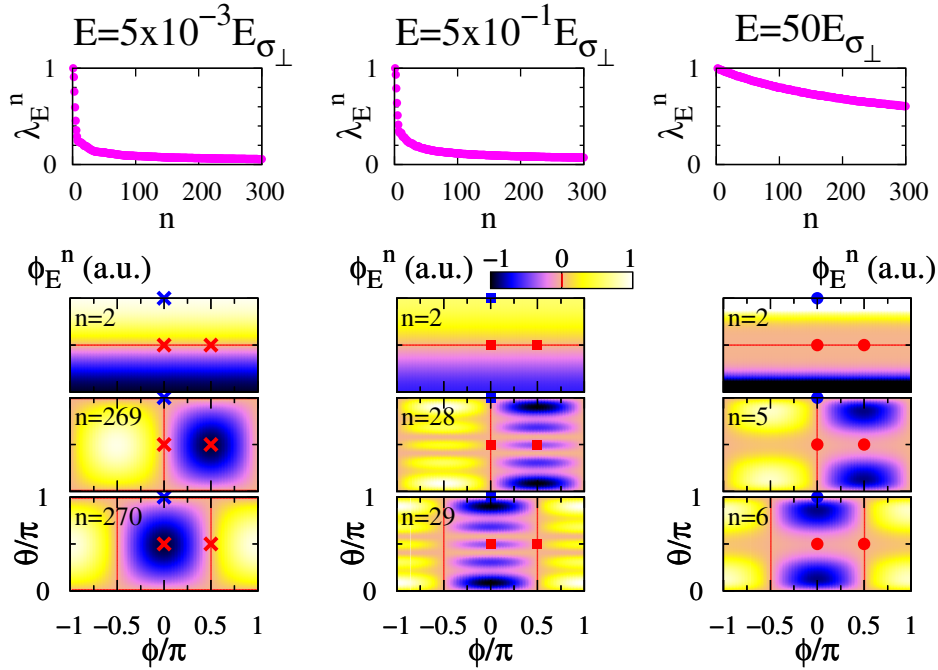


Figure 6.4: *Single-speckle* case. Eigenvalues of Eq. (5.22) at various energies indicated on the figure (top row). Topography of the eigenvectors  $\phi_{E,\hat{\mathbf{k}}}^n$ , at the same energies, which mainly contribute to  $D_B^x$  (bottom row),  $D_B^y$  (2<sup>nd</sup> row) and  $D_B^z$  (3<sup>rd</sup> row) respectively [with the parametrization  $\hat{\mathbf{k}} = (\hat{\mathbf{k}}_x, \hat{\mathbf{k}}_y, \hat{\mathbf{k}}_z) \equiv (\sin \theta \cos \phi, \sin \theta \sin \phi, \cos \theta)$ ]. The values of  $n$  are indicated on the figure, the red lines locate the nodal lines. The points are color- and shape-coded to match those of Fig. 6.2.

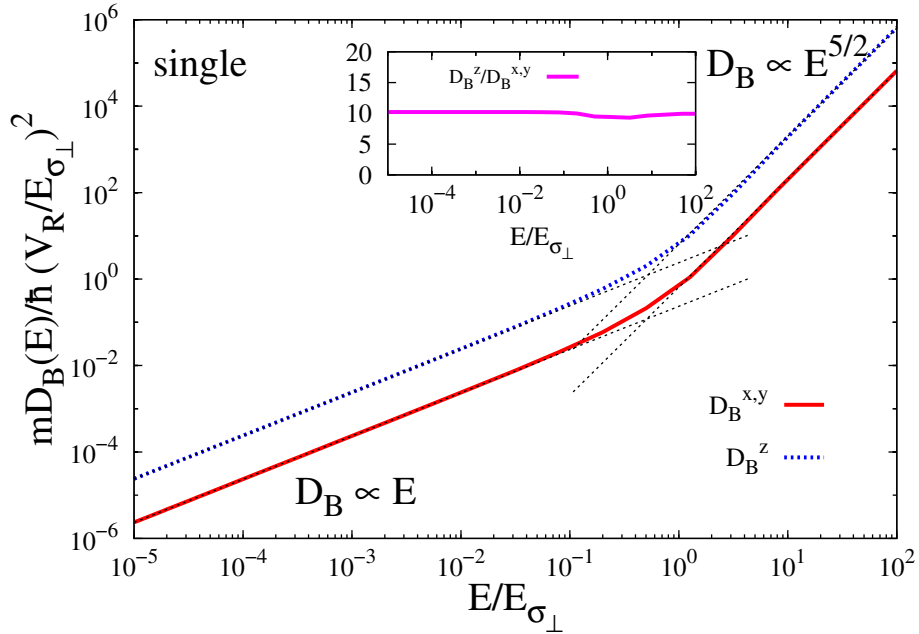


Figure 6.5: Boltzmann diffusion coefficients along the transport eigenaxes (eigencomponents of  $\mathbf{D}_B$ ) for the *single-speckle* configuration and for the parameters of Fig. 6.1. The dotted lines are power-law fits ( $D_B^u \propto E^{\gamma_u}$ ) to the data in the low and high energy limits. The inset show the transport anisotropy factor  $D_B^z/D_B^{x,y}$ .

$Y_1^0$ -like orbital ( $n = 2$  at all energies). For  $k_E \sigma_\perp \gg 1$ , the situation changes: while  $D_B^z$  is still dominated by the  $Y_1^0$ -like orbital,  $D_B^x$  is now dominated by the  $Y_1^{+1}$ -like orbitals and  $D_B^y$  by the  $Y_1^{-1}$ -like orbitals (respectively  $n = 6$  and  $5$  at  $E = 50E_{\sigma_\perp}$  in Fig. 6.4) with a contribution of the  $Y_3^{\pm 1}$ -like orbitals increasing<sup>3</sup> with  $E$ . Several remarks are worth stressing:

Firstly, as already discussed for the 2D case, the transport and scattering mean free times can be very different quantities in correlated disorder, and, in particular the anisotropy of  $\mathbf{D}_B$  can be very different from that of  $\tau_{E,\hat{\mathbf{k}}}$ . Here we find that the diffusion tensor is larger along axis  $z$  ( $D_B^z > D_B^{x,y}$ ) for all values of  $E$  (see Fig. 6.5), and the anisotropy of  $\mathbf{D}_B$  is thus reversed with respect to that of  $\tau_{E,\hat{\mathbf{k}}}$  (we recall that we found  $\tau_{E,\hat{\mathbf{k}}z} < \tau_{E,\hat{\mathbf{k}}\{x,y\}}$  for any  $E$ , see Sec. 6.2.1). This is due to the fact that the ( $Y_1^0$ -like) orbitals contributing to  $D_B^z$  are associated to values of  $\lambda_E^n$  larger than those contributing to  $D_B^{x,y}$  (in Fig. 6.4, the  $\phi_{E,\hat{\mathbf{k}}}^n$  are numbered by decreasing eigenvalues)

Secondly,  $\tilde{C}(\mathbf{k})$  shows a strong anisotropic, infrared divergence in the paraxial approximation (see Secs. 6.1.1 and 6.2.1). Following-up with the scaling of  $\tilde{c}_{1\text{sp}}(\mathbf{k})$ , Eq. (6.8), used to show that  $\tau_{\mathbf{k},E}$  is independent of energy for  $k_E \sigma_\perp \ll 1$ , and inserting it into Eq. (5.22) and the associated normalization, we find that  $\lambda_E^n$  does not depend on  $E$ , and  $\phi_{E,\hat{\mathbf{k}}}^n$  is of the form  $\varphi^n(\hat{\mathbf{k}})/\sqrt{k_E}$ . Then, all terms in Eq. (5.21) are topologically unchanged and scale as  $E$  at low energy. The anisotropy of  $\mathbf{D}_B$  thus persists down to arbitrary low values of  $E$  and  $D_B^u \propto E$ , as observed in the left-hand side of Fig. 6.5 for  $k_E \sigma_\perp \ll 1$  (i.e.  $E \ll E_{\sigma_\perp}$ ). This is another manifestation of the absence of white-noise limit<sup>4</sup>, and the persistence of anisotropy down to arbitrary low energy.

Thirdly, we found  $\tau_{E,\hat{\mathbf{k}}} \propto \sqrt{E}$ , and assuming weak topological change of the orbitals and the scaling  $1 - \lambda_E^n \propto 1/E$  (confirmed numerically), we get  $\phi_{E,\hat{\mathbf{k}}}^n \propto 1/k_E$  and  $D_B^u(E) \propto E^{5/2}$ . This scaling is confirmed in Fig. 6.5 by fits to the data for  $E \gg E_{\sigma_\perp}$  (right-hand side dotted lines). This scaling was also found in our 2D example and for isotropic 3D speckle disorder (see Ref. [16] and appendix C.2). Remarkably, in spite of the different contributing terms in Eq. (5.21) at low and high values of  $E$ , the transport anisotropy is nearly independent of  $E$  with  $D_B^z/D_B^{x,y} \simeq 10$  [see inset of Fig. 6.5].

**Orthogonally-crossed speckles** – Let us turn to the crossed-speckles configurations, whose diffusion coefficients are plotted in Fig. 6.6. Note first that in both the incoherent- and coherent-speckles configurations we recover the same general properties as for the single-speckle case, in particular the reversed anisotropies of scattering ( $\tau_{E,\hat{\mathbf{k}}\{X,Z\}} < \tau_{E,\hat{\mathbf{k}}Y}$ ) and diffusion ( $D_B^{X,Z} > D_B^Y$ ), the anisotropic suppression of the white-noise limit, and the scaling of the diffusion coefficients at low [ $D_B^u(E) \propto E$ ] and high [ $D_B^u(E) \propto E^{5/2}$ ] energy (see left- and right-hand dotted lines in Fig. 6.6). Here however, the transport eigenaxes are the bisectors  $\{\hat{\mathbf{X}}, \hat{\mathbf{Z}}\} = (\hat{\mathbf{x}} \mp \hat{\mathbf{z}})/\sqrt{2}$  and the axis  $\hat{\mathbf{Y}} = \hat{\mathbf{y}}$ , which are symmetry axes for both correlation functions (see Fig. 6.1).

In the *incoherent-speckles* case [Fig. 6.6(a)],  $\mathbf{D}_B$  is isotropic in the  $(X, Z)$  plane, even though the correlation function and the scattering time are not. This is due to the topology

3. At high energy, we find that the nodal lines of the  $Y_3^{\pm 1}$ -like orbitals calculated numerically are displaced compared to the associated spherical harmonics, therefore their contribution does not cancel out for symmetry reasons anymore.

4. A 3D white-noise limit would lead to the scaling  $D_B^u(E) \propto \sqrt{E}$  and an isotropic limit at low energy.

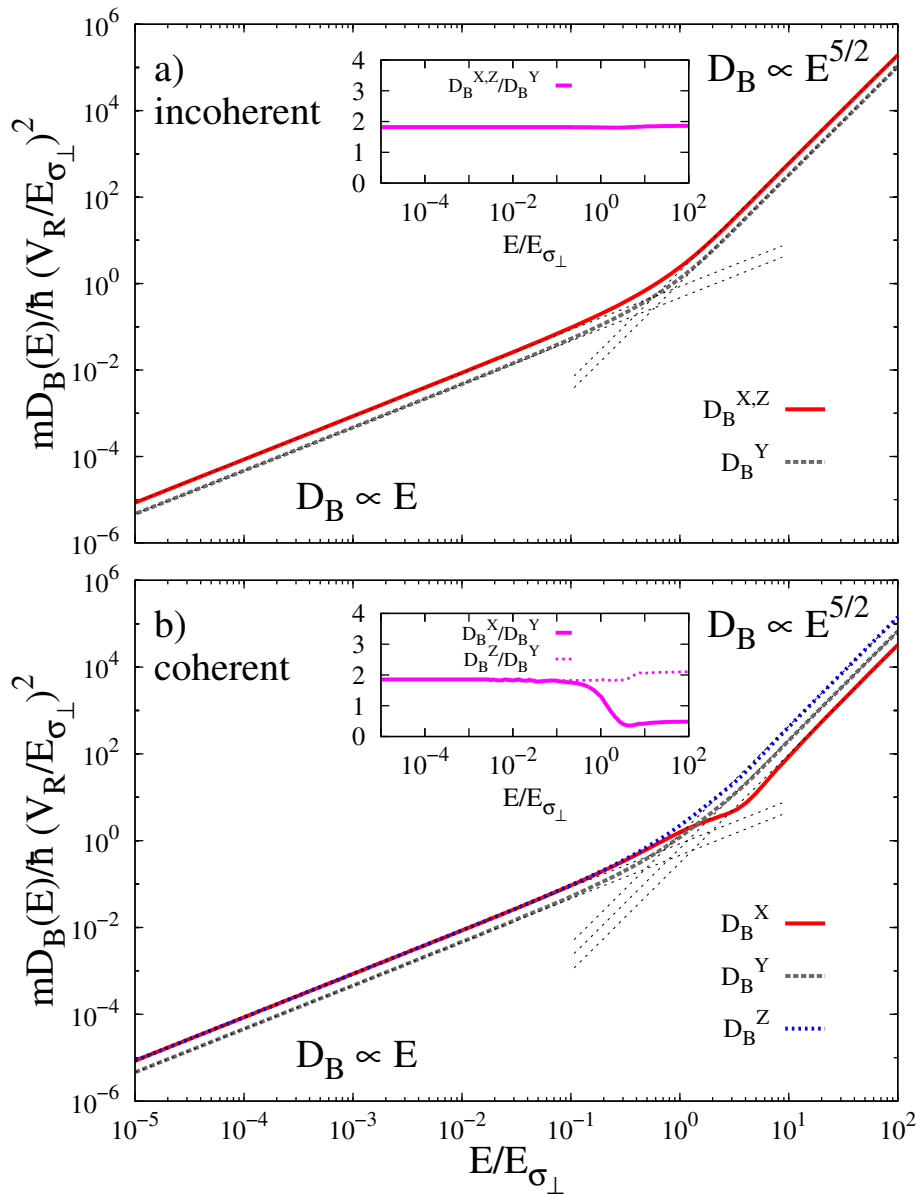


Figure 6.6: Components of the diffusion tensor:  $D_B^X$  (solid red line),  $D_B^Y$  (dashed gray line) and  $D_B^Z$  (dotted blue line) for the 3D *incoherent*- (top) and *coherent*- (bottom) *speckles* cases. The dotted lines are power-law fits ( $D_B^u \propto E^{\gamma_u}$ ) to the data in the low and high energy limits. The insets show the transport anisotropy factors  $D_B^X/D_B^Y$  and  $D_B^Z/D_B^Y$ .

of  $\tilde{C}(\mathbf{k})$  which bears four symmetry axes in this plane ( $\hat{\mathbf{k}}_x, \hat{\mathbf{k}}_z, \hat{\mathbf{k}}_X$  and  $\hat{\mathbf{k}}_Z$ )<sup>5</sup>. We find that the  $\phi_{E,\hat{\mathbf{k}}}^n$  contributing to the diffusion tensor are distorted compared to the single-speckle case but the number of nodal lines and their positions are still reminiscent of the  $Y_1^m$  spherical harmonics. In the end, the behaviour of the diffusion tensor is very similar to the single-speckle one and  $D_B^X \simeq D_B^Z > D_B^Y$ . The transport anisotropy is nearly constant, but significantly reduced with respect to the single-speckle case,  $D_B^{X,Z}/D_B^Y \simeq 1.8$ .

In the *coherent-speckles* configuration [Fig. 6.6(b)], as long as  $2k_E\sigma_\perp \ll 3.8$ , the behavior of

5. The propagation kernel has to bear the symmetries of the power spectrum  $\tilde{C}(\mathbf{k})$ .

$\mathbf{D}_B(E)$  is governed by the central structure of  $\tilde{C}(\mathbf{k})$  since, in the on-shell Born approximation, a particle of energy  $E$  probes  $\tilde{C}(\mathbf{k})$  inside the  $\mathbf{k}$ -space sphere of radius  $2k_E$  centered at the origin. In this regime the coherent- and incoherent-speckles are very similar. The most interesting effect appears for  $2k_E\sigma_\perp \gtrsim 3.8$  (i.e.  $E \gtrsim 1.8E_{\sigma_\perp}$ ), when the bumps of  $\tilde{C}(\mathbf{k})$  contribute to scattering and transport. The scattering time  $\tau_{E,\hat{\mathbf{k}}}$  becomes highly anisotropic [see Fig. 6.3(b)] and the orbital dominating  $D_B^X$  is distorted compared to the incoherent case. As a result,  $D_B^X$  is reduced and the corresponding anisotropy factor drops by a factor of  $\simeq 4$ . This effect happens to be strong enough to lead to the inversion of the transport anisotropy and we find  $D_B^X < D_B^Y < D_B^Z$  for  $E \gtrsim 1.8E_{\sigma_\perp}$  [see inset of Fig. 6.6(b)].

### 6.2.3 Localization

**Self-consistent theory: 3D case** – In order to analyze strong localization effects, we now solve the self-consistent equation (5.37) for the 3D case in the long time limit ( $\omega \rightarrow 0$ ). A threshold energy  $E_c$  (mobility edge) appears, solution of  $D_B^{\text{av}}(E_c) \equiv \det\{\mathbf{D}_B(E_c)\}^{1/3} = \hbar/\sqrt{3\pi m}$ .

- For  $E < E_c$ , one finds  $\mathbf{D}_*(\omega, E) \sim 0^+ - i\omega\mathbf{L}_{\text{loc}}^2(E)$  for  $\omega \rightarrow 0^+$ , where  $\mathbf{L}_{\text{loc}}(E)$  is a real positive definite tensor. As in 2D, it characterizes exponential localization within the propagation kernel (2.35) with the anisotropic localization tensor  $\mathbf{L}_{\text{loc}}(E)$ . The localization tensor is diagonal in the same basis as the Boltzmann diffusion tensor  $\mathbf{D}_B$ . Explicitely,

$$L_{\text{loc}}^u = L_{\text{loc}}^{\text{av}} \sqrt{\frac{D_B^u}{D_B^{\text{av}}}}, \quad (6.12)$$

where  $L_{\text{loc}}^{\text{av}} = \det\{\mathbf{L}_{\text{loc}}(E)\}^{1/3}$  is the unique solution of

$$\frac{L_{\text{loc}}^{\text{av}}}{l_B^{\text{av}}} \left[ 1 - \frac{\pi}{3} (k_E l_B^{\text{av}})^2 \right] = \arctan \left( \frac{L_{\text{loc}}^{\text{av}}}{l_B^{\text{av}}} \right). \quad (6.13)$$

- For  $E > E_c$ ,  $\mathbf{D}_*(\omega, E)$  converges to a real definite positive tensor when  $\omega \rightarrow 0$ . It describes anisotropic normal diffusive dynamics, characterized by the propagation kernel (2.33) where  $\mathbf{D}(E)$  is replaced by the quantum-corrected diffusion tensor

$$\mathbf{D}_*(E) \equiv \lim_{\omega \rightarrow 0} \mathbf{D}_*(\omega, E) = \left[ 1 - \frac{\hbar^2}{3\pi m^2 \{D_B^{\text{av}}(E)\}^2} \right] \mathbf{D}_B(E). \quad (6.14)$$

**Single- and orthogonally-crossed speckles** – Figure 6.7 shows the components of  $\mathbf{L}_{\text{loc}}$  (for  $E < E_c$ ) and  $\mathbf{D}_*$  (for  $E > E_c$ ) for the single-, incoherent- and coherent-speckles cases, and for typical parameters of Refs. [18, 19]. As already mentioned in Sec. 5.3.1 the behavior of  $\mathbf{L}_{\text{loc}}$  and  $\mathbf{D}_*$  is completely determined by that of  $\mathbf{D}_B$  in our approach. The anisotropies of  $\mathbf{L}_{\text{loc}}(E)$  are the square roots of those of  $\mathbf{D}_B(E)$  [see Eq. (6.12)] and the anisotropies of  $\mathbf{D}_*(E)$  are the same as those of  $\mathbf{D}_B(E)$  [see Eq. (6.14)]. Therefore, as for  $\mathbf{D}_B$ , we observe that the anisotropy factors of  $\mathbf{L}_{\text{loc}}$  and  $\mathbf{D}_*$  are nearly independent of  $E$ , except for the inversion of anisotropy of the coherent-speckles case. In the single-speckle case we find  $L_{\text{loc}}^z/L_{\text{loc}}^{x,y} \simeq 3.2$  and  $D_*^z/D_*^{x,y} \simeq 10$ . For the incoherent-speckles configuration we find  $L_{\text{loc}}^{X,Z}/L_{\text{loc}}^Y \simeq 1.3$  and

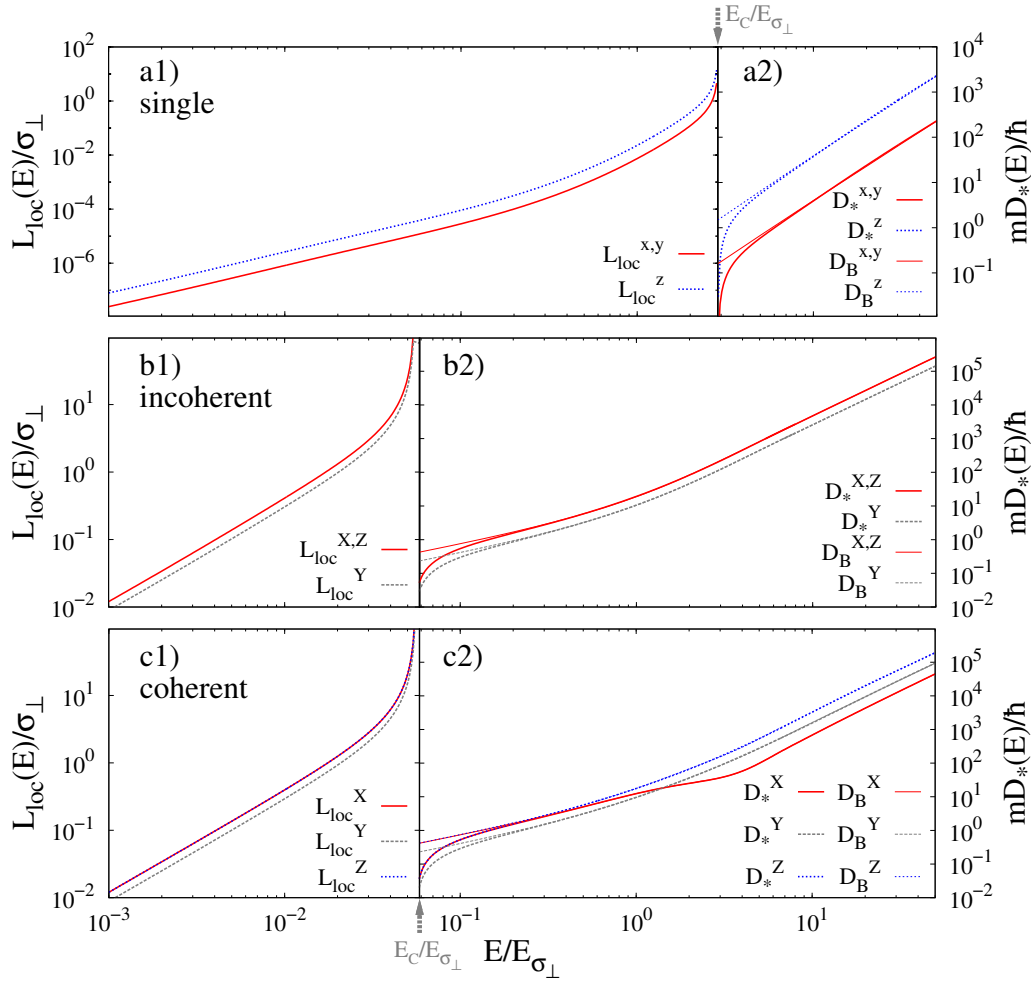


Figure 6.7: Components of the localization tensor  $\mathbf{L}_{loc}$  (left side, for  $E < E_c$ ) and quantum-corrected diffusion tensor  $\mathbf{D}_*$  (right side, for  $E > E_c$ ) in the single- (upper row;  $V_R = 7.1E_{\sigma_{\perp}}$ ), incoherent- (central row;  $V_R = 0.35E_{\sigma_{\perp}}$ ) and coherent- (lower row;  $V_R = 0.35E_{\sigma_{\perp}}$ ) speckles cases. The components of  $\mathbf{D}_B$  are plotted for comparison (thin lines on the right column). We have used the parameters of Refs. [18,19] and Fig. 6.1.

$D_*^{X,Z}/D_*^Y \simeq 1.8$ . For the coherent-speckles configuration we find the same values at low energy, and at high energy we have  $D_*^X/D_*^Y \simeq 0.5$  and  $D_*^Z/D_*^Y \simeq 2.1$ .

Figures 6.7(a1), (b1) and (c1) present the results in the localized regime. At low energy, using the scaling of  $D_B^u(E)$  obtained previously we find  $L_{loc}^u(E) \propto (D_B^u/D_B^{av})^{1/2} E^{3/2}$ . When  $E$  increases,  $L_{loc}^u(E)$  grows and finally diverges at  $E_c$ .

Figures 6.7(a2), (b2) and (c2) present the results in the diffusive regime, the quantum corrections are significant only close to  $E_c$ , while for higher values of  $E$ ,  $\mathbf{D}_*(E) \simeq \mathbf{D}_B(E)$ . Therefore, in the high  $E$  limit we have  $D_*^u(E) \propto (D_B^u/D_B^{av}) E^{5/2}$  as found previously (see Sec. 6.2.2). For the *coherent-speckles* case, we recover the inversion of anisotropy predicted in Sec. 6.2.2. For the parameters of Fig. 6.7(c) it occurs in the diffusion regime. For higher values of  $V_R$ , however, it can be in the localization regime.

## 6.3 About the 3D mobility edge

The self-consistent approach used here is expected to fairly describe the quantum transport properties [16, 42, 153]. It gives some quantitative estimates consistent with numerical calculations [196] and experimental data [19, 30]. It however has important flaws.

On the one hand, in the framework of the self-consistent theory, we find that the localization length diverges as  $L_{\text{loc}}^u(E) \propto (E_c - E)^{-\nu}$  with  $\nu = 1$ . Just above the mobility edge  $E_c$ , the corrected diffusion tensor increases as  $D_*^u(E) \propto (E - E_c)^s$  with  $s = 1$ . Those critical exponents  $\nu$  and  $s$  are consistent with the scaling theory, which predicts  $s = \nu(d - 2)$  (see Sec. 1.2.2 and Refs. [56, 65]) and they are independent of the choice of cut-off that we made. However, it is known from advanced numerical calculations on the disordered tight-binding model of the Anderson model [61, 197] and from experiments [144] that they are not correct and that one should take into account the fractal nature of the wave functions to correctly account for the behaviour at the transition [68].

On the other hand, in the on-shell approximation used so far, one neglects the structure of the spectral function of the particle in the disordered medium, which may renormalize energies. This specific approximation is thus poor to determine values of  $E_c$ .

### 6.3.1 Method

The main flaw of the self-consistent theory is therefore predicting wrong critical exponents at the transition. But, up to now, the prediction of the critical exponents from a theoretical point of view remains an open question. However, the location of the critical region can be fair [42, 196], provided that the spectral function is taken into account.

In order to improve our method, one could in principle use the more sophisticated approaches of Refs. [141, 169, 196] which do incorporate the spectral function. However, since we are interested in continuous disordered potential with fine anisotropic structures, it makes these methods hardly practicable, even numerically. To overcome this issue, we have proposed in Ref. [26] an original method based on the assumption that the leading term missing in the on-shell approximation is the real part of the self energy,

$$\Sigma'(E, \mathbf{k}) \equiv \text{P} \int \frac{d\mathbf{k}'}{(2\pi)^d} \frac{\tilde{C}(\mathbf{k} - \mathbf{k}')}{E - \epsilon_{\mathbf{k}'}} \quad (6.15)$$

where P is the Cauchy principal value, see Eq. (5.3). This term produces a shift of the energy states: A quasi-particle of momentum  $\mathbf{k}$  has an energy  $E$ , solution of  $E - \epsilon(\mathbf{k}) - \Sigma'(E, \mathbf{k}) = 0$ . Here, we incorporate  $\Sigma'(E, \mathbf{k})$  into the theory by averaging, in first approximation, its  $\mathbf{k}$ -angle dependence. It amounts to replace the on-shell prescription by  $\epsilon(\mathbf{k}) = E' \equiv E - \Delta(E)$  with

$$\Delta(E) \equiv \frac{1}{4\pi} \int_{\epsilon(\mathbf{k})=E-\Delta(E)} d\Omega_{\hat{\mathbf{k}}} \Sigma'(E, \mathbf{k}). \quad (6.16)$$

Within this approach, all previous quantities are now regarded as functions of  $E'$  instead of  $E$ . One then has to replace  $E$  by  $E'$  [for  $\mathbf{D}_B(E)$ ,  $\mathbf{D}_*(E)$  and  $\mathbf{L}_{\text{loc}}(E)$ ] in the preceding section, and compute  $E'$  as a function of  $E$  thanks to Eq. (6.16). We will now focus on the 3D mobility edge  $E_c$ , which is the solution of  $E_c - \Delta(E_c) = E'_c$ , where  $E'_c$  is determined using the on-shell approach. The above equation is solved self-consistently for  $E_c$ .

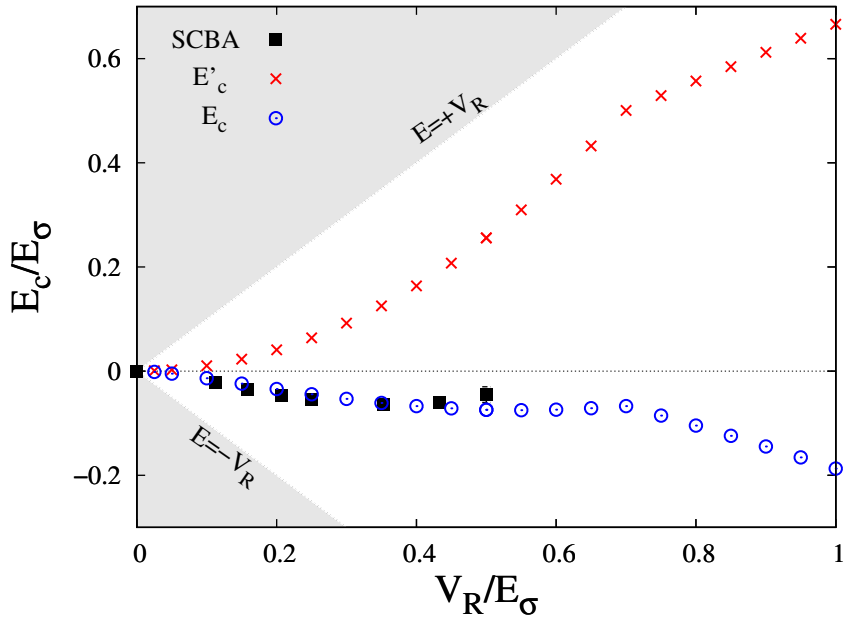


Figure 6.8: Comparison of the mobility edge as calculated with the SCBA method (the full black squares are the results obtained by A. Yedjour and B. van Tiggelen in Ref. [169], that we reproduce here) and our approach [on-shell  $E'_c$  (red crosses) and the corrected  $E_c$  (thick blue circles) mobility edges], for an isotropic 3D speckle potential. When comparing to Fig. 8 of Ref. [169], note that in Ref. [169] the reference of energy is the minimum value of the disorder and we have the correspondence  $E_\xi = E_\sigma/2$  is the correlation energy, and  $U = V_R^2$  is the squared amplitude of the disorder.

### 6.3.2 Three-dimensional isotropic speckle

In order to validate our approach, we first consider 3D correlated disorder with an isotropic correlation function. In this case, the isotropy provides a great simplification, and other methods, such as the self-consistent Born approximation, can be used to calculate the self-energy [141, 169] hence providing a test-bed of our approach. For a speckle disorder obtained inside an integrating sphere lit with a laser beam, the real-space correlation function reads [16, 169]

$$C(\mathbf{r}) = V_R^2 \frac{\sin(|\mathbf{r}|/\sigma)^2}{(|\mathbf{r}|/\sigma)^2}, \quad (6.17)$$

where  $\sigma$  is the correlation length. The associated power spectrum (see appendix C.2) is isotropic and bears the same infrared divergence as the anisotropic models of 3D disorder considered in this work:  $\tilde{C}(\mathbf{k}) \propto 1/|\mathbf{k}|$  when  $|\mathbf{k}| \rightarrow 0$ . It therefore appears to be the closest isotropic model to what we are interested in. Figure 6.8 shows the on-shell mobility edge  $E'_c$  (as calculated in Ref. [16]), the true mobility edge  $E_c$  calculated by our method [i.e. the solution of  $E_c - \Sigma'(E_c, k_{E'_c}) = E'_c$ ], and the mobility edge found using the self-consistent Born approximation in Ref. [169]. As it is clearly seen in Fig. 6.8, the real-part of the self energy plays a very important role for the prediction of the mobility edge<sup>6</sup>. While  $E'_c$  is positive and

6. The slope break on Fig. 6.8 is reminiscent of the slope break of the Boltzmann diffusion coefficient (see Fig. E.2), which comes from the sharp edges of the power spectrum [see Eq. (E.1)].

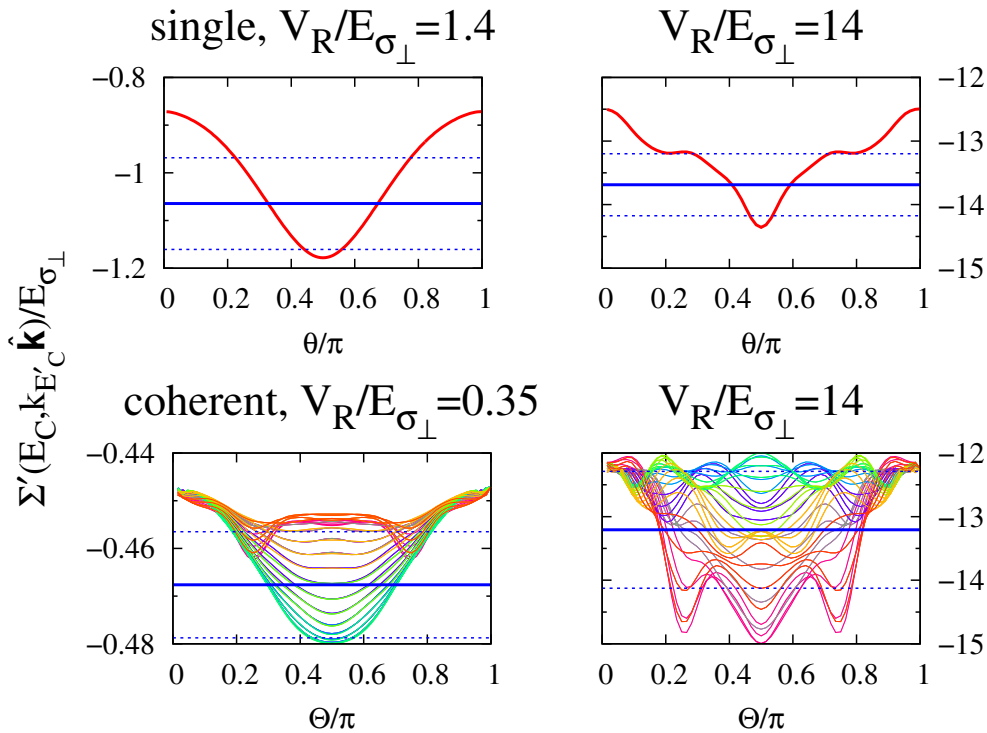


Figure 6.9: Angular dependence of  $\Sigma'(E_c, k_{E_c}, \hat{\mathbf{k}})$  (red points) for the single- [upper row; with  $\theta = (\hat{\mathbf{k}}, \hat{\mathbf{k}}_z)$ ] and the coherent-speckles [lower row; with  $\Theta = (\hat{\mathbf{k}}, \hat{\mathbf{k}}_z)$ ] with the dispersion representing the variations for  $\hat{\mathbf{k}}$  rotating around  $\hat{\mathbf{k}}_z$ , for different values of  $V_R$  (indicated on the figure). The solid blue line is the mean value and the dashed blue lines represent the standard deviation around the mean, both calculated over the  $\hat{\mathbf{k}}$ -solid angle.

increases with energy, the corrected mobility edge  $E_c$  is negative and decreases with  $E$ . Most importantly, we find that our method predicts values of  $E_c$  in very good agreement (within 5 – 7%) with the self-consistent Born method.

### 6.3.3 Three-dimensional disorder with structured correlations

These results support our method to estimate  $E_c$ , which we now apply to anisotropic disorder in the single-speckle, incoherent-speckles and coherent-speckles configurations. The mobility edge is found by searching the root of the self-consistent equation (6.16). Note that the averaging of the angular dependence of  $\Sigma'$  in Eq. (6.16) is justified *a posteriori* by the weak  $\hat{\mathbf{k}}$ -angle variations of  $\Sigma'$  found around its mean value at  $E_c$  (with standard deviations less than 10 – 15%). This is illustrated in Fig. 6.9 which presents the angular variations obtained numerically in the calculation of  $\Delta(E_c)$  in the single and coherent-speckles cases, for typical values of  $V_R$ .

The on-shell ( $E'_c$ ) and corrected ( $E_c$ ) mobility edges for the three anisotropic models of disorder are shown in Fig. 6.10. As for isotropic disorder, it is eye-catching that the shift of the energy states completely changes the behavior of the mobility edge. While  $E'_c$  is positive and increases with  $V_R$ , we find that  $E_c$  is negative and decreases with  $V_R$ . For  $V_R \lesssim E_{\sigma_{\perp}}$ , this behavior is qualitatively similar to that obtained in Fig. 6.8 (see also Ref. [169]). For larger values of  $V_R$ ,  $E_c$  further decreases, consistently with the idea that it should approach

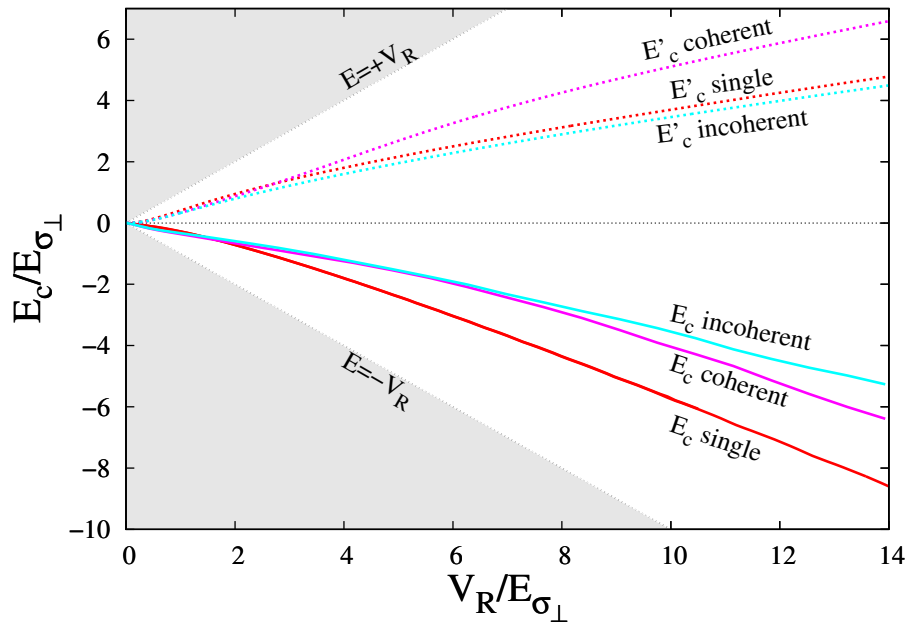


Figure 6.10: On-shell ( $E'_c$ ) [ $E'_c$  is the solution of  $\det\{\mathbf{D}_B(E'_c)\}^{1/3} = \hbar/\sqrt{3\pi m}$  (see Sec. 6.2.3) where  $\mathbf{D}_B$  is the Boltzmann diffusion tensor as calculated in Sec. 6.2.2] and corrected ( $E_c$ ) mobility edges [ $E_c$  is the solution of  $E_c - \Sigma'(E_c, k_{E'_c}) = E'_c$ ] as a function of the disorder amplitude  $V_R$  for the single-, incoherent- and coherent-speckles cases and for the parameters of Fig. 6.1.

the percolation threshold deep in the classical disorder regime ( $V_R \gg E_{\sigma_{\perp}}$ ) [198].

The consequences of these results will be further discussed in the analysis of cold-atom experiments in Chap. 7.

## Conclusion

We have applied the theory for matter wave transport in disordered potentials introduced in Chap. 5 to three-dimensional models of disorder with structured, anisotropic correlations.

We have shown that the latter can induce very rich and counter-intuitive transport and Anderson localization properties, such as the suppression of the white-noise limit (with persistence of the anisotropy down to zero energy) and an inversion of transport anisotropy with energy. We made predictions for the quantum corrected regime in the framework of the self-consistent theory. The on-shell approximation that we used is expected to correctly account for transport properties. However, it is limited in view of locating the critical region, which would necessitate to include the full structure of the spectral function, which is hardly practicable for the models of disorder considered here. Therefore, to estimate a correction to the on-shell mobility edge, we have included the real part of the self-energy by incorporating a disorder-induced shift of the energy states in the theory. We find that the prediction of our method agree very well with a more sophisticated approach, applied earlier to isotropic disorder [169], which validates our approach. It completely changes the behaviour of  $E_c$ , and is consistent with experimental observations in the same configuration [19], as we will see in the following chapter.

The models of disorder we have considered here are directly relevant to recent experiments

on localization of ultra-cold atoms in 3D speckle potentials [18, 19]. In the next chapter we discuss them in view of the theoretical results obtained here. Beyond these direct applications, our results pave the way to further studies of anisotropy effects in coherent transport and Anderson localization. On the one hand, even more complex correlations can be designed in ultracold-atom experiments in 1D, 2D and 3D (see Chap. 8 and Ref. [26]). On the other hand, it would be interesting to explore counter-parts of the discussed effects for waves with different dispersion relations and/or in other kinds of controlled disorder [76, 194, 195].

From a theoretical viewpoint, it would be interesting to go further on several points. First, it would be worth estimating possible corrections of the anisotropy factors in the localized regime, which can be expected to be significant in strongly anisotropic disorder. This would require an approach in which the preservation of the Boltzmann transport anisotropy in the quantum-corrected tensor is not built in the theory, as in the self-consistent approach used here. Second, it would certainly be instructive to go beyond the shifted on-shell approach used here, and incorporate the full structure of the particle spectral function. Both points are fulfilled by the approach of Ref. [169], which can be extended to anisotropic disorder. However, we expect the numerical implementation for 3D anisotropic disorder to be quite heavy.



## Chapter 7

# Matterwaves in three-dimensional speckle potentials: experiment versus theory

### Abstract

The results presented in the preceding chapters are directly relevant to experiments on ultracold-matter waves in optical disorder. In 3D, evidence of Anderson localization in non-interacting Fermi [18] and Bose [19] gases in speckle potentials has been reported. Here we discuss the results of Chap. 6 in view of what has been experimentally achieved. Concerning the experiment by Kondov *et al.* the spatial anisotropy and the position of the mobility edge are available for comparison with our predictions, however no quantitative agreement is found. We however argue that the method used by Kondov *et al.* to determine the position of the mobility edge is questionable. Concerning the experiment by Jendrzejewski *et al.*, we detail the analysis of the experimental results that we carried out. A semi-quantitative agreement is found between theory and experiments. This analysis gives new insight into experimental results, and we suggest routes to address the questions that are left open.

### Résumé

Les résultats présentés dans les chapitres précédents sont directement pertinents pour les expériences avec des ondes de matière ultrafroide dans des désordres optiques. En 3D, des observations de localisation d'Anderson dans des gaz de fermions [18] et de bosons [19] sans interaction dans des potentiels de speckle ont été apportées. Ici nous discutons les résultats du Chap. 6 à la lumière de ce qui a été réalisé expérimentalement. En ce qui concerne l'expérience de Kondov *et al.*, l'anisotropie spatiale et la position du seuil de mobilité peuvent être comparés à nos prédictions, cependant, aucun accord quantitatif n'a pu être trouvé. Nous estimons cependant que la méthode utilisée par Kondov *et al.* pour déterminer la position du seuil de mobilité est contestable. En ce qui concerne l'expérience de Jendrzejewski *et al.*, nous détaillons l'analyse des résultats expérimentaux que nous avons menée. Un accord semi-quantitatif

est trouvé entre la théorie et l'expérience. Cette analyse donne un éclairage nouveau aux résultats expérimentaux, et nous suggérons des pistes pour répondre aux questions laissées ouvertes.

## Introduction: The interplay between theory and experiments

Localization effects show a widely universal behaviour [56], but observable features significantly depend on the details of the system. The field of Anderson localization gained a renewed interest in the context of ultracold matter waves [12,13,21,199,200]. The microscopic parameters in these systems are precisely known and, in many cases, tunable, which paves the way to unprecedented direct comparison between experiments and theory [8,22]. This is a great advantage of ultracold atoms, compared to traditional condensed matter systems. Major advances reported so far are the observation of one-dimensional (1D) Anderson localization of matterwaves [9,10], and studies of the effects of weak [95,96,98,101,103,104,129,181,201,202] and strong [7,127,136,203] interactions in disordered gases. All those studies have much benefited from the close interplay between theory and experiments.

In Chap. 6 we have studied transport and localization properties of matter waves in three models of 3D anisotropic optical speckle potentials, that are relevant to two recent experiments:

- The first one has been carried out in Brian DeMarco’s group from the University of Illinois at Urbana-Champaign (U.S.A.) [18].
- The second one has been carried out in Alain Aspect’s group<sup>1</sup> (team of Philippe Bouyer and Vincent Josse) at Institut d’Optique (France) [19].

The aim of this chapter is to discuss the observations of these two experiments in view of our theoretical work, reported in Chap. 6. This work is actually a wonderful example of the interplay of experiments and theory, which is at the very heart of current research on quantum simulators based on ultracold atoms [120,121]. On one hand, we collaborated with the experimental group at Institut d’Optique on Ref. [19]. The comparison between experiments and theory showed a good agreement on the diffusive tensor and the overall density profile. The analysis of the localized fraction however showed the necessity to extend existing approaches, which stimulated our work reported in Ref. [25] and Sec. 6.3. On the other hand, this theoretical work shows interesting anisotropy effects beyond what was observed experimentally, and provides the first estimate for the mobility edge in those correlated disordered potentials, which could be tested in more elaborate experiments. Both should stimulate further experimental and theoretical works.

When comparing experiments with theory in the context of ultra-cold atoms, the first question is to determine the initial joint position-energy distribution  $\mathcal{D}_0(\mathbf{r}', E)$ ,

$$\mathcal{D}_0(\mathbf{r}', E) = \int \frac{d\mathbf{k}'}{(2\pi)^d} A(E, \mathbf{k}') W_0(\mathbf{r}', \mathbf{k}'), \quad (7.1)$$

where  $W_0(\mathbf{r}', \mathbf{k}')$  is the initial Wigner function [see Sec. 2.3 and Eq. (2.31)]. Indeed, in the preceding chapter, we have computed the probability of quantum transport for matter waves with a given energy  $E$ ,  $P(\mathbf{R}, t|E)$ . In the case of ultracold atoms the transport properties can be probed by imaging the atoms in-situ, i.e. the direct observable is the density distribution

---

1. For details of the experimental setup and measurements refer to the PhD thesis of Fred Jendrzejewski [204].

of the atoms<sup>2</sup>  $n(\mathbf{r}, t)$ . As for the 1D case analyzed previously (see Sec. 4) the two above quantities are related through the relation

$$\bar{n}(\mathbf{r}, t) = \int \frac{dE}{2\pi} \int d\mathbf{r}' \mathcal{D}_0(\mathbf{r}', E) P(\mathbf{r} - \mathbf{r}', t - t_0 | E) \quad (7.2)$$

In the following, in both cases we are analyzing, the initial distribution is assumed to be decoupled:  $\mathcal{D}_0(\mathbf{r}', E) \simeq n_0(\mathbf{r}') \times \mathcal{D}_E(E)$  (see below). The key issue will then be to determine the energy distribution of the atoms in the disorder,  $\mathcal{D}_E(E)$ . The latter is a difficult task, in particular because it depends on the exact experimental sequence, and may be altered by heating processes or any experimental imperfection. As discussed below, the poor knowledge of  $\mathcal{D}_E(E)$  is the present major bottleneck to determine experimentally the mobility edge.

## 7.1 Urbana-Champaign experiment

In Ref. [18], evidence of Anderson localization of ultracold gases of fermionic spin-polarized <sup>40</sup>K atoms, in a *single-speckle* configuration<sup>3</sup> is reported (see Sec. 6.1.1 for the configuration). The atoms are initially confined in a harmonic trap and the disorder is slowly turned on. When the disorder amplitude has reached its nominal value, the trap is suddenly switched off, and the atoms expand in the disorder. Initial temperatures are of the order, or higher, than the Fermi temperature of the gas, such that the atoms approximately form a thermal gas at temperature  $T$ . The gas expansion is probed by observing the evolution of the atomic density of the gas. The observed behaviour of the gas then suggest a two-component density profile, with:

- A mobile component which expands ballistically, with a larger velocity than the thermal gas expanding in free-space, and rapidly leaves the experimentally-observable window;
- A localized component formed by the atoms that stay immobile in the duration of the experiment.

**Anisotropy of the localized profile** – As the gas is thermal, one can decouple the position and energy of the atoms initially. In the single-speckle case (see Secs. 6.2.2 and 6.2.3), we found almost energy-independent anisotropy factors ( $D_*^z/D_*^{x,y} \simeq 10$  and  $L_{\text{loc}}^z/L_{\text{loc}}^{x,y} \simeq 3.2$ ), so that the energy distribution is not very important for the analysis of the anisotropy. The initial density profile is however important. Indeed, in Ref. [18] [see Fig. 2 therein, reproduced here in Fig. (7.1)] the localized profile in the transverse directions ( $x$  and  $y$ ) is a replica of the initial profile, indicating that the localization lengths in these directions are of the order or smaller, than the initial size and the imaging resolution. In the longitudinal direction  $z$ , the profile was fitted to an exponential, which suggests that the localization profile (somehow averaged over the energy) is observable. Although no precise value of the anisotropy of the localized profile has been extracted, the experimental data thus indicate an anisotropy significantly larger than

---

2. The atoms can also be imaged after a time-of-flight, which gives access to their momentum distribution  $\mathcal{D}_k(\mathbf{k}, t)$ .

3. The setup used to create the speckle in Ref. [18] is that of the single-speckle, but the correlation function in real space is fitted by a Gaussian function in all directions, which doesn't directly give access to  $\sigma_{\parallel}$ . However, the authors find the geometrical anisotropy factor  $\zeta_z/\zeta_{x,y} \simeq 1600 \text{ nm}/270 \text{ nm} = 5.9$ , which is consistent with  $\sigma_{\parallel}/\sigma_{\perp} \simeq 5.8$ , as used in this Chapter.

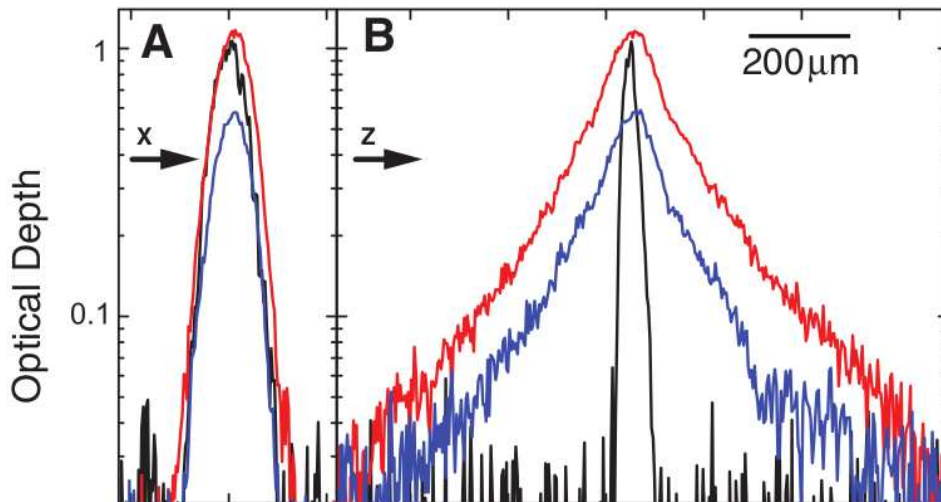


Figure 7.1: Urbana-Champaign experiment. Localization of a gas of initial temperature  $T = 390$  nK with disorder amplitude  $V_R = 600$  nK  $\times k_B$ . The figure shows the initial density profile (black lines) and the localized density profiles after 40 ms (red lines) and 140 ms (blue lines) along the x (A) and z (B) directions. Figure extracted from Ref. [18].

3.2. The authors of Ref. [18] actually indicate that the data is consistent with an anisotropy of the localization length greater than 36. Such a strong anisotropy is surprising in view of our analysis. It is larger than the geometrical anisotropy, which is expected in the classical disorder regime, and even larger than the squared geometrical anisotropy, which would be expected in a simple brownian motion when a particle jumps in a random direction every time  $\tau$  on a stretched lattice. A possible source of discrepancy may be that the correlation function we use is not the exact one of the experimental setup. Although it was not measured with sufficient accuracy, it may be compatible with a 3D Gaussian with anisotropy  $\zeta_z/\zeta_{x,y} \simeq 5.9$  [205]. We have also computed the Boltzmann and localization tensors in this case. The results are shown in appendix E.2. The overall behaviour is qualitatively different (i.e. this model has a white-noise limit, and the anisotropies are not independent of the energy). However, we find  $1 < L_{loc}^z/L_{loc}^{x,y} \lesssim 4.5$ , which is not consistent with the experimental observations either. Further analysis would be required to clarify the origin of such a discrepancy. In this respect, the analysis of a diffusive part (which is apparently absent in Ref. [18]) would be of outmost interest.

**Mobility edge** – In Urbana-Champaign experiment, the fraction of the atoms that remain localized is measured for different initial temperatures of the gas. It directly gives the localized fraction  $f_{loc}$ . Solving for  $E_c$  the equation

$$f_{loc} = \int_{-\infty}^{E_c} \frac{dE}{2\pi} \mathcal{D}_E(E) \quad (7.3)$$

can then give access to the mobility edge  $E_c$ , provided that one knows the energy distribution of the atoms in the disorder. To determine it, Kondov *et al.* measure the momentum distribution of the gas in the disorder  $\mathcal{D}_k(\mathbf{k})$ . It is found that it does not significantly differ from that of the initial thermal gas. In principle, the energy distribution can be determined via Eq. (2.18). In the absence of a direct measurement of  $A(E, \mathbf{k})$ , Kondov *et al.* approximate it

by its disorder-free value:

$$A_0(E, \mathbf{k}) = 2\pi\delta[E - \epsilon(\mathbf{k})], \quad (7.4)$$

which may be valid for weak disorder if the energy reference is chosen such that  $\bar{V} = 0$ . One then finds  $\mathcal{D}_E(E) \simeq 2\pi N_0(E)\mathcal{D}_k(k_E)$ , where

$$\mathcal{D}_k(k) = \left(\frac{2\pi\hbar^2}{mk_B T}\right)^{3/2} e^{-\frac{\hbar^2 k^2}{2mk_B T}} \quad (7.5)$$

is the Maxwell-Boltzmann momentum distribution of a gas at temperature  $T$ , with  $k_B$  the Boltzmann constant. The inferred position of the mobility edge [using Eq. (7.3)] as a function of the disorder amplitude is presented in Fig. 3(B) of Ref. [18]: They find a positive mobility edge (i.e. above the disorder mean-value). It significantly differs from our calculations (see solid red curve in Fig. 6.10), which predict a negative mobility edge. For example, at  $V_R = 600 \text{ nK} \times k_B \simeq 7.1E_{\sigma_\perp}$ , we find  $E_c \simeq -300 \text{ nK} \times k_B$ , while  $+900 \text{ nK} \times k_B$  is measured. We argue that the experimental method to infer  $E_c$  from the localized fraction is not reliable. Indeed, contrary to one dimension where localization is observed in the weak disorder regime, and the approximation (7.4) is valid for several orders of magnitude for the density profiles (see Chap. 4), localization in 3D occurs for strong disorder in a regime where the approximation (7.4) is not valid. Neglecting the disorder-induced distortion of the energy distribution does not hold because the latter is, in particular, necessary to account for negative energy states (i.e. below the disorder mean value). The full spectral function should therefore be taken into account to compare with our theoretical estimate.

## 7.2 Palaiseau experiment

In Ref. [19] observation of localization of a Bose-Einstein condensate of  $^{87}\text{Rb}$  atoms in a *coherent-speckles* field is reported (see Sec. 6.1.2 for the configuration). In this experiment the atomic gas (of chemical potential  $\mu$ ) is initially confined in a shallow trap. The scenario is then the straightforward extension to 3D of that discussed in 1D in Sec. 4. The trap is first switched off, and the atoms are let to expand freely, here suspended against gravity. When the density is low-enough – so that the energy associated to inter-atomic interactions is negligible compared to the amplitude of the disorder to come – the speckle potential is abruptly switched on at time  $t_0$ .

**Position-energy distribution** – During the free expansion stage, the interaction energy is converted into kinetic energy [178, 179], and, at time  $t_0$ , the momentum distribution of the atoms extends from  $k = 0$  to  $k \simeq k_\mu = \sqrt{2m\mu}/\hbar$ . When switching on the disorder, the parameters are such that  $\mu \ll V_R$ , therefore one can consider that the atoms all have  $k \simeq 0$  initially. The initial joint position-energy density is then decoupled and reads  $\mathcal{D}_0(\mathbf{r}', E) \simeq n_0(\mathbf{r}') \times A(E, \mathbf{k} = 0)$ .

To carry through the analysis, the spectral function at  $\mathbf{k} = 0$  is estimated numerically thanks to direct diagonalizations of the Hamiltonian  $H = -\hbar^2\nabla^2/2m + V(\mathbf{r})$  [see definition of  $A$  in Eq. (2.13)] for different realizations of the disorder  $V(\mathbf{r})$ . One has  $A(E, \mathbf{k} = 0) = 2\pi\sum_n \delta(E - E_n)|\psi_n(\mathbf{k} = 0)|^2$ , where  $\psi_n$  is the eigenfunction of  $H$  associated to the eigenvalue  $E_n$ . The numerical results are obtained in a box of linear length  $\sim 15\lambda_L$  and of grid step

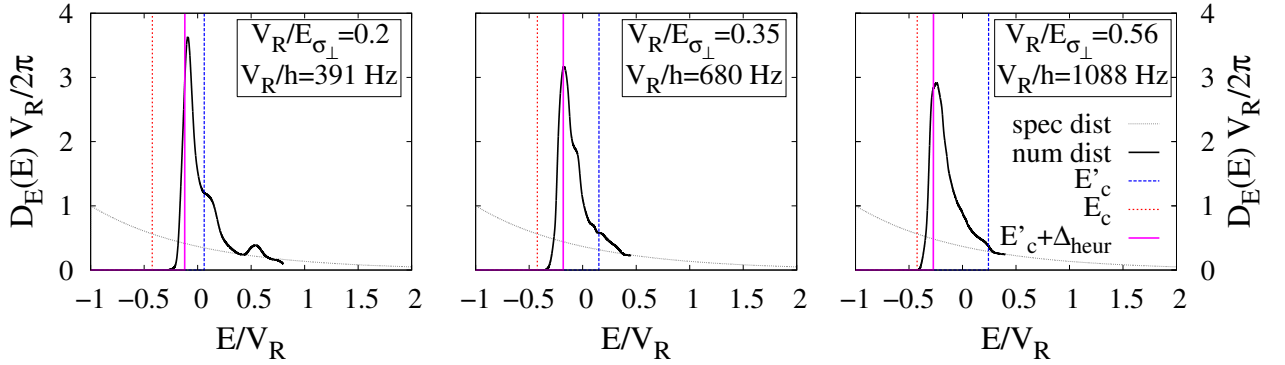


Figure 7.2: Energy distributions estimated numerically (solid black lines) for the Palaiseau experiment, together with distributions of the potential values  $V$  (stippled grey line) [see Eqs. (3.10) and (3.26)] and positions of the on-shell mobility edge  $E'_c$  (dashed blue line), the shifted mobility edge  $E_c$  (dotted red line) and  $E'_c - \Delta_{\text{heur}}$  (solid pink line).

$\sim 0.2\lambda_L$ . The disorder average is performed over 100 numerical realizations of  $V(\mathbf{r})$  in the coherent-speckles configuration. Some of the energy distributions thus obtained are presented in Fig. 7.2 (see solid black lines). We observe that the energy distribution is strongly peaked, roughly around the average value of the disorder,  $\bar{V} = 0$ . Therefore, a significant fraction of the atoms is predicted to have negative energy (i.e. below the disorder mean value). Finally, the experimental initial density distribution is fitted by a Thomas-Fermi profile for a Bose-Einstein condensate in an isotropic Gaussian trap<sup>4</sup> with thermal wings, giving the initial  $n_0(\mathbf{r}')$ .

### 7.2.1 Two-component density profiles

The expansion of the atoms in the disorder is first analyzed phenomenologically. In the experiment, one can identify a localized component, which is the replica of the initial density profile  $n_0(\mathbf{r}')$ , and an expanding diffusive component, consistently with the localization scenario expected in 3D. One can then make the ansatz

$$n(\mathbf{r}, t) = f_{\text{loc}} n_0(\mathbf{r}) + n_{\text{D}}(\mathbf{r}, t), \quad (7.6)$$

where  $f_{\text{loc}}$  is the localized fraction,  $n_0(\mathbf{r})$  is the initial density and  $n_{\text{D}}(\mathbf{r}, t)$  is the time-dependent density of the diffusive part. In this experiment, both localized and diffusive components are observed as we discuss now.

**Localized fraction** – The localized fraction can be extracted from the experimental observations by monitoring the gas column density<sup>5</sup>  $\hat{n}(y, z, t) = \int dx n(\mathbf{r}, t)$  at the center. In the presence of a localized fraction, it should asymptotically tend to the finite value  $f_{\text{loc}} \hat{n}_0(0, 0)$ , giving access to  $f_{\text{loc}}$  from the knowledge of the initial density at the center  $\hat{n}_0(0, 0)$ . Moreover, if the initial size of the cloud can be neglected, one expects the dynamics  $n_{\text{D}}^{\circ}(0, 0, t) \propto (t - t_0)^{-1}$ ,

4. As visible in Fig. 7.6, the initial trap is slightly anisotropic. However, taking the anisotropy of the initial profile into account doesn't significantly modify the results of the following.

5. Due to the absorption imaging technique, the experimental profiles are integrated along the  $x$  direction.

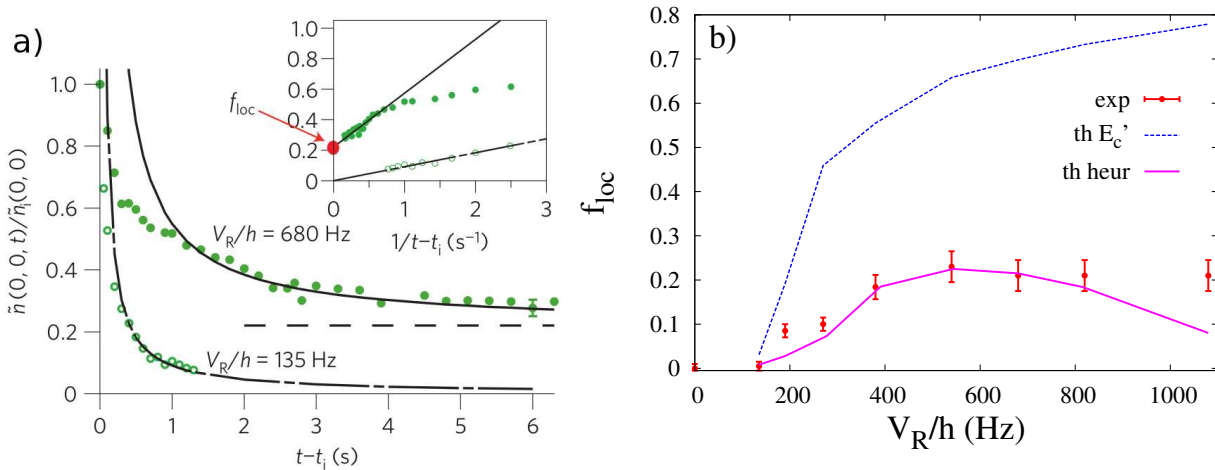


Figure 7.3: Palaiseau experiment. (a) Evolution of the column density at the centre of the atomic cloud for  $V_R/h = 135$  Hz and 680 Hz, and determination of its asymptotic value, yielding the localized fraction  $f_{loc}$  (asymptotic value of the fitted black solid line, see text). Figure extracted from Ref. [19]. (b) Localized fraction versus disorder amplitude. The red points give the experimental localized fraction  $f_{loc}$  determined from the decay of the central density. The error bars reflect the uncertainty on each individual fit and the fluctuations from shot to shot. The dashed blue line shows the results of the theoretical calculation, using the on-shell mobility edge  $E'_c$ . The solid pink line shows the results of the theoretical calculation, including the heuristic relative energy shift explained in the text.

which is reminiscent of the behaviour of the diffusive part<sup>6</sup>. More precisely, the localized fraction can be determined by fitting  $\hat{n}(0,0,t)/\hat{n}_0(0,0)$  by  $f_{loc} + B/(t - t_0)$  with  $f_{loc}$  and  $B$  as fitting parameters. This procedure is presented in Fig. 7.3(a) for two values of  $V_R$ , and the extracted values<sup>7</sup> versus the amplitude of the disorder  $V_R$  are reported in Fig. 7.3(b) (see red dots). As shown in Fig. 7.3(a) [see also the inset], the observed behaviour of  $\hat{n}(0,0,t)$  is consistent with this behaviour at large times.

In order to compare experiment and theory, we started by calculating the localized fraction with

$$f'_{loc} = \int_{-\infty}^{E'_c} \frac{dE}{2\pi} \mathcal{D}_E(E) \quad (7.7)$$

where  $E'_c$  is the on-shell mobility edge (see Sec. 6.3 and Fig. 6.10) and  $\mathcal{D}_E(E)$  is computed numerically (see Fig. 7.2). These predictions are presented in Fig. 7.3(b) as a function of  $V_R$  (see dashed blue line). They significantly overestimate the localized fraction (by a factor 3 to 4)<sup>8</sup>.

Nevertheless, this calculation has several sources of uncertainty. From an experimental point of view the parameters of the Hamiltonian are not known exactly. Some undesired heating effects can occur during the experiment, and in particular when the disorder is abruptly switched on. For this reason, a direct experimental measure of  $\mathcal{D}_E(E)$  would be needed. The numerical estimation of  $A(E, \mathbf{k} = 0)$  is probably reasonable because the size of the box, and

6. The density at the origin is expected to decrease as  $n_D(\mathbf{r} = 0, t) \propto (t - t_0)^{-3/2}$  [see Eq. (2.33)], and the column integral gives the  $(t - t_0)^{-1}$  behaviour.

7. If the initial width of the density profile is not strictly negligible, the decrease is expected to be slower and the localized fraction might be slightly over-estimated by the  $(t - t_0)^{-1}$  fit.

8. As could be expected from the conclusions of Sec. 6.3.

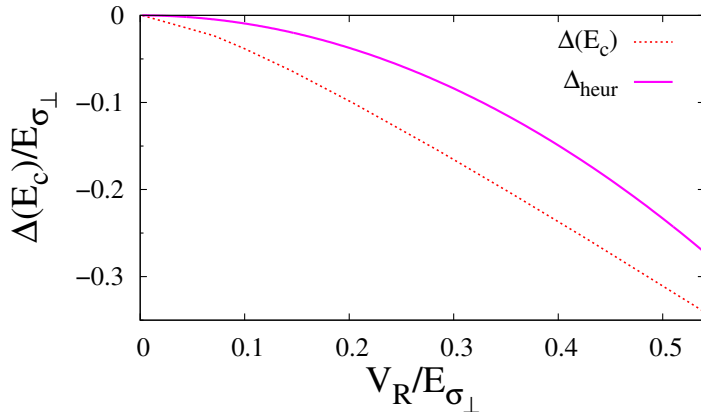


Figure 7.4: Comparison between the theoretical shift  $[\Delta(E_c)$ , dotted red line] as calculated in Sec. 6.3 and the heuristic shift ( $\Delta_{\text{heur}}$ , solid pink line) introduced in the analysis of the experiment of Ref. [19].

the grid step are properly chosen compared to  $\lambda_L$  and  $\sigma_R$  (see above). However our limited computational facilities didn't enable us to check those calculations by further decreasing the space step and increasing the size of the box. From a theoretical point of view, the self-consistent computation of the mobility edge is approximate, and in particular, as we have seen, the on-shell approximation does not correctly predict the location of the critical region.

At the time of the analysis, we knew that the on-shell approximation was not accurate for giving the position of the mobility edge, but we had not calculated the correction introduced in Sec. 6.3 yet. As discussed above, another major issue was that the energy distribution  $\mathcal{D}_E(E)$  is not measured directly in the experiment. As shown on Fig. 7.2 the estimated energy distributions are strongly peaked at negative energy, and therefore a small change in the position of  $E_c$ , or a small discrepancy with the energy distribution actually realized in the experiment can significantly change the predicted localized fraction.

In order to take all those remarks into account, we have introduced one free parameter in the analysis of the experiment. The effect of the above remarks on the mobility edge is a pure shift,  $E_c - E'_c$ , while their effect on the energy distribution is most likely a broadening, in the eventuality of heating effects. In order to introduce a single free parameter, we have chosen to introduce a relative shift between  $\mathcal{D}_E(E)$  and  $E'_c$ . Here we want to point out that, even if the shift is inspired by the effect of the theoretical uncertainties on  $E'_c$ , it cannot be attributed to this sole effect, as the uncertainty on  $\mathcal{D}_E(E)$  will also contribute. In the experiment, the 'origin' of the shift, i.e. determining if it accounts for the uncertainty on  $\mathcal{D}_E(E)$  or on the mobility edge, cannot be specified; and it is probably an interplay between the two. In order to make this point clear, below we write equations in the two forms.

More precisely, we have looked for a simple form of this shift, and we found that the best is a relative shift of the form  $\Delta_{\text{heur}} \propto V_R^2$ , where the proportionality coefficient is determined by adjusting the theoretical localized fractions,

$$f_{\text{loc}} = \int_{-\infty}^{E'_c + \Delta_{\text{heur}}} \frac{dE}{2\pi} \mathcal{D}_E(E) = \int_{-\infty}^{E'_c} \frac{dE}{2\pi} \mathcal{D}_E(E + \Delta_{\text{heur}}), \quad (7.8)$$

to the experimental points. We found that  $\Delta_{\text{heur}} = -0.92V_R^2/E_{\sigma_\perp}$  leads to a fair agreement with the experimental results [see solid pink line in Fig. 7.3(b)], except for the lowest and highest values of  $V_R$ . This fair agreement is not surprising in itself, because we have ensured it. However, as we will see below, the introduction of the shift is consistent with the other measurements.

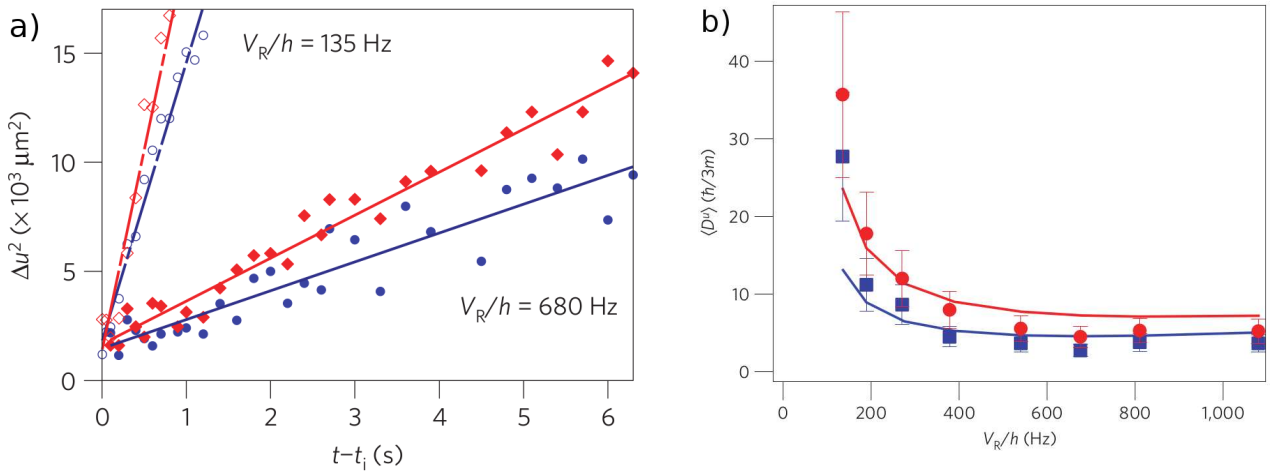


Figure 7.5: Palaiseau experiment. (a) Time evolution of the mean squared widths along  $y$  (blue) and  $z$  (red) of the column density profiles  $\hat{n}(y, z, t)$  for two values of the disorder amplitude  $V_R$  (indicated on the figure), and their fits by straight lines, yielding the diffusion coefficients along  $y$  and  $z$  [see (b)]. (b) Diffusion coefficient versus disorder amplitude. The points indicate the values of the diffusion coefficients,  $\langle D^u \rangle$ , along the  $u = y, z$  axes (blue and red points respectively), measured by the fits presented in (a). The error bars reflect the effect of background noise on the mean squared widths. The solid blue ( $y$ ) and red ( $z$ ) lines show the results of the theoretical calculation of these coefficients, using the heuristic energy shift  $\Delta_{\text{heur}}$ . Figures reproduced from Ref. [19].

It is finally very interesting to compare this heuristic shift  $\Delta_{\text{heur}}$  with the theoretical shift  $\Delta(E_c)$  calculated in Sec. 6.3. Both are shown in Fig. 7.4. We find that they are of the same order of magnitude (e.g. for  $V_R = h \times 680$  Hz  $\simeq 0.35E_{\sigma_{\perp}}$ , we find  $\Delta(E_c)/h = -390$  Hz and the heuristic shift is  $-225$  Hz). It is thus tempting to conclude that the calculated shift is relevant and explains at least partially the origin of the heuristic shift introduced in the analysis of the experiment [19]. A precise test of the theory of Sec. 6.3 would however require a reliable determination of the energy distribution in ultracold-atom experiments, which is not available so far.

**Diffusion coefficients** – The mobile component  $n_D(\mathbf{r}, t)$  is monitored as a function of time. Its evolution shows a clear diffusive behaviour, i.e. its mean squared widths along directions  $u = y, z$  increase linearly with time:

$$\Delta u(t)^2 = \Delta u(t_0)^2 + 2\langle D^u \rangle(t - t_0), \quad (7.9)$$

as is shown on Fig. 7.5(a). The average diffusion coefficients can be fitted, with results displayed in Fig. 7.5(b), together with the results of our theoretical computations (see Sec. 6.2.3). For consistency in these calculations we use the same energy shift introduced in the calculation of the localized fraction, i.e. we calculate

$$\begin{aligned} \langle D_*^u \rangle &= \int_{E'_c}^{\infty} \frac{dE}{2\pi} \mathcal{D}_E(E + \Delta_{\text{heur}}) \hat{\mathbf{u}} \cdot \mathbf{D}_*(E) \cdot \hat{\mathbf{u}} \\ &= \int_{E'_c + \Delta_{\text{heur}}}^{\infty} \frac{dE}{2\pi} \mathcal{D}_E(E) \hat{\mathbf{u}} \cdot \mathbf{D}_*(E - \Delta_{\text{heur}}) \cdot \hat{\mathbf{u}} \end{aligned} \quad (7.10)$$

where  $\hat{\mathbf{u}}$  is the unit vector pointing along the  $u \in \{y, z\}$  axis. As shown in Fig. 7.5(b), we then find a fair agreement between the results of the calculations and the experimental data. In particular, the anisotropy of the diffusion tensor is well reproduced. Note that the theoretical calculations do not involve any free parameter, apart from the heuristic energy shift discussed above. If the heuristic shift is not included in Eq. (7.10), the theoretical calculations shown in Fig. 7.5(b) are not modified a lot, however, the agreement with experimental data is not as good as here.

**Density profiles** – Let us finally discuss the behaviour of the integrated density profiles. Figure 7.6 shows the comparison between the theoretical and experimental density profiles, at various times  $t$ , in the case  $V_R/h = 680$  Hz. The theoretical profiles represent Eq. (7.2), where  $\mathcal{D}_0(\mathbf{r}', E) \simeq n_0(\mathbf{r}') \times A(E, \mathbf{k} = 0)$  is calculated as explained above [ $n_0(\mathbf{r}')$  is fitted to the initial profile and  $A(E, \mathbf{k} = 0)$  is estimated numerically] and  $P(\mathbf{r}, t|E)$  is computed using Eqs. (2.33) and (2.35) and the results of Sec. 6.2.3. The heuristic shift is also taken into account:

$$\begin{aligned} \bar{n}(\mathbf{r}, t) &= \int \frac{dE}{2\pi} \int d\mathbf{r}' n_0(\mathbf{r}') \mathcal{D}_E(E + \Delta_{\text{heur}}) P(\mathbf{r} - \mathbf{r}', t - t_0|E) \\ &= \int \frac{dE}{2\pi} \int d\mathbf{r}' n_0(\mathbf{r}') \mathcal{D}_E(E) P(\mathbf{r} - \mathbf{r}', t - t_0|E - \Delta_{\text{heur}}). \end{aligned} \quad (7.11)$$

The localized part (red area) is then given by

$$\begin{aligned} n_{\text{loc}}(\mathbf{r}) &= \int_{-\infty}^{E'_c} \frac{dE}{2\pi} \int d\mathbf{r}' n_0(\mathbf{r}') \mathcal{D}_E(E + \Delta_{\text{heur}}) P(\mathbf{r} - \mathbf{r}', t \rightarrow \infty|E) \\ &= \int_{-\infty}^{E'_c + \Delta_{\text{heur}}} \frac{dE}{2\pi} \int d\mathbf{r}' n_0(\mathbf{r}') \mathcal{D}_E(E) P(\mathbf{r} - \mathbf{r}', t \rightarrow \infty|E - \Delta_{\text{heur}}) \end{aligned} \quad (7.12)$$

where the probability of quantum diffusion is given by Eq. (2.35). The localization lengths [i.e. the components of  $\mathbf{L}_{\text{loc}}(E)$ ] are found to be much shorter than the width of  $n_0(\mathbf{r})$ . Although the localization lengths diverges below the mobility edge, the critical region is quite narrow in energy, and it concerns very few atoms in this experiment (typically less than 2%). The approximation  $n_{\text{loc}}(\mathbf{r}) \simeq f_{\text{loc}} n_0(\mathbf{r})$  where  $f_{\text{loc}}$  is the localized fraction measured experimentally<sup>9</sup>, is thus good for the whole range of Fig. 7.6. The evolving diffusive part is calculated in the same manner, with the quantum corrected diffusion tensor  $\mathbf{D}_*(E)$  of Sec. 6.2.3:

$$\begin{aligned} n_{\text{D}}(\mathbf{r}, t) &= \int_{E'_c}^{\infty} \frac{dE}{2\pi} \int d\mathbf{r}' n_0(\mathbf{r}') \mathcal{D}_E(E + \Delta_{\text{heur}}) P(\mathbf{r} - \mathbf{r}', t \rightarrow \infty|E) \\ &= \int_{E'_c + \Delta_{\text{heur}}}^{\infty} \frac{dE}{2\pi} \int d\mathbf{r}' n_0(\mathbf{r}') \mathcal{D}_E(E) P(\mathbf{r} - \mathbf{r}', t \rightarrow \infty|E - \Delta_{\text{heur}}), \end{aligned} \quad (7.13)$$

with the probability of quantum diffusion given by Eq. (2.33). The green area in Fig. 7.6 represents the diffusive part and the green line is the sum of the localized and diffusive parts. The fair agreement with experimental profiles at various delays shows the consistency of our theoretical analysis (including the heuristic energy shift) with the experimental observations<sup>10</sup>.

9. As shown on Fig. 7.3(b), the measured localized fraction, and the one calculated with the heuristic shift are almost equal at  $V_R = 680 \text{ Hz} \times h$ .

10. The theoretical profile is slightly above the experimental one at the center, which might indicate that the localized fraction extracted as explained above is slightly over-estimated.

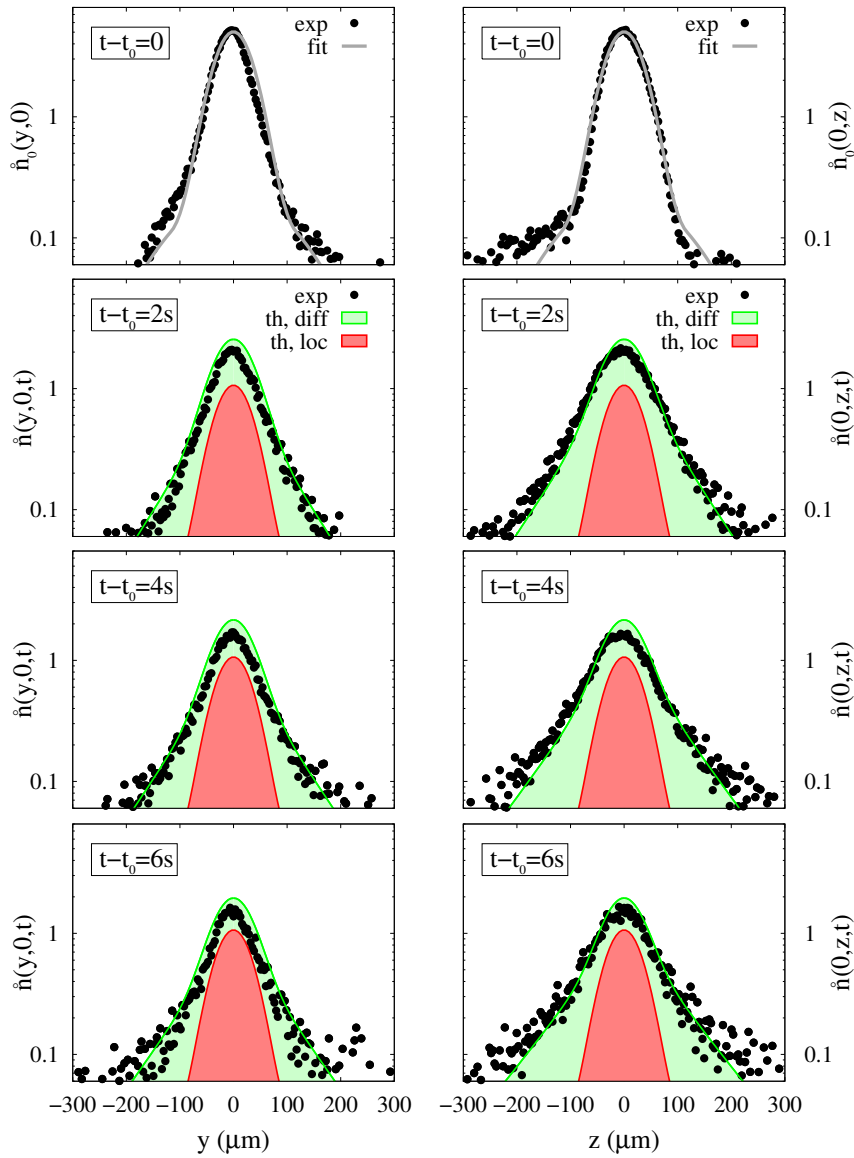


Figure 7.6: Palaiseau experiment. Evolution of the density profiles in a strong disorder ( $V_R/h = 680$  Hz): experiment versus quantum transport and Anderson localization theory including the heuristic shift. The figure shows cuts of the column density profiles along  $y$  [ $\hat{n}_0(y, 0, t)$ , left column] and  $z$  [ $\hat{n}_0(0, z, t)$ , right column], at various delays after application of the disorder. The solid black points are the experimental data. In the top panels (corresponding to the initial time  $t = t_0$  when the disorder is switched on), the solid gray lines are fits to the data. In all other panels (corresponding to  $t > t_0$ ), the solid red lines are these fitted initial profiles multiplied by the localized fraction experimentally measured,  $f_{\text{loc}} = 0.22$ , hence describing the localized part. Adding the theoretically determined diffusive parts at various delays, we obtain the green profiles, which reproduce well the experimental profiles.

### 7.2.2 Evidence of Anderson localization?

The scenario observed in the experiment is the one expected for Anderson localization, and the measured localized fractions, diffusive constants and density profiles are consistent with self-consistent calculations, with only one free parameter in the theory. It is natural to

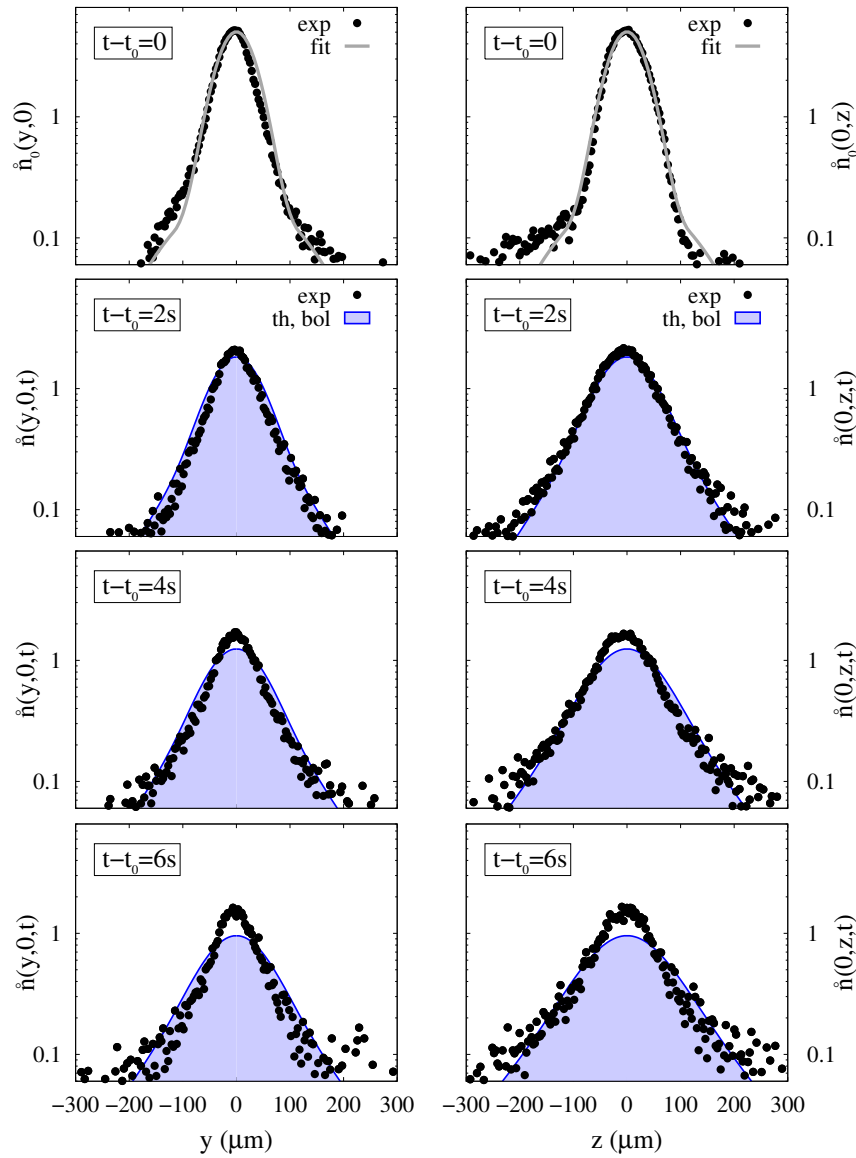


Figure 7.7: Palaiseau experiment. Evolution of the density profiles in a strong disorder ( $V_R/h = 680$  Hz): experiment versus classical transport theory. The figure shows cuts of the column density profiles along  $y$  [ $\hat{n}_0(y, 0, t)$ , left column] and  $z$  [ $\hat{n}_0(0, z, t)$ , right column], at various delays after application of the disorder. The solid black points are the experimental data. In the top panels (corresponding to the initial time  $t = t_0$  when the disorder is switched on), the solid gray lines are fits to the data. In all other panels (corresponding to  $t > t_0$ ), the solid blue lines are the profiles determined theoretically with a full Boltzmann description in Eq. (7.11) at various delays.

ask: Is it really Anderson localization which is observed? To answer that question one can look for simpler scenarios that could reproduce the observations as well.

**Boltzmann diffusion** – For typical values of the energy in the experiment (e.g. around the mobility edge) the Boltzmann diffusion coefficients  $D_B^u$  are small (typically  $\hbar/\sqrt{3\pi m}$ ), and one can wonder if the 'localized part' is not simply a very slow Boltzmann diffusion. We have

considered a full description with Boltzmann diffusion:

$$\begin{aligned}\bar{n}(\mathbf{r}, t) &= \int \frac{dE}{2\pi} \int d\mathbf{r}' n_0(\mathbf{r}') \mathcal{D}_E(E + \Delta_{\text{heur}}) \frac{e^{-[\mathbf{r}-\mathbf{r}'] \cdot \mathbf{D}_B^{-1}(E) \cdot [\mathbf{r}-\mathbf{r}']/4t}}{\sqrt{(4\pi t)^d \det \{\mathbf{D}_B(E)\}}} \\ &= \int \frac{dE}{2\pi} \int d\mathbf{r}' n_0(\mathbf{r}') \mathcal{D}_E(E) \frac{e^{-[\mathbf{r}-\mathbf{r}'] \cdot \mathbf{D}_B^{-1}(E - \Delta_{\text{heur}}) \cdot [\mathbf{r}-\mathbf{r}']/4t}}{\sqrt{(4\pi t)^d \det \{\mathbf{D}_B(E - \Delta_{\text{heur}})\}}}\end{aligned}\quad (7.14)$$

at all energies, which is presented in Fig. 7.7<sup>11</sup>. It gives much less consistent shapes and evolution of the profiles than Fig. 7.6. We see that in this description the profiles are expected to decay more rapidly at the center than what is observed. The 'pointy' shape of the experimental profiles comes therefore as a clue that a fraction of the atoms is truly localized.

**Percolation threshold** – There remains the possibility that those localized atoms are classically trapped. Classically, in a disordered potential, a particle can be trapped if it is surrounded by areas where the potential is higher than its own energy. On the contrary, if the topography of the disorder is such that the particle can move across the system, we say that it can percolate. Therefore we have evaluated numerically the percolation threshold  $E_{\text{per}}$  of a 3D coherent-speckles potential, which is the energy such that all classical particles with energy  $E < E_{\text{per}}$  are trapped in finite-size regions. Using various values of the grid step, Luca Pezzé has carried out extensive numerical calculations, which provide an upper bound for the percolation threshold,  $E_{\text{per}} - V_{\text{min}} \leq 0.004V_{\text{R}}$ , where  $V_{\text{min}}$  is the minimum of the disordered potential (here  $V_{\text{min}} = -V_{\text{R}}$ ). Using the energy distribution  $\mathcal{D}_E(E)$  calculated numerically we find that the fraction of classically trapped particles is negligible ( $\ll 1\%$ ), including or not the heuristic energy shift. This is a major advantage of using two coherent crossed-speckles<sup>12</sup>, rather than two incoherent speckles. In the case of incoherent-speckles, the numerical calculation indeed yields a much larger percolation threshold:  $E_{\text{per}} - V_{\text{min}} \simeq 0.18V_{\text{R}}$  (for the incoherent-speckles configuration, we also have  $V_{\text{min}} = -V_{\text{R}}$ )<sup>13</sup>.

For a *coherent-speckles* potential, the classical percolation threshold  $E_{\text{per}}$  is therefore such that it eliminates the possibility of classical trapping of the atoms, which typically have energies around  $\bar{V} = 0$  (with our energy reference, see Fig. 7.2). Moreover, the correlation energy of the speckle [16]  $E_{\sigma_{\perp}} = \hbar^2/m\sigma_{\perp}^2$  is larger than the disorder amplitudes  $V_{\text{R}}$  used in the experiment ( $E_{\sigma_{\perp}}/h = 1.9\text{ kHz}$ ). Then, the local minima of the disordered potential do not support bound states, ruling out the possibility of quantum trapping in individual local minima.

Therefore, we know of no other explanation than Anderson localization for the experimental observations. Moreover, the self-consistent theory applied to the exact experimental situation

11. If the heuristic shift is not taken into account, in the on-shell approximation, all the atoms with  $E < 0$  have a null Boltzmann diffusion constant. For  $V_{\text{R}}/h = 680\text{ Hz}$ , it represents 58% of the atoms that would be artificially localized, which is non-physical, and does not match the experimental profiles either.

12. It is also a major advantage of being in three dimension. The percolation threshold in 2D is found to be much higher (at  $E_{\text{per}} - V_{\text{min}} \simeq 0.52V_{\text{R}}$  [23]), making it more difficult to experimentally discriminate classical ('trivial') and quantum ('genuine') localization.

13. Note that with our definition of  $V_{\text{R}}$  [see Eq. (3.26) and Sec. 6.1], in the incoherent-speckles case,  $|V_{\text{R}}|$  is not the standard deviation of the potential  $V$ . In this case we have  $\overline{V^2} = V_{\text{R}}/\sqrt{2}$ . However, as our notations suggest, it is the standard deviation for all the other models of speckles and coherent superpositions of speckles considered in this thesis.

yields good quantitative agreement with the experimental results, provided we use the energy distribution of the atoms, which is strongly modified by the sudden application of the disorder, and displace it by a heuristic shift. The comparison is, however, too sensitive to uncertainties in the experimental parameters and to approximations in the theory to be considered fully quantitative at this stage.

## Conclusion

In this chapter we have compared the study led in Chap. 6 to ultra-cold atom experiments, to which it directly applies. In the experiments of Refs. [18, 19], the transport properties are probed by direct imaging of the atoms, which can be related to our energy-dependent calculations using the energy distribution. For instance, in the single-speckle case, we predicted almost constant anisotropy factors ( $D_*^z/D_*^{x,y} \simeq 10$  and  $L_{\text{loc}}^z/L_{\text{loc}}^{x,y} \simeq 3.2$ ), and experimental data can be compared to these predictions almost independently of the energy distribution. Although no precise value has been extracted from the experiment of Ref. [18], the experimental data indicate significantly larger anisotropy. Further analysis would be required to clarify the origin of such a discrepancy. In particular, information about the diffusive part, which is surprisingly not observed in the experiment, would be of outmost interest. Conversely, in the coherent-speckles case, the diffusion constants, and in particular their anisotropies were shown to be in fair quantitative agreement with the theory [19]. The inversion of the transport anisotropy predicted in Sec. 6.2 was however not observed because the images were taken in the  $(y, z)$  plane: It only gives access to  $D^y = D^Y$  and  $D^z = (D^X + D^Z)/2$ , which do not show the inversion. In order to observe it, it would be required to image the atoms along the transport eigenaxes and to tune the balance between the populations of low- and high-energy states. In this case, the control of the energy distribution is not expected to necessitate fine tuning because of the strong energy-dependence of the diffusion tensor in the two regions with different anisotropies.

Another major challenge is the evaluation of the mobility edge in 3D disorder with structured correlations. In the preceding chapter we have proposed and used an applicable approach to estimate the position of the mobility edge in anisotropic 3D speckles. It yields a mobility edge which is negative (i.e., below the disorder mean value  $\bar{V}$ ), as also predicted for isotropic speckle potentials [169]. Hence, comparing to Ref. [18], where the authors find a positive mobility edge, our calculations significantly differ from experimental values. However, the method used in Ref. [18] to infer  $E_c$  from the localized fraction uses the free-space kinetic energy distribution, neglecting the disorder-induced distortion of the energy distribution. We argued that it is questionable because the latter is, in particular, necessary to account for negative energy states (i.e. below the disorder average value). Comparing to Ref. [19], we find that  $\Delta(E_c)$  as calculated here is of the same order of magnitude as the heuristic shift introduced in Ref. [19]. Given systematic uncertainties in the analysis of the experimental data, it is a reasonable agreement, which supports the importance of going beyond pure on-shell calculations. A precise test of the theory of Sec. 6.3 and Ref. [25] would however require a reliable determination of the energy distribution in ultracold-atom experiments, which is not available so far.



## Chapter 8

# Tailoring Anderson localization by disorder correlations in speckle potentials

### Abstract

The dependence of the properties of Anderson localization on the correlations of the disorder outlined in Chaps. 5 and 6 is rich of counter-intuitive consequences and can be particularly exploited in matter wave experiments. There, the disordered potential can be tailored and controlled, and anisotropies are naturally present. Here we show that, in contrast to immediate intuition, Anderson localization of noninteracting matter waves induced by a disordered potential in free space can increase (i.e. the localization length can decrease) when the particle energy increases, for appropriately tailored disorder correlations. By considering suitable models of disorder, we predict the effect in one, two and three dimensions, and propose a simple method to observe it using ultracold atoms placed in optical disorder. We also show that the increase of localization with the particle energy can serve to discriminate quantum versus classical localization.

### Résumé

La dépendance des propriétés de la localisation d'Anderson par rapport aux corrélations du désordre, qui a été mise en évidence dans les Chaps. 5 and 6, est riche de conséquences contre-intuitives et peut être exploitée dans les expériences avec des ondes de matière. Dans ce cas, le potentiel désordonné peut être adapté et contrôlé et des anisotropies sont naturellement présentes. Ici nous montrons que, contrairement à l'intuition, la localisation d'Anderson d'ondes de matière sans interaction, induite par un potentiel désordonné dans l'espace libre, peut s'accroître (i.e. la longueur de localisation décroître) quand l'énergie de la particule augmente, pour des corrélations du désordre astucieusement adaptées. En considérant des modèles de désordre appropriés, nous prédisons l'effet à un, deux et trois dimensions, et nous

proposons une méthode simple pour l'observer au moyen d'atomes ultrafroids placés dans un désordre optique. Nous montrons aussi que l'accroissement de la localisation avec l'énergie de la particule peut être utilisée pour distinguer localisation quantique et localisation classique.

## Introduction: Localization length vs. particle energy

We now focus on the qualitative behaviour of the localization properties as a function of energy. To start with, consider a wave propagating among randomly distributed point scatterers [such as in Fig. 1.2(b), but with very  $\delta$ -peaks]. In this case the disorder is not correlated. In the absence of interference, the propagation is dominated by diffusion. The diffusive medium is characterized by the length scale (transport mean free path, which is equal to the scattering mean free path in this case)  $l_B = v\tau$ , where  $v = |\partial E(k)/\partial k|/\hbar$  is the wave velocity,  $E(k)$  is the dispersion relation, and  $\tau$  is the scattering time. Then, localization arises from the interference of the diffusive paths, which is expected to be stronger for larger wave lengths (i.e. smaller wave vectors  $k$ ) compared to  $l_B$ . It can thus be inferred that the Lyapunov exponent (inverse localization length), which characterizes the localization strength, reads  $\gamma = l_B^{-1}F_d(kl_B)$  where  $F_d$  is a decreasing function of the disorder parameter  $kl_B$ , which strongly depends on the spatial dimension  $d$ . This assumption is confirmed by the results found in the self-consistent theory, as we will see. For a scalar matter wave in free space and weak disorder,  $v \propto k$ ,  $\tau$  is proportional to the inverse of density of states,  $\rho \propto k^{d-2}$ , as given by the Fermi golden rule, and finally  $l_B \propto 1/k^{d-3}$ , as we found previously for the white-noise limit. It results that for any  $d \leq 3$ ,  $\gamma$  is a decreasing function of  $k$ . We thus conclude that, in the absence of correlations of the disorder, localization decreases when the particle energy  $E = \hbar^2 k^2/2m$  increases, which conforms to natural intuition.

It is however clear that this behavior strongly depends on the microscopic details of the system, namely on the dispersion relation and the behavior of the scattering time. For instance, it does not hold for lattice systems, such as electrons in disordered crystals, because the band structure leads to a nonmonotonic behavior of  $v$  versus  $E$ , which can lead to a function  $\gamma(E)$  approximately symmetric with respect to the band center [206, 207]. In other systems, such as light waves in dielectric media,  $\tau$  can strongly vary with the energy [41], leading to a nonmonotonic behavior of  $\gamma(E)$ . For particles in continuous disorder, structured correlations can change the picture. For instance, disorder correlations with a finite support in momentum space were shown to induce effective mobility edges in 1D disorder [8, 81, 82], which was used to create materials with alternating localizing and almost transparent frequency windows [194], to enhance localization [76] in microwave systems, and to propose realization of atomic band-pass filters [186]. Such correlations are also responsible for algebraic localization of matter waves with broad energy distributions [8, 9, 22].

Here we are interested in a more exotic effect of the disorder correlations. We show that for matter waves in free space, localization can increase with energy, provided that the disorder correlations are appropriately tailored. The basic idea behind our work is that for non-point scatterers, the disorder power spectrum  $\tilde{C}_2(k)$  appears in the denominator of the scattering time  $\tau$ . Then, if the disorder has strong spatial frequency components around a particular value  $k_0$ , the scattering strength may not vary monotonously with  $E$  around  $E(k_0)$ , and  $\gamma(E)$  can then increase with  $E$ . We first study the 1D case, which allows for exact calculations of  $\gamma(E)$  and for explicit test of an efficient scheme to observe the effect with ultracold atoms. We then extend our analysis to 2D and 3D systems using the self-consistent theory of Anderson localization. We finally discuss how the increase of  $\gamma(E)$  with  $E$  can serve to discriminate quantum versus classical localization of particles, which is of particular interest for ultracold atoms. This chapter is adapted from Refs. [26, 27]

## 8.1 Tailoring correlations in speckle potentials

A key ingredient of our work is the possibility of tailoring the disorder correlations. Any method for doing it would have its own constraints. Let us consider the specific example of speckle potentials, as described in Chap. 3 and used in Refs. [9, 17–19, 127] for instance. The atoms are subjected to a potential, which, up to an arbitrary shift, is proportional to the light intensity  $\mathcal{I}$ . As in previous chapters, we define  $V(\mathbf{r}) \equiv V_R \times \{\mathcal{I}(\mathbf{r})/\bar{\mathcal{I}} - 1\}$  [see Eq. (3.26)], so that  $\bar{V} = 0$  and  $\overline{V^2} = V_R^2$ . The sign of  $V_R$  can be positive or negative depending on the detuning of the laser with respect to the atomic resonance [see Eq. (3.1)]. All statistical properties of the disordered potential  $V(\mathbf{r})$  follow from basic laws of optics [see Chap. 3 for details]. For instance, we have shown that in the paraxial approximation for the scheme of Fig. 3.2(a) the disorder power spectrum (Fourier transform of the disorder correlation function) in the focal plane  $(x, y)$  of the lens is the auto-convolution of the pupil function [see Eq. (3.16)]. The major constraints on  $\tilde{C}_2(\mathbf{k})$  follow from Eq. (3.16) and from the fact that  $I_D(\rho)$  is nonnegative and of finite integral. Firstly, the Cauchy-Schwarz inequality<sup>1</sup> applied to Eq. (3.16) shows that  $\tilde{C}_2(\mathbf{k})$  is a decreasing function of  $|\mathbf{k}|$  for small values of  $|\mathbf{k}|$ .

Secondly, in practice,  $I_D(\rho)$  decays at long distance so that  $\tilde{C}_2(\mathbf{k})$  also decays in the large  $|\mathbf{k}|$  limit. Apart from these constraints, control of  $I_D(\rho)$  offers freedom for tailoring the disorder power spectrum, which we will write  $\tilde{C}_2(\mathbf{k}) = V_R^2 \sigma_R^d \tilde{c}(\mathbf{k}\sigma_R)$  with  $\sigma_R$  the correlation length. We now show that it allows us to strongly affect the qualitative behavior of Anderson localization for noninteracting matter waves.

## 8.2 One-dimensional speckle

To start with, let us consider the 1D case. We first show how speckle allow design of disorder correlations to realize the desired effect [26]. We study two alternative possibilities, which require only slight modifications of existing schemes to create speckles [9, 137, 161, 162]. We then calculate the localization of the single-particle eigenstates, using both numerical calculations, based on the transfer-matrix approach, and the so-called *phase formalism*, which is well suited for perturbative expansion in 1D transmission schemes for a matterwave of fixed energy (see Chap. 4 for details of the method and the application to standard speckle potentials). Lowest-order analytical calculations reproduce the main physics. These calculations however show significant deviations with numerical data, but we show that they are quantitatively accounted for by next-order calculations. We finally discuss how to observe the nonmonotonic behavior of the localization length with energy with expanding ultracold-atom gases, and explicitly show that standard schemes should be adapted.

### 8.2.1 Tailored correlations in 1D speckle potentials

Working in the Born approximation, valid in the weak disorder limit [i.e. for  $\gamma(E) \ll k_E, \sigma_R^{-1}$ ], exact calculations can be performed [37] [see Chap. 4 and Eqs. (4.5) and (4.17) in

---

1. Eq. (3.16) gives  $\tilde{C}_2(\mathbf{k})/V_R^2(\lambda_L f)^2 = \int d^2\rho I_D(\rho) I_D\left(\rho + \frac{\lambda_L f}{2\pi} \mathbf{k}\right) / \left[\int d^2\rho I_D(\rho)\right]^2$  and the Cauchy-Schwarz inequality implies  $\tilde{C}_2(\mathbf{k})/V_R^2(\lambda_L f)^2 < \int d^2\rho |I_D(\rho)|^2 / \left[\int d^2\rho I_D(\rho)\right]^2$ . Therefore we have  $\tilde{C}_2(\mathbf{k}) \leq \tilde{C}_2(0)$  for any  $\mathbf{k}$ , and  $\tilde{C}_2(\mathbf{k})$  is a decreasing function of  $|\mathbf{k}|$  at small  $|\mathbf{k}|$ .

particular], yielding the Lyapunov exponent

$$\gamma(E) = L_{\text{loc}}^{-1}(E) \simeq \frac{m^2 V_{\text{R}}^2 \sigma_{\text{R}}}{2\hbar^4 k_E^2} \tilde{c}(2k_E \sigma_{\text{R}}), \quad (8.1)$$

where  $k_E = \sqrt{2mE}/\hbar$  is the wavevector associated to energy  $E$  and  $m$  is the mass of the particle. As can be explicitly seen in Eq. (8.1), if the disorder supports no particular correlations, i.e. if  $\tilde{c}(\kappa)$  is a constant or decreasing function of  $\kappa$ , as for the usual speckle [Eq. (3.19)], then  $\gamma(E)$  decreases monotonically with  $E$ , and the localization is weaker for higher energy. In order to invert this behavior in a given energy window, it is necessary to tailor the disorder correlations so that  $\tilde{c}(2k_E \sigma_{\text{R}})$  increases with  $k_E$  strongly enough to overcome the  $1/k_E^2$  decrease of the prefactor in Eq. (8.1). To do so, we consider two configurations. In the first configuration (named *double-slit speckle*), we propose to use a square aperture of length  $D$  with a mask of width  $2r$ , creating a double-slit [see Sec. 3.2.1 and Fig. 3.4(b1)]. This option has also been proposed to realize atomic band-pass filters [186]. In this case the potential correlation function is given by [see Eqs. (3.20) and (3.28)]

$$\tilde{C}_2(k) = \frac{\pi V_{\text{R}}^2 \sigma_{\text{R}}}{(1-\beta)^2} \left\{ [1 - \beta - |k|\sigma_{\text{R}}]_{\oplus} + \frac{1}{2} [1 - \beta - ||k|\sigma_{\text{R}} - (\beta + 1)|]_{\oplus} \right\}, \quad (8.2)$$

where  $\sigma_{\text{R}} = \lambda_{\text{L}} f / \pi D$  and  $\beta = 2r/D$  and  $[g(x)]_{\oplus} = g(x)$  if  $g(x) > 0$  and 0 otherwise. As shown in Fig. 3.4(b2), it shows an increase on a certain interval of  $k$  for any  $\beta > 0$ , which is all the more marked that  $\beta$  is large. In the second configuration, we propose to illuminate an infinitely-long slit by two mutually coherent Gaussian laser beams of waist  $w$  along  $\rho_x$  and centered at  $\rho_x = \pm\Delta/2$ . The two-point correlation function is then given by<sup>2</sup>

$$\tilde{C}_2(k) = \frac{\sqrt{\pi} V_{\text{R}}^2 \sigma_{\text{R}}}{4} \left[ e^{-\frac{(k\sigma_{\text{R}} - \kappa_0)^2}{4}} + 2e^{-\frac{(k\sigma_{\text{R}})^2}{4}} + e^{-\frac{(k\sigma_{\text{R}} + \kappa_0)^2}{4}} \right], \quad (8.3)$$

with  $\sigma_{\text{R}} = \lambda_{\text{L}} f / \pi w$  and  $\kappa_0 = 2\Delta/w$ , the values of which can be independently controlled. The properties of the disordered potentials obtained in this configuration are shown in Fig. 8.1 for various values of  $\kappa_0$ . For  $\kappa_0 = 0$  (lower row), the disordered potential features structures of typical width  $\sigma_{\text{R}}$  in real space (central column). The corresponding power spectrum  $\tilde{C}_2(k)$  has a single Gaussian peak of rms width  $\sqrt{2}/\sigma_{\text{R}}$  centered in  $k = 0$  (right column). For  $\kappa_0 \neq 0$ , the disordered potential develops additional structures of typical width  $\sigma_{\text{R}}/\kappa_0$ , corresponding in  $\tilde{C}_2(k)$  to an additional peak centered in  $k \simeq \kappa_0/\sigma_{\text{R}}$ . For  $\kappa_0 \gtrsim 3.7$ , this function increases on a certain interval of  $k$ , and for  $\kappa_0$  large enough it happens in a significant range (upper rows). We will see in the following that the increase of  $\tilde{C}_2(k)$  in both the double-slit and the double-Gaussian configurations can lead to an enhancement of localization with energy.

## 8.2.2 Anderson localization in 1D tailored speckle potentials

Let us first consider the standard experiment of the transmission of a wave through a disordered medium. As in Chap. 4, we will compute the Lyapunov exponent both analytically (by the so-called phase formalism introduced in Sec. 4.1.1) and numerically (with transfer matrices, see Sec. 4.1.2) for the models of speckle introduced above.

2. As the pupil function is separable in  $\rho_x$  and  $\rho_y$  [ $I_{\text{D}}(\rho) = f(\rho_x) \times g(\rho_y)$ ], it is equivalent to consider the correlations, along the axis  $x$ , of the 3D speckle pattern obtained by two parallel and mutually coherent Gaussian beams, as shown in appendix D.3.3 [see Eq. (D.16)].

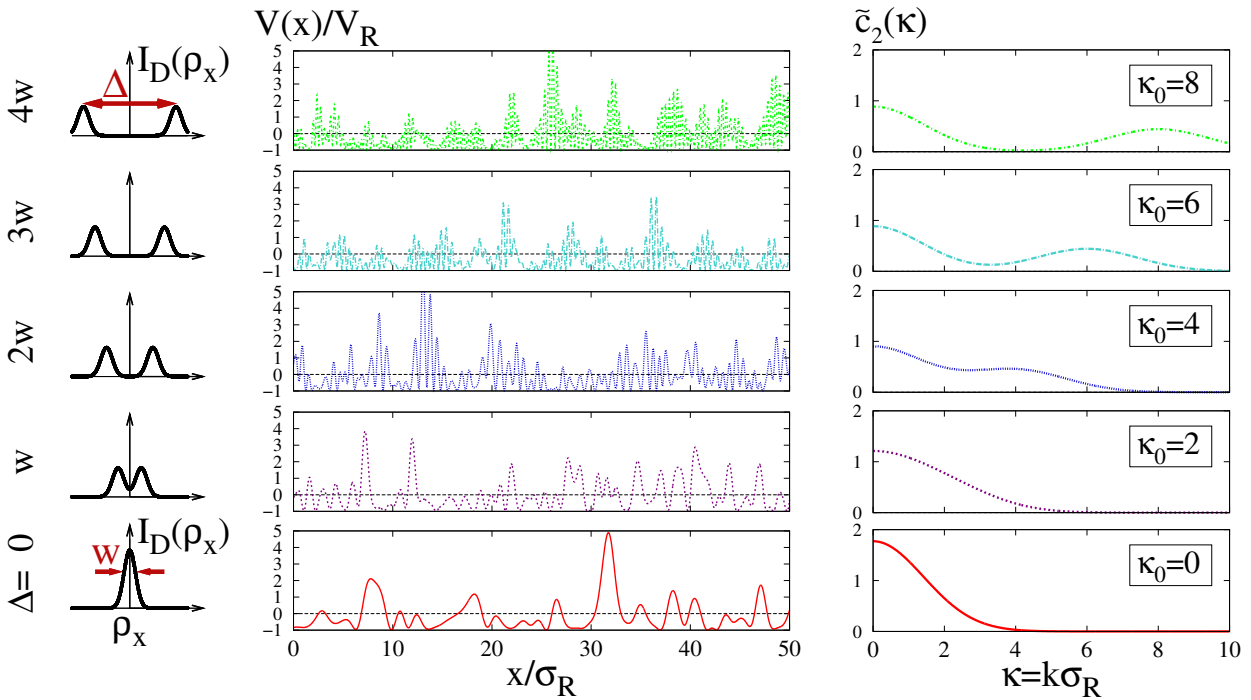


Figure 8.1: Tailoring correlations in 1D speckle potentials. One-dimensional speckle potentials realized with a pupil function obtained with two incident Gaussian beams of waist  $w$  and centered at  $\rho_x = \pm\Delta/2$ . The figure shows a sketch of  $I_D$  (1<sup>st</sup> column), a realization of  $V(x)$  (2<sup>nd</sup> column), and the reduced disorder spectrum in  $k$ -space,  $\tilde{c}_2(k\sigma_R)$  (3<sup>rd</sup> column) for various values of  $\Delta/w$ .

**Double-slit speckle** – As shown in Sec. 4.1, for standard disorder, i.e. with a power spectrum  $\tilde{C}_2$  that is a constant or decreasing function of  $k$ , the Lyapunov exponent  $\gamma^{(2)}(E)$  decreases with the energy  $E$  (see Fig. 4.1). Let us now consider the double-slit configuration, of correlation function given by Eq. (8.2). Inserting the latter into Eq. (4.4), we find that, for  $\beta > 0.25$ ,  $\gamma^{(2)}(E)$  shows an increase in a certain interval of  $k$ , which is all the more pronounced that  $\beta$  approaches 1. This indicates that in those tailored potentials,  $\gamma(E)$  can counter-intuitively increase with energy. In order to study this effect precisely, we performed numerical (transfer-matrix approach) and analytical (phase formalism approach) calculations for the considered tailored speckle potential with  $\beta = 1/3$ , as done previously for the standard speckle potential in Sec. 4.1. The results of the numerical calculations (blue squares and red diamonds) and of analytical calculations up to order three in the phase formalism (dotted blue and red lines) are shown on Fig. 8.2. They confirm that, for both blue and red detunings,  $\gamma(E)$  exhibits an increase with  $E$  for  $k_E\sigma_R \in [0.35, 0.6]$ . As for the standard speckle potential, the numerical results follow the trend of the 2<sup>nd</sup> order term in the phase formalism (solid black line in Fig. 8.2). However, there is a non-negligible discrepancy, which depends on the sign of  $V_R$ . To describe it, we include the 3<sup>rd</sup> order term, which is given in the appendix A.1 [Eq. (A.2)]. For  $k_E\sigma_R \in [0.4, 1]$ , it accounts very well for the discrepancy between the numerics and the 2<sup>nd</sup> order term (solid black line). For low energy (i.e.  $k_E\sigma_R \lesssim 0.4$ ), the 4<sup>th</sup> and higher order terms play a more important role, which is expected as we are approaching the limits of validity of the perturbative development, which is valid for  $\gamma(E) \ll k_E$ .

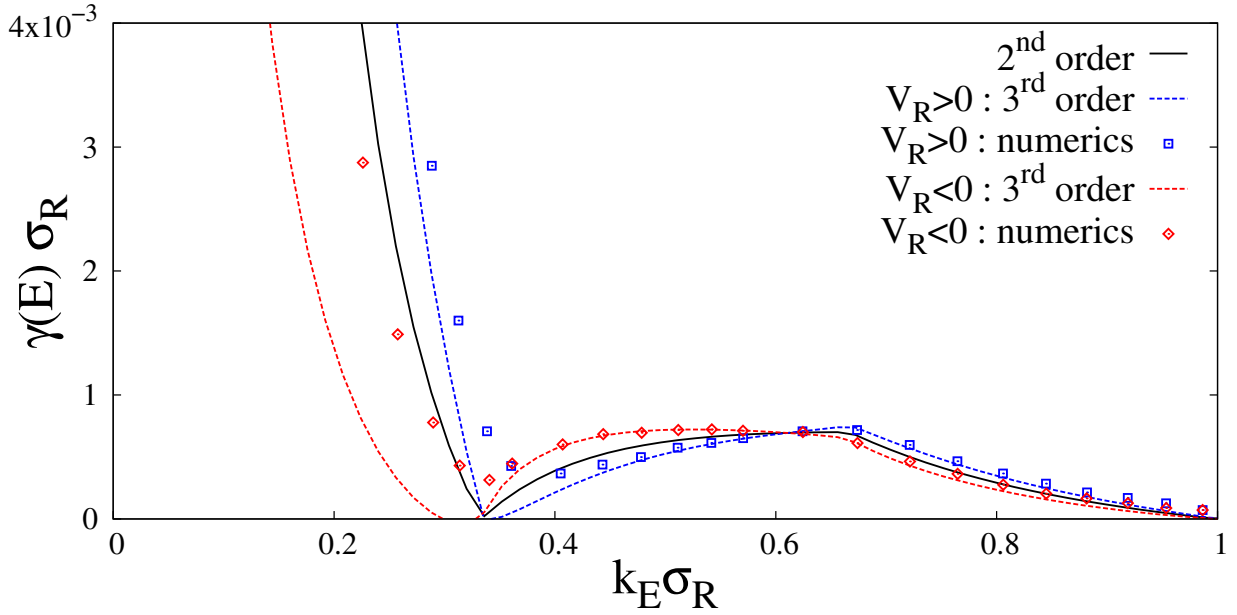


Figure 8.2: Lyapunov exponent for speckles with the tailored correlation function (8.2) with  $\beta = 1/3$ , using the same methods and parameters as in Fig. 4.1 (space step of  $\Delta x = 0.1\sigma_R$  and total system size of  $L_{tot} = 411775\sigma_R$  with random initial conditions) averaged over 500 disorder realizations. Blue squares: numerical results (extracted from transfer matrix calculations) with  $V_R > 0$ ; Red diamonds: numerical results with  $V_R < 0$ ; Solid black line: order 2 in the phase formalism; Dotted blue and red lines: up to order 3 in the phase formalism.

**Double-Gaussian speckle** – In the above double-slit configuration,  $\gamma(E)$  has a slope break near its maximum [see Eqs. (8.2), and (A.2) and Fig. 8.2], which is reminiscent of the sharp edges of the pupil function [see Fig. 3.4(b1)]. As it will presumably be inconvenient for experimental observations, we now consider the double-Gaussian configuration, which is obtained using two mutually coherent Gaussian beams shone onto an infinite diffusive plate, giving the power spectrum (8.3) [26]. For this configuration,  $\gamma^{(2)}(E)$  shows an increase when  $\kappa_0 \gtrsim 5.3$ , which is all the more marked than  $\kappa_0$  is large. In Fig. 8.3, we show the Lyapunov exponents obtained in this case for  $\kappa_0 = 8.88$ , with transfer matrices (blue squares and red diamonds) and with the phase formalism, up to order 2 (solid black line) and up to order 3 (dotted blue and red lines; see Eq. (A.3) in appendix A.1 for the 3<sup>rd</sup> order term). In this configuration, we recover the same trend as in the other configuration, namely the Lyapunov exponent shows a significant increase between  $k_E \simeq 2.3\sigma_R^{-1}$  and  $k_E \simeq 4.2\sigma_R^{-1}$ , the second order term,  $\gamma^{(2)}(E)$ , captures the main physics, and the discrepancy between the numerical results and  $\gamma^{(2)}(E)$  are well accounted by the third order term, except at very low energy where the perturbative expansion breaks down. As expected, the behavior of  $\gamma(E)$  is smoother for the double-Gaussian configuration compared to the double-slit configuration.

In Fig. 8.3 we have shown the average value of the Lyapunov exponent, which is written  $\bar{\gamma}$  in this paragraph. To be complete, we study here the distributions of  $\gamma(E)$ . In Fig. 8.4(a) we show several distributions of the Lyapunov exponents  $\gamma(E)$  that were found in the double-Gaussian speckle when generating Fig. 8.3 (see dashed lines), for both  $V_R > 0$  [(a1) and (b1)] and  $V_R < 0$  [(a2) and (b2)]. Those distributions indeed follow the theoretical distribution

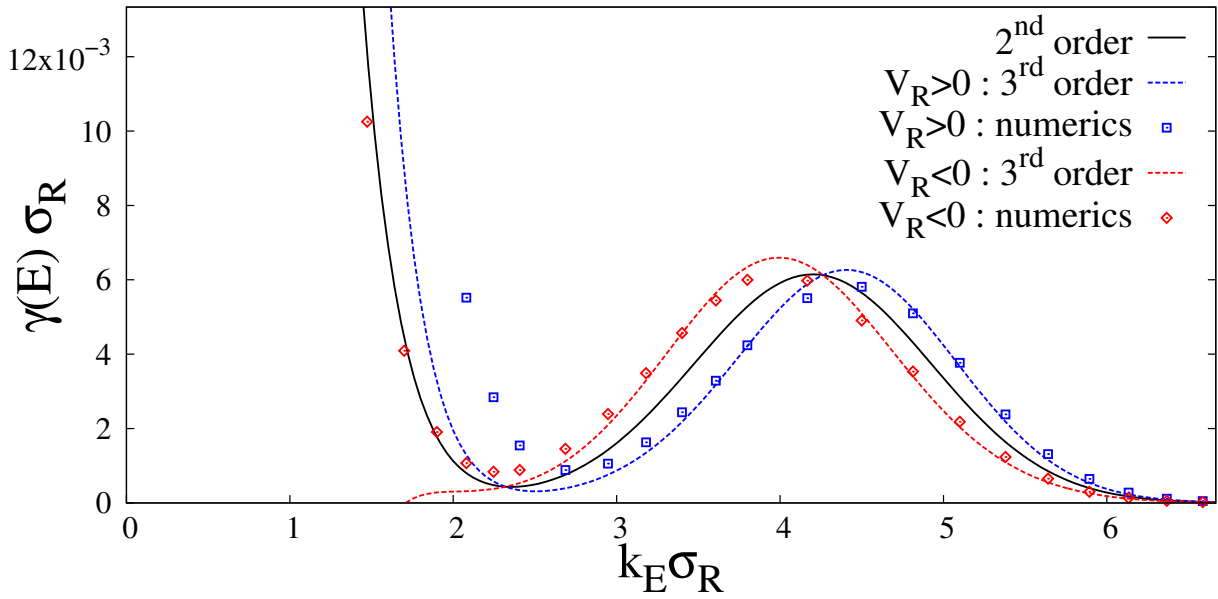


Figure 8.3: Lyapunov exponent for speckles with the tailored correlation function (8.3) with  $\kappa_0 = 8.88$  and  $V_R = \pm 0.72(\hbar^2/m\sigma_R^2)$ , using the same method as in Figs. 4.1 and 8.2 (with space step of  $\Delta x = 0.015\sigma_R$  and total system size of  $L_{tot} = 30880\sigma_R$  with random initial conditions) averaged over 500 disorder realizations. The solid lines are the corresponding theoretical distributions (4.8).

introduced earlier [see Eq. (4.8)]:

$$P(\gamma) = \frac{1}{\sqrt{2\pi}\Delta_\gamma} \exp\left[-\frac{(\gamma - \bar{\gamma})^2}{2\Delta_\gamma^2}\right] \quad (8.4)$$

where  $\Delta_\gamma = \sqrt{\bar{\gamma}/L_{tot}}$  and  $L_{tot}$  is the system size, for both blue and red detunings (see solid lines). Here we are comparing the statistics of Lyapunov exponents obtained in tailored correlations with the prediction (8.4) which was obtained in the  $\delta$ -correlated case, and which also held in the single-slit case [see Sec. 4.1.2 and Eq. (4.8) in particular]. It indicates that the statistics of the Lyapunov exponent only depend on its average value  $\bar{\gamma}$  and on the system size  $L_{tot}$ . In particular, the distributions are very similar when the same value of  $\bar{\gamma}$  is reached for different energies [e.g. compare  $k_E\sigma_R = 2.08$  and  $4.50$  on Fig. 8.4(a1)]. To study the influence of  $L_{tot}$ , we have also computed Lyapunov exponents in a smaller box, with much higher averaging at four different energies [see Fig. 8.4(b)]. In this case the distributions are also Gaussian functions of standard width  $\Delta_\gamma = \sqrt{\bar{\gamma}/L_{tot}}$ . This plot reveals a slight difference between the blue- and red-detuned cases: the fluctuations are greater in the case  $V_R > 0$ . More precisely, when fitting the distributions of Fig. 8.4(b1) for  $k_E\sigma_R = 2.25$  and  $2.41$  by Gaussian functions we find that their rms width are greater than  $\Delta_\gamma$  by approximately 7%. These distributions may be broadened by the occurrence of rare very high peaks in some realizations of the blue-detuned potential leading to macroscopic reflections of the wavefunction, which might increase the dispersion of the Lyapunov exponents.

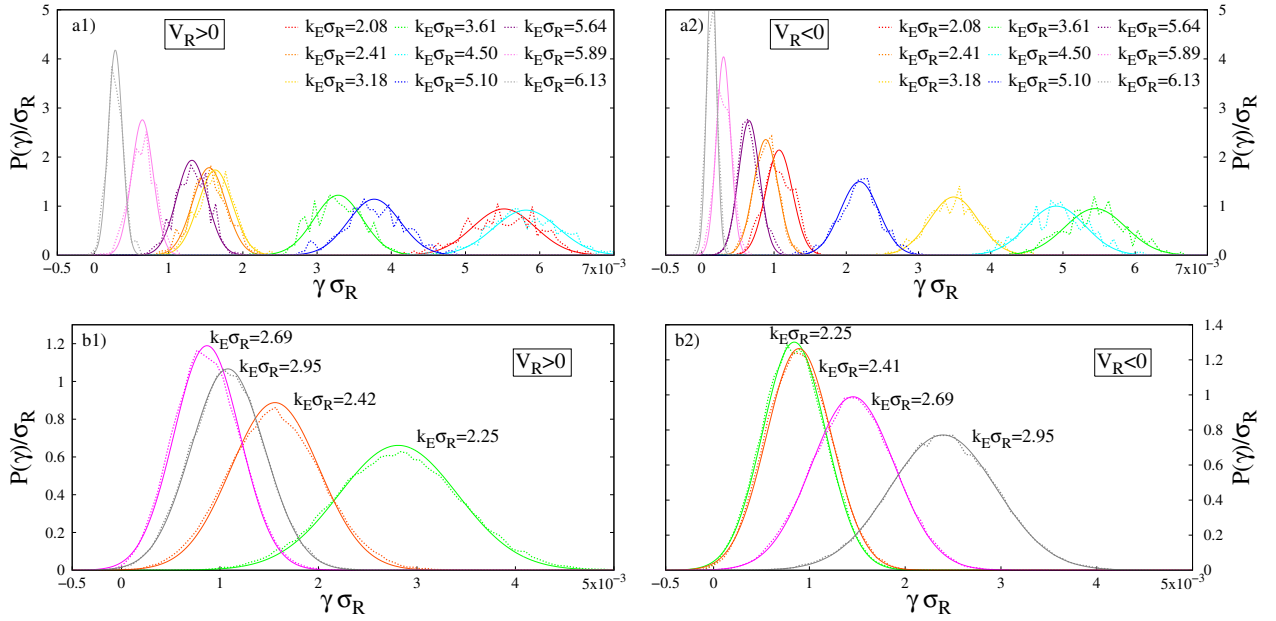


Figure 8.4: Probability distributions of the Lyapunov exponents (dotted lines) for the disorder parameters of Fig. 8.3 at various energies (indicated on the figure). (a) Distributions found for 500 disorder realizations in a system of size  $L_{tot} = 30880\sigma_R$  with  $V_R > 0$  (a1) and  $V_R < 0$  (a2). (b) Distributions found for 50000 disorder realizations in a system of size  $L_{tot} = 7720\sigma_R$  with  $V_R > 0$  (b1) and  $V_R < 0$  (b2).

### 8.2.3 Observation schemes with ultracold atoms

In order to probe the nonmonotonous behavior of  $\gamma(E)$  discussed above, one can use ultracold atoms, which proved a good means to observe 1D Anderson localization of matter waves with pseudo-periodic [10] and speckle [9] potentials. The preceding calculations of the Lyapunov exponent (a self-averaging quantity) directly apply to a 1D transmission scheme of a wave with fixed energy  $E$ . In ultracold-atom experiments [9, 10, 18, 19] however, a matter-wavepacket with a broad energy distribution should be considered, and the measured quantity is the density profile obtained after releasing the atoms in the disorder, which is not directly related to the above calculations (see Chap. 4). As shown in Sec. 2.3 [see Eq. (2.31)], the average stationary density of a noninteracting atomic gas, with initial negligible width, after evolution in the disorder reads [8, 22, 82]  $n_\infty(x) = \int dE \mathcal{D}_E(E) P_\infty(x|E)$ , where  $\mathcal{D}_E(E) = \int \frac{dk}{2\pi} A(E, k) \mathcal{D}_k(k)$  is the energy distribution of the atoms and the probability of quantum diffusion in the long-time limit  $P_\infty(x|E)$  is given by Eq. (4.17) in a weak disorder calculation with  $\gamma = \gamma(E)$  given by Eq. (8.1) (see details of the in appendix B) [70, 71, 155].

**Thomas-Fermi distribution** – A (naive) first attempt to observe the nonmonotonous behavior of  $\gamma(E)$  may be to consider the experimental scheme of Ref. [9]. In this case, as detailed in Chap. 4, an interacting condensate is first produced in the Thomas-Fermi regime in a harmonic trap of frequency  $\omega$ , and the trap is then switched-off at time  $t = 0$ . As described in Sec. 4.2.2, in a first stage the expansion of the atoms is driven by their interaction energy, and one can neglect the disordered potential. At  $t_0 \gg 1/\omega$ , it produces an almost noninteracting

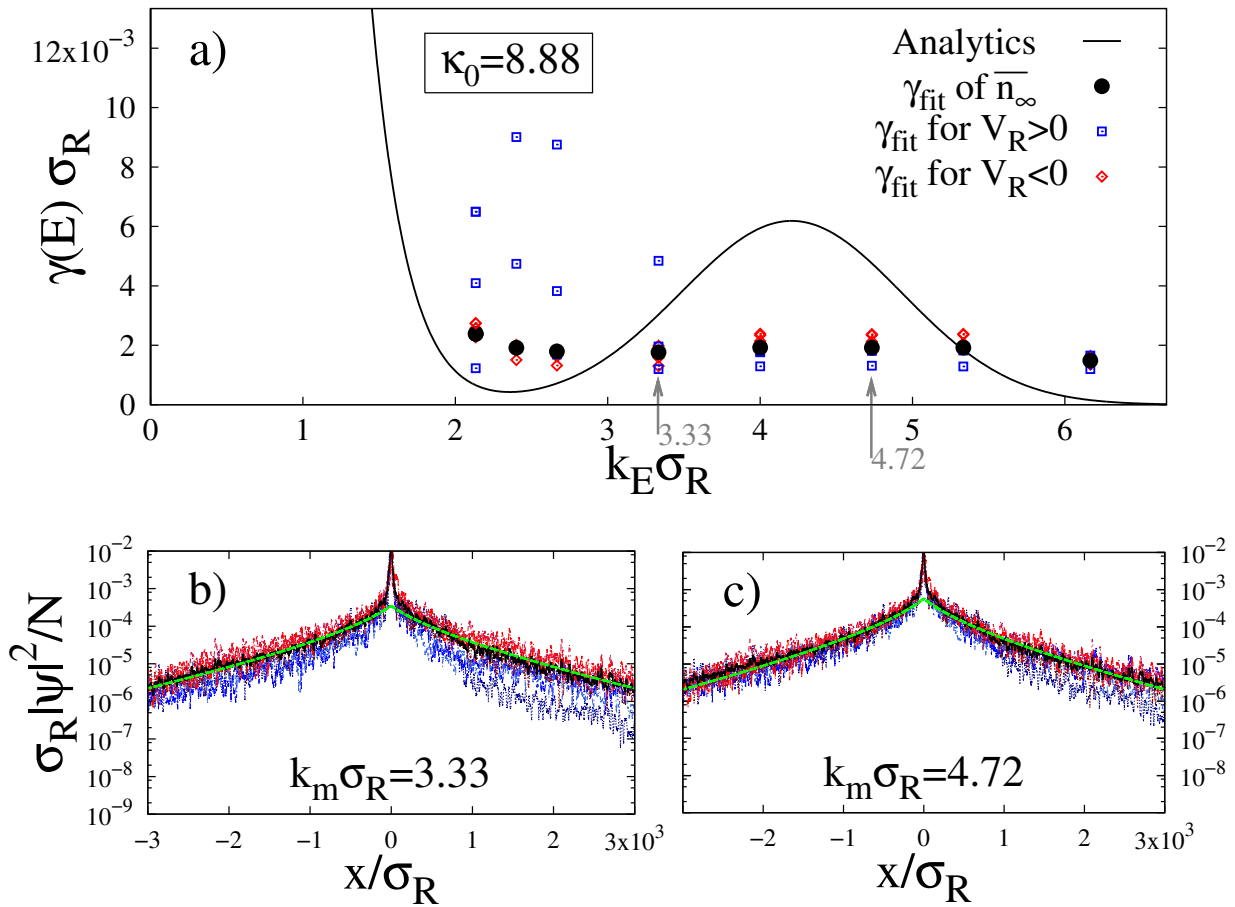


Figure 8.5: Anderson localization in speckle potentials in the double-Gaussian configuration with  $\kappa_0 = 8.88$  and  $V_R = \pm 0.72(\hbar^2/m\sigma_R^2)$  with initial Thomas-Fermi momentum distributions [Eq. (8.5)]. (a) Lyapunov exponent versus particle energy as obtained from Eq. (8.1) (solid black line) and from fits of Eq. (4.17) to the numerical data (points). (b-c) Stationary density profiles obtained numerically using the initial momentum distribution (8.5) with two different values of  $k_m$ . The figures show the results for six realizations of the disorder [three with  $V_R > 0$  (blue data) and three with  $V_R < 0$  (red data)], the averaged density profile (black data) and the fits of  $P_\infty(x)$  to the latter (green line). The extracted values of  $\gamma_{\text{fit}}$  for each realization and for the averaged profile are reported in (a).

gas with momentum distribution [178, 179]

$$\mathcal{D}_{k,0}(k) = 2\pi \frac{3N}{4k_m} \left[ 1 - \left( \frac{k}{k_m} \right)^2 \right]_{\oplus}. \quad (8.5)$$

which has a cut-off at  $k = k_m$ , and therefore, in weak disorder the energy distribution extends from  $E = 0$  to  $E = \hbar^2 k_m^2 / 2m \simeq 2\mu$ , and the effects of the spectral broadening only show up at very large distances. We have performed numerical integration of the time-dependent Schrödinger equation for a particle with the initial momentum distribution (8.5) in the double-Gaussian tailored disordered potential with correlation function (8.3) and disorder parameters as in Fig. 8.3, for six realizations of the disordered potential [three with blue ( $V_R > 0$ ) and

three with red ( $V_R < 0$ ) detuning]<sup>3</sup>. The stationary density profiles  $n_\infty(z)$  that we obtain are shown in Fig. 8.5(b) and (c) for two different values of  $k_m$  (red and blue lines). After averaging them over the six realizations (solid black line), we fit  $\ln[P_\infty(z)]$  as given by Eq. (4.17) to  $\ln[\overline{n_\infty}(z)]$  with  $\gamma$  as the only fitting parameter<sup>4</sup>. The results, plotted on Fig. 8.5<sup>5</sup>, show that the fitted Lyapunov exponent (black dots) slightly decreases with  $k_m$  ( $k_E$  on the figure) and saturates roughly beyond the minimum of the calculated  $\gamma^{(2)}$ . This is because the long distance behavior of  $n_\infty(z)$  is dominated by the energy components with the largest localization lengths, i.e. those with the smallest  $\gamma(E)$  [8, 22, 82]. Since for a broad energy distribution extending from 0 to  $\mu$  the minimum is below the region where  $\gamma(E)$  increases, this scheme does not enable us to probe the region of interest.

**Gaussian momentum distribution** – In order to observe the upturn of  $\gamma(E)$ , we propose to use an atomic energy distribution much narrower in energy and strongly peaked at a given  $E_{\text{at}}$ , so that  $n_\infty(z) \simeq P_\infty(z|E_{\text{at}})$ . It can be realized by either giving a momentum kick to a noninteracting initially trapped gas or using an atom laser, both with a narrow energy width [208–210]. The momentum distribution can be represented by a 1D Gaussian function of width  $k_w$  centered around a controllable value  $k_{\text{at}}$  [208–210]:

$$\mathcal{D}_{k,0}(k) = 2\pi \frac{N}{\sqrt{2\pi}k_w} e^{-(k-k_{\text{at}})^2/2k_w^2}. \quad (8.6)$$

For weak disorder the corresponding energy distribution is weakly affected by the disorder-induced spectral broadening, so that it is strongly peaked at  $E_{\text{at}} \simeq \hbar^2 k_{\text{at}}^2/2m$  [22]. As above, we have performed numerical integrations of the time-dependent Schrödinger equation for a particle in the disordered potential with the initial momentum distribution (8.6) and disorder parameters as in Figs. 8.3 and 8.5. Contrary to the Thomas-Fermi case considered above, the gas has a non-zero average velocity, but during the expansion, back and forth scattering processes quickly redistribute left- and right-moving atoms. The center of the cloud hardly moves and the wings gradually form a nearly symmetrical stationary density profile  $n_\infty(x)$ , shown in Figs. 8.6(b) and (c) for two values of  $k_{\text{at}}$  and for six realizations of the disordered potential: three with blue detuning ( $V_R > 0$ ) and three with red detuning ( $V_R < 0$ ). The density profile averaged over the six realizations,  $\overline{n_\infty}(x)$ , is also displayed (black line). After averaging, one can then extract the values of  $\gamma(E_{\text{at}})$  by the same fitting procedure as above: we fit  $\ln[P_\infty(x)]$  [Eq. (4.17)] to  $\ln[\overline{n_\infty}(x)]$  with  $\gamma$  as the only fitting parameter. Although the fits are performed in a limited space window ( $-300\sigma_R < x < +300\sigma_R$ , corresponding to an experimentally accessible width of 1mm for  $\sigma_R = 1.6\mu\text{m}$ ), we find that they are good on the total space window ( $|x|$  up to  $3000\sigma_R$ ). As shown in Fig. 8.6(a), the extracted values  $\gamma_{\text{fit}}$  (black dots) fairly agree with Eq. (8.1), except for low energy where the Born approximation breaks down. The values extracted in the same manner for each realization of the disordered potential are also shown (blue squares and red diamonds). We find nonnegligible difference between

3. As in Refs. [22, 26], we use a Crank-Nicolson algorithm with numerical parameters: space step  $\Delta x = 0.03\sigma_R$ , time step  $\Delta t = 1.1\hbar/E_{\sigma_R}$ , boxes of size  $12 \times 10^3\sigma_R$ .

4. The fits are performed in the space windows  $-300\sigma_R < z < -50\sigma_R$  and  $+50\sigma_R < z < +300\sigma_R$ , corresponding to an experimentally accessible width of 1 mm for  $\sigma_R = 1.6\mu\text{m}$ .

5. In Fig. 8.5, there is one of the blue-detuned disorder realizations for which a very high reflection is found around  $x = 1 \times 10^3\sigma_R$  for a low-energy component; it induces the fluctuations on the right-hand side of (b) and (c) where one realization is below the other ones, and it corresponds to the anomalously high values of  $\gamma(E)$  found for  $k_E\sigma_R \in [2.4, 3.5]$  in (a).

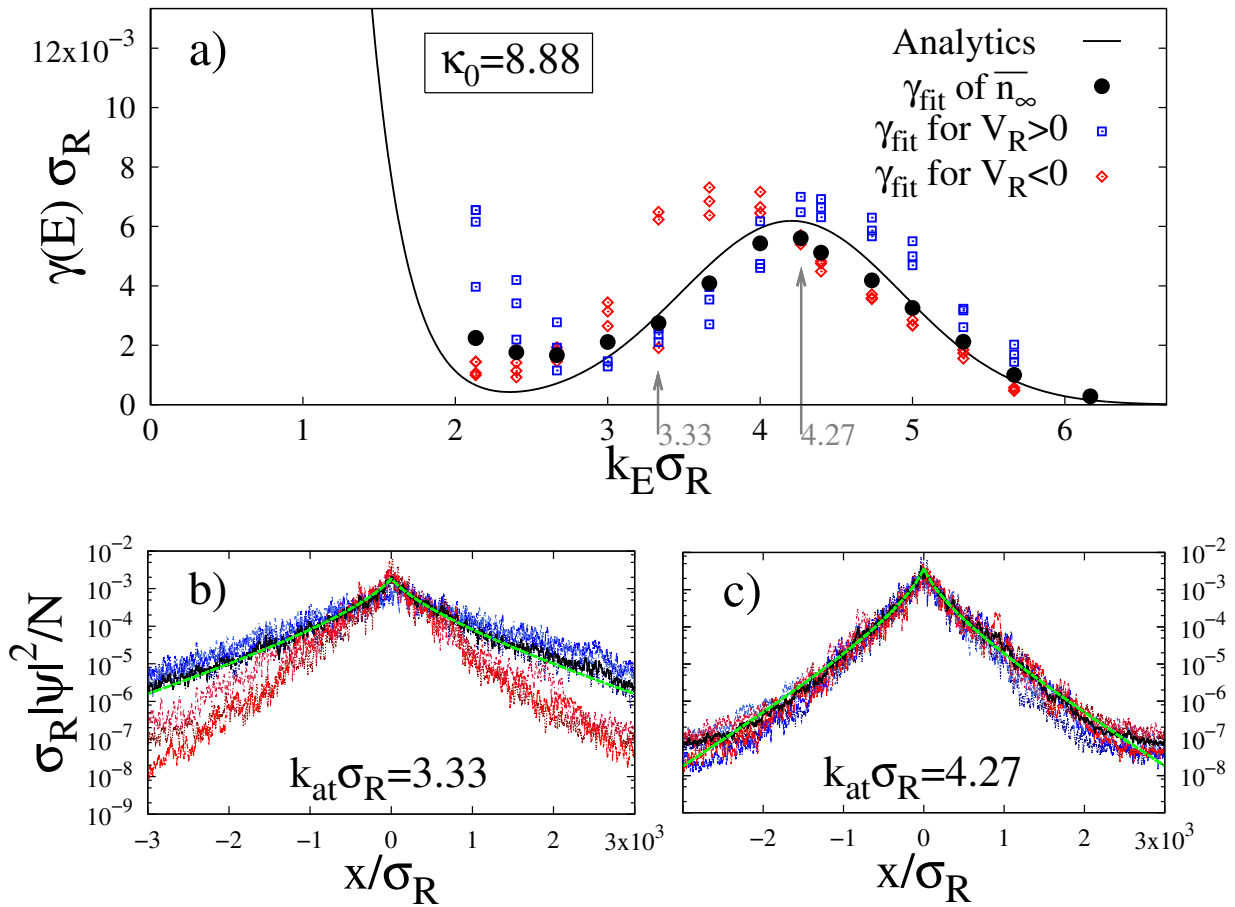


Figure 8.6: Anderson localization in 1D speckle potentials with the autocorrelation function (8.3),  $\kappa_0 = 8.88$  and  $V_R = \pm 0.72(\hbar^2/m\sigma_R^2)$ . (a) Lyapunov exponent versus particle energy as obtained from Eq. (4.4) (solid black line) and from fits of Eq. (4.17) to numerical data (points). (b-c) Stationary density profiles obtained numerically using the initial state (8.6) with  $k_w \sigma_R = 0.24$  and two different values of  $k_{at}$ . The figures show the results for six realizations of the disorder [three with  $V_R > 0$  (blue data) and three with  $V_R < 0$  (red data)], the averaged density profile (black data) and the fits of  $P_\infty(x)$  to the latter (green line). The extracted values of  $\gamma_{fit}$  for each realization and for the averaged profile are reported in (a).

blue and red detunings (see Fig. 8.6), which can be ascribed to higher-order terms in the Born expansion. Indeed, they are consistent with the numerical results of Fig. 8.2, including the change of sign found around the local maximum of  $\gamma(E)$ . As outlined above, the Lyapunov exponent calculated from the phase formalism, and the quantity fitted in Figs. 8.5 and 8.6 are not the same, but they are closely related. Nevertheless, this difference is small and the strong increase of  $\gamma(E)$  appears for each realization in approximately the same region as predicted by Eq. (8.1). The parameters we used are relevant to current experiments as regards disorder [9, 17], observable space [9], and width of atom lasers [208–210]. The scheme, which requires a small change in current experiments hence allows one to directly observe the nonmonotonic behavior of  $\gamma(E)$  induced by the tailored correlations.

We have checked that the other speckle configuration (double-slit) leads to qualitatively

similar results. However, the two-Gaussian scheme allows for more compact formulas and avoids slope breaks of the  $\tilde{C}_2(k)$  function. The accuracy of the fitted  $\gamma(E)$  is then better and less sensitive to the width of the atomic momentum distribution  $k_w$ .

## 8.3 Higher dimensions

We now generalize the above results to higher dimensions ( $d > 1$ ), for which the localization scenario is more involved. Consider a particle of energy  $E$  undergoing multiple scattering in the disordered potential. At intermediate distance (between the Boltzmann mean free path  $l_B$  and the localization length  $L_{loc}$ ), the interference between the multiple scattering paths plays a negligible role, and normal diffusion dominates, with the diffusion constant  $D_B(E) = (\hbar/m)k_E l_B(E)/d$  [148, 149]. For weak, isotropic disorder [i.e. for  $\tilde{c}(\kappa) = \tilde{c}(|\kappa|)$ ], one finds (see appendix C.2)

$$l_B^{-1} = \frac{m^2 V_R^2 \sigma_R^d}{(2\pi)^{d-1} \hbar^4 k_E^{3-d}} \int d\Omega_d (1 - \cos \theta) \tilde{c}(2k_E \sigma_R |\sin(\theta/2)|) \quad (8.7)$$

with  $\Omega_d$  the hyperspherical angle in dimension  $d$ . On length scales larger than  $l_B$ , interference of multiple scattering paths can induce Anderson localization. In the framework of the self-consistent theory, one finds in 2D,  $\gamma(E) = l_B^{-1} \exp(-\pi k_E l_B/2)$  (see Sec. 5.3.3). In 3D,  $\gamma(E)$  is the unique solution of  $[1 - (\pi/3)(k_E l_B)^2] = \gamma l_B \times \arctan(1/\gamma l_B)$ , which exists only below the localization threshold (mobility edge), i.e. for  $k_E l_B < \sqrt{3/\pi}$  (see Ref. [16] and Sec. 6.2.3). In both cases the Lyapunov exponent can be formally written  $\gamma(E) = l_B^{-1} F_d(k_E l_B)$  where  $F_d$  is a decreasing function of  $k_E l_B$ , as conjectured in the introduction. It follows from Eq. (8.7) that, if  $\tilde{c}(\kappa)$  is as usual a constant or decreasing function of  $\kappa$ , then  $l_B(E)$  increases with  $E$ , and  $\gamma(E)$  decreases when  $E$  increases. As for the 1D case, this standard behavior can be changed by tailoring the disorder correlations so that  $\tilde{C}_2(\mathbf{k})$  increases strongly enough in a certain window, and observed in the same way.

**Two-dimensional speckle** – In 2D, we extend the previous double-slit scheme and we propose to use a speckle potential with isotropic correlations created by a uniformly illuminated ring-shaped diffuser of inner radius  $r$  and outer radius  $D/2$  (see ‘2D ring-shaped aperture’ in Sec. 3.2.1). For a thin enough ring ( $0.77D \lesssim 2r < D$ ), we find that  $\gamma(E)$  is nonmonotonous with a marked local maximum, so that the localization increases with the energy in a given window (as presented in Fig. 8.7). For the parameters of Fig. 8.7,  $\gamma(E)$  peaks to about  $5 \times 10^{-4} \sigma_R^{-1}$ , where  $\sigma_R = \lambda_L f / \pi D$ . For  $\sigma_R = 0.25 \mu\text{m}$ , it corresponds to  $L_{loc} \simeq 500 \mu\text{m}$ , which is within experimental reach [9]. Moreover, the width of the maximum is  $\Delta k \sim 0.1 \sigma_R^{-1}$ , which can be probed with the same atom laser as used in Fig. 8.6, the width of which is  $p_w = 0.0375 \hbar \sigma_R^{-1}$  (note that  $\sigma_R$  is a factor of 6.4 larger in the 1D double-Gaussian case presented in Sec. 8.2).

**Three-dimensional speckle** – In 1D and 2D we found simple setups to obtain the desired effect in speckles with isotropic correlations. The natural extension of the previous schemes in 3D would be a speckle obtained inside an integrating sphere in paraxial conditions, by a laser of wavelength  $k_L$  with a finite spectral width  $\delta_k$ . The correlation function in  $k$ -space is then given by the convolution of two 3D-shells of radius  $k_L$  and width  $\delta_k$ , and, for any value

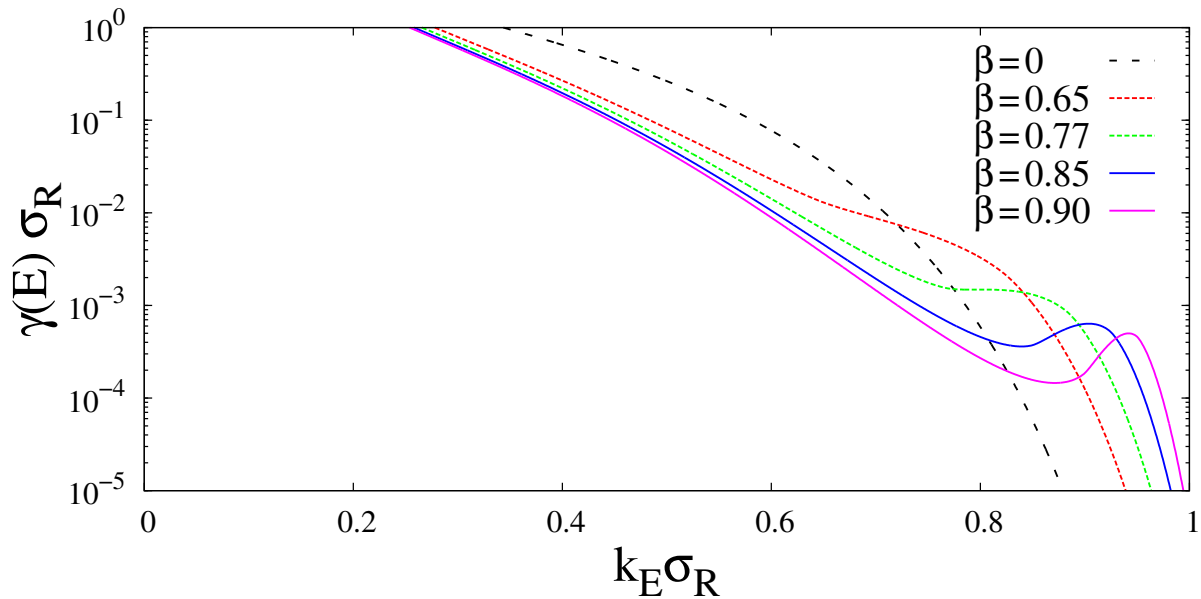


Figure 8.7: Lyapunov exponent versus energy in 2D speckle potentials created with a ring-shaped diffuser of inner radius  $r$  and outer radius  $D/2$  [see Fig. 3.5(b1)], for various values of  $\beta = 2r/D$  (indicated in the figure) and  $|V_R| = 0.25(\hbar^2/m\sigma_R^2)$ .

of  $\delta_k/k_L$ ,  $\tilde{C}_2(k)$  is decreasing; ruling out the possibility of obtaining  $\gamma(E)$  increasing with  $E$  with that scheme.

We found that it is easier in practice to tailor  $\tilde{C}_2(\mathbf{k})$  in anisotropic models. Then, Eq. (8.7) does not hold, and one has to use the tools of Chap. 2 and 5 to compute  $l_B(E)$  (see also Chap. 6). It can however be anticipated that tailoring the correlations in anisotropic models of disorder can also invert the standard behavior of  $\gamma(E)$ . Consider the 3D speckle potential obtained by one Gaussian laser beam, of waist  $w$  (in both transverse directions) [so-called *single-speckle* configuration in Chap. 6]. Due to the anisotropy of the disorder, the localization is described by an anisotropic Lyapunov tensor [ $\gamma(E) \equiv \mathbf{L}_{\text{loc}}^{-1}(E)$ ] of eigenaxes  $x$ ,  $y$  and  $z$ , and the Lyapunov exponent in all directions decreases [i.e.  $L_{\text{loc}}^u(E)$  increases] monotonically with  $E$ , as shown in Fig. 6.7(a). Let us now consider two coherent parallel Gaussian beams (propagating along  $z$ ), both of waist  $w$  and separated by a distance  $\Delta$  along  $\rho_x$ , similarly as for the double-Gaussian scheme in the 1D case (see Fig. 8.1). This scheme resembles that of the coherent-speckles, but here the two Gaussian beams are parallel, and not orthogonally-crossed. The correlation function obtained in this configuration is computed in appendix D.3.3 [see Eq. (D.15)] and displayed in Fig. D.5 for  $\Delta/w = 4$  and 16 (and  $\sigma_{\parallel}/\sigma_{\perp} = 5.8$ , as throughout Chap. 6). The interference between the two speckles create two bumps in  $\tilde{C}_2(\mathbf{k})$  at  $\mathbf{k} \simeq \pm k_0 \hat{\mathbf{k}}_z$  with  $k_0 = \sqrt{2}\pi\Delta/\lambda_L f$ . These two bumps are expected to strongly enhance localization around the energy  $E \propto \hbar^2 k_0^2/2m$ . Figure 8.8 shows the Lyapunov exponents found using the self-consistent theory of Anderson localization for anisotropic disorder presented in Chap. 2<sup>6</sup>. For all the configurations of Fig. 8.8, we find one or several mobility edges (indicated by the arrows), and  $\gamma^u(E)$  exhibits, below the right most mobility edge, a local maximum in each direction  $u$ , hence realizing the desired effect. As expected, the maximum is found for approximately  $k_E \propto k_0$ . For the parameters of the right (purple) curve,  $\gamma(E)$  vanishes (i.e.

6. We use the same numerical procedure than in Chap. 6, with the correlation function given by Eq. (D.15).

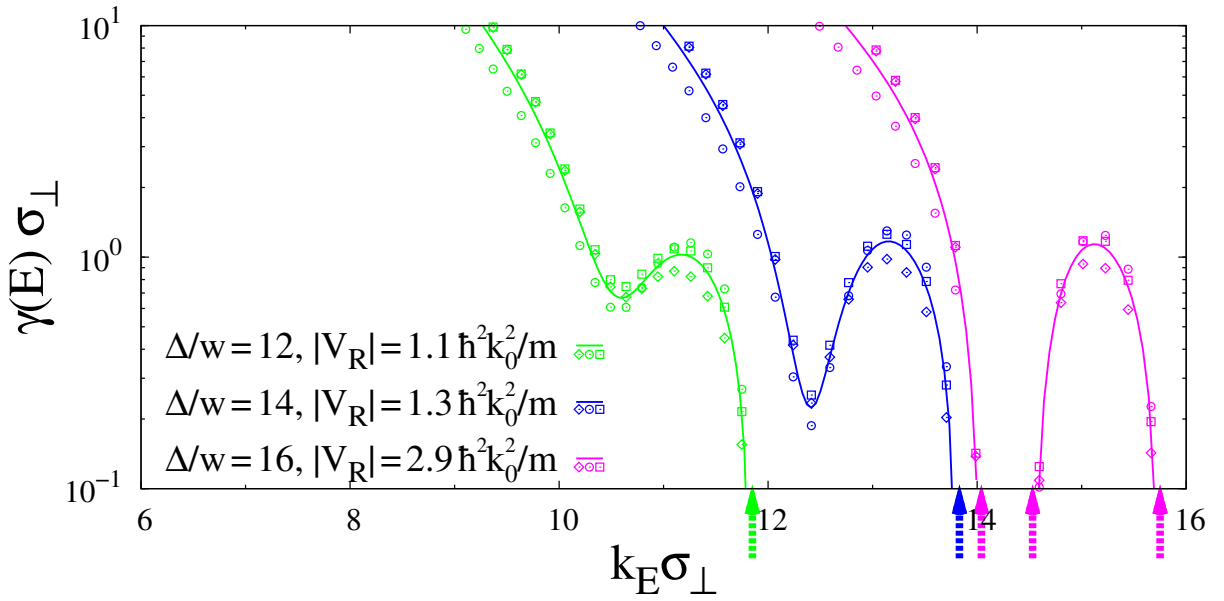


Figure 8.8: Lyapunov exponents along the transport eigenaxes ( $x$ : diamonds;  $y$ : dots;  $z$ : squares) and their geometric average (lines) versus energy in a 3D speckle potential created by two Gaussian beams (waist  $w$  and separation  $\Delta$ ) for various parameters (indicated in the figure) and  $\sigma_{\parallel}/\sigma_{\perp} = 5.8$ . The arrows indicate the mobility edges. We recall that  $\sigma_{\perp} = \lambda_L f / \pi w$ .

the localization length diverges) in a given energy window, thus opening a band of extended states inside the localized region, delimited by two new mobility edges.

## Conclusion

In summary, we have shown that the Anderson localization of noninteracting quantum particles (matter waves) induced by a correlated disorder in free space can increase with the particle energy in a given window. In contrast to other systems where this behavior is more common, e.g. electrons in crystal lattices or light waves in dielectric materials, it is here purely due to appropriately tailored correlations of the disorder. We have proposed suitable methods to tailor the correlations in optical disorder, which require moderate modifications of existing schemes in 1D [9], 2D [17], and 3D [18, 19] and involve two laser beams or a mask on the diffusive plate. We have proposed a method to observe it in any dimension, using a strongly peaked atomic energy distribution, which conversely differs from standard schemes used so far with ultracold atoms, and explicitly demonstrated its efficiency in the 1D case.

Let us finally discuss how the increase of  $\gamma(E)$  with  $E$  can serve as a smoking-gun evidence of quantum versus classical localization of particles. For any experiment on localization, Anderson localization should be discriminated from other possible effects. For light waves for instance, it is necessary to distinguish it from absorption, which also produces exponential decay of the intensity. This can be done by analyzing the statistics of transmission [30, 111]. In contrast, ultracold atoms are not subjected to absorption, but they can be classically localized (trapped) in potential wells, below the localization threshold. Then, absence of diffusion and exponential decay of density profiles can hardly be viewed as indisputable proof of Anderson localization. For instance, classical particle localization in some non-percolating

media can lead to qualitatively similar effects, for instance in 2D speckle potentials [23]. For *any model of disorder* however, the *classical localization length*, defined as the average size of the classically-allowed patches [211], increases with the particle energy. Hence, the decrease of the *quantum localization length* with the particle energy discussed in this work has no classical equivalent, and can be viewed as a smoking gun of quantum localization for particles. This effect could be useful to demonstrate Anderson localization of ultracold atoms, in particular for 2D speckle potentials, which have a percolation threshold significantly higher than their 3D counterparts. From a practical point of view, it does not require accumulation of many statistical data, in contrast to standard methods used for classical waves [30, 111].

# Conclusion

**Summary** – In this manuscript we have studied transport and Anderson localization of quantum waves in a disordered potential, with a special emphasis on the effects of disorder correlations, which in dimensions  $d > 1$  are usually anisotropic. Those are particularly relevant for speckle potentials, in which correlations are naturally anisotropic and can be tailored.

We first studied Anderson localization in one dimension (see Chap. 4 and Ref. [22]), for which exact calculations can be performed. The phase formalism permits to compute the average Lyapunov exponent in a perturbative approach. By comparing to numerical calculations, we found that the first correction to Born order is non-negligible in standard speckle potentials, for typical experimental parameters. It is different for  $V_R > 0$  and  $V_R < 0$ , and may be observed by comparing the effect of blue and red-detuned potentials. We then revisited the theoretical model for the expansion of a matter wave packet in a disordered potential by including the initial phase-space density distribution and the disorder-induced spectral broadening. We found that both play a significant role, and lead to a profile more complex than a simple exponential decay. In particular, we predict a crossover between a short- and a long-distance exponential decays, due to the specific behaviour of the probability of quantum transport. It may explain the large distance behaviour of experimental data, where signs of such a deviation is observed.

We then studied Boltzmann transport and Anderson localization, with the self-consistent theory, in dimension higher than one.

In two dimensions, we studied a very simple model that features anisotropic correlations: an anisotropic Gaussian correlation function (see Chap. 5). In spite of its simplicity, it shows a non-trivial transport behaviour. For any geometrical anisotropy factor, we found a non-monotonous behaviour of the anisotropies of scattering and diffusion with energy. Applying the self-consistent theory to this model we recovered that the localization length diverges exponentially with energy, thus rendering its experimental measurement and the observation of Anderson localization in 2D, challenging. However, as this model of disorder has already been implemented experimentally and our approach here is quantitative, we expect those results to serve as a guideline for future experiments in 2D. In three dimensions, we studied three models of speckle disorder with anisotropic fine-structured correlations (see Chap. 6 and Ref. [25]). We also found various interesting anisotropic quantum transport effects, such as the anisotropic suppression of the white-noise limit and an inversion of the transport anisotropy with energy. Applying the self-consistent theory, we recovered that there is a transition between a localized and a diffusive regime, separated by a mobility edge.

We then proposed a method to go beyond the on-shell calculation of the mobility edge, by estimating a disorder-induced correction. To do so, we have included the effect of the real-part of the self-energy, which induces a shift of the on-shell prescription. When comparing to

another method applicable to isotropic speckle disorder [169], which includes the full structure of the spectral function, but which is difficult to implement for anisotropic correlations, we find a good agreement. It validates our method, and supports the idea that we have probably retained the main effect. The advantages of our method are (i) that it is of clear physical meaning and (ii) that it can be implemented for disorder with structured correlations. We have applied it to the same three models of speckle potentials and find that the added term (the real part of the self-energy) plays a major role for determining the mobility edge.

Our calculations allow for direct comparison with recent experimental achievements (see Chap. 7). When comparing with Ref. [18] we found that their measurements do not compare well with our calculations. First, no quantitative agreement was found for the anisotropy of the localized component. Further experimental and theoretical work would be needed to understand this discrepancy. On one hand, we have argued that the observed anisotropy is surprisingly large. On the other hand corrections to our calculations cannot be excluded at this stage. They may result from details of the experimentally realized correlation function and from relevant diagrams that are not included in our calculations. Second, the discrepancy of the experimentally inferred and the calculated mobility edge is even qualitative. While we predict a mobility edge below the average value of the disorder, the experimental estimate is above. We however argued that the method to infer the mobility edge is not reliable. In this case, an experimental determination of the energy distribution would be required. In the discussion of Ref. [19], we found a semi-quantitative agreement. By introducing a single free-parameter (the 'heuristic shift') in the analysis, we found a fair overall agreement between theory and experiment. It is actually the introduction of the heuristic shift that stimulated the calculations on the mobility edge underlined above [25]. The estimated shift of the mobility edge and the heuristic shift agree within a factor of the order of 1.7. At this stage, it is a fair agreement, which seems to support our calculations. A precise test of the latter would however require an experimental determination of the energy distribution in disordered ultra-cold atomic gases, which is not available so far.

Finally we have shown (see Chap. 8 and Refs. [26,27]) that tuning disorder correlations can permit to induce further counter-intuitive effects than those introduced above. For example, by tailoring speckle correlations, we have predicted that Anderson localization can increase with energy in 1D, 2D and 3D. We have proposed a scheme to observe this effect in all dimensions, and numerically verified it for the 1D case. We also argued that observing the localization length increase with energy can serve to discriminate quantum versus classical localization of particles in continuous disorder. This could be particularly useful for experiments in 2D speckle potentials, for which the classical percolation threshold is high.

**Outlook** – The field of disordered quantum gases is just emerging. On one hand, if had landmark successes in the very last years, in particular evidence of Anderson localization in one dimension [9,10] and three dimensions [18,19]. On the other hand, many questions remain open. Hereafter, we limit ourselves to those that directly follow from the work reported in this thesis.

In dimension  $d = 1$ , we now have a good understanding of Anderson localization in expanding, non-interacting, ultra-cold gases. We have shown that corrections to lowest-order calculations are not negligible. In order to explain the discrepancy between blue and red detunings, it would be interesting to go beyond second order in the calculation of the probability of quantum diffusion in a Berezinskii-Gogolin-like formalism, which is directly

related to the observed density profiles (in contrast to the phase formalism). It would be enlightening to estimate the effect of interactions in similar experiments. From a theoretical point of view, the effect of interactions is of notorious difficulty. Including them in theoretical calculations or numerics would obviously be of outmost interest. It might further modify the shape of the localized density profile.

The possibility to study the effect of disorder correlations is also a great asset of ultra-cold atoms, which has not been much exploited so far. In this thesis, we have pointed out several interesting effects, which can be addressed experimentally thanks to optical control of the disorder. From a theoretical perspective, there are still open questions in dimensions  $d > 1$ . In the on-shell self-consistent approach used here, we have selected some diagrams to compute quantum corrections. The choice of diagrams we made was motivated by previous studies, and is expected to be relevant [41, 153, 154, 189], in particular in isotropic disorder. In anisotropic disorder the anisotropy of Boltzmann diffusion is preserved by those quantum corrections. In our cases, we find a rather moderate anisotropy of the diffusion tensor, and the self-consistent hypothesis seems reasonable. As pointed out above, however, a correction to the anisotropy factors in the localized regime cannot be excluded, which may be large for strongly anisotropic disorder. It would be interesting to develop theories going beyond the self-consistent theory. It would require an approach where the anisotropies of the quantum corrected tensor are not the same as those of Boltzmann diffusion by construction. A possibility would be to resolve the full quantum Boltzmann equation, or implement an approach such as that of Ref. [169] for anisotropic disorder. In addition, such an approach would allow one to include the full structure of the spectral function into the theory, which, in 3D, would also permit to compare our shifted on-shell approach. From a practical point of view, it is however not clear that such an approach is practicable without relying on some symmetries of the problem. Then, as it was done all along advances in the field of disordered quantum gases, strong interplay between experiments and theory would be of outmost importance.

## Version française

**Résumé** – Dans ce mémoire nous avons étudié le transport et la localisation d’Anderson d’ondes de matière dans un potentiel désordonné, en mettant l’accent sur les effets des corrélations du désordre, qui sont souvent anisotropes en dimensions  $d > 1$ . Ceci est particulièrement pertinent pour les potentiels de speckle, pour lesquels les corrélations sont naturellement anisotropes et peuvent être adaptées.

Dans un premier temps, nous avons étudié la localisation d’Anderson dans le cas unidimensionnel (cf Chap. 4 et Réf. [22]), dans lequel des calculs exacts peuvent être menés. Le formalisme de phase permet de calculer l’exposant de Lyapunov de façon perturbative. En comparant à des simulations numériques, nous avons trouvé que la première correction à l’ordre de Born est non-négligeable dans des potentiels de speckle standards, pour des paramètres expérimentaux typiques. Elle est différente pour  $V_R > 0$  et  $V_R < 0$ , et pourrait être mesurée en comparant les effets d’un potentiel décalé vers le bleu, et d’un potentiel décalé vers le rouge. Nous avons ensuite revisité le modèle théorique de l’expansion d’un paquet d’onde de matière dans un potentiel désordonné en incluant la densité initiale dans l’espace des phases et l’élargissement spectral induit par le désordre. Nous avons trouvé que les deux jouent un rôle significatif et conduisent à un profil de densité plus complexe qu’une simple décroissance exponentielle. En particulier, nous avons prédit un crossover entre des décroissances exponentielles à courte et à longue distance, qui est dû au comportement spécifique de la probabilité de transport quantique. Cela pourrait expliquer le comportement à grande distance des données expérimentales, où des signes d’une telle déviation sont observés.

Nous avons ensuite étudié la diffusion de Boltzmann et la localisation d’Anderson, dans le cadre de la théorie « self-consistent », en dimensions supérieures à un.

A deux dimensions, nous avons étudié un modèle simple qui présente des corrélations anisotropes : une fonction de corrélation gaussienne et anisotrope (cf Chap. 5). Bien qu’il soit très simple, ce modèle présente des propriétés de transport non-triviales. Quelque soit le facteur d’anisotropie géométrique, nous avons trouvé un comportement non-monotone des anisotropies de scattering et de diffusion en fonction de l’énergie. En appliquant la théorie « self-consistent » à ce modèle nous avons retrouvé que la longueur de localisation diverge exponentiellement avec l’énergie, ce qui la rend difficile à mesurer expérimentalement, et qui fait de l’observation de la localisation d’Anderson à 2D un défi. Cependant, comme ce modèle de désordre a déjà été implémenté dans des expériences et comme notre approche est quantitative, ces résultats sont destinés à servir de guide pour les expériences à venir en 2D. A trois dimensions, nous avons étudié trois modèles de speckle ayant des corrélations anisotropes présentant de fines structures (cf Chap. 6 et Réf. [25]). De même, nous avons trouvé divers effets intéressants de transport quantique anisotrope, tels que la suppression anisotrope de la limite de bruit blanc, et une inversion de l’anisotropie de transport avec l’énergie. En utilisant la théorie « self-consistent », nous avons retrouvé qu’il y a une transition entre des régimes localisé et diffusif, séparés par un seuil de mobilité.

Nous avons ensuite proposé une méthode pour aller au-delà du calcul « on-shell » du seuil de mobilité, en estimant une correction induite par le désordre. Pour cela, nous avons inclus l’effet de la partie réelle de la « self-energy », qui revient à une renormalisation de la prescription « on-shell ». En comparant à une autre méthode applicable à un modèle de speckle isotrope [169], qui inclut la structure complète de la fonction spectrale, mais qui est difficile à implémenter pour des corrélations anisotropes, nous avons trouvé un bon accord. Cela valide notre méthode, et montre que nous avons probablement retenu l’effet principal.

Les avantages de notre méthode sont (i) qu'elle a un sens physique clair et (ii) qu'elle peut être implémentée pour un désordre ayant des corrélations structurées. Nous l'avons appliquée aux trois modèles de potentiels de speckle précédents et nous avons trouvé que le terme pris en compte (la partie réelle de la « self-energy ») joue un rôle majeur dans la détermination du seuil de mobilité.

Nos calculs permettent une comparaison directe avec les observations expérimentales récentes (cf Chap. 7). En comparant à la Réf. [18] nous avons trouvé que leurs mesures ne se comparent pas bien à nos calculs. Premièrement, aucun accord quantitatif n'a été trouvé en ce qui concerne l'anisotropie de la composante localisée. Un travail expérimental et théorique plus approfondi semble nécessaire pour comprendre cette différence. D'un côté, nous avons argumenté que l'anisotropie observée est étonnamment grande. De l'autre, de possibles corrections à nos calculs ne peuvent être exclues. Elles pourraient résulter des détails de la fonction de corrélation réalisée expérimentalement et de diagrammes pertinents qui ne sont pas inclus dans nos calculs. Deuxièmement, l'écart entre la seuil de mobilité déduit des expériences et calculé est même qualitatif. Alors que nous prédisons un seuil de mobilité en-dessous de la valeur moyenne du désordre, l'estimation expérimentale se trouve au-dessus. Nous estimons cependant que la méthode utilisée par Kondov *et al.* pour déduire le seuil de mobilité n'est pas fiable. Dans ce cas, une détermination expérimentale de la distribution d'énergie serait nécessaire. Dans l'analyse de la Réf. [19], nous avons trouvé un accord semi-quantitatif. En introduisant un seul paramètre libre (le « shift heuristique ») dans l'analyse, nous avons trouvé un bon accord général entre la théorie et l'expérience. C'est en réalité l'introduction de ce shift heuristique qui a stimulé les calculs sur le seuil de mobilité évoqués ci-dessus [25]. Le décalage estimé du seuil de mobilité et le shift heuristique coïncident avec un facteur 1.7. A ce stade il s'agit d'un accord correct, ce qui va dans le sens de nos calculs. Un test précis de ces derniers nécessiterait cependant la détermination expérimentale de la distribution d'énergie d'un gaz d'atomes ultrafroids désordonnés, qui n'est pas disponible pour l'instant.

Pour finir, nous avons montré (cf Chap. 8 et Réfs. [26, 27]) que modifier les corrélations du désordre permet d'induire d'autres effets contre-intuitifs que ceux introduits ci-dessus. Par exemple, en adaptant les corrélations d'un speckle, nous avons prédit que la localisation d'Anderson peut augmenter avec l'énergie à 1D, 2D et 3D. Nous avons proposé une méthode pour observer cet effet en toute dimensionnalité, et nous l'avons vérifiée numériquement dans le cas 1D. Nous avons aussi argumenté qu'observer la longueur de localisation augmenter avec l'énergie peut être utile pour distinguer la localisation quantique de la localisation classique de particules dans un désordre continu. Ceci pourrait être particulièrement intéressant pour les expériences utilisant des potentiels de speckle 2D, dans lesquels le seuil de percolation classique est élevé.

**Perspectives** – Le domaine des gaz quantiques désordonnés est en train d'émerger. D'un côté il a connu des succès remarquables dans les toutes dernières années, en particulier grâce aux preuves de localisation d'Anderson à une dimension [9, 10] et trois dimensions [18, 19]. De l'autre, de nombreuses questions restent encore ouvertes. Ci-après, nous nous limitons à celles qui découlent directement du travail présenté dans ce mémoire.

En dimension  $d = 1$ , nous avons maintenant une bonne compréhension de la localisation d'Anderson dans des gaz d'atomes ultrafroids, sans interaction, en expansion. Nous avons montré que les corrections aux calculs au premier ordre ne sont pas négligeables. Pour expliquer l'écart entre les speckles décalés vers le bleu et vers le rouge, il serait intéressant d'aller

au-delà du deuxième ordre dans le calcul de la probabilité de diffusion quantique, dans un formalisme similaire à celui de Berezinskii-Gogolin, qui est directement relié aux profils de densité observés (contrairement au formalisme de phase). Il serait instructif d'estimer l'effet des interactions dans de telles expériences. D'un point de vue théorique, l'effet des interactions est un problème notoirement difficile. Les inclure dans des calculs théoriques ou numériques serait du plus grand intérêt. Cela pourrait modifier encore l'allure du profil de densité localisé.

La possibilité d'étudier l'effet des corrélations du désordre est aussi un grand atout des atomes ultrafroids, qui n'a pas été très exploité jusqu'à présent. Dans ce mémoire, nous avons signalé plusieurs effets intéressants, qui peuvent être abordés expérimentalement grâce à un contrôle optique du désordre. D'un point de vue théorique, il reste des questions ouvertes en dimensions  $d > 1$ . Dans l'approche « on-shell self-consistent » utilisée ici, nous avons sélectionné quelques diagrammes pour calculer les corrections quantiques. Notre choix a été motivé par de précédentes études, et est censé être pertinent [41, 153, 154, 189], en particulier pour un désordre isotrope. Pour un désordre anisotrope, l'anisotropie de la diffusion de Boltzmann est préservée par ces corrections quantiques. Dans nos cas, on a trouvé des tenseurs de diffusion ayant des anisotropies modérées, et l'hypothèse « self-consistent » semble raisonnable. Cependant, comme signalé ci-dessus, une éventuelle correction aux facteurs d'anisotropie dans le régime localisé ne peut être exclue, et elle pourrait être importante pour des désordres fortement anisotropes. Il serait intéressant de développer des théories permettant d'aller au-delà de la théorie « self-consistent ». Cela nécessiterait de développer une approche dans laquelle les anisotropies du tenseur corrigé quantiquement ne sont pas les mêmes que celles de l'anisotropie de Boltzmann par construction. Une possibilité serait de résoudre l'équation de Boltzmann quantique, ou d'implémenter une approche telle que celle de la Réf. [169] dans un désordre anisotrope. D'un point de vue pratique, il n'est pas clair qu'une telle approche puisse être mise en oeuvre sans utiliser des symétries du problème. Ainsi, comme cela a été le cas au cours des avancées dans le domaine des gaz quantiques désordonnés, une forte interaction entre les expériences et la théorie sera de la plus grande importance.

# Appendix A

## Tools for Lyapunov exponents calculations in one dimension

### A.1 Third order of the phase-formalism

In Chap. 4 we have described the phase formalism and given the formulas for the 2<sup>nd</sup> order. Here we provide explicit formulas for the 3<sup>rd</sup> order term for several models of disorder used in the manuscript. The expression of the third-order term of the phase formalism is given by Eq. (4.6).

For the single-slit configuration (also called square aperture, see Sec. 3.2.1), the  $f_3$  function that intervenes in Eq. (4.3) is [14]

$$f_3(\kappa) = \frac{-\pi}{8} [(1 - \kappa) \ln(1 - \kappa) + \kappa \ln(\kappa)] \Theta(1 - \kappa). \quad (\text{A.1})$$

For the double-slit configuration (see Sec. 8.2.2), the  $f_3$  function reads

$$f_3(\kappa) = \frac{\pi}{8(1 - \beta)^3} \left\{ \Theta\left(\frac{1 - \beta}{2} - \kappa\right) f_{3,1}(\kappa) + \Theta\left(\frac{1 - \beta}{2} - \left|\kappa - \frac{\beta + 1}{2}\right|\right) \right. \\ \left. \times \left[ \Theta\left(\kappa - \frac{\beta + 1}{2}\right) f_{3,2}(\kappa) + \Theta\left(\frac{\beta + 1}{2} - \kappa\right) f_{3,3}(\kappa) \right] \right\}, \quad (\text{A.2})$$

with

$$f_{3,1}(\kappa) = g(2) - g[2(1 - \kappa)] - 2g(2\kappa) + 2g(1 - \beta) - g(2\beta) - 2g(1 - \beta - 2\kappa) \\ + g(1 - 2\kappa + \beta) + g[2(\kappa + \beta)] - g(1 + 2\kappa + \beta),$$

$$f_{3,2}(\kappa) = -g(2\kappa) - g(1 - \beta) + g(2\beta) + g(2\kappa + 1 - \beta) \\ + g(2\kappa - 2\beta) - g(1 + \beta) + g(1 - 2\kappa + \beta),$$

and

$$f_{3,3}(\kappa) = g(2) - g[2(1 - \kappa)] - g(2\kappa) + g(1 - \beta) - g(-1 + 2\kappa - \beta) \\ - g(1 + \beta) + g(2\kappa - 1 - \beta)$$

where  $g(x) \equiv x \ln(x)$ .

For the double-Gaussian configuration (see also Sec. 8.2.2), we find :

$$\begin{aligned}
f_3(\kappa) = & \frac{1}{32\sqrt{3}} \left\{ 4\pi e^{-\frac{4}{3}\kappa^2} \operatorname{erfi} \left( \frac{\kappa}{\sqrt{3}} \right) + 2\pi e^{-\kappa^2} \times \right. \\
& \left[ \left\{ e^{-\frac{1}{3}(\kappa+\kappa_0)^2} \operatorname{erfi} \left( \frac{\kappa+\kappa_0}{\sqrt{3}} \right) + e^{-\frac{1}{3}(\kappa-\kappa_0)^2} \operatorname{erfi} \left( \frac{\kappa-\kappa_0}{\sqrt{3}} \right) \right\} \right. \\
& + 2e^{-\frac{\kappa_0^2}{4}} \cosh(\kappa\kappa_0) \left\{ e^{-\frac{1}{3}(\kappa+\frac{\kappa_0}{2})^2} \operatorname{erfi} \left( \frac{\kappa+\kappa_0/2}{\sqrt{3}} \right) \right. \\
& \left. \left. \left. + e^{-\frac{1}{3}(\kappa-\frac{\kappa_0}{2})^2} \operatorname{erfi} \left( \frac{\kappa-\kappa_0/2}{\sqrt{3}} \right) \right\} \right] \right\} \quad (\text{A.3})
\end{aligned}$$

where  $\operatorname{erfi}(z) \equiv -i \operatorname{erf}(iz)$  is the imaginary error function, with  $\operatorname{erf}(x) \equiv 2 \int_0^x dt e^{-t^2} / \sqrt{\pi}$  the error function.

## A.2 Transfer matrix calculations

We describe here the numerical method used to determine the Lyapunov exponent for transmission schemes in 1D disorder.

**Numerical technique** – To study numerically the eigenstate  $\phi_E(x)$  associated to energy  $E$ , for the Schrödinger equation (4.1), one can rewrite it:

$$\partial_x \phi_E(x) = \phi'_E(x) \quad (\text{A.4a})$$

$$\partial_x \phi'_E(x) = \frac{2m}{\hbar^2} [V(x) - E] \phi_E(x), \quad (\text{A.4b})$$

which can be expressed in the compact form

$$\partial_x \Psi(x) = M(x) \Psi(x) \quad (\text{A.5})$$

with

$$\Psi(x) = \begin{pmatrix} \phi_E(x) \\ \phi'_E(x) \end{pmatrix} \quad \text{and} \quad M(x) = \begin{pmatrix} 0 & 1 \\ \frac{2m}{\hbar^2} [V(x) - E] & 0 \end{pmatrix} \quad (\text{A.6})$$

Let us fix the energy  $E$  and take for initial conditions<sup>1</sup>  $\Psi(x=0) = \{1, k_E / \tan(\theta)\}$  where  $\theta \in [0, 2\pi]$  is a random phase. We now discretize the system with a spatial step  $\Delta x$  and solve Eq. (A.5) by recursion using the fourth-order Runge-Kutta algorithm [180]. The solution at large distance  $x$  is, on average, the superposition of an exponentially-growing (as  $e^{\gamma(E)x}$ ) and an exponentially-decreasing (as  $e^{-\gamma(E)x}$ ) wave function. Therefore in practice we find that, on average, the solution grows exponentially across the system<sup>2</sup>. We then extract

1. It amounts to setting the incoming wave:  $\phi_E(x \leq 0) = \cos(k_E x + \theta)$  and  $\phi'_E(x \leq 0) = k_E \sin(k_E x + \theta)$ .

2. We do not find an extinction of the incoming wave, as would be expected in a transmission scheme experiment, because our limiting conditions do not model such an experiment. Here we set  $\phi_E(x \leq 0) = \cos(k_E x + \theta)$ , whereas in a transmission experiment the wave function at  $x < 0$  is the sum of the incoming wave and a reflected one  $\phi_E(x < 0) = A_1 \cos(k_E x + \theta) + A_2 \sin(k_E x + \theta')$ .

the Lyapunov exponent  $\gamma(E)$  for each realization by fitting  $A + \gamma(E)|x|$  to  $\ln[r(x)/r(0)] = \ln\left(\sqrt{\phi_E(x)^2 + [\phi_E(x)/k_E]^2}\right)$  across the sample (see Sec. 4.1.1). By repeating the simulation for many realizations of the disorder, we have access to the full distribution of Lyapunov exponents. After averaging, we get the average Lyapunov exponent  $\bar{\gamma}(E)$ . It is shown as a function of energy in different disorder configurations in Figs. 4.1, 8.2 and 8.3.

**Statistics** – One can show that for  $\delta$ -point scatterers, the transmission probability across a system of length  $L$ ,  $T(L) = [r(L)/r(0)]^2$ , is a random quantity which follows a random walk, and that the distribution of its logarithm in weak disorder, and for large-enough systems ( $L \gg \bar{\gamma}^{-1}$ ), is given by [37, 176]:

$$P[\ln(T)] = \frac{1}{2\sqrt{2\pi\bar{\gamma}L}} \exp\left[-\frac{(\ln(T) + 2\bar{\gamma}L)^2}{8\bar{\gamma}L}\right]. \quad (\text{A.7})$$

It gives that the transmission follows a log-normal distribution:

$$P(T) = \frac{1}{2T\sqrt{2\pi\bar{\gamma}L}} \exp\left[-\frac{(\ln(T) + 2\bar{\gamma}L)^2}{8\bar{\gamma}L}\right]. \quad (\text{A.8})$$

When  $L \rightarrow \infty$ , Eq. (A.7) converges to a Dirac distribution. Therefore, in infinite systems, the logarithm of the transmission  $\ln[T(L)]$  is a self-averaging quantity [37]: it converges to its statistical average  $\overline{\ln[T(L)]} = -2\bar{\gamma}L$ . However, for  $\bar{\gamma}L \gg 1$ , we find in Eq. (A.8) that the relative fluctuations of the transmission coefficient increase with  $L$

$$\frac{\Delta T}{\bar{T}} = \frac{\sqrt{2\pi\bar{\gamma}L}}{3} \exp\left[\frac{\bar{\gamma}L}{4}\right], \quad (\text{A.9})$$

i.e.  $T$  does not converge to a deterministic value when  $L$  increases, it is not a self-averaging quantity.

Finally, we find that the Lyapunov exponent  $\gamma \equiv -\ln[T(L)]/2L \xrightarrow{L \rightarrow \infty} \bar{\gamma}$  is also a self-averaging quantity, and its probability distribution is given by Eq. (4.8).



## Appendix B

# Probability of quantum transport in one dimension

### B.1 Introduction

In Sec. 2, we have introduced the probability of transport between two points  $\mathbf{r}$  and  $\mathbf{r}'$  for a particle of energy  $E$  in any dimension. For  $t > 0$ , it is explicitly given by [see Eqs. (2.20)-(2.22) and (2.31)]

$$P(\mathbf{r} - \mathbf{r}_0, t|E) = \frac{1}{2\pi N(E)} \int \frac{d\hbar\omega}{2\pi} e^{-i\omega t} \int \frac{d\mathbf{k}}{(2\pi)^d} \int \frac{d\mathbf{k}'}{(2\pi)^d} \quad (\text{B.1})$$

$$\times \int \frac{d\mathbf{q}}{(2\pi)^d} e^{i\mathbf{q}\cdot\mathbf{r}} \int \frac{d\mathbf{q}'}{(2\pi)^d} e^{-i\mathbf{q}'\cdot\mathbf{r}_0} \overline{\langle \mathbf{k}_+ | G(E_+) | \mathbf{k}'_+ \rangle \langle \mathbf{k}'_- | G^\dagger(E_-) | \mathbf{k}_- \rangle}.$$

**Real-space formulation** – In 1D we will see that it is convenient to work with the diagrams in real space instead of momentum space. Using the transformation

$$\int \frac{d\mathbf{q}}{(2\pi)^d} e^{i\mathbf{q}\cdot\mathbf{r}} \int \frac{d\mathbf{q}'}{(2\pi)^d} e^{-i\mathbf{q}'\cdot\mathbf{r}_0} \overline{\langle \mathbf{k}_+ | G(E_+) | \mathbf{k}'_+ \rangle \langle \mathbf{k}'_- | G^\dagger(E_-) | \mathbf{k}_- \rangle} \quad (\text{B.2})$$

$$= \int d\mathbf{r}' e^{-i\mathbf{k}\cdot\mathbf{r}'} \int d\mathbf{r}'' e^{i\mathbf{k}'\cdot\mathbf{r}''} \overline{\langle \mathbf{r}_+ | G(E_+) | \mathbf{r}_{0+} \rangle \langle \mathbf{r}_{0-} | G^\dagger(E_-) | \mathbf{r}_- \rangle}$$

where  $\mathbf{r}_\pm = \mathbf{r} \pm \mathbf{r}'/2$  and  $\mathbf{r}_{0\pm} = \mathbf{r}_0 \pm \mathbf{r}''/2$ , therefore we find (for  $t > 0$ )

$$P(\mathbf{r} - \mathbf{r}_0, t|E) = \frac{1}{2\pi N(E)} \int \frac{d\hbar\omega}{2\pi} e^{-i\omega t} \overline{\langle \mathbf{r} | G(E_+) | \mathbf{r}_0 \rangle \langle \mathbf{r}_0 | G^\dagger(E_-) | \mathbf{r} \rangle}. \quad (\text{B.3})$$

**Assumptions** – The following calculation of the probability of quantum transport [Eq. (B.3)] relies on the one-dimensional approach introduced by Berezinskii in Ref. [155] and extended to correlated disorder by Gogolin *et al.* [70,71]. As explained in the following, this approach is well suited for exact calculations in the weak disorder limit. The two-point correlation function of the disorder, written  $C_2(x - x') = \overline{V(x)V(x')}$  [with  $\overline{V} = 0$ ], is of typical width  $\sim \sigma_R$ . We will assume  $\sigma_R \ll l_s(E)$  and  $\lambda_E \ll l_s(E)$  where  $\lambda_E = 2\pi/k_E$  is the particle wavelength and  $l_s(E)$  is the on-shell scattering mean free path (i.e. the typical distance between successive

scattering events), which is true in the weak disorder limit. At the end of the calculation we also consider the long-time limit,  $\omega \rightarrow 0$ , more precisely we assume that we have  $\omega \ll E/\hbar$ .

Note that in Refs. [70, 71, 155], the initial state is a statistical superposition with an given energy distribution (e.g. Fermi distribution), and it is the density-density correlation function  $\overline{\text{Tr} [\delta(E - \hat{H})\hat{n}(x, t)\hat{n}(x_0, t_0)]}$  which is computed. However the formalism presented in Chap. 2 and here is slightly more general as it doesn't rely on any assumption on the initial density matrix  $\rho(t_0)$ . The quantity  $\overline{\text{Tr} [\delta(E - \hat{H})\hat{n}(x, t)\hat{n}(x_0, t_0)]}$  can be expressed as

$$\overline{\text{Tr} [\delta(E - \hat{H})\hat{n}(x, t)\hat{n}(x_0, t_0)]} = \frac{1}{2\pi} \int \frac{d\hbar\omega}{2\pi} e^{-i\omega t} \left[ \overline{\langle x|G(E_+)|x_0\rangle\langle x_0|G^\dagger(E_-)|x\rangle} - \overline{\langle x|G(E_+)|x_0\rangle\langle x_0|G(E_-)|x\rangle} \right]. \quad (\text{B.4})$$

It is therefore the sum of  $N(E)P(x-x_0, t-t_0|E)$ , computed here, plus another term containing correlations between  $G(E_+)$  and  $G(E_-)$  that was neglected in Refs. [70, 71, 155]. The final expressions is therefore the same.

## B.2 Diagrammatic technique and selection of diagrams

**Diagrammatic representation** – We want to calculate

$$j_E^0(x' - x, \omega) = N(E) \int dt e^{i\omega t} \Theta(t) P(x' - x, t|E) = \overline{\langle x'|G(E_+)|x\rangle\langle x|G^\dagger(E_-)|x'\rangle}. \quad (\text{B.5})$$

Using the perturbative development of the Green functions  $G = G_0 + G_0VG_0 + \dots$  and  $G^\dagger = G_0^\dagger + G_0^\dagger VG_0^\dagger + \dots$ , where  $G_0$  and  $G_0^\dagger$  are the disorder-free Green functions, we get, up to second order (when  $\overline{V} = 0$ ),

$$\begin{aligned} \overline{\langle x'|G(E_+)|x\rangle\langle x|G^\dagger(E_-)|x'\rangle} &= \langle x'|G_0(E_+)|x\rangle\langle x|G_0^\dagger(E_-)|x'\rangle \\ &+ \overline{\langle x'|G_0(E_+)VG_0(E_+)|x\rangle\langle x|G_0^\dagger(E_-)VG_0^\dagger(E_-)|x'\rangle} + \dots \\ &= \langle x'|G_0(E_+)|x\rangle\langle x|G_0^\dagger(E_-)|x'\rangle \\ &+ \int dy_1 \int dy_1' \langle x'|G_0(E_+)|y_1\rangle\langle y_1|G_0(E_+)|x\rangle\langle x|G_0^\dagger(E_-)|y_1'\rangle \\ &\quad \times \langle y_1'|G_0^\dagger(E_-)|x'\rangle \overline{V(y_1)V(y_1')} + \dots, \end{aligned}$$

that we represent by diagrammatically (in real space)

$$\begin{array}{c} \begin{array}{ccc} x' \xrightarrow{G(E_+)} x & x' \xrightarrow{G_0(E_+)} x & x' \xrightarrow{\quad} y_1 \xrightarrow{\quad} x \\ x' \xleftarrow{G^\dagger(E_-)} x & x' \xleftarrow{G_0^\dagger(E_-)} x & x' \xleftarrow{\quad} y_1' \xleftarrow{\quad} x \end{array} \\ = \begin{array}{ccc} & & + \dots \end{array} \end{array} \quad (\text{B.6})$$

where  $y_i$  and  $y_i'$  are typically within one correlation length  $\sigma_R$ . One has to take into account as many combinations of potential correlators as possible. Note that here the conventions



$$\begin{array}{c} \text{---} y_i \\ \text{---} \text{---} y_i' \\ \text{---} \text{---} \end{array} = \frac{e^{2ik_\omega^2 x_i/k_E}}{l_s^-(E)} \quad \text{and} \quad \begin{array}{c} y_i \text{---} \\ \text{---} \text{---} y_i' \\ \text{---} \text{---} \end{array} = \frac{e^{-2ik_\omega^2 x_i/k_E}}{l_s^-(E)} \quad (\text{B.9})$$

$$\begin{array}{c} \text{---} y_i \\ \text{---} \text{---} y_i' \\ \text{---} \text{---} \end{array} = \begin{array}{c} \text{---} y_i \\ \text{---} \text{---} y_i' \\ \text{---} \text{---} \end{array} = \frac{-1}{l_s^+(E)} \quad (\text{B.10})$$

$$\begin{array}{c} \text{---} y_i \\ \text{---} \text{---} y_i' \\ \text{---} \text{---} \end{array} = \begin{array}{c} \text{---} y_i \\ \text{---} \text{---} y_i' \\ \text{---} \text{---} \end{array} = \frac{-1}{l_s^-(E)} \quad (\text{B.11})$$

$$\begin{array}{c} y_i \\ \text{---} \text{---} y_i' \\ \text{---} \text{---} \end{array} = -\frac{1}{2l_s^+(E)} - \frac{1}{2l_s^-(E)} - \frac{i}{2l_s^0(E)} \quad \text{and} \quad \begin{array}{c} y_i \\ \text{---} \text{---} y_i' \\ \text{---} \text{---} \end{array} = -\frac{1}{2l_s^+(E)} - \frac{1}{2l_s^-(E)} + \frac{i}{2l_s^0(E)} \quad (\text{B.12})$$

where  $l_s^+(E) = \left[ \frac{m^2}{\hbar^4 k_E^2} \tilde{C}_2(0) \right]^{-1}$  is the on-shell scattering mean free path with respect to forward scattering,  $l_s^-(E) = \left[ \frac{m^2}{\hbar^4 k_E^2} \tilde{C}_2(2k_E) \right]^{-1}$  is the mean free path with respect to backward scattering and  $l_s^0(E) = \left( \Im \left[ \frac{2m^2}{\hbar^4 k_E^2} \int_0^\infty C_2(y) e^{2ik_E y} dy \right] \right)^{-1}$ . And the on-shell scattering mean free path, as defined in Sec. 2, reads  $l_s(E)^{-1} = l_s^+(E)^{-1} + l_s^-(E)^{-1}$ .

We also have to consider the 2 possibilities for the entrance (B.13) and exit (B.14) vertices.

$$V_{\text{in}}^+(x') = \begin{array}{c} \text{---} \\ \text{---} \text{---} \\ \text{---} \end{array} x' = \frac{m}{\hbar^2 k_E} e^{-ik_\omega^2 x'/k_E} \quad \text{or} \quad V_{\text{in}}^-(x') = \begin{array}{c} \text{---} \\ \text{---} \text{---} \\ \text{---} \end{array} x' = \frac{m}{\hbar^2 k_E} e^{ik_\omega^2 x'/k_E} \quad (\text{B.13})$$

$$V_{\text{out}}^-(x) = \begin{array}{c} \text{---} \\ \text{---} \text{---} \\ \text{---} \end{array} x = \frac{m}{\hbar^2 k_E} e^{-ik_\omega^2 x/k_E} \quad \text{or} \quad V_{\text{out}}^+(x) = \begin{array}{c} \text{---} \\ \text{---} \text{---} \\ \text{---} \end{array} x = \frac{m}{\hbar^2 k_E} e^{ik_\omega^2 x/k_E} \quad (\text{B.14})$$

**Born approximation** – When selecting diagrams we have limited ourselves to the Born approximation, that is to say we have only considered the second order correlations, and we have neglected the weight of diagrams containing higher-order correlators. More explicitly, we have only considered the Gaussian part of the higher order correlators as sketched in Eq. (B.15)

$$\begin{array}{c} x_1 x_2 \\ \text{---} \text{---} \\ \text{---} \text{---} \\ \text{---} \text{---} \\ x_4 x_3 \end{array} \simeq \begin{array}{c} x_1 x_2 \\ \text{---} \text{---} \\ \text{---} \text{---} \\ \text{---} \text{---} \\ x_4 x_3 \end{array} + \begin{array}{c} x_1 x_2 \\ \text{---} \text{---} \\ \text{---} \text{---} \\ \text{---} \text{---} \\ x_4 x_3 \end{array} + \begin{array}{c} x_1 x_2 \\ \text{---} \text{---} \\ \text{---} \text{---} \\ \text{---} \text{---} \\ x_4 x_3 \end{array} \quad (\text{B.15})$$

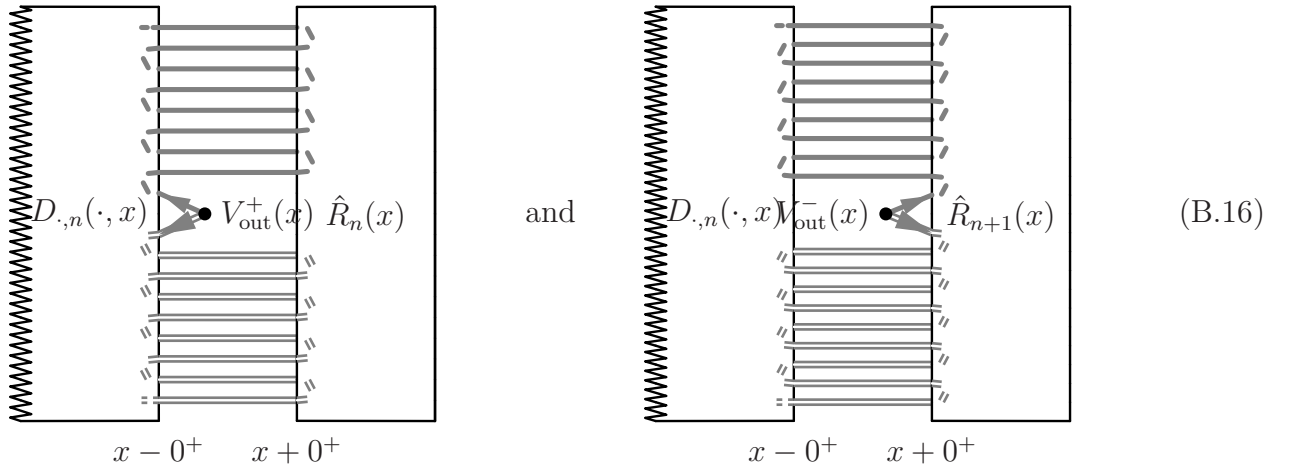
Therefore, for non-Gaussian disorder, i.e. speckle disorder as well as the models discussed in Refs. [70,71,155] there exists corrections. However, the non-Gaussian part of the fourth-order correlation function will be significant only when  $x_1, x_2, x_3$  and  $x_4$  are within an interval  $\sigma_R$ , and the associated corrections to Eq. (B.15) can be expected to be small when  $l_s(E) \gg \sigma_R$ , i.e. in the weak disorder limit.

### B.3 Basic equations on the diagrams

**Building elements** – We now separate each diagram into three parts:  $] - \infty, x'[, [x', x]$  and  $]x, \infty[$  (if  $x' < x$ ). The number of open lines at the borders is fixed.

We define the building blocks :

- $\hat{R}_n(x)$  the sum of all right contributions that have  $g = g' = 2n$  free lines at the border in  $x$
- $\check{R}_{n'}(x')$  the same thing for the left part
- $D_{n',n}(x', x)$  the sum of all contributions from the central part having  $2n' + 1$  open lines in  $x'$  on the left, and  $2n + 1$  open lines on the right, excluding the entrance and exit vertices
- $Z_{\cdot,n}^+(\cdot, x)$  is the association of  $D_{\cdot,n}(\cdot, x)$  with the exit vertex  $V_{\text{out}}^+(x)$  defined in Eq. (B.14) (right), matching  $\hat{R}_n(x)$ , as illustrated in Eq. (B.16)(left) for  $n = 4$
- $Z_{\cdot,n}^-(\cdot, x)$  is the association of  $D_{\cdot,n}(\cdot, x)$  with the exit vertex  $V_{\text{out}}^-(x)$  defined in Eq. (B.14) (left), matching  $\hat{R}_{n+1}(x)$ , as illustrated in Eq. (B.16)(right) for  $n = 4$
- $Z_{n',\cdot}^+(x', \cdot)$  is the association of  $D_{n',\cdot}(x', \cdot)$  with the entrance vertex  $V_{\text{in}}^+(x')$  defined in Eq. (B.13)(left), matching  $\check{R}_{n'}(x')$
- $Z_{n',\cdot}^-(x', \cdot)$  is the association of  $D_{n',\cdot}(x', \cdot)$  with the entrance vertex  $V_{\text{in}}^-(x')$  defined in Eq. (B.13)(right), matching  $\check{R}_{n'+1}(x')$



We then get

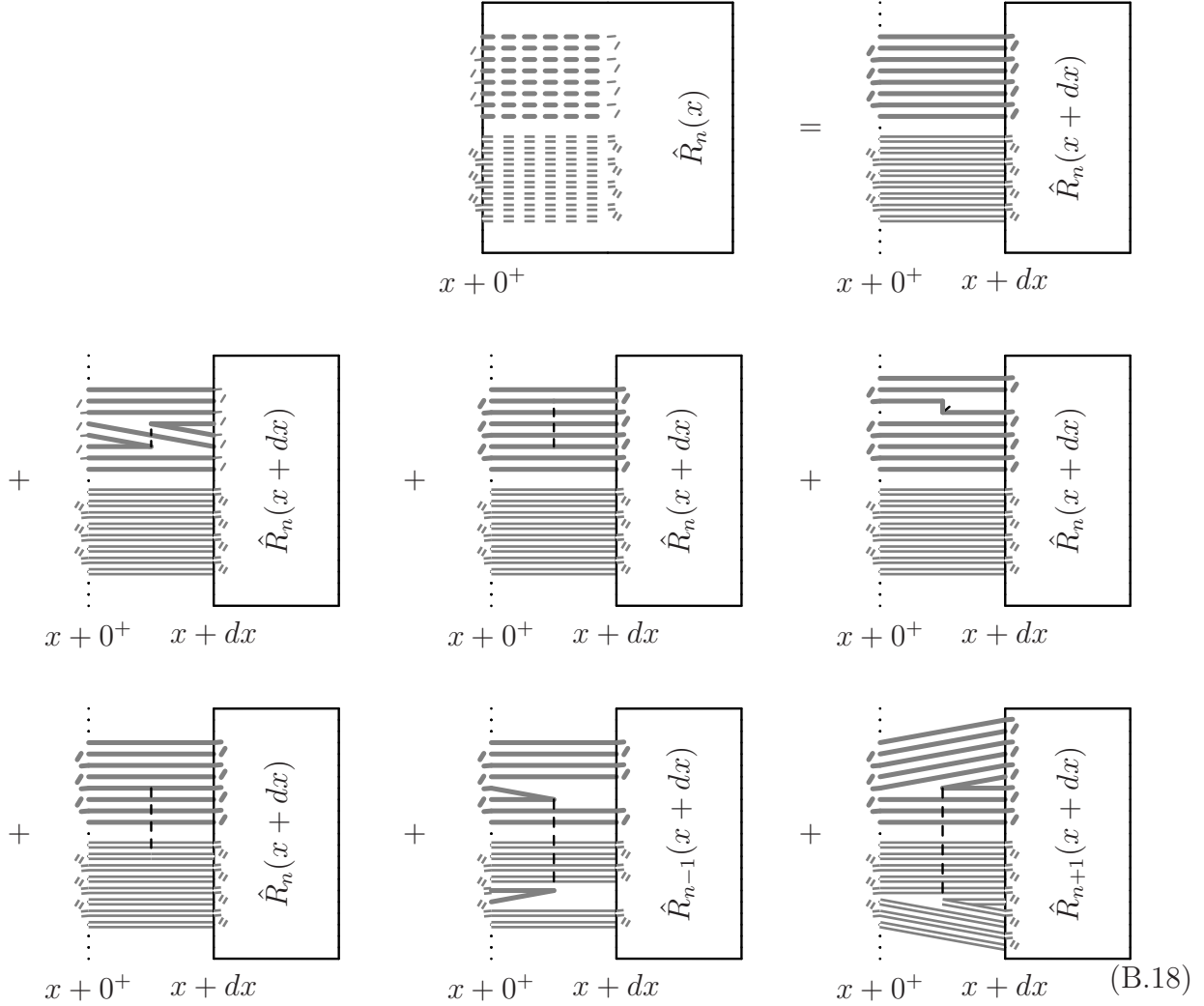
$$j_E^0(x' - x, \omega) = \{\Gamma_{++}(x' - x) + \Gamma_{--}(x' - x) + \Gamma_{+-}(x' - x) + \Gamma_{-+}(x' - x)\} \quad (\text{B.17})$$

with

$$\begin{aligned} \Gamma_{++}(x-x') &= \sum_{n,n'} \check{R}_{n'}(x') Z_{n',n}^{++}(x', x) \hat{R}_n(x) = \sum_{n,n'} \check{R}_{n'}(x') V_{\text{in}}^+(x') D_{n',n}(x', x) V_{\text{out}}^+(x) \hat{R}_n(x) \\ \Gamma_{+-} &= \sum_{n,n'} \check{R}_{n'} Z_{n',n}^{+-} \hat{R}_{n+1} = \sum_{n,n'} \check{R}_{n'} V_{\text{in}}^+ D_{n',n} V_{\text{out}}^- \hat{R}_{n+1} \\ \Gamma_{-+} &= \sum_{n,n'} \check{R}_{n'+1} Z_{n',n}^{-+} \hat{R}_n = \sum_{n,n'} \check{R}_{n'+1} V_{\text{in}}^- D_{n',n} V_{\text{out}}^+ \hat{R}_n \\ \Gamma_{--} &= \sum_{n,n'} \check{R}_{n'+1} Z_{n',n}^{--} \hat{R}_{n+1} = \sum_{n,n'} \check{R}_{n'+1} V_{\text{in}}^- D_{n',n} V_{\text{out}}^- \hat{R}_{n+1} \end{aligned}$$

**Equations on  $\hat{R}_n(x)$  and  $\check{R}_n(x)$**  – We will now analyze the different blocks separately. In Eq. (B.18) we sketch the construction of the right-hand side block  $\hat{R}_n(x)$  from  $\hat{R}_{n-1}(x + dx)$ ,  $\hat{R}_n(x + dx)$  and  $\hat{R}_{n+1}(x + dx)$  by considering all the scattering events that can happen in the

infinitesimal interval  $[x, x + dx]$ , in order to obtain a differential equation.



By considering the number of possible branchings for each type of vertices introduced in Eqs.(B.8) to (B.12) and their weights, we translate those diagrams into the following

$$\begin{aligned}
\hat{R}_n(x) &= 1 \times \hat{R}_n(x+dx) \\
&\quad - \frac{2n(n-1)}{l_s^-(E)} \hat{R}_n(x+dx)dx - \frac{2n(2n-1)}{l_s^+(E)} \hat{R}_n(x+dx)dx \\
&\quad - 2n \left[ \frac{1}{l_s^+(E)} + \frac{1}{l_s^-(E)} \right] \hat{R}_n(x+dx)dx + \frac{4n^2}{l_s^+(E)} \hat{R}_n(x+dx)dx \\
&\quad + \frac{n^2}{l_s^-(E)} e^{\frac{2ik_\omega^2 x}{kE}} \hat{R}_{n-1}(x+dx)dx + \frac{n^2}{l_s^-(E)} e^{-\frac{2ik_\omega^2 x}{kE}} \hat{R}_{n+1}(x+dx)dx, \quad (B.19)
\end{aligned}$$

and we get

$$-\frac{d\hat{R}_n(x)}{dx} = \frac{1}{l_s^-(E)} \left\{ n^2 \hat{R}_{n+1}(x) e^{-\frac{2ik_\omega^2 x}{kE}} - 2n^2 \hat{R}_n(x) + n^2 \hat{R}_{n-1}(x) e^{\frac{2ik_\omega^2 x}{kE}} \right\}. \quad (B.20)$$

For the left part, by constructing  $\check{R}_{n'}(x')$  from  $\check{R}_{n'-1}(x'-dx')$ ,  $\check{R}_{n'}(x'-dx')$  and  $\check{R}_{n'+1}(x'-dx')$  we get almost the same equation:

$$\frac{d\check{R}_n(x')}{dx'} = \frac{1}{l_s^-(E)} \left\{ n^2 \check{R}_{n+1}(x') e^{-\frac{2ik_\omega^2 x'}{k_E}} - 2n^2 \check{R}_n(x') + n^2 \check{R}_{n-1}(x') e^{\frac{2ik_\omega^2 x'}{k_E}} \right\}. \quad (\text{B.21})$$

**Equation on  $Z_{n',n}(x',x)$**  – By the definitions of Sec. B.3 we have

$$Z_{\cdot,n}^\pm(\cdot, x) = D_{\cdot,n}(\cdot, x) \frac{m}{\hbar^2 k_E} e^{\pm ik_\omega^2 x/k_E} \quad (\text{B.22})$$

and

$$Z_{n',\cdot}^\pm(x', \cdot) = D_{n',\cdot}(x', \cdot) \frac{m}{\hbar^2 k_E} e^{\mp ik_\omega^2 x'/k_E}. \quad (\text{B.23})$$

Therefore

$$Z_{n',\cdot}^-(x', \cdot) = e^{2ik_\omega^2 x'/k_E} Z_{n',\cdot}^+(x', \cdot), \quad (\text{B.24})$$

$$Z_{\cdot,n}^-(\cdot, x) = e^{-2ik_\omega^2 x/k_E} Z_{\cdot,n}^+(\cdot, x) \quad (\text{B.25})$$

and

$$\frac{dZ_{\cdot,n}^+(\cdot, x)}{dx} = \frac{ik_\omega^2}{k_E} Z_{\cdot,n}^+(\cdot, x) + \frac{dD_{\cdot,n}(\cdot, x)}{dx} \frac{m}{\hbar^2 k_E} e^{ik_\omega^2 x/k_E}. \quad (\text{B.26})$$

We are now looking for an equation on  $D_{\cdot,n}(\cdot, x)$ . We proceed in the same way as in Sec. B.3: working on the right end of  $D$ , we construct  $D_{\cdot,n}(\cdot, x)$  from  $D_{\cdot,n-1}(\cdot, x-dx)$ ,  $D_{\cdot,n}(\cdot, x-dx)$  and  $D_{\cdot,n+1}(\cdot, x-dx)$ . By considering the possible vertices that can occur in  $[x-dx, x]$  in the same manner as in Eqs. (B.18) and (B.19), we get

$$\begin{aligned} D_{\cdot,n}(\cdot, x) &= 1 \times D_{\cdot,n}(\cdot, x-dx) \\ &\quad - \frac{2n^2}{l_s^-(E)} D_{\cdot,n}(\cdot, x-dx) dx - \frac{2n(2n+1)}{l_s^+(E)} D_{\cdot,n}(\cdot, x-dx) dx \\ &\quad - (2n+1) \left[ \frac{1}{l_s^+(E)} + \frac{1}{l_s^-(E)} \right] D_{\cdot,n}(\cdot, x-dx) dx + \frac{(2n+1)^2}{l_s^+(E)} D_{\cdot,n}(\cdot, x-dx) dx \\ &\quad + \frac{(n+1)^2}{l_s^-(E)} e^{\frac{2ik_\omega^2 x}{k_E}} D_{\cdot,n}(\cdot, x-dx) dx + \frac{n^2}{l_s^-(E)} e^{-\frac{2ik_\omega^2 x}{k_E}} D_{\cdot,n}(\cdot, x-dx) dx \end{aligned} \quad (\text{B.27})$$

and therefore

$$\begin{aligned} \frac{dD_{\cdot,n}(\cdot, x)}{dx} &= \frac{1}{l_s^-(E)} \left\{ (n+1)^2 D_{\cdot,n+1}(\cdot, x) e^{\frac{2ik_\omega^2 x}{k_E}} - [n^2 + (n+1)^2] D_{\cdot,n}(\cdot, x) \right. \\ &\quad \left. + n^2 D_{\cdot,n-1}(\cdot, x) e^{-\frac{2ik_\omega^2 x}{k_E}} \right\}. \end{aligned} \quad (\text{B.28})$$

Using Eq. (B.26), we get for  $Z_{\cdot,n}^+(\cdot, x)$

$$\begin{aligned} \frac{dZ_{\cdot,n}^+(\cdot, x)}{dx} &= \frac{ik_\omega^2}{k_E} Z_{\cdot,n}^+(\cdot, x) + \frac{1}{l_s^-(E)} \left[ (n+1)^2 Z_{\cdot,n+1}^+(\cdot, x) e^{\frac{2ik_\omega^2 x}{k_E}} - [n^2 + (n+1)^2] Z_{\cdot,n}^+(\cdot, x) \right. \\ &\quad \left. + n^2 Z_{\cdot,n-1}^+(\cdot, x) e^{-\frac{2ik_\omega^2 x}{k_E}} \right]. \end{aligned} \quad (\text{B.29})$$

Note that the final equations (B.20) and (B.29) only contain  $l_s^-(E)$ . The mean free path for elastic backscattering is therefore the only relevant length in 1D.

## B.4 Solution of the equations

**Rewriting the equations** – Starting from Eqs. (B.20) and (B.21), we set  $\hat{R}_n(x) = e^{2in'k_\omega^2 x/k_E} R_n$  and  $\check{R}_{n'}(x') = e^{-2in'k_\omega^2 x'/k_E} R_{n'}$ , where  $R_n$  is the same in both cases and follows the equation

$$i\nu R_n + n(R_{n+1} - 2R_n + R_{n-1}) = 0 \quad (\text{B.30})$$

with  $\nu = 2l_s^-(E)k_\omega^2/k_E$ . We also set  $P_n = \frac{1}{2}(R_n + R_{n+1})$ . From Eq. (B.17) we find

$$j_E^0(x' - x, \omega) = 4 \sum_{n,n'} P_{n'} e^{-2in'k_\omega^2 x'/k_E} Z_{n',n}^{++}(x', x) e^{2ink_\omega^2 x/k_E} P_n \quad (\text{B.31})$$

and

$$\begin{aligned} j_E^0(q, \omega) &= 4 \int dx' (x' - x) e^{iq(x' - x)} \sum_{n,n'} P_{n'} e^{-2in'k_\omega^2 x'/k_E} Z_{n',n}^{++}(x', x) e^{2ink_\omega^2 x/k_E} P_n \\ &= 4l_s^-(E) \sum_n P_n [Q_n(\omega, q) + Q_n(\omega, -q)] \end{aligned} \quad (\text{B.32})$$

with  $l_s^-(E)Q_n(\omega, q) = \sum_{n'} \int_{x'}^\infty dx e^{iq(x' - x)} e^{-2in'k_\omega^2 x'/k_E} Z_{n',n}^{++}(x', x) e^{2ink_\omega^2 x/k_E} P_{n'}$ , where  $e^{-2in'k_\omega^2 x'/k_E} Z_{n',n}^{++}(x', x) e^{2ink_\omega^2 x/k_E}$  depends on  $x' - x$  only (due to the invariance by translation of the disorder). For Eq. (B.29), we then obtain

$$i\nu(n + 1/2)Q_n + (n + 1)^2\{Q_{n+1} - Q_n\} - n^2\{Q_n - Q_{n-1}\} - i\kappa Q_n + \frac{m^2}{\hbar^4 k_E^2} P_n = 0 \quad (\text{B.33})$$

where  $\kappa = ql_s^-(E)$ .

**Solution for  $R_n$**  – One can easily check that the solution of Eq. (B.30) can be written as

$$R_n = -i\nu \int_0^\infty ds e^{i\nu s} (1 + s^{-1})^{-n}. \quad (\text{B.34})$$

As we are interested in the long-time limit  $\omega \rightarrow 0$  (i.e.  $\nu \rightarrow 0$ ), the most important contribution comes from the diagrams with high values of  $n$ . In Eq. (B.34) the limits  $\nu \rightarrow 0$  and  $n \rightarrow \infty$  are ill defined if they are taken separately, but the limit ( $\nu \rightarrow 0; n \rightarrow \infty$ ) with  $p = -i\nu n$  finite is well defined. As  $n$  is big we take it as a continuous value, and we find

$$R(p) \simeq P(p) \simeq p \int_0^\infty ds e^{-ps} e^{-1/s} = 2p^{1/2} K_1(2p^{1/2}) \quad (\text{B.35})$$

where  $K_1$  is the modified Bessel function, solution of  $x^2 \frac{d^2 K_\alpha}{dx^2} + x \frac{dK_\alpha}{dx} - (x^2 + \alpha^2) K_\alpha = 0$ .

**Solution for  $Q_n$**  – In this limit, Eq. (B.33) becomes

$$-pQ(p) + \frac{d}{dp} \left[ p^2 \frac{dQ}{dp} \right] - i\kappa Q(p) + \frac{m^2}{\hbar^4 k_E^2} R(p) = 0. \quad (\text{B.36})$$

By setting  $z = 2p^{1/2}$ , one can write the equation for  $\mathcal{Q}(z) = Q(z^2/4)$  and show that  $\mathcal{G}(z) = z\mathcal{Q}(z)$  follows an inhomogenous Bessel equation:

$$z [z\mathcal{Q}''(z) + 2\mathcal{Q}'(z)] + [z\mathcal{Q}'(z) + \mathcal{Q}(z)] - z^2\mathcal{Q}(z) - (4i\kappa + 1)\mathcal{Q}(z) = -4z \frac{m^2}{\hbar^4 k_E^2} K_1(z) \quad (\text{B.37})$$

$$z^2\mathcal{G}''(z) + z\mathcal{G}'(z) - z^2\mathcal{G}(z) - (4i\kappa + 1)\mathcal{G}(z) = -4z^2 \frac{m^2}{\hbar^4 k_E^2} K_1(z). \quad (\text{B.38})$$

When solving it and setting  $\alpha = (4i\kappa + 1)^{1/2}$ , we find

$$Q\left(\frac{z^2}{4}\right) = \mathcal{Q}(z) = \frac{\mathcal{G}(z)}{z} = \frac{4}{z} \frac{m^2}{\hbar^4 k_E^2} \left[ I_\alpha(z) \int_z^\infty \xi d\xi K_\alpha(\xi) K_1(\xi) + K_\alpha(z) \int_0^z \xi d\xi I_\alpha(\xi) K_1(\xi) \right]. \quad (\text{B.39})$$

**Computation of  $P(x, t \rightarrow \infty | E)$**  – In our continuous limit for  $m$ , we have

$$\begin{aligned} j_E^0(\omega, q) &= 4 \frac{\nu k_E}{2k_\omega^2} \int_0^\infty dn P(-i\nu n) [Q(-i\nu n, \kappa) + Q(-i\nu n, -\kappa)] \\ &= 4 \frac{k_E}{-i2k_\omega^2} \int_0^\infty d\zeta P(\zeta) [Q(\zeta, \kappa) + Q(\zeta, -\kappa)]. \end{aligned} \quad (\text{B.40})$$

In Eq. (B.5) we have defined  $j_E^0(\omega, q)$  as the Fourier transform of a retarded function. We find  $j_E^0(\omega, q) \sim_{\omega \rightarrow 0} -A(q)/i\omega$ , and one can show that  $\lim_{t \rightarrow \infty} j_E^0(t, q) = \hbar A(q)$ . Consequently, we have

$$j_E^0(t \rightarrow \infty, q) = 4 \frac{\hbar^2 k_E}{2m} \int_0^\infty d\zeta P(\zeta) [Q(\zeta, \kappa) + Q(\zeta, -\kappa)]. \quad (\text{B.41})$$

Therefore we can compute the desired quantity

$$\begin{aligned} P(x, t \rightarrow \infty | E) &= \frac{1}{2\pi N(E)} \int_{-\infty}^\infty \frac{dq}{2\pi} e^{iqx} j_E^0(t \rightarrow \infty, q) \\ &= \frac{1}{8\pi^2 N(E)} \frac{4\hbar^2 k_E}{m l_s^-(E)} \int_{-\infty}^\infty d\kappa e^{i\kappa x/l_s^-} [\mathcal{F}(\kappa) + \mathcal{F}(-\kappa)], \end{aligned} \quad (\text{B.42})$$

where, thanks to Eq. (B.39),

$$\mathcal{F}(\kappa) = \int_0^\infty d\zeta P(\zeta) Q(\zeta, \kappa) = 4 \frac{m^2}{\hbar^4 k_E^2} \int_0^\infty zdz K_1(z) I_\alpha(z) \int_z^\infty \xi d\xi K_\alpha(\xi) K_1(\xi) \quad (\text{B.43})$$

with  $\alpha = (1 + 4i\kappa)^{1/2}$ . We then get

$$\begin{aligned} P(x, t \rightarrow \infty | E) &= \frac{1}{2\pi N(E)} \frac{4m}{2\hbar^2 k_E} \frac{4}{2\pi l_s^-(E)} \int_0^\infty zdz K_1(z) \int_z^\infty \xi d\xi K_1(\xi) \\ &\quad \int_{-\infty}^\infty d\kappa e^{i\kappa x/l_s^-} I_\alpha(z) K_\alpha(\xi) \end{aligned} \quad (\text{B.44})$$

and, by choosing the appropriate integration path, one can show that

$$P(x, t \rightarrow \infty | E) = \frac{1}{2\pi N(E)} \frac{4m}{2\hbar^2 k_E} \frac{2}{\pi^2 l_s^-(E)} \int_0^\infty \eta d\eta \sinh(\pi\eta) e^{-\frac{1+\eta^2}{4l_s^-(E)}|x|} \quad (\text{B.45})$$

$$\times \int_0^\infty z dz K_1(z) K_{i\eta}(z) \int_z^\infty \xi d\xi K_1(\xi) K_{i\eta}(\xi).$$

Thanks to Eq. (6.576) of Ref. [212] (p. 693), we find

$$\int_0^\infty z dz K_1(z) K_{i\eta}(z) \int_z^\infty \xi d\xi K_1(\xi) K_{i\eta}(\xi) \quad (\text{B.46})$$

$$= \frac{1}{8} \left[ \Gamma\left(\frac{3+i\eta}{2}\right) \Gamma\left(\frac{1+i\eta}{2}\right) \Gamma\left(\frac{3-i\eta}{2}\right) \Gamma\left(\frac{1-i\eta}{2}\right) \right]^2.$$

Eventually, using Eq. (8.332) of Ref. [212] (p. 937), we find

$$\Gamma\left(\frac{3+i\eta}{2}\right) \Gamma\left(\frac{1+i\eta}{2}\right) \Gamma\left(\frac{3-i\eta}{2}\right) \Gamma\left(\frac{1-i\eta}{2}\right) = \frac{\pi^2}{2} \frac{(1+\eta^2)}{\cosh(\pi\eta) + 1} \quad (\text{B.47})$$

Finally, in our weak disorder approximation, we have  $2\pi N(E) \simeq 2\pi N_0(E) = 2m/\hbar^2 k_E$ , and

$$P(x, t \rightarrow \infty | E) = \frac{1}{l_s^-(E)} \frac{\pi^2}{16} \int_0^\infty \eta d\eta \sinh(\pi\eta) \left[ \frac{(1+\eta^2)}{\cosh(\pi\eta) + 1} \right]^2 e^{-\frac{1+\eta^2}{4l_s^-(E)}|x|}. \quad (\text{B.48})$$

where we had defined  $l_s^-(E) = \left[ \frac{m^2}{\hbar^4 k_E^2} \tilde{C}_2(2k_E) \right]^{-1}$ . We therefore have  $l_s^-(E) = 1/2\gamma(E)$  where  $\gamma(E)$  has been defined in Chap. 4 [see Eq. (4.18)], and Eq. (B.48) gives Eq. (4.17).

## Appendix C

# Quantum transport in $d \geq 2$ : Tools and technical calculations

### C.1 Intensity kernel

In this section we show the step-by-step calculation of the long-time and large-distance limit of the intensity kernel given by Eqs. (5.16), (5.17) and (5.19) and the diffusion tensor Eq. (5.21). As explained in Sec. 2.3, the solution of the Bethe-Salpeter equation (2.23)-(2.24) can be obtained by inverting the operator  $\Lambda \equiv 1 - \overline{G} \otimes \overline{G}^\dagger U$  [see Eq. (2.26)]. To this aim, we diagonalize the operator  $\overline{G} \otimes \overline{G}^\dagger U$  in the  $(\mathbf{q}, \omega) \rightarrow (0, 0)$  limit, and it is crucial to discuss in details the properties of its eigenvalues and eigenvectors. They are found by solving

$$\int \frac{d\mathbf{k}'}{(2\pi)^d} U_{\mathbf{k},\mathbf{k}'}^E f_{E,\mathbf{k}'} \phi_{E,\mathbf{k}'}^n = \lambda_E^n \phi_{E,\mathbf{k}}^n \quad (\text{C.1})$$

where  $U_{\mathbf{k},\mathbf{k}'}^E = U_{\mathbf{k},\mathbf{k}'}(\mathbf{q} = 0, \omega = 0, E)$ .

**Preliminary remark** – First, let us notice that, for  $\mathbf{q} = 0$  and  $\omega = 0$ , Eq. (2.28) can be rewritten as

$$f_{E,\mathbf{k}} \equiv \overline{G}(E, \mathbf{k}) \overline{G}^\dagger(E, \mathbf{k}) = \frac{A(E, \mathbf{k})}{-2\Sigma''(E, \mathbf{k})} = \frac{\tau_s(E, \mathbf{k})}{\hbar} A(E, \mathbf{k}), \quad (\text{C.2})$$

where  $A(E, \mathbf{k})$  is the spectral function defined in Eq. (2.15) and  $\tau_s(E, \mathbf{k})$  is the scattering mean free time defined in Eq. (2.17).

**Properties of Eq. (C.1)** – The main properties of Eq. (C.1) and of its eigenfunctions are listed below:

1. The eigenvalues  $\lambda_E^n$  and the eigenvectors  $\phi_{E,\mathbf{k}}^n$  of Eq. (C.1) are real.

*Proof.* By multiplying Eq. (C.1) by  $\overline{G}^\dagger(E, \mathbf{k})$ , we obtain

$$\int \frac{d\mathbf{k}'}{(2\pi)^d} M_{\mathbf{k},\mathbf{k}'}^E \overline{G}^\dagger(E, \mathbf{k}') \phi_{E,\mathbf{k}'}^n = \lambda_E^n \overline{G}^\dagger(E, \mathbf{k}) \phi_{E,\mathbf{k}}^n, \quad (\text{C.3})$$

where  $M_{\mathbf{k},\mathbf{k}'}^E \equiv \overline{G^\dagger}(E, \mathbf{k}) U_{\mathbf{k},\mathbf{k}'}^E \overline{G}(E, \mathbf{k}')$ . The latter is Hermitian since  $\overline{G^\dagger}(E, \mathbf{k})^* = \overline{G}(E, \mathbf{k})$  and  $U_{\mathbf{k},\mathbf{k}'}^E$  is real and symmetric. Therefore all the eigenvalues  $\lambda_E^n$  are real. By taking the complex conjugate of Eq. (C.3), dividing by  $\overline{G}(E, \mathbf{k})$  and comparing it to Eq. (C.1), we obtain that the functions  $\phi_{E,\mathbf{k}}^n$  are real.

If  $U_{\mathbf{k},\mathbf{k}'}^E$  is positive-definite, the eigenvalues  $\lambda_E^n$  are positive. In particular, this is always true in the Born approximation<sup>1</sup>. When  $U_{\mathbf{k},\mathbf{k}'}^E$  is symmetric and positive-definite, we can write it as  $U_{\mathbf{k},\mathbf{k}'}^E = \int \frac{d\mathbf{k}''}{(2\pi)^d} Q_{\mathbf{k},\mathbf{k}''} d_{\mathbf{k}'',\mathbf{k}'} Q_{\mathbf{k}'',\mathbf{k}'}^T$ , where  $d_{\mathbf{k}'',\mathbf{k}'} > 0$  and  $Q$  is an orthogonal operator. For any vector of components  $x_{\mathbf{k}}$ , we have  $\int \frac{d\mathbf{k}}{(2\pi)^d} \frac{d\mathbf{k}'}{(2\pi)^d} x_{\mathbf{k}} M_{\mathbf{k},\mathbf{k}'}^E x_{\mathbf{k}'} = \int \frac{d\mathbf{k}}{(2\pi)^d} d_{\mathbf{k}} |y_{\mathbf{k}}|^2 > 0$ , where  $y_{\mathbf{k}} \equiv \int \frac{d\mathbf{k}'}{(2\pi)^d} \overline{G^\dagger}(E, \mathbf{k}') x_{\mathbf{k}'} Q_{\mathbf{k}',\mathbf{k}}$ . It shows that  $M_{\mathbf{k},\mathbf{k}'}^E$  is positive definite. Its eigenvalues  $\lambda_E^n$  are therefore positive.  $\square$

2. The eigenvectors  $\phi_{E,\mathbf{k}}^n$  can be chosen to satisfy the orthonormalization condition

$$\int \frac{d\mathbf{k}}{(2\pi)^d} f_{E,\mathbf{k}} \phi_{E,\mathbf{k}}^n \phi_{E,\mathbf{k}}^m = \delta_{n,m}. \quad (\text{C.4})$$

*Proof.* This is an immediate consequence of the fact that, according to Eq. (C.3), the functions  $\overline{G^\dagger}(E, \mathbf{k}) \phi_{E,\mathbf{k}}^n$  are eigenfunctions of the Hermitian operator  $M_{\mathbf{k},\mathbf{k}'}^E$ .  $\square$

3. The eigenvectors  $\phi_{E,\mathbf{k}}^n$  satisfy the completeness relation

$$f_{E,\mathbf{k}} \sum_n \phi_{E,\mathbf{k}}^n \phi_{E,\mathbf{k}'}^n = (2\pi)^d \delta(\mathbf{k} - \mathbf{k}'). \quad (\text{C.5})$$

*Proof.* This follows from the fact that the eigenfunctions  $\overline{G^\dagger}(E, \mathbf{k}) \phi_{E,\mathbf{k}}^n$  of the matrix  $M_{\mathbf{k},\mathbf{k}'}^E$ , Eq. (C.3), form a complete basis.  $\square$

4. The irreducible vertex function  $U_{\mathbf{k},\mathbf{k}'}^E$  can be expressed as

$$U_{\mathbf{k},\mathbf{k}'}^E = \sum_n \lambda_E^n \phi_{E,\mathbf{k}}^n \phi_{E,\mathbf{k}'}^n. \quad (\text{C.6})$$

*Proof.* We multiply both terms of Eq. (C.1) by  $\phi_{E,\mathbf{k}'}^n$  and sum over  $n$ . Equation (C.6) is recovered by using the completeness relation Eq. (C.5).  $\square$

5. The most important property of Eq. (C.1) is that one of the eigenvalues is

$$\lambda_E^{n=1} = 1, \quad (\text{C.7})$$

and the corresponding eigenvector is proportional to the inverse scattering mean free time:

$$\phi_{E,\mathbf{k}}^{n=1} = \sqrt{\hbar} \frac{[\tau_s(E, \mathbf{k})]^{-1}}{\sqrt{\frac{d\mathbf{k}'}{(2\pi)^d} A(E, \mathbf{k}) [\tau_s(E, \mathbf{k})]^{-1}}}. \quad (\text{C.8})$$

---

1. In our case,  $U_{\mathbf{k},\mathbf{k}'}^E = \tilde{C}(\mathbf{k} - \mathbf{k}')$  is symmetric and positive-definite. This latter property is assured for any disordered potential by the fact that the power spectrum  $\tilde{C}(\mathbf{k})$ , being the Fourier Transform of the autoconvolution product of the potential, is positive for any  $\mathbf{k}$ .

*Proof.* This is a direct consequence of the Ward identity [149]:

$$\Delta\Sigma_{\mathbf{k}}(\mathbf{q}, \omega, E) = \int \frac{d\mathbf{k}'}{(2\pi)^d} U_{\mathbf{k},\mathbf{k}'}(\mathbf{q}, \omega, E) \Delta G_{\mathbf{k}}(\mathbf{q}, \omega, E), \quad (\text{C.9})$$

where  $\Delta\Sigma_{\mathbf{k}}(\mathbf{q}, \omega, E) = \Sigma(E_+, \mathbf{k}_+) - \Sigma^\dagger(E_-, \mathbf{k}_-)$  and  $\Delta G_{\mathbf{k}}(\mathbf{q}, \omega, E) = \overline{G}(E_+, \mathbf{k}_+) - \overline{G}^\dagger(E_-, \mathbf{k}_-)$ . For  $(\mathbf{q}, \omega) = (0, 0)$  it becomes

$$\Delta\Sigma_{\mathbf{k}}(0, 0, E) = \int \frac{d\mathbf{k}'}{(2\pi)^d} U_{\mathbf{k},\mathbf{k}'}^E f_{E,\mathbf{k}} \Delta\Sigma_{\mathbf{k}}(0, 0, E). \quad (\text{C.10})$$

When comparing Eq. (C.10) to Eq. (C.1), we obtain that  $\Delta\Sigma_{\mathbf{k}}(0, 0, E) = -i\hbar/\tau_s(E, \mathbf{k})$  is a solution of Eq. (C.1) with unit eigenvalue. Using Eq. (C.2) and the orthonormalization condition (C.4) one then easily finds Eq. (C.8).  $\square$

6. The eigenfunctions  $\phi_{E,\mathbf{k}}^n$  have the parity properties:

$$\phi_{E,-\mathbf{k}}^{n=1} = \phi_{E,\mathbf{k}}^{n=1} \quad (\text{C.11})$$

$$\phi_{E,-\mathbf{k}}^n = -\phi_{E,\mathbf{k}}^n \quad \text{for } n > 1. \quad (\text{C.12})$$

*Proof.* This is a consequence of the parity of the vertex  $U_{\mathbf{k},\mathbf{k}'}^E$ , in particular,  $U_{-\mathbf{k},-\mathbf{k}'}^E = U_{\mathbf{k},\mathbf{k}'}^E$ . Using Eq. (C.6) we have  $\sum_n \lambda_E^n \phi_{E,\mathbf{k}}^n \phi_{E,\mathbf{k}'}^n = \sum_n \lambda_E^n \phi_{E,-\mathbf{k}}^n \phi_{E,-\mathbf{k}'}^n$ , which can only be satisfied if the eigenfunctions  $\phi_{E,\mathbf{k}}^n$  have a well defined parity. The eigenfunction  $\phi_{E,\mathbf{k}}^{n=1}$  is given by Eq. (C.8) and it is even. In addition, using Eqs. (C.2) and (C.8) in the orthonormalization condition (C.4), we have  $\int \frac{d\mathbf{k}}{(2\pi)^d} A(E, \mathbf{k}) \phi_{E,\mathbf{k}}^n = 0$  for  $n > 1$ . Which shows that  $\phi_{E,\mathbf{k}}^n$  are odd functions of  $\mathbf{k}$ .  $\square$

**Solution of the BSE** – Note first that, if Eq. (C.1) could be diagonalized with all eigenvalues different from one ( $\lambda_E^n \neq 1$  for all  $n$ ), it is straightforward to show, using Eq. (C.5), that we would have  $\Lambda_{\mathbf{k},\mathbf{k}'}^{-1}(0, 0, E) = \sum_n [1/(1 - \lambda_E^n)] f_{\mathbf{k}} \phi_{\mathbf{k}}^n \phi_{\mathbf{k}'}^n$ . In this case no diffusion would be observed. As noticed above, however, the conservation of particle number, through the Ward identity, imposes that there is one eigenvalue equal to one. As there is no other conserved quantity in the system we are considering, we can assume that the eigenvalue  $\lambda = 1$  is not degenerated, and that there is a finite gap between this eigenvalue and the rest of the spectrum when  $(\mathbf{q}, \omega) \rightarrow 0$  [213, 214]. This suggests the following ansatz for the solution of the BSE (2.23)-(2.24) [see Eq. (2.26)], in the small (but non-zero)  $\mathbf{q}$  and  $\omega$  limit:

$$\Phi_{\mathbf{k},\mathbf{k}'}(\mathbf{q}, \omega, E) = f_{E,\mathbf{k}} \frac{\phi_{\mathbf{k}}^1(\mathbf{q}, \omega, E) \phi_{\mathbf{k}'}^1(\mathbf{q}, \omega, E)}{\lambda(\mathbf{q}, \omega, E)} f_{E,\mathbf{k}'} + \sum_{\lambda_E^n \neq 1} \frac{1}{1 - \lambda_E^n} f_{E,\mathbf{k}} \phi_{E,\mathbf{k}}^n \phi_{E,\mathbf{k}'}^n f_{E,\mathbf{k}'}, \quad (\text{C.13})$$

where  $\phi_{\mathbf{k}}^1(\mathbf{q}, \omega, E)$  and  $1 + \lambda(\mathbf{q}, \omega, E)$  are the first eigenvalue and eigenvector at small  $(\mathbf{q}, \omega)$ , corresponding to Eqs. (C.7) and (C.8), respectively. They satisfy the eigenequation

$$\int \frac{d\mathbf{k}'}{(2\pi)^d} U_{\mathbf{k},\mathbf{k}'}^E f_{\mathbf{k}}(\mathbf{q}, \omega, E) \phi_{\mathbf{k}'}^1(\mathbf{q}, \omega, E) = [1 + \lambda(\mathbf{q}, \omega, E)] \phi_{\mathbf{k}}^1(\mathbf{q}, \omega, E). \quad (\text{C.14})$$

We write  $f_{\mathbf{k}}(\mathbf{q}, \omega, E) = f_{E,\mathbf{k}} + F_{\mathbf{k}}(\mathbf{q}, \omega, E)$ , the small  $(\mathbf{q}, \omega)$  expansion of  $f_{\mathbf{k}}(\mathbf{q}, \omega, E)$ . Making the ansatz  $\phi_{\mathbf{k}}^1(\mathbf{q}, \omega, E) = \sum_n a_n(\mathbf{q}, \omega, E) \phi_{E,\mathbf{k}}^n$ , we find

$$\lambda(\mathbf{q}, \omega, E) = \sum_n \frac{a_n(\mathbf{q}, \omega, E)}{a_1(\mathbf{q}, \omega, E)} \int \frac{d\mathbf{k}}{(2\pi)^d} \phi_{E,\mathbf{k}}^0 F_{\mathbf{k}}(\mathbf{q}, \omega, E) \phi_{E,\mathbf{k}}^n. \quad (\text{C.15})$$

Finally, the coefficients  $a_n(\mathbf{q}, \omega, E)$  are found by imposing that Eq. (C.13) solves the BSE. After some algebra one finds  $a_1(\mathbf{q}, \omega, E) = 1$  and  $a_n(\mathbf{q}, \omega, E) = \frac{\lambda_E^n}{1-\lambda_E^n} \int \frac{d\mathbf{k}}{(2\pi)^d} \phi_{E,\mathbf{k}}^0 F_{\mathbf{k}}(\mathbf{q}, \omega, E) \phi_{E,\mathbf{k}}^n$ , for  $n > 1$ .

**On-shell approximation** – We now proceed to the on-shell (weak disorder) approximation, and we neglect the effect of disorder on the spectral function. Equation (C.2) becomes

$$f_{E,\mathbf{k}} \approx \frac{\tau_{E,\hat{\mathbf{k}}}}{\hbar} A_0(\mathbf{k}, E), \quad (\text{C.16})$$

where  $\tau_{E,\hat{\mathbf{k}}}$  is the on-shell scattering mean free time [ $\tau_{E,\hat{\mathbf{k}}} \equiv \tau_s(E, k_E \hat{\mathbf{k}})$ ],  $A_0(\mathbf{k}, E) = 2\pi \delta[E - \epsilon(\mathbf{k})]$  and  $\epsilon(\mathbf{k})$  are, respectively, the disorder-free particle spectral function and dispersion relation.

The small  $(\mathbf{q}, \omega)$  expansion of  $f_{\mathbf{k}}(\mathbf{q}, \omega, E)$  requires special attention in the on-shell approximation. Let us consider for instance the first order term in  $\omega$ . We find  $F_{\mathbf{k}}(\mathbf{q}, \omega, E) \approx \frac{\hbar\omega}{2} [f_{E,\mathbf{k}} \overline{G}^\dagger(E, \mathbf{k}) - f_{E,\mathbf{k}} \overline{G}(E, \mathbf{k})]$ . In the on-shell approximation this equation appears to go as the square of a  $\delta$ -function, and one has to handle this divergence correctly [90]: we assume that  $f_{E,\mathbf{k}} \overline{G}(E, \mathbf{k}) \sim 2\pi c \delta(E - \epsilon(\mathbf{k}))$ , where the factor  $c$  is calculated by imposing that the integral over energy of  $f_{E,\mathbf{k}} \overline{G}(E, \mathbf{k})$  remains invariant, i.e.  $c = \int \frac{dE}{2\pi} f_{E,\mathbf{k}} \overline{G}(E, \mathbf{k})$ . With this method, we find  $f_{E,\mathbf{k}} \overline{G}(E, \mathbf{k}) = i(\tau_{E,\hat{\mathbf{k}}}^2/\hbar^2) A_0(\mathbf{k}, E)$  and therefore  $F_{\mathbf{k}}(\mathbf{q}, \omega, E) \approx \hbar\omega i(\tau_{E,\hat{\mathbf{k}}}^2/\hbar^2) A_0(\mathbf{k}, E)$ , as in Eq. (C.17). Following the same method we can calculate the other terms in Eq. (C.17). Finally note that Eq. (C.17) also assumes that  $\tau_s(E, \mathbf{k})$  is a smooth function of  $\mathbf{k}$ , such that  $\nabla_{\mathbf{k}} \tau_s(E, \mathbf{k}) \approx 0$ . A full calculation in the small  $(\mathbf{q}, \omega)$  limit gives

$$F_{\mathbf{k}}(\mathbf{q}, \omega, E) = \left\{ \frac{i\tau_{E,\hat{\mathbf{k}}}^2}{\hbar^2} [\hbar\omega - \mathbf{q} \cdot \nabla_{\mathbf{k}} \epsilon(\mathbf{k})] + \frac{2\tau_{E,\hat{\mathbf{k}}}^3}{\hbar^3} \hbar\omega [\mathbf{q} \cdot \nabla_{\mathbf{k}} \epsilon(\mathbf{k})] - \frac{\tau_{E,\hat{\mathbf{k}}}^3}{\hbar^3} [\mathbf{q} \cdot \nabla_{\mathbf{k}} \epsilon(\mathbf{k})]^2 \right\} \times A_0(\mathbf{k}, E) + O(\omega^2, q^3). \quad (\text{C.17})$$

Then, making use of the parity properties of the functions  $\phi_{E,\hat{\mathbf{k}}}^n$  [Eqs. (C.11) and (C.12)],  $\tau_{E,\hat{\mathbf{k}}}$  (even function of  $\hat{\mathbf{k}}$ ) and  $\nabla_{\mathbf{k}} \epsilon(\mathbf{k})$  (odd function of  $\mathbf{k}$ ), we finally obtain  $\phi_{\mathbf{k}}^1(\mathbf{q}, \omega, E) f_{E,\mathbf{k}} = 2\pi \gamma_{\mathbf{k}}(\mathbf{q}, E) / \sqrt{\hbar \langle \tau_{E,\hat{\mathbf{k}}}^{-1} \rangle}$  where  $\gamma_{\mathbf{k}}$  is given by Eq. (5.20) and  $\lambda(\mathbf{q}, \omega, E) = 2N_0(E) [i\hbar\omega - \hbar \mathbf{q} \cdot \mathbf{D}(E) \cdot \mathbf{q}] / \hbar \langle \tau_{E,\hat{\mathbf{k}}}^{-1} \rangle$  with the diffusion tensor of Eq. (5.21). The solution of the BSE is thus given by Eq. (5.16) with Eqs. (5.17) and (5.19). Note that this expression for the diffusion constant is quite general (only the on-shell approximation has been made), provided that the full irreducible vertex function  $U$  is considered in the eigenequation (C.1). In Sec. 5.2.1 the Born and Boltzmann approximations are made  $U = U_B$  [see Eq. (5.22)].

## C.2 Isotropic disorder

For disorder with isotropic correlation function, we define, as in Ref. [16],  $p(k, \theta) \equiv \tilde{C}(k|\hat{\mathbf{k}} - \hat{\mathbf{k}}'|) = \tilde{C}(2k|\sin(\theta/2)|)$ , where  $\theta$  is the angle between the unit vectors  $\hat{\mathbf{k}}$  and  $\hat{\mathbf{k}}'$  and  $k \equiv |\mathbf{k}| = |\mathbf{k}'|$ . In this case, rotation invariance ensures that the eigenproblem (5.22) is solved by cylindrical (2D) or spherical (3D) harmonics.

### C.2.1 Two-dimensional case

In the 2D isotropic case, inserting the cylindrical harmonics  $Z_0 = 1$ ,  $Z_l^{+1} = \cos(l\theta)$  and  $Z_l^{-1} = \sin(l\theta)$  into Eq. (5.22), we find

$$\lambda_E^{l,m} = \frac{\int_0^{2\pi} d\theta p(k_E, \theta) \cos(l\theta)}{\int_0^{2\pi} d\theta p(k_E, \theta)}, \quad (\text{C.18})$$

where  $l \geq 0$  and  $m \in \{-1, +1\}$  are integer numbers. In particular, we find  $\lambda_E^{l=0} = 1$  in agreement with Eq. (C.7). They are doubly-degenerated for  $l > 0$  and the corresponding normalized eigenfunctions are proportional to the orthonormal cylindrical harmonics, with the prefactor determined by the normalization condition (C.4):

$$\phi_{E,\hat{\mathbf{k}}}^{l=0} = Z_0(\theta) \sqrt{\frac{\int_0^{2\pi} d\theta' p(k_E, \theta')}{\pi}}, \quad (\text{C.19})$$

and

$$\phi_{E,\hat{\mathbf{k}}}^{l,\pm 1} = Z_l^{\pm 1}(\theta) \sqrt{\frac{\int_0^{2\pi} d\theta' p(k_E, \theta')}{\pi}}. \quad (\text{C.20})$$

In the calculation of the diffusion constant, it is actually possible to see that only the first term plus the  $l = 1$  terms (with  $m = -1, +1$ ) in the summation of the right-hand side of Eq. (5.21), contribute to the diffusion coefficient. More precisely the on-shell scattering mean free time  $\tau_{E,\hat{\mathbf{k}}}$  does not depend on  $\hat{\mathbf{k}}$ ,  $v_x$  (respectively  $v_y$ ) is a  $2\pi$ -periodic and even (resp. odd) function of  $\theta$ , and  $Z_l^{+1}$  (resp.  $Z_l^{-1}$ ) is  $2\pi/l$ -periodic and even (resp. odd). Therefore, when performing the angular averaging of the product  $\tau_{E,\hat{\mathbf{k}}} v_i \phi_{E,\hat{\mathbf{k}}}^n$  in Eq. (5.21), one finds that only the term with  $l = 1$  and  $m = +1$  (resp.  $m = -1$ ) couples to  $v_x$  (resp.  $v_y$ ) and contribute to  $D_B^x$  (resp.  $D_B^y$ ). Then, inserting Eqs. (C.18), (C.19) and (C.20) into Eq. (5.21), we find

$$D_B(E) = \frac{\hbar E}{mN_0(E)} \frac{1}{\int_0^{2\pi} d\theta (1 - \cos \theta) p(k_E, \theta)}. \quad (\text{C.21})$$

This formula agrees with the result of Ref. [16], obtained by a different approach.

### C.2.2 Three-dimensional case

In the 3D isotropic case, proceeding in a similar way, we find that the eigenvalues of Eq. (5.22) are given by

$$\lambda_E^{l,m} = \frac{\int_0^\pi d\theta \sin \theta p(k_E, \theta) P_l(\cos \theta)}{\int_0^\pi d\theta \sin \theta p(k_E, \theta)}, \quad (\text{C.22})$$

with the index  $l = 0, 1, \dots, +\infty$  and  $m = -l, -l + 1, \dots, +l$  and where  $P_l(\cos \theta)$  are the Legendre polynomials. The eigenvalues are  $(2l + 1)$ -degenerated and the corresponding normalized eigenfunctions are proportional to orthonormal spherical harmonics, with the prefactor determined by the normalization condition (C.4):

$$\phi_{E,\mathbf{k}}^{l,m} = Y_l^m(\theta, \phi) \sqrt{2\pi \int_0^\pi d\theta' \sin \theta' p(k_E, \theta')}, \quad (\text{C.23})$$

In the calculation of the diffusion constant, using the same type of symmetry arguments as in the 2D case, we find that only the  $l = 1$  (with  $m = -1, 0, 1$ ) terms couple to  $\mathbf{v}$  and contribute in the summation of Eq. (5.21). We thus find

$$D_B(E) = \frac{2}{3\pi} \frac{\hbar E}{m N_0(E)} \frac{1}{\int_0^\pi d\theta \sin \theta (1 - \cos \theta) p(k_E, \theta)}, \quad (\text{C.24})$$

which agrees with the expression found in Ref. [16].

**White-noise disorder** – In the case of white-noise disorder, the power spectrum is constant:  $p(k, \theta) = V_0^2 \sigma^d$ , where  $V_0$  is a typical amplitude of the disorder, and  $\sigma$  a characteristic length. We find that, for  $n > 1$  the eigenvalues of Eq. (5.22) are null ( $\lambda_E^{n \neq 1} = 0$ ). The diffusion coefficient is then given by the first term in the right-hand side of Eq. (5.21), and we find  $D_B(E) = \hbar E / 2\pi m N_0(E) V_0^2 \sigma^2$  in 2D, and  $D_B(E) = \hbar E / 3\pi m N_0(E) V_0^2 \sigma^3$  in 3D.

**Free density of states** – In  $d$  dimensions, the disorder-free density of states, when  $\epsilon(\mathbf{k}) = \hbar^2 \mathbf{k}^2 / 2m$ , reads

$$N_0(E) = \frac{\Omega_d}{2} \left( \frac{\sqrt{2m}}{2\pi\hbar} \right)^d E^{d/2-1}, \quad (\text{C.25})$$

where  $\Omega_d$  is the total solid angle (2 in 1D,  $2\pi$  in 2D and  $4\pi$  in 3D).

## C.3 Conductivity

### C.3.1 Einstein relation

As presented in Sec. 2.4, we expect  $\boldsymbol{\sigma}(\omega = 0) \propto \mathbf{D}$  in the linear response regime. Here we calculate  $\boldsymbol{\sigma}_B(\omega = 0)$  in the Boltzmann approximation and verify this relation explicitly, which enables us to find the proportionality factor in Eq. (2.38).

Let us first rewrite the Boltzmann diffusion tensor as

$$D_B^{i,j}(E) = \frac{1}{\hbar N_0(E)} \langle \tau_{E,\hat{\mathbf{k}}} v_i J_{\mathbf{k},j} \rangle, \quad (\text{C.26})$$

where  $\mathbf{J}_{\mathbf{k}}$  is the renormalized current vertex :

$$\frac{\mathbf{J}_{\mathbf{k}}}{\hbar} = \mathbf{v} + \frac{2\pi}{\hbar} \sum_{\lambda_E^n \neq 1} \frac{\lambda_E^n}{1 - \lambda_E^n} \langle \tau_{E,\hat{\mathbf{k}}} \mathbf{v}' \phi_{E,\hat{\mathbf{k}}}^n \rangle \phi_{E,\hat{\mathbf{k}}}^n. \quad (\text{C.27})$$

We want to calculate the conductivity  $\sigma_B$  in the ladder approximation. We have to evaluate

$$\sigma_B = \text{Diagram 1} + \text{Diagram 2} \quad (\text{C.28})$$

which reads

$$\sigma_B^{i,j}(E) = \int \frac{d\mathbf{k}}{(2\pi)^d} v_i f_{E,\mathbf{k}} v_j + \int \frac{d\mathbf{k}}{(2\pi)^d} \frac{d\mathbf{k}'}{(2\pi)^d} v_i f_{E,\mathbf{k}} \Gamma_{\mathbf{k},\mathbf{k}'}(0,0,E) f_{E,\mathbf{k}'} v_j'. \quad (\text{C.29})$$

As<sup>2</sup>  $\Gamma_{\mathbf{k},\mathbf{k}'}(0,0,E) = \sum_{\lambda_E^n \neq 1} \frac{\lambda_E^n}{1-\lambda_E^n} \phi_{E,\hat{\mathbf{k}}}^n \phi_{E,\hat{\mathbf{k}'}}^n$ , and  $f_{E,\mathbf{k}} \simeq \tau_{E,\hat{\mathbf{k}}} A_0(E,\mathbf{k})/\hbar$ , one easily finds

$$\begin{aligned} \sigma_B^{i,j}(E) &= \frac{2\pi}{\hbar} \left\{ \langle \tau_{E,\hat{\mathbf{k}}} v_i v_j \rangle + \frac{2\pi}{\hbar} \right. \\ &\quad \left. \times \sum_{\lambda_E^n \neq 1} \frac{\lambda_E^n}{1-\lambda_E^n} \langle \tau_{E,\hat{\mathbf{k}}} v_i \phi_{E,\hat{\mathbf{k}}}^n \rangle \langle \tau_{E,\hat{\mathbf{k}'}} v_j \phi_{E,\hat{\mathbf{k}'}}^n \rangle \right\}. \end{aligned} \quad (\text{C.30})$$

Therefore, we have  $\sigma_B = 2\pi N_0(E) \mathbf{D}_B/\hbar$ . We have thus verified Einstein's relation for the classical dc conductivity in anisotropic disorder.

### C.3.2 Current vertex renormalization

The DC conductivity  $\sigma_B$  in the Boltzmann approximation reads (see appendix C.3.1)

$$\sigma_B^{i,j}(E) = \frac{2\pi}{\hbar} \left\langle \tau_{E,\hat{\mathbf{k}}} v_i \frac{J_{\mathbf{k},j}}{\hbar} \right\rangle, \quad (\text{C.31})$$

where  $\mathbf{J}_{\mathbf{k}}$ , the renormalized vertex function, is given by Eq. (C.27). Diagrammatically we can absorb this renormalization in one of the vertices as shown in Eq. (C.32). This is a standard procedure for anisotropic scattering, which is presented for example in Ref. [41].

$$\text{Diagram 1} + \text{Diagram 2} = \text{Diagram 3} \quad (\text{C.32})$$

### C.3.3 Weak-localization correction

**The cooperon** – We calculate the bare cooperon correction, with renormalized current vertices, Diag. (5.28) translates into

$$\Delta\sigma_{(X)}^{i,j}(\omega, E) = \int \frac{d\mathbf{k}}{(2\pi)^d} \frac{d\mathbf{k}'}{(2\pi)^d} \frac{J_{\mathbf{k},i}}{\hbar} f_{E,\mathbf{k}} X_{\mathbf{k},\mathbf{k}'}(0,\omega,E) f_{E,\mathbf{k}'} \frac{J_{\mathbf{k}',j}}{\hbar}. \quad (\text{C.33})$$

2. Equation (5.15) gives  $\Gamma = U_B[1 - \overline{G} \otimes \overline{G}^\dagger U]^{-1}$ , and the components  $\Gamma_{\mathbf{k},\mathbf{k}'}(0,0,E)$  can be found from the results of appendix C.1.

Considering that the dominant contribution in the integral comes from  $\mathbf{Q} \simeq \mathbf{k} + \mathbf{k}' \sim 0$  [see Eq (5.33)], and that  $f_{E,\mathbf{k}}^2 \sim 2(\tau_{E,\hat{\mathbf{k}}}/\hbar)^3 A_0(E, \mathbf{k})$  in the on-shell approximation<sup>3</sup>, we get

$$\Delta\sigma_{(X)}^{i,j}(\omega, E) = -\frac{2}{\hbar N_0(E)} \left\langle \frac{J_{\mathbf{k},i} J_{\mathbf{k},j}}{\hbar^2} \tau_{E,\hat{\mathbf{k}}} \right\rangle \int \frac{d\mathbf{Q}}{(2\pi)^d} \frac{1}{-i\hbar\omega + \hbar\mathbf{Q} \cdot \mathbf{D}_B(E) \cdot \mathbf{Q}}. \quad (\text{C.34})$$

**Hikami contributions** – We now calculate the Hikami corrections [see Diags. (5.29) and (5.30)]

$$\begin{aligned} \Delta\sigma_{(H_1)}^{i,j}(\omega, E) &= \int \frac{d\mathbf{k}}{(2\pi)^d} \frac{d\mathbf{k}'}{(2\pi)^d} \frac{d\mathbf{k}''}{(2\pi)^d} \frac{J_{\mathbf{k},i}}{\hbar} f_{E,\mathbf{k}} U_{B\mathbf{k},\mathbf{k}'} G(E, \mathbf{k}'') X_{\frac{\mathbf{k}+\mathbf{k}''}{2}, \mathbf{k}'+\frac{\mathbf{k}''-\mathbf{k}}{2}}(\mathbf{k}'' - \mathbf{k}, \omega, E) \\ &\quad \times G(E, \mathbf{k}' + \mathbf{k}'' - \mathbf{k}) f_{E,\mathbf{k}'} \frac{J_{\mathbf{k}',j}}{\hbar}. \end{aligned} \quad (\text{C.35})$$

In the same way as before, and using the on-shell approximation formulas<sup>3</sup>  $G(E, \mathbf{k}) f_{E,\mathbf{k}} \sim -i(\tau_{E,\hat{\mathbf{k}}}/\hbar)^2 A_0(E, \mathbf{k})$ , and  $G^\dagger(E, \mathbf{k}) f_{E,\mathbf{k}} \sim i(\tau_{E,\hat{\mathbf{k}}}/\hbar)^2 A_0(E, \mathbf{k})$  we get  $\Delta\sigma_{(H_1)} \simeq \Delta\sigma_{(H_2)}$  and

$$\begin{aligned} \Delta\sigma_{(H)}^{i,j}(\omega, E) &= \Delta\sigma_{(H_1)}^{i,j}(\omega, E) + \Delta\sigma_{(H_2)}^{i,j}(\omega, E) \\ &= \frac{2}{\hbar N_0(E)} \left\langle \frac{J_{\mathbf{k},i}}{\hbar} \tau_{E,\hat{\mathbf{k}}} \int \frac{d\mathbf{k}'}{(2\pi)^d} U_{B\mathbf{k},\mathbf{k}'} f_{E,\mathbf{k}'} \frac{J_{\mathbf{k}',j}}{\hbar} \right\rangle \int \frac{d\mathbf{Q}}{(2\pi)^d} \frac{1}{-i\hbar\omega + \hbar\mathbf{Q} \cdot \mathbf{D}_B(E) \cdot \mathbf{Q}}. \end{aligned}$$

**Corrected conductivity tensor** – We now consider the quantity  $\mathbf{J}_{\mathbf{k}} - \int \frac{d\mathbf{k}'}{(2\pi)^d} U_{B\mathbf{k},\mathbf{k}'} f_{E,\mathbf{k}'} \mathbf{J}_{\mathbf{k}'}$ . Using the relation  $U_{B\mathbf{k},\mathbf{k}'} = \sum_{\lambda_E^n \neq 1} \lambda_E^n \phi_{E,\mathbf{k}}^n \phi_{E,\mathbf{k}'}^n$ , and the parities of the functions  $\phi_{E,\mathbf{k}}^n$  [see Eqs. (C.11) and (C.12)], one can show that

$$\mathbf{J}_{\mathbf{k}} - \int \frac{d\mathbf{k}'}{(2\pi)^d} U_{B\mathbf{k},\mathbf{k}'} f_{E,\mathbf{k}'} \mathbf{J}_{\mathbf{k}'} = \hbar \mathbf{v}. \quad (\text{C.36})$$

Therefore the Hikami contributions renormalize one of the  $\mathbf{J}_{\mathbf{k}}/\hbar$  back to the bare vertex  $\mathbf{v}$ , and we have

$$\begin{aligned} \Delta\sigma^{i,j}(\omega, E) &= \Delta\sigma_{(X)}^{i,j}(\omega, E) + \Delta\sigma_{(H)}^{i,j}(\omega, E) \\ &= -\frac{2}{\hbar N_0(E)} \left\langle \frac{J_{\mathbf{k},i}}{\hbar} v_j \tau_{E,\hat{\mathbf{k}}} \right\rangle \int \frac{d\mathbf{Q}}{(2\pi)^d} \frac{1}{-i\hbar\omega + \hbar\mathbf{Q} \cdot \mathbf{D}_B(E) \cdot \mathbf{Q}}, \end{aligned} \quad (\text{C.37})$$

which gives the final expression (5.34).

---

3. The same procedure as described in Sec. C.1 is used to obtain those expressions in the on-shell approximation.

## Appendix D

# Speckle potentials: 3D correlations in various configurations

Speckle patterns and their simplest statistical properties have been described in the introductory chapter 3. In this appendix we calculate their two-point correlation functions in 3D, for different configurations which are considered in Chaps. 6 and 8.

### D.1 Single-speckle

We first consider the configuration used in Secs. 3.2.2 and 6.1.1 in which a diffusive plate is illuminated by a single beam of wavelength  $\lambda_L = 2\pi/k_L$ . The geometry of the setup, and the notations are recalled in Fig. D.1.

In order to calculate the two-point correlation function of the disorder, which is the quantity of interest (see Secs. 5.1.1 and 5.2.1), we start from the complex amplitude of the field  $\mathcal{E}(\mathbf{r})$  as given by the Rayleigh-Sommerfeld formula (3.2). The intensity  $\mathcal{I}$  of the field is observed at the points  $\mathbf{r}$  and  $\mathbf{r}'$ . We choose  $\mathbf{r}' = \{0, 0, 0\}$  and  $\mathbf{r} = \{x, y, z\}$  (it is possible because translational invariance is assumed) with  $|x|, |y|, |z| \ll f$ , where  $f$  is the focal length of the lense that creates the speckle (see Fig. D.1). Therefore the field-field correlation function is

$$\overline{\mathcal{E}(\mathbf{r})\mathcal{E}^*(\mathbf{r}')}\simeq \frac{f(f+z)}{\lambda_L^2} \int d^2\rho |\epsilon(\rho)|^2 \frac{e^{ik_L(x_1-x_2)}}{x_1^2 x_2^2} \quad (\text{D.1})$$

with  $x_1 = \sqrt{\rho_x^2 + \rho_y^2 + f^2}$  and  $x_2 = \sqrt{(\rho_x - x)^2 + (\rho_y - y)^2 + (f+z)^2}$ , and we have  $\overline{\mathcal{I}(\mathbf{r}')}\simeq \overline{\mathcal{I}(\mathbf{r})} = \overline{\mathcal{E}(\mathbf{r})\mathcal{E}^*(\mathbf{r})} = \overline{\mathcal{I}}$ . With the definitions of Chap. 3 [see Eqs. (3.26) and (3.27)], the two-point correlation function of the disorder then reads

$$C_2(\mathbf{r} - \mathbf{r}') \equiv C(\mathbf{r} - \mathbf{r}') = V_R^2 \left| \frac{\overline{\mathcal{E}(\mathbf{r})\mathcal{E}^*(\mathbf{r}')}}{\overline{\mathcal{I}}} \right|^2, \quad (\text{D.2})$$

where  $V_R$  is the amplitude of the disorder [defined by Eq. (3.26)]. In the single-speckle case, it is also the standard deviation of the potential, as we have  $\overline{V^2} \equiv C(0) = V_R^2$ .

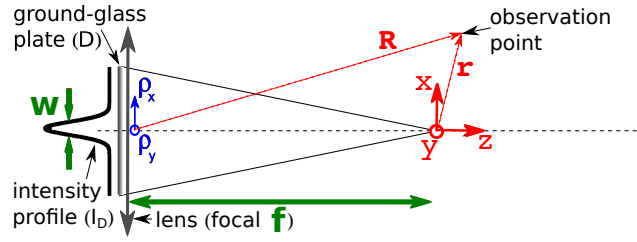


Figure D.1: Geometry and notations considered in the *single-speckle* configuration [reproduction of Fig. 3.2(b)]. A speckle pattern is obtained when a laser beam is diffracted by a ground-glass plate diffuser (D) of pupil function  $I_D(\boldsymbol{\rho})$ , where  $\boldsymbol{\rho} \equiv (\rho_x, \rho_y)$  spans the diffuser, which imprints a random phase on the various light paths. The intensity of the field,  $\mathcal{I}(\mathbf{r})$  is observed in the focal plane of a converging lens.

**Paraxial approximation** – In the paraxial approximation, we assume  $|\rho_x|, |\rho_y| \ll f$ . We then have

$$x_1 \simeq f + \frac{\rho_x^2 + \rho_y^2}{2f}$$

and

$$x_2 \simeq f + z + (\rho_x^2 + \rho_y^2) \left( \frac{1}{2f} - \frac{z}{2f^2} \right) + (x^2 + y^2) \left( \frac{1}{2f} - \frac{z}{2f^2} \right) - (\rho_x x + \rho_y y) \left( \frac{1}{f} - \frac{z}{f^2} \right).$$

Inserting these formulas into Eq. (D.1), we then get

$$\overline{\mathcal{E}(\mathbf{r})\mathcal{E}^*(\mathbf{r}')} = \frac{e^{-ik_L z} e^{-i\frac{k_L}{2f}(x^2+y^2)}}{f^2 \lambda_L^2} \int d^2\rho |\epsilon(\rho)|^2 e^{i\frac{k_L z}{2f^2}(\rho_x^2 + \rho_y^2)} e^{i\frac{k_L}{f}(\rho_x x + \rho_y y)}. \quad (\text{D.3})$$

**Gaussian beam** – We now consider an isotropic Gaussian beam  $|\epsilon(\rho)|^2 = I_0 e^{-2(\rho_x^2 + \rho_y^2)/w^2}$ , as used in Sec. 6.1.1. Using Eq. (D.3) we get

$$\overline{\mathcal{E}(\mathbf{r})\mathcal{E}^*(\mathbf{r}')} = \frac{e^{-ik_L z} e^{-i\frac{k_L}{2f}(x^2+y^2)}}{f^2 \lambda_L^2} \times \frac{\pi}{2/w^2 - ik_L z/2f^2} e^{-\frac{k_L^2}{4f^2} \frac{x^2+y^2}{2/w^2 - ik_L z/2f^2}} \quad (\text{D.4})$$

and  $\overline{\mathcal{I}} = \pi w^2/2\lambda_L^2 f^2$ . Inserting Eq. (D.4) into Eq. (D.2), we then find

$$C(\mathbf{r}) = \frac{V_R^2}{1 + 4z^2/\sigma_{\parallel}^2} e^{-\frac{1}{\sigma_{\perp}^2} \frac{1}{1+4z^2/\sigma_{\parallel}^2} (x^2+y^2)}, \quad (\text{D.5})$$

with  $\sigma_{\perp} = \frac{\lambda_L f}{\pi w}$  and  $\sigma_{\parallel} = \frac{4\lambda_L f^2}{\pi w^2}$ , which are the transverse and longitudinal correlation lengths. In Fourier space, with the definition  $\tilde{C}(\mathbf{k}) = \int d^3\mathbf{r} C(\mathbf{r}) e^{-i\mathbf{k}\cdot\mathbf{r}}$ , we finally get

$$\tilde{C}(\mathbf{k}) = V_R^2 \pi^{3/2} \frac{\sigma_{\perp} \sigma_{\parallel}}{\sqrt{k_x^2 + k_y^2}} e^{-\frac{\sigma_{\perp}^2}{4} (k_x^2 + k_y^2)} e^{-\frac{1}{4} \left( \frac{\sigma_{\parallel}}{\sigma_{\perp}} \right)^2 \frac{k_z^2}{k_x^2 + k_y^2}}. \quad (\text{D.6})$$

This power spectrum, which determines transport properties in the medium, is plotted in Fig. 6.1(a) for the parameters of Ref. [18].

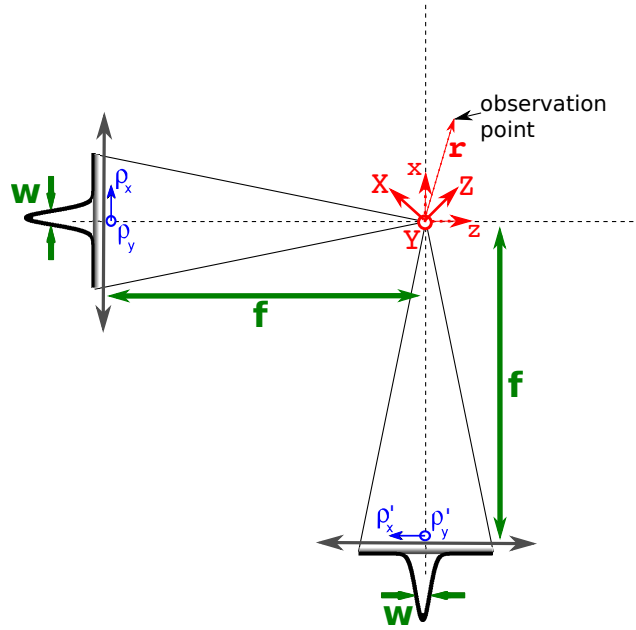


Figure D.2: Geometry and notations considered for *orthogonally-crossed speckles*. Two setups to create speckle patterns, such as that presented in Fig. D.1, are orthogonally-crossed.

## D.2 Orthogonally-crossed speckles

### D.2.1 Orthogonal incoherent-speckles

Here, we use the geometry and notations presented in Fig. D.2, where two laser beams are orthogonally crossed. We consider here that the laser beams are incoherent:  $\mathcal{I}(\mathbf{r}) = \mathcal{I}_1(\mathbf{r}) + \mathcal{I}_2(\mathbf{r})$  and use the same strategy as above. Both focal distances are the same ( $f$ ), and we will use the coordinates  $x = (X + Z)/\sqrt{2}$ ,  $y = Y$  and  $z = (Z - X)/\sqrt{2}$ , which are the symmetry axes of the setups. As above, we choose the observation points  $\mathbf{r}' = \{0, 0, 0\}$  and  $\mathbf{r} = \{X, Y, Z\}$  with  $|X|, |Y|, |Z| \ll f$ , and we get

$$C^{\text{incoh}}(\mathbf{r}) = (V_{R,1} + V_{R,2})^2 \left[ \left| \frac{\overline{\mathcal{E}_1(\mathbf{r})\mathcal{E}_1^*(\mathbf{r}')}}{\overline{\mathcal{I}_1}} \right|^2 \left( \frac{V_{R,1}}{V_{R,1} + V_{R,2}} \right)^2 + \left| \frac{\overline{\mathcal{E}_2(\mathbf{r})\mathcal{E}_2^*(\mathbf{r}')}}{\overline{\mathcal{I}_2}} \right|^2 \left( \frac{V_{R,2}}{V_{R,1} + V_{R,2}} \right)^2 \right], \quad (\text{D.7})$$

where  $V_{R,1} \propto \overline{\mathcal{I}_1}$  and  $V_{R,2} \propto \overline{\mathcal{I}_2}$  are the disorder amplitudes associated to each speckle field. We then have  $V_R = V_{R,1} + V_{R,2}$  is the amplitude of the incoherent-speckles pattern. In this case, the standard deviation is  $\sqrt{V^2} \equiv \sqrt{C(0)} = \sqrt{V_{R,1}^2 + V_{R,2}^2} \neq V_R$ .

**Paraxial approximation and Gaussian beams** – We now consider that both speckles are obtained in the paraxial approximation. To calculate  $\left| \frac{\overline{\mathcal{E}_1(\mathbf{r})\mathcal{E}_1^*(\mathbf{r}')}}{\overline{\mathcal{I}_1}} \right|^2$  and  $\left| \frac{\overline{\mathcal{E}_2(\mathbf{r})\mathcal{E}_2^*(\mathbf{r}')}}{\overline{\mathcal{I}_2}} \right|^2$  we can use Eq. (D.3) with  $\{x, y, z\} = \{(X + Z)/\sqrt{2}, Y, (Z - X)/\sqrt{2}\}$  and  $\{x, y, z\} \rightarrow \{x', y', z'\} = \{-z, y, x\}$ . We also assume  $|\epsilon_1(\rho)|^2 = |\epsilon_2(\rho)|^2 = I_0 e^{-2(\rho_x^2 + \rho_y^2)/w^2}$ . Since the two speckles are

independent, we can use Eq. (D.5) for each speckle, which yields

$$\frac{C^{\text{incoh}}(\mathbf{r})}{V_{\text{R}}^2} = \frac{1}{4} \left[ \frac{1}{1 + 4z^2/\sigma_{\parallel}^2} e^{-\frac{1}{2\sigma_{\perp}^2} \frac{1}{1+4z^2/\sigma_{\parallel}^2} (x^2+y^2)} + \frac{1}{1 + 4x^2/\sigma_{\parallel}^2} e^{-\frac{1}{2\sigma_{\perp}^2} \frac{1}{1+4x^2/\sigma_{\parallel}^2} (y^2+z^2)} \right],$$

In Fourier space, it becomes

$$\frac{\tilde{C}^{\text{incoh}}(\mathbf{k})}{V_{\text{R}}^2} = \frac{\pi^{3/2}}{4} \sigma_{\perp} \sigma_{\parallel} \left[ \frac{e^{-\frac{\sigma_{\perp}^2}{4}(k_x^2+k_y^2)} e^{-\frac{1}{4} \left(\frac{\sigma_{\parallel}}{\sigma_{\perp}}\right)^2 \frac{k_z^2}{k_x^2+k_y^2}}}{\sqrt{k_x^2 + k_y^2}} + \frac{e^{-\frac{\sigma_{\perp}^2}{4}(k_z^2+k_y^2)} e^{-\frac{1}{4} \left(\frac{\sigma_{\parallel}}{\sigma_{\perp}}\right)^2 \frac{k_x^2}{k_z^2+k_y^2}}}{\sqrt{k_z^2 + k_y^2}} \right]. \quad (\text{D.8})$$

This power spectrum is presented in Fig. 6.1(b).

## D.2.2 Orthogonal coherent-speckles

Here, we still consider the same geometry (see Fig. D.2), but we now assume that the two laser beams are mutually coherent. Although  $\bar{\mathcal{I}} = \bar{\mathcal{I}}_1 + \bar{\mathcal{I}}_2$ , as for the incoherent-speckles configuration, it is no longer true without averaging. In order to compute the disorder correlation function, we start from

$$\overline{\mathcal{E}(\mathbf{r})\mathcal{E}^*(\mathbf{r}')} = \overline{\mathcal{E}_1(\mathbf{r})\mathcal{E}_1^*(\mathbf{r}')} + \overline{\mathcal{E}_2(\mathbf{r})\mathcal{E}_2^*(\mathbf{r}')}. \quad (\text{D.9})$$

For  $\mathbf{r}' = \{0, 0, 0\}$  and  $\mathbf{r} = \{X, Y, Z\}$  where  $|X|, |Y|, |Z| \ll f$ , we have

$$\frac{C^{\text{coh}}(\mathbf{r})}{V_{\text{R}}^2} = \frac{C^{\text{incoh}}(\mathbf{r})}{V_{\text{R}}^2} + 2\Re \left\{ \frac{\overline{\mathcal{E}_1(\mathbf{r})\mathcal{E}_1^*(\mathbf{r}') \mathcal{E}_2^*(\mathbf{r})\mathcal{E}_2(\mathbf{r}')}}{\overline{\mathcal{I}_1 \mathcal{I}_2}} \right\} \frac{V_{\text{R},1} V_{\text{R},2}}{V_{\text{R}}^2}, \quad (\text{D.10})$$

where  $V_{\text{R}} = V_{\text{R},1} + V_{\text{R},2}$ .

**Paraxial approximation and Gaussian beams** – We now consider that both speckles are obtained in the paraxial approximation and that they have a Gaussian intensity profile  $|\epsilon_1(\rho)|^2 = |\epsilon_2(\rho)|^2 = I_0 e^{-2(\rho_x^2 + \rho_y^2)/w^2}$ . Using Eq. (D.4) for both speckles, it yields

$$\frac{C^{\text{coh}}(\mathbf{r})}{V_{\text{R}}^2} = \frac{C^{\text{incoh}}(\mathbf{r})}{V_{\text{R}}^2} + 2 \frac{e^{-\frac{1}{2\sigma_{\perp}^2} \frac{x^2+y^2}{1+4z^2/\sigma_{\parallel}^2}} e^{-\frac{1}{2\sigma_{\perp}^2} \frac{y^2+z^2}{1+4x^2/\sigma_{\parallel}^2}}}{(1 + 4z^2/\sigma_{\parallel}^2)(1 + 4x^2/\sigma_{\parallel}^2)} \times \left\{ \left(1 + 4 \frac{xz}{\sigma_{\parallel}^2}\right) \cos[\phi(\mathbf{r})] + 2 \frac{x-z}{\sigma_{\parallel}} \sin[\phi(\mathbf{r})] \right\} \quad (\text{D.11})$$

where  $\phi(\mathbf{r}) = \frac{2\pi}{\lambda_{\text{L}}}(x-z) - \frac{z}{\sigma_{\perp}^2 \sigma_{\parallel}} \frac{x^2+y^2}{1+4z^2/\sigma_{\parallel}^2} - \frac{x}{\sigma_{\perp}^2 \sigma_{\parallel}} \frac{y^2+z^2}{1+4x^2/\sigma_{\parallel}^2}$ . We didn't find any analytical solution for the Fourier transform, therefore we calculated it numerically. This power spectrum is presented in Fig. 6.1(c) for the parameters of Ref. [19]. In the coherent-speckles configuration, the standard deviation is  $\sqrt{V_{\text{R}}^2} = V_{\text{R}}$ , as for the single-speckle.

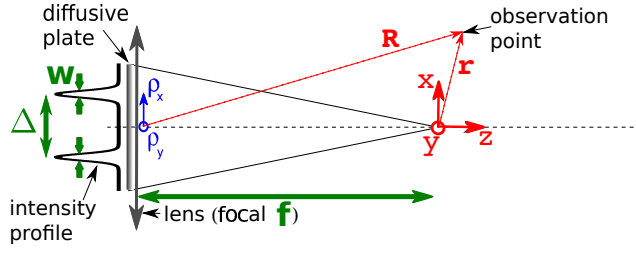


Figure D.3: Geometry and notations considered for *parallel speckles*. In the setup of Fig. D.1, the diffusive plate is illuminated by two parallel Gaussian laser beams.

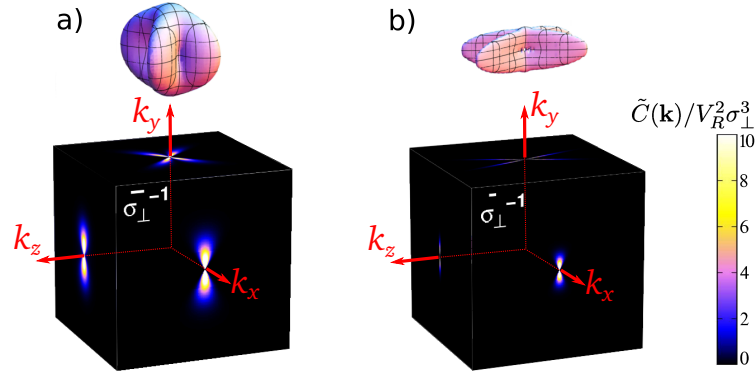


Figure D.4: Power spectrum of the disorder  $\tilde{C}(\mathbf{k})$  for the *parallel incoherent-speckles* case with (a)  $\Delta/w = 4$  and (b)  $\Delta/w = 16$  (with  $\sigma_{\parallel}/\sigma_{\perp} \simeq 5.8$ ). The functions  $\tilde{C}(\mathbf{k})$  are represented as iso-value surfaces (at  $0.1V_R^2\sigma_{\perp}^3$ ) and cuts in the planes defined by the symmetry axes.

## D.3 Parallel speckles

We are now interested in the geometry and notations presented in Fig. D.3, where two parallel Gaussian laser beams illuminate the diffusive plate.

### D.3.1 Single shifted speckle

For a single Gaussian beam centered at  $\rho_x = \Delta/2$  [i.e. we take  $|\epsilon(\rho)|^2 = I_0 e^{-2[(\rho_x - \Delta/2)^2 + \rho_y^2]/w^2}$ ], we get in the paraxial approximation

$$\left| \frac{\overline{\mathcal{E}(\mathbf{r})\mathcal{E}^*(\mathbf{r}')}}{\overline{\mathcal{I}}} \right|^2 = \frac{e^{-(\frac{\Delta}{w})^2}}{1 + 4z^2/\sigma_{\parallel}^2} e^{-\frac{1}{\sigma_{\perp}^2} \frac{1}{1+4z^2/\sigma_{\parallel}^2} (x^2 + y^2 + 4xz \frac{\sigma_{\perp}}{\sigma_{\parallel}} \frac{\Delta}{w} - \sigma_{\perp}^2 \frac{\Delta^2}{w^2})}. \quad (\text{D.12})$$

In Fourier space, we then get in 3D :

$$\tilde{C}^{\text{shifted}}(\mathbf{k}) = V_R^2 \pi^{3/2} \frac{\sigma_{\perp} \sigma_{\parallel}}{\sqrt{k_x^2 + k_y^2}} e^{-\frac{\sigma_{\perp}^2}{4} (k_x^2 + k_y^2)} e^{-\frac{1}{4} \left( \frac{\sigma_{\parallel}}{\sigma_{\perp}} \right)^2 \frac{(k_z - k_x \frac{\sigma_{\perp}}{\sigma_{\parallel}} \frac{\Delta}{w})^2}{k_x^2 + k_y^2}}. \quad (\text{D.13})$$

Note that for  $\Delta = 0$  we recover Eqs. (D.5) and (D.6), as expected.

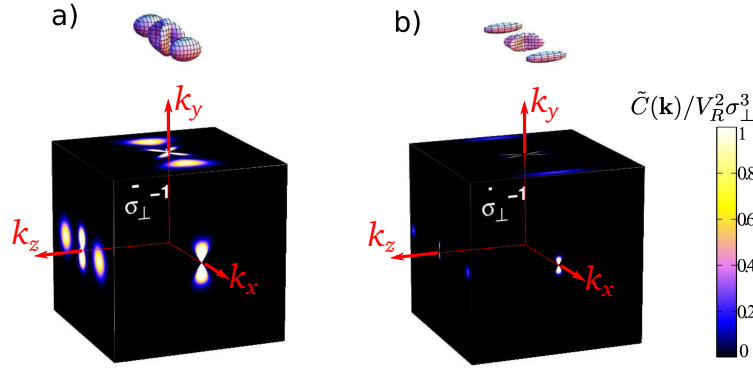


Figure D.5: Power spectrum of the disorder  $\tilde{C}(\mathbf{k})$  for the *parallel coherent-speckles* case with (a)  $\Delta/w = 4$  and (b)  $\Delta/w = 16$  (with  $\sigma_{\parallel}/\sigma_{\perp} \simeq 5.8$ ). The functions  $\tilde{C}(\mathbf{k})$  are represented as iso-value surfaces (at  $0.1V_R^2\sigma_{\perp}^3$ ) and cuts in the planes defined by the symmetry axes.

### D.3.2 Parallel incoherent-speckles

We now consider two incoherent Gaussian beams centered in  $\rho_x = \Delta/2$  and  $\rho_x = -\Delta/2$  respectively [i.e. we take  $|\epsilon_1(\rho)|^2 = I_0 e^{-2[(\rho_x - \Delta/2)^2 + \rho_y^2]/w^2}$  and  $|\epsilon_2(\rho)|^2 = I_0 e^{-2[(\rho_x + \Delta/2)^2 + \rho_y^2]/w^2}$ ]. As in Sec. D.2.1, we can use Eq. (D.7), and we find

$$\frac{C^{\text{incoh,P}}(\mathbf{r})}{V_R^2} = \frac{1}{4} \frac{e^{-\frac{\Delta^2}{w^2}}}{1 + 4z^2/\sigma_{\parallel}^2} e^{-\frac{1}{\sigma_{\perp}^2} \frac{1}{1+4z^2/\sigma_{\parallel}^2} \left(x^2 + y^2 - \sigma_{\perp}^2 \frac{\Delta^2}{w^2}\right)} 2 \cosh \left[ \frac{4xz}{\sigma_{\parallel}\sigma_{\perp}} \frac{\Delta}{w} \frac{1}{1 + 4z^2/\sigma_{\parallel}^2} \right],$$

where  $V_R = V_{R,1} + V_{R,2}$  and

$$\frac{\tilde{C}^{\text{incoh,P}}(\mathbf{k})}{V_R^2} = \frac{\pi^{3/2}}{4} \frac{\sigma_{\perp}\sigma_{\parallel}}{\sqrt{k_x^2 + k_y^2}} e^{-\frac{\sigma_{\perp}^2}{4}(k_x^2 + k_y^2)} \left[ e^{-\frac{1}{4} \frac{\sigma_{\parallel}^2}{\sigma_{\perp}^2} \frac{\left(k_z - k_x \frac{\sigma_{\perp}}{\sigma_{\parallel}} \frac{\Delta}{w}\right)^2}{k_x^2 + k_y^2}} + e^{-\frac{1}{4} \frac{\sigma_{\parallel}^2}{\sigma_{\perp}^2} \frac{\left(k_z + k_x \frac{\sigma_{\perp}}{\sigma_{\parallel}} \frac{\Delta}{w}\right)^2}{k_x^2 + k_y^2}} \right]. \quad (\text{D.14})$$

This power spectrum is plotted in Fig. D.4 for  $\Delta/w = 4$  and 16. In this case, we have  $\sqrt{V^2} \equiv \sqrt{C(0)} = V_R/\sqrt{2}$ , as in the orthogonal incoherent-speckles.

### D.3.3 Parallel coherent-speckles

**In 3D** – If the preceding Gaussian beams are now mutually coherent, Eq. (D.10) holds, and we obtain

$$\frac{C^{\text{coh,P}}(\mathbf{r})}{V_R^2} = \frac{C^{\text{incoh,P}}(\mathbf{r})}{V_R^2} + 2 \frac{1}{4} \frac{e^{-\frac{1}{\sigma_{\perp}^2} \frac{x^2 + y^2}{1+4z^2/\sigma_{\parallel}^2}} e^{-4 \frac{z^2}{\sigma_{\parallel}^2} \frac{\Delta^2}{w^2} \frac{1}{1+4z^2/\sigma_{\parallel}^2}}}{1 + 4z^2/\sigma_{\parallel}^2} \cos \left( \frac{2}{1 + 4z^2/\sigma_{\parallel}^2} \frac{x}{\sigma_{\perp}} \frac{\Delta}{w} \right)$$

where  $V_R = V_{R,1} + V_{R,2}$ , and

$$\frac{\tilde{C}^{\text{coh,P}}(\mathbf{k})}{V_R^2} = \frac{\tilde{C}^{\text{incoh,P}}(\mathbf{k})}{V_R^2} + \frac{\pi^{3/2}}{2} \frac{\sigma_{\perp}\sigma_{\parallel}}{\sqrt{k_x^2 + k_y^2}} e^{-\frac{\sigma_{\perp}^2}{4}(k_x^2 + k_y^2)} e^{-\frac{1}{4} \left(\frac{\sigma_{\parallel}}{\sigma_{\perp}}\right)^2 \frac{k_z^2}{k_x^2 + k_y^2}} \cosh \left( \sigma_{\perp} k_x \frac{\Delta}{w} \right). \quad (\text{D.15})$$

This power spectrum is plotted in Fig. D.5 for  $\Delta/w = 4$  and 16. In this coherent configuration, the standard deviation is  $\sqrt{V^2} = V_R$ , as for the orthogonal coherent-speckles and the single-speckle.

**In 1D** – Even if here we have focused on the 3D correlations functions, we also used this configuration in 1D in Sec. 8.2. We therefore write the correlation function obtained in a 1D scheme (for  $y = z = 0$ )

$$\frac{C^{\text{coh,P}}(x)}{V_R^2} = \frac{e^{-x^2/\sigma_R^2}}{2} [1 + \cos(\kappa_0 x/\sigma_R)],$$

with  $\sigma_R \equiv \sigma_\perp$  and  $\kappa_0 = 2\Delta/w$  and the one-dimensional Fourier transform gives

$$\boxed{\frac{\tilde{C}^{\text{coh,P}}(\hat{k}_x)}{V_R^2} = \frac{\pi^{1/2}}{4} \sigma_R \left[ e^{-\frac{(k_x \sigma_R - \kappa_0)^2}{4}} + 2e^{-\frac{(k_x \sigma_R)^2}{4}} + e^{-\frac{(k_x \sigma_R + \kappa_0)^2}{4}} \right]}. \quad (\text{D.16})}$$



# Appendix E

## Complementary models of three-dimensional disorder correlations

### E.1 Three-dimensional isotropic speckle

A simple model of 3D speckle with isotropic correlation properties, is found when considering the light pattern obtained inside an integrating sphere lit by a laser beam of wavevector  $k_L$  [16, 169]. The real-space correlation function is given in Eq. (6.17) and the associated power spectrum

$$\tilde{C}(\mathbf{k}) = \frac{V_R^2 \pi^2 \sigma^2}{|\mathbf{k}|} \Theta(2\sigma^{-1} - |\mathbf{k}|), \quad (\text{E.1})$$

where  $\Theta(x) = 1$  if  $x > 0$  and  $\Theta(x) = 0$  otherwise. It is isotropic and bears the same divergence as the 3D models of disorder considered in Sec. 6 and appendix D:  $\tilde{C}(\mathbf{k}) \propto 1/|\mathbf{k}|$  when  $|\mathbf{k}| \rightarrow 0$ . It is therefore a relevant model for comparison with the models of speckle considered in this work (see Sec. 6.3.2 for example), even if rather unrealistic from an experimental point of view.

An interesting test of the numerical procedure used in Chap. 6 3D anisotropic models of disorder, is to perform the same numerical procedure [i.e. diagonalizing the integral operator (5.22) and incorporating the results in Eq. (5.21)] with this isotropic model for which analytical calculations can be performed. As previously, we use  $2^7 \times 2^7$  points regularly spaced on the  $\mathbf{k}$ -space shell  $|\mathbf{k}| = k_E$ . Some eigenfunctions and eigenvalues of Eq. (5.22) are presented in Fig. E.1. We indeed find spherical harmonics [see Eq. (C.23)], and the eigenvalues  $\lambda_E^n$  agree well with theory [Eq. (C.22) with  $\tilde{C}$  given by Eq. (E.1), not shown on the figure]. Figure E.2 presents the numerical results for the Boltzmann diffusion constant (red dots) which agree very well with the analytic formula (solid black line) found when incorporating Eq. (E.1) into Eq. (C.24):

$$D_B(E) = \frac{\hbar}{m} \left( \frac{E_\sigma}{V_R} \right)^2 \frac{k_E^2 \sigma^2}{(2\pi)^2} \left[ k_E^3 \sigma^3 \Theta(k_E \sigma - 1) + \Theta(1 - k_E \sigma) \right] \quad (\text{E.2})$$

Note that we recover the same asymptotic behaviours as for our anisotropic cases [ $D_B(E) \propto E$  for  $E/E_\sigma < 1/2$  and  $D_B(E) \propto E^{5/2}$  for  $E/E_\sigma \geq 1/2$ ]. Those tests confort us in the idea that the discretization used here correctly treats the  $|\mathbf{k}| \rightarrow 0$  divergence.

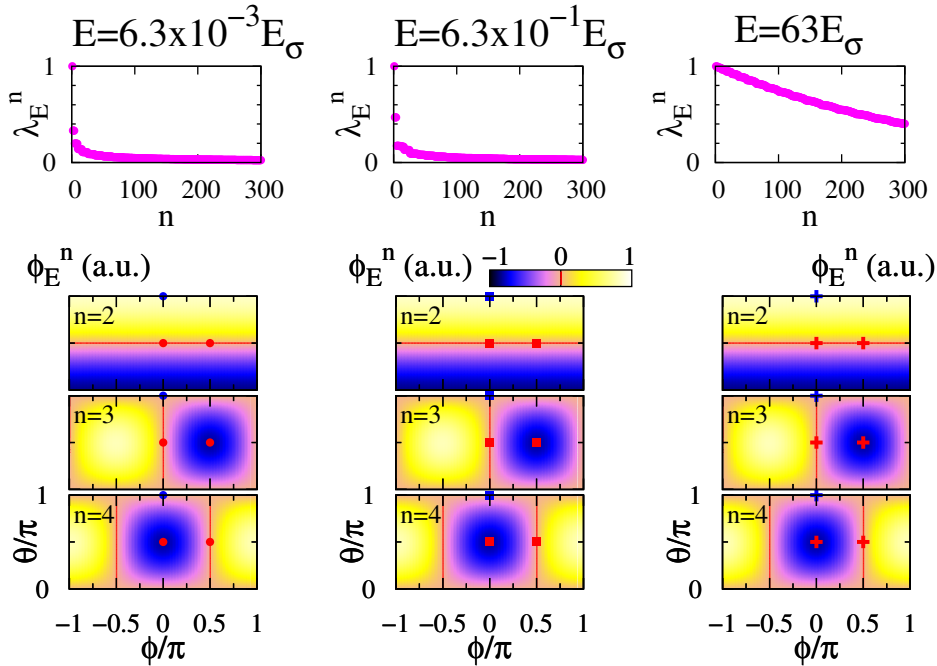


Figure E.1: *Isotropic speckle*. Eigenvalues of Eq. (5.22) (top row) for the correlation function of Eq. (E.1). Topology of the eigenvectors  $\phi_{E,\hat{\mathbf{k}}}^n$  contributing to  $D_B^x$  (bottom row),  $D_B^y$  (2<sup>nd</sup> row) and  $D_B^z$  (3<sup>rd</sup> row) [with the parametrization  $\hat{\mathbf{k}} = (\hat{\mathbf{k}}_x, \hat{\mathbf{k}}_y, \hat{\mathbf{k}}_z) \equiv (\sin \theta \cos \phi, \sin \theta \sin \phi, \cos \theta)$ ], the red lines locate the nodal lines. We find spherical harmonics:  $\phi_{E,\hat{\mathbf{k}}}^2$  is proportional to  $Y_1^0$ ,  $\phi_{E,\hat{\mathbf{k}}}^3$  to  $Y_1^{-1}$  and  $\phi_{E,\hat{\mathbf{k}}}^4$  to  $Y_1^{+1}$ . From left to right  $E = 6.3 \times 10^{-3} E_\sigma$ ,  $E = 6.3 \times 10^{-1} E_\sigma$  and  $E = 63 E_\sigma$ .

The eigenvalues and eigenfunctions found in the numerical procedure are shown in Fig. E.1. As explained in appendix C.2, we find that the eigenfunctions are spherical harmonics, and that only the  $p$ -level spherical harmonics contribute to  $D_B(E)$ . More precisely, at any energy,  $Y_1^{+1}$  contributes to  $D_B^x$ ,  $Y_1^{-1}$  to  $D_B^y$  and  $Y_1^0$  to  $D_B^z$ . The contribution of the other harmonics is found negligible numerically (less than  $10^{-3}\%$ ), as expected.

## E.2 Anisotropic Gaussian correlation function (3D)

In Ref. [18] they use a single-speckle configuration to create a speckle pattern. However, Kondov *et al.* fit the correlation function in real space by a three dimensional Gaussian, and the fit does not permit to distinguish between a Lorentzian [as expected in the single-speckle case, see Eq. (D.5)] and a Gaussian in the  $z$  direction [205]. In order to be complete, we consider here an anisotropic Gaussian correlation function.

We have computed numerically the Boltzmann diffusion tensor in the case for the power spectrum

$$\tilde{C}(\mathbf{k}) = V_R^2 \pi^{3/2} \xi \sigma_R^3 e^{-\frac{\sigma_R^2}{4}(k_x^2 + k_y^2 + \xi^2 k_z^2)}, \quad (\text{E.3})$$

where  $\xi \equiv \sigma_{Rz}/\sigma_{Rx,y}$  is the configuration anisotropy factor. Although such correlations can hardly be obtained with a speckle pattern in principle, it can model anisotropic impurities randomly scattered in an isotropic medium (so-called Edwards model [41], see Sec. 1.1.3).

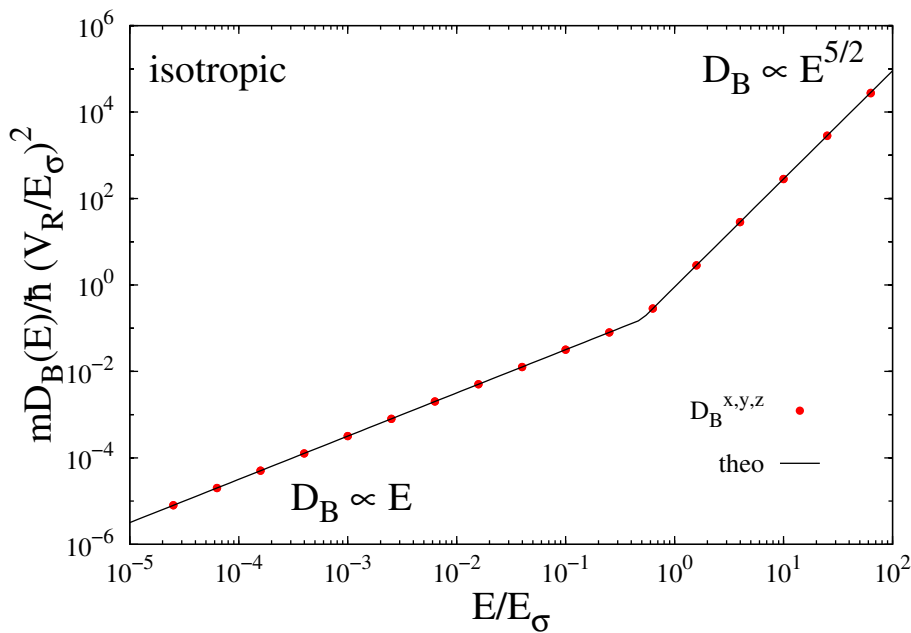


Figure E.2: Boltzmann diffusion coefficient for the *isotropic speckle* configuration (red dots). The solid black line is the theoretical value.

We have performed the same numerical procedure as for the 3D speckle models considered in this thesis (see Chap. 6) for  $\xi = 6$ . As previously, we use  $2^7 \times 2^7$  points regularly spaced on the  $\mathbf{k}$ -space shell  $|\mathbf{k}| = k_E$ . The results are shown in Fig. E.3. They are interesting in two respects.

First, this model is close to the single-speckle case with  $\sigma_{\parallel}/\sigma_{\perp} \simeq 5.8$  [see Eqs. (6.3) and (6.4)], except that the shape of the correlations in the  $z$ -direction are different. In contrast to the single-speckle case, this model bears a white-noise limit: for  $|\mathbf{k}| \ll \sigma_R^{-1}, (\xi\sigma_R)^{-1}$  one finds  $\tilde{C}(\mathbf{k}) \simeq V_R^2 \pi^{3/2} \xi \sigma_R^3$ . By comparing Fig. E.3 and Fig. 6.5, one can see the importance of the shape of the correlations. The behaviour of the anisotropy factor with energy are very different. Equation (E.3) has a white-noise limit, which shows up in Fig. E.3 by the low-energy scaling  $D_B^u(E) \propto E^{1/2}$  and Boltzmann anisotropy factor is  $D_B^z(E)/D_B^{x,y}(E) \simeq 1$  at low energy. When the energy increases it shows a non monotonous behaviour (as for the 2D anisotropic Gaussian see Fig. 5.7). At high energy it reaches a constant value  $D_B^z/D_B^{x,y} \simeq 18.5$ . We recall that in Fig. 6.5 we found an anisotropy factor almost independent of energy:  $D_B^z/D_B^{x,y} \simeq 10$ .

Second, as explained above, in Ref. [18] the power spectrum is fitted by Eq. (E.3), with  $\xi = 5.9$ . It is interesting to note that in this model we find  $1 < D_B^z/D_B^{x,y} \lesssim 20$ , therefore the self-consistent theory predicts  $1 < L_{\text{loc}}^z/L_{\text{loc}}^{x,y} \lesssim 4.5$ , which is not consistent with the observations of Ref. [18] (see Sec. 7 for details).

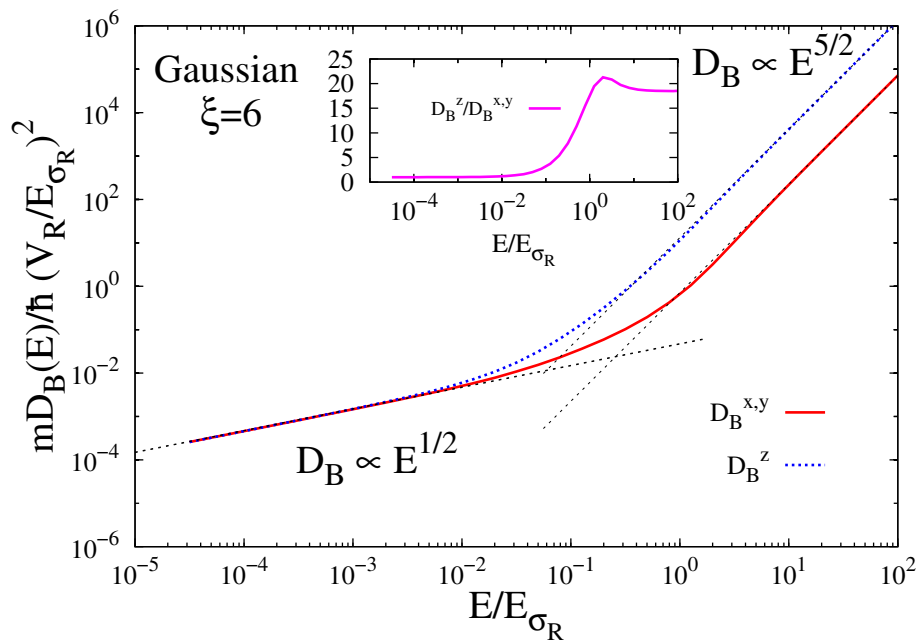


Figure E.3: *Anisotropic 3D Gaussian*. Components of the diffusion tensor:  $D_B^{x,y}$  (solid red line) and  $D_B^z$  (dotted blue line) for the power spectrum (E.3) and  $\xi = 6$ . The dotted lines are power-law fits ( $D_B^u \propto E^{\gamma_u}$ ) to the data in the low and high energy limits. The inset shows the transport anisotropy factor  $D_B^z/D_B^{x,y}$ .

# Bibliography

- [1] P. W. ANDERSON. More is different. *Science*, **177** 393, 1972.
- [2] P. W. ANDERSON. Absence of diffusion in certain random lattices. *Phys. Rev.*, **109** 1492–1505, 1958.
- [3] P. A. LEE AND T. V. RAMAKRISHNAN. Disordered electronic systems. *Rev. Mod. Phys.*, **57** 287–337, 1985.
- [4] H. BOUCHIAT. Experimental signatures of phase coherent transport. In *Mesoscopic Quantum Physics, E. Akkermans et al. eds., Proceedings of the Les Houches Summer School of Theoretical Physics, Vol. LXI*, 1994.
- [5] D. S. WIERSMA, P. BARTOLINI, AD LAGENDIJK, AND R. RIGHINI. Localization of light in a disordered medium. *Nature (London)*, **390** 671–673, 1997.
- [6] M. STÖRZER, P. GROSS, C. M. AEGERTER, AND G. MARET. Observation of the critical regime near Anderson localization of light. *Phys. Rev. Lett.*, **96** 063904, 2006.
- [7] B. DAMSKI, J. ZAKRZEWSKI, L. SANTOS, P. ZOLLER, AND M. LEWENSTEIN. Atomic Bose and Anderson glasses in optical lattices. *Phys. Rev. Lett.*, **91** 080403, 2003.
- [8] L. SANCHEZ-PALENCIA, D. CLÉMENT, P. LUGAN, P. BOUYER, G. V. SHLYAPNIKOV, AND A. ASPECT. Anderson localization of expanding Bose-Einstein condensates in random potentials. *Phys. Rev. Lett.*, **98** 210401, 2007.
- [9] J. BILLY, V. JOSSE, Z. ZUO, A. BERNARD, B. HAMBRECHT, P. LUGAN, D. CLÉMENT, L. SANCHEZ-PALENCIA, P. BOUYER, AND A. ASPECT. Direct observation of Anderson localization of matter waves in a controlled disorder. *Nature (London)*, **453** 891–894, 2008.
- [10] G. ROATI, C. D’ERRICO, L. FALLANI, M. FATTORI, C. FORT, M. ZACCANTI, G. MODUGNO, M. MODUGNO, AND M. INGUSCIO. Anderson localization of a non-interacting Bose-Einstein condensate. *Nature (London)*, **453** 895–898, 2008.
- [11] AD LAGENDIJK, B. A. VAN TIGGELEN, AND D. S. WIERSMA. Fifty years of Anderson localization. *Phys. Today*, **62** 24–29, 2009.
- [12] A. ASPECT AND M. INGUSCIO. Anderson localization of ultracold atoms. *Phys. Today*, **62** 30–35, 2009.
- [13] L. SANCHEZ-PALENCIA AND M. LEWENSTEIN. Disordered quantum gases under control. *Nature Phys.*, **6** 87–95, 2010.
- [14] P. LUGAN, A. ASPECT, L. SANCHEZ-PALENCIA, D. DELANDE, B. GRÉMAUD, C. A. MÜLLER, AND C. MINIATURA. One-dimensional Anderson localization in certain correlated random potentials. *Phys. Rev. A*, **80** 023605, 2009.

- [15] E. GUREVICH AND O. KENNETH. Lyapunov exponent for the laser speckle potential: A weak disorder expansion. *Phys. Rev. A*, **79** 063617, 2009.
- [16] R. C. KUHN, O. SIGWARTH, C. MINIATURA, D. DELANDE, AND C. A. MÜLLER. Coherent matter wave transport in speckle potentials. *New J. Phys.*, **9** 161, 2007.
- [17] M. ROBERT-DE-SAINT-VINCENT, J.-P. BRANTUT, B. ALLARD, T. PLISSON, L. PEZZÉ, L. SANCHEZ-PALENCIA, A. ASPECT, T. BOURDEL, AND P. BOUYER. Anisotropic 2D diffusive expansion of ultracold atoms in a disordered potential. *Phys. Rev. Lett.*, **104** 220602, 2010.
- [18] S. S. KONDOV, W. R. MCGEHEE, J. J. ZIRBEL, AND B. DEMARCO. Three-dimensional Anderson localization of ultracold fermionic matter. *Science*, **334** 66–68, 2011.
- [19] F. JENDRZEJEWSKI, A. BERNARD, K. MÜLLER, P. CHEINET, V. JOSSE, M. PIRAUD, L. PEZZÉ, L. SANCHEZ-PALENCIA, A. ASPECT, AND P. BOUYER. Three-dimensional localization of ultracold atoms in an optical disorder. *Nature Phys.*, **8** 398, 2012.
- [20] D. CLÉMENT, A. F. VARÓN, J. A. RETTER, L. SANCHEZ-PALENCIA, A. ASPECT, AND P. BOUYER. Experimental study of the transport of coherent interacting matter-waves in a 1D random potential induced by laser speckle. *New J. Phys.*, **8** 165, 2006.
- [21] B. SHAPIRO. Cold atoms in the presence of disorder. *J. Phys. A: Math. Theor.*, **45** 143001, 2012.
- [22] M. PIRAUD, P. LUGAN, P. BOUYER, A. ASPECT, AND L. SANCHEZ-PALENCIA. Localization of a matter wave packet in a disordered potential. *Phys. Rev. A*, **83** 031603(R), 2011.
- [23] L. PEZZÉ, M. ROBERT-DE-SAINT-VINCENT, T. BOURDEL, J.-P. BRANTUT, B. ALLARD, T. PLISSON, A. ASPECT, P. BOUYER, AND L. SANCHEZ-PALENCIA. Regimes of classical transport of cold gases in a two-dimensional anisotropic disorder. *New J. Phys.*, **13** 095015, 2011.
- [24] M. PIRAUD, L. PEZZÉ, AND L. SANCHEZ-PALENCIA. Quantum transport of atomic matterwaves in anisotropic 2D and 3D disorder. In preparation, 2012.
- [25] M. PIRAUD, L. PEZZÉ, AND L. SANCHEZ-PALENCIA. Matter wave transport and Anderson localization in anisotropic three-dimensional disorder. *Europhys. Lett.*, **99** 50003, 2012.
- [26] M. PIRAUD, A. ASPECT, AND L. SANCHEZ-PALENCIA. Anderson localization of matter waves in tailored disordered potentials. *Phys. Rev. A*, **85** 063611, 2012.
- [27] M. PIRAUD AND L. SANCHEZ-PALENCIA. Tailoring Anderson localization by disorder correlations in 1D speckle potentials. arXiv:1209.1606, to be published in Eur. Phys. J. Special Topics, 2012.
- [28] R. HULET. private communication.
- [29] S. JOHN. Electromagnetic absorption in a disordered medium near a photon mobility edge. *Phys. Rev. Lett.*, **53** 2169–2172, 1984.
- [30] H. HU, A. STRYBULEVYCH, J. H. PAGE, S. E. SKIPETROV, AND B. A. VAN TIGGELLEN. Localization of ultrasound in a three-dimensional elastic network. *Nature Phys.*, **4** 845–848, 2008.

- [31] E. LAROSE, L. MARGERIN, B. A. VAN TIGGELEN, AND M. CAMPILLO. Weak localization of seismic waves. *Phys. Rev. Lett.*, **93** 048501, 2004.
- [32] D. BELITZ AND T. R. KIRKPATRICK. The Anderson-Mott transition. *Rev. Mod. Phys.*, **66** 261–380, 1994.
- [33] M. MA, B. I. HALPERIN, AND P. A. LEE. Strongly disordered superfluids: Quantum fluctuations and critical behavior. *Phys. Rev. B*, **34** 3136–3143, 1986.
- [34] NEIL W. ASHCROFT AND N. DAVID MERMIN. *Solid State Physics*. Thomson Learning, New York, 1976.
- [35] CHARLES KITTEL. *Introduction to Solid State Physics*. John Wiley & Sons, 2004.
- [36] <http://www.ndt-ed.org/EducationResources/CommunityCollege/Materials/Structure/solidstate.htm>.
- [37] IL'YA M. LIFSHITS, SERGUEI A. GREDESKUL, AND LEONID A. PASTUR. *Introduction to the Theory of Disordered Systems*. Wiley, New York, 1988.
- [38] PAOLO M. OSSI. *Disordered materials: an introduction*. Springer & Verlag, Berlin, 2006.
- [39] PING SHENG. *Scattering and localization of classical waves in random media*. Directions in Condensed Matter Physics, Vol. 8. World Scientific, Singapore, 1990.
- [40] AD LAGENDIJK AND B. A. VAN TIGGELEN. Resonant multiple scattering of light. *Phys. Rep.*, **270** 143–215, 1996.
- [41] ERIC AKKERMANS AND GILLES MONTAMBAUX. *Mesoscopic Physics of Electrons and Photons*. Cambridge University Press, 2007.
- [42] DIETER VOLLHARDT AND PETER WÖLFLE. Self-consistent theory of Anderson localization. In W. Hanke and Y.V. Kopalev, editors, *Electronic Phase Transitions*, pages 1–78. Elsevier, Berlin, 1992.
- [43] P. W. ANDERSON. Theory of dirty superconductors. *J. Phys. Chem. Sol.*, **11** 26–30, 1959.
- [44] J. T. EDWARDS. *Philos. Mag.*, **3** 1020, 1958.
- [45] G. BERGMANN. Weak localization in thin films. *Phys. Rep.*, **107** 1, 1984.
- [46] M. E. GERSHENSON B. L. ALTSHULER, A. G. ARONOV AND YU. V. SHARVIN. Quantum effects in disordered metal films. *Phys. Rev., Sov. Sci. Rev.*, **9** 225, 1987.
- [47] G. LABEYRIE, F. DE TOMASI, J.-C. BERNARD, C. A. MÜLLER, C. MINIATURA, AND R. KAISER. Coherent backscattering of light by cold atoms. *Phys. Rev. Lett.*, **83** 5266–5269, 1999.
- [48] Y. KUGA AND A. ISHIMARU. Retroreflectance from a dense distribution of spherical particles. *J. Opt. Soc. Am. A*, **1** 831, 1984.
- [49] P.-E. WOLF AND G. MARET. Weak localization and coherent backscattering of photons in disordered media. *Phys. Rev. Lett.*, **55** 2696–2699, 1985.
- [50] M. P. VAN ALBADA AND AD LAGENDIJK. Observation of weak localization of light in a random medium. *Phys. Rev. Lett.*, **55** 2692–2695, 1985.
- [51] D. S. WIERSMA, M. P. VAN ALBADA, B. A. VAN TIGGELEN, AND AD LAGENDIJK. Experimental evidence for recurrent multiple scattering events of light in disordered media. *Phys. Rev. Lett.*, **74** 4193–4196, 1995.

- [52] G. LABEYRIE, T. KARPIUK, B. GRÉMAUD, C. MINIATURA, AND D. DELANDE. Coherent backscattering of a dilute Bose-Einstein condensate. arXiv:1206.0845, 2012.
- [53] F. JENDRZEJEWSKI, K. MÜLLER, J. RICHARD, A. DATE, T. PLISSON, P. BOUYER, A. ASPECT, AND V. JOSSE. Coherent backscattering of ultracold atoms. *Phys. Rev. Lett.*, **109** 195302, 2012.
- [54] NEVILL F. MOTT. *Metal-Insulator Transitions*. Taylor & Francis, London, UK, 1990.
- [55] A. F. IOFFE AND A. R. REGEL. Non crystalline, amorphous, and liquid electronic semiconductors. *Prog. Semicond.*, **4** 237 – 291, 1960.
- [56] E. ABRAHAMS, P. W. ANDERSON, D. C. LICCIARDELLO, AND T. V. RAMAKRISHNAN. Scaling theory of localization: Absence of quantum diffusion in two dimensions. *Phys. Rev. Lett.*, **42** 673–676, 1979.
- [57] D. J. THOULESS. Electron in disordered systems and the theory of localization. *Phys. Rep.*, **13** 93, 1974.
- [58] JØRGEN RAMMER. *Quantum Transport Theory*. Perseus Books, Reading, Mass., 1998.
- [59] B. L. ALTSHULER, D. KHMEL’NITZKII, A. I. LARKIN, AND P. A. LEE. Magnetoresistance and hall effect in a disordered two-dimensional electron gas. *Phys. Rev. B*, **22** 5142–5153, 1980.
- [60] I. L. ALEINER, B. L. ALTSHULER, AND K. B. EFETOV. Localization and critical diffusion of quantum dipoles in two dimensions. *Phys. Rev. Lett.*, **107** 076401, 2011.
- [61] B. KRAMER AND A. MACKINNON. Localization: theory and experiment. *Rep. Prog. Phys.*, **56** 1469–1564, 1993.
- [62] B. L. ALTSHULER, V. E. KRAVTSOV, AND I. V. LERNER. Statistical properties of mesoscopic fluctuations and similarity theory. *JETP Lett.*, **43** 441, 1986.
- [63] B. SHAPIRO. Probability distributions in the scaling theory of localization. *Phys. Rev. B*, **34** 4394–4397, 1986.
- [64] F. J. WEGNER. *Z. Phys. B*, **51** 279, 1983.
- [65] D. VOLLHARDT AND P. WÖLFLE. Scaling equations from a self-consistent theory of Anderson localization. *Phys. Rev. Lett.*, **48** 699–702, 1982.
- [66] E. P. WIGNER. On a class of analytic functions from the quantum theory of collisions. *Ann. Math.*, **53** 36, 1951.
- [67] K. B. EFETOV. Supersymmetry and theory of disordered metals. *Adv. Phys.*, **32** 53–127, 1983.
- [68] F. EVERS AND A. D. MIRLIN. Anderson transitions. *Rev. Mod. Phys.*, **80** 1355–1417, 2008.
- [69] ELIHU ABRAHAMS *et al.*. *50 years of Anderson Localization*. World Scientific, Singapore, 2010.
- [70] A. A. GOGOLIN, V. I. MEL’NIKOV, AND E. I. RASHBA. *Sov. Phys. JETP*, **42** 168, 1976.
- [71] A. A. GOGOLIN. *Sov. Phys. JETP*, **44** 1003, 1976.
- [72] S. AUBRY AND G. ANDRE. Analyticity breaking and Anderson localization in incommensurate lattices. *Ann. Israel Phys. Soc.*, **3** 133, 1980.

- [73] J. BELLISSARD, A. FORMOSO, R. LIMA, AND D. TESTARD. Quasiperiodic interaction with a metal-insulator transition. *Phys. Rev. B*, **26** 3024–3030, 1982.
- [74] R. JOHNSTON AND B. KRAMER. Localization in one dimensional correlated random potentials. *Z. Phys. B*, 1986.
- [75] V. BELLANI, E. DIEZ, R. HEY, L. TONI, L. TARRICONE, G. B. PARRAVICINI, F. DOMÍNGUEZ-ADAME, AND R. GÓMEZ-ALCALÁ. Experimental evidence of delocalized states in random dimer superlattices. *Phys. Rev. Lett.*, **82** 2159–2162, 1999.
- [76] U. KUHL, F. M. IZRAILEV, AND A. A. KROKHIN. Enhancement of localization in one-dimensional random potentials with long-range correlations. *Phys. Rev. Lett.*, **100** 126402, 2008.
- [77] C. FLORES. Transport in models with correlated diagonal and off-diagonal disorder. *J. Phys.: Cond. Matt.*, **1** 8471, 1989.
- [78] D. H. DUNLAP, H.-L. WU, AND P. PHILLIPS. Absence of localization in a random-dimer model. *Phys. Rev. Lett.*, **65** 88, 1990.
- [79] P. PHILLIPS AND H.-L. WU. Localization and its absence: A new metallic state for conducting polymers. *Science*, **252** 1805, 1991.
- [80] H.-L. WU AND P. PHILLIPS. Polyaniline is a random-dimer model: A new transport mechanism for conducting polymers. *Phys. Rev. Lett.*, **66** 1366, 1991.
- [81] F. M. IZRAILEV AND A. A. KROKHIN. Localization and the mobility edge in one-dimensional potentials with correlated disorder. *Phys. Rev. Lett.*, **82** 4062–4065, 1999.
- [82] L. SANCHEZ-PALENCIA, D. CLÉMENT, P. LUGAN, P. BOUYER, AND A. ASPECT. Disorder-induced trapping versus Anderson localization in Bose-Einstein condensates expanding in disordered potentials. *New J. Phys.*, **10** 045019, 2008.
- [83] F.A.B.F. DE MOURA AND M. L. LYRA. Delocalization in the 1D Anderson model with long-range correlated disorder. *Phys. Rev. Lett.*, **81** 3735, 1998.
- [84] F.A.B.F. DE MOURA AND M. L. LYRA. Correlations-induced metal-insulator transition in the one-dimensional Anderson model. *Physica A*, **266** 465, 1999.
- [85] G.-P. ZHANG AND S.-J. XIONG. Localization-delocalization transition in one-dimensional system with long-range correlated diagonal disorder. *Eur. Phys. J. B*, **29** 491, 2002.
- [86] W.-S. LIU, S. Y. LIU, AND X. L. LEI. Metal-insulator transition in two-dimensional systems with long-range correlated disorder. *Eur. Phys. J. B*, **33** 293, 2003.
- [87] F.A.B.F. DE MOURA. Absence of localization on the 2D model with long-range correlated off-diagonal disorder. *Eur. Phys. J. B*, **78** 335, 2010.
- [88] N. F. MOTT. The basis of the electron theory of metals, with special reference to the transition metals. *Proc. Phys. Soc.*, **A 62** 416, 1949.
- [89] N. F. MOTT. Metal-insulator transition. *Rev. Mod. Phys.*, **40** 677–683, 1968.
- [90] GERALD D. MAHAN. *Many-Particle Physics*. Kluwer Academic/ Plenum Publishers, 2000.
- [91] J. BARDEEN, L. N. COOPER, AND J. R. SCHRIEFFER. Theory of superconductivity. *Phys. Rev.*, **108** 1175–1204, 1957.

- [92] E. P. GROSS. Structure of a quantized vortex in boson systems. *Il Nuovo Cimento*, **20** 454–477, 1961.
- [93] L. P. PITAEVSKII. Vortex lines in an imperfect bose gas. *Sov. Phys. JETP*, **13** 451, 1961.
- [94] T. SCHWARTZ, G. BARTAL, S. FISHMAN, AND M. SEGEV. Transport and Anderson localization in disordered two-dimensional photonic lattices. *Nature (London)*, **446** 52–55, 2007.
- [95] A. S. PIKOVSKY AND D. L. SHEPELYANSKY. Destruction of Anderson localization by a weak nonlinearity. *Phys. Rev. Lett.*, **100** 094101, 2008.
- [96] S. FLACH, D. O. KRIMER, AND CH. SKOKOS. Universal spreading of wave packets in disordered nonlinear systems. *Phys. Rev. Lett.*, **102** 024101, 2009.
- [97] T. GIAMARCHI AND H. J. SCHULZ. Localization and interactions in one-dimensional quantum fluids. *Europhys. Lett.*, **3** 1287, 1987.
- [98] P. LUGAN, D. CLÉMENT, P. BOUYER, A. ASPECT, M. LEWENSTEIN, AND L. SANCHEZ-PALENCIA. Ultracold Bose gases in 1D disorder: From lifshits glass to Bose-Einstein condensate. *Phys. Rev. Lett.*, **98** 170403, 2007.
- [99] L. FONTANESI, M. WOUTERS, AND V. SAVONA. Superfluid to Bose-glass transition in a 1D weakly interacting Bose gas. *Phys. Rev. Lett.*, **103** 030403, 2009.
- [100] D.M. BASKO, I.L. ALEINER, AND B.L. ALTSHULER. Metal-insulator transition in a weakly interacting many-electron system with localized single-particle states. *Ann. Phys.*, **321** 1126, 2006.
- [101] I. L. ALEINER, B. L. ALTSHULER, AND G. V. SHLYAPNIKOV. A finite-temperature phase transition for disordered weakly interacting bosons in one dimension. *Nature Phys.*, **6** 900–904, 2010.
- [102] N. BILAS AND N. PAVLOFF. Anderson localization of elementary excitations in a one-dimensional Bose-Einstein condensate. *Eur. Phys. J. D*, **40** 387–397, 2006.
- [103] P. LUGAN, D. CLÉMENT, P. BOUYER, A. ASPECT, AND L. SANCHEZ-PALENCIA. Anderson localization of Bogolyubov quasiparticles in interacting Bose-Einstein condensates. *Phys. Rev. Lett.*, **99** 180402, 2007.
- [104] P. LUGAN AND L. SANCHEZ-PALENCIA. Localization of Bogoliubov quasiparticles in interacting Bose gases with correlated disorder. *Phys. Rev. A*, **84** 013612, 2011.
- [105] A. T. FIORY AND A. F. HEBARD. Electron mobility, conductivity, and superconductivity near the metal-insulator transition. *Phys. Rev. Lett.*, **52** 2057, 1984.
- [106] G. HERTEL, D. J. BISHOP, E. G. SPENCER, J. M. ROWELL, AND R. C. DYNES. Tunneling and transport measurements at the metal-insulator transition of amorphous nb: Si. *Phys. Rev. Lett.*, **50** 743–746, 1983.
- [107] T. F. ROSENBAUM, R. F. MILLIGAN, M. A. PAALANEN, G. A. THOMAS, R. N. BHATT, AND W. LIN. Metal-insulator transition in a doped semiconductor. *Phys. Rev. B*, **27** 7509–7523, 1983.
- [108] M. R. HAUSER, R. L. WEAVER, AND J. P. WOLFE. Internal diffraction of ultrasound in crystals: Phonon focusing at long wavelengths. *Phys. Rev. Lett.*, **68** 2604–2607, 1992.

- [109] F. SCHEFFOLD, R. LENKE, R. TWEER, AND G. MARET. Localization or classical diffusion of light? *Nature (London)*, **398** 206, 1999.
- [110] D. S. WIERSMA, J. GÓMEZ RIVAS, P. BARTOLINI, AD LAGENDIJK, AND R. RIGHINI. Reply: Localization or classical diffusion of light? *Nature (London)*, **398** 207, 1999.
- [111] A. A. CHABANOV, M. STOYTCHEV, AND A. Z. GENACK. Statistical signatures of photon localization. *Nature (London)*, **404** 850–853, 2000.
- [112] H.-J. MIESNER D. S. DURFEE D. M. KURN W. KETTERLE M. R. ANDREWS, C. G. TOWNSEND. Observation of interference between two Bose condensates. *Science*, **275** 637, 1997.
- [113] B. DEMARCO AND D. S. JIN. Onset of Fermi degeneracy in a trapped atomic gas. *Science*, **285** 1703–1706, 1999.
- [114] F. SCHRECK, L. KHAYKOVICH, K. L. CORWIN, G. FERRARI, T. BOURDEL, J. CUBIZOLLES, AND C. SALOMON. Quasipure Bose-Einstein condensate immersed in a Fermi sea. *Phys. Rev. Lett.*, **87** 4, 2001.
- [115] D. JAKSCH, C. BRUDER, J. I. CIRAC, C. W. GARDINER, AND P. ZOLLER. Cold bosonic atoms in optical lattices. *Phys. Rev. Lett.*, **81** 3108–3111, 1998.
- [116] M. GREINER, I. BLOCH, O. MANDEL, T. W. HÄNSCH, AND T. ESSLINGER. Exploring phase coherence in a 2D lattice of Bose-Einstein condensates. *Phys. Rev. Lett.*, **87** 160405, 2001.
- [117] Z. HADZIBABIC, P. KRÜGER, M. CHENEAU, B. BATTELIER, AND J. DALIBARD. Berezinskii-Kosterlitz-Thouless crossover in a trapped atomic gas. *Nature (London)*, **441** 1118–1121, 2006.
- [118] M. ANDERLINI, P. J. LEE, B. L. BROWN, J. SEBBY-STRABLEY, W. D. PHILLIPS, AND J. V. PORTO. Controlled exchange interaction between pairs of neutral atoms in an optical lattice. *Nature (London)*, **448** 452–456, 2007.
- [119] S. TROTZKY, P. CHEINET, S. FÖLLING, M. FELD, U. SCHNORRBERGER, A. M. REY, A. POLKOVNIKOV, E. A. DEMLER, M. D. LUKIN, AND I. BLOCH. Time-resolved observation and control of superexchange interactions with ultracold atoms in optical lattices. *Science*, **319** 295–299, 2008.
- [120] J. I. CIRAC AND P. ZOLLER. Goals and opportunities in quantum simulation. *Nature Phys.*, **8** 264–266, 2012.
- [121] I. BLOCH, J. DALIBARD, AND S. NASCIMBÈNE. Many-body physics with ultracold gases. *Nature Phys.*, **8** 267–276, 2012.
- [122] P. VIGNOLO, Z. AKDENIZ, AND M. P. TOSI. The transmittivity of a Bose-Einstein condensate on a lattice: interference from period doubling and the effect of disorder. *J. Phys. B: At. Mol. Opt. Phys.*, **36** 4535, 2003.
- [123] U. GAVISH AND Y. CASTIN. Matter-wave localization in disordered cold atom lattices. *Phys. Rev. Lett.*, **95** 020401, 2005.
- [124] B. PAREDES, F. VERSTRAETE, AND J. I. CIRAC. Exploiting quantum parallelism to simulate quantum random many-body systems. *Phys. Rev. Lett.*, **95** 140501, 2005.
- [125] J.-F. SCHAFF, Z. AKDENIZ, AND P. VIGNOLO. Localization-delocalization transition in the random dimer model. *Phys. Rev. A*, **81** 041604, 2010.

- [126] M. PASIENSKI AND B. DEMARCO. A high-accuracy algorithm for designing arbitrary holographic atom traps. *Opt. Express*, **16** 2176–2190, 2008.
- [127] M. WHITE, M. PASIENSKI, D. MCKAY, S. Q. ZHOU, D. CEPERLEY, AND B. DEMARCO. Strongly interacting bosons in a disordered optical lattice. *Phys. Rev. Lett.*, **102** 055301, 2009.
- [128] T. SCHUMM, J. ESTÈVE, C. FIGL, J.-B. TREBBIA, C. AUSSIBAL, H. NGUYEN, D. MAILLY, I. BOUCHOULE, C.I. WESTBROOK, AND A. ASPECT. Atom chips in the real world: the effects of wire corrugation. *Eur. Phys. J. D*, **32** 171, 2005.
- [129] B. DEISSLER, M. ZACCANTI, G. ROATI, C. D’ERRICO, M. FATTORI, M. MODUGNO, G. MODUGNO, AND M. INGUSCIO. Delocalization of a disordered bosonic system by repulsive interactions. *Nature Phys.*, **6** 354–358, 2010.
- [130] B. DEISSLER, E. LUCIONI, M. MODUGNO, G. ROATI, L. TANZI, M. ZACCANTI, M. INGUSCIO, AND G. MODUGNO. Correlation function of weakly interacting bosons in a disordered lattice. *New J. Phys.*, **13** 023020, 2011.
- [131] E. LUCIONI, B. DEISSLER, L. TANZI, G. ROATI, M. ZACCANTI, M. MODUGNO, M. LARCHER, F. DALFOVO, M. INGUSCIO, AND G. MODUGNO. Observation of subdiffusion in a disordered interacting system. *Phys. Rev. Lett.*, **106** 230403, 2011.
- [132] T. SCHULTE, S. DRENKELFORTH, J. KRUSE, W. ERTMER, J. ARLT, K. SACHA, J. ZAKRZEWSKI, AND M. LEWENSTEIN. Routes towards Anderson-like localization of Bose-Einstein condensates in disordered optical lattices. *Phys. Rev. Lett.*, **95** 170411, 2005.
- [133] J. E. LYE, L. FALLANI, M. MODUGNO, D. S. WIERSMA, C. FORT, AND M. INGUSCIO. Bose-Einstein condensate in a random potential. *Phys. Rev. Lett.*, **95** 070401, 2005.
- [134] C. FORT, L. FALLANI, V. GUARRERA, J. E. LYE, M. MODUGNO, D. S. WIERSMA, AND M. INGUSCIO. Effect of optical disorder and single defects on the expansion of a Bose-Einstein condensate in a one-dimensional waveguide. *Phys. Rev. Lett.*, **95** 170410, 2005.
- [135] D. CLÉMENT, A. F. VARÓN, M. HUGBART, J. A. RETTER, P. BOUYER, L. SANCHEZ-PALENCIA, D. M. GANGARDT, G. V. SHLYAPNIKOV, AND A. ASPECT. Suppression of transport of an interacting elongated Bose-Einstein condensate in a random potential. *Phys. Rev. Lett.*, **95** 170409, 2005.
- [136] M. PASIENSKI, D. MCKAY, M. WHITE, AND B. DEMARCO. A disordered insulator in an optical lattice. *Nature Phys.*, **6** 677–680, 2010.
- [137] D. DRIES, S. E. POLLACK, J. M. HITCHCOCK, AND R. G. HULET. Dissipative transport of a Bose-Einstein condensate. *Phys. Rev. A*, **82** 033603, 2010.
- [138] B. ALLARD, T. PLISSON, M. HOLZMANN, G. SALOMON, A. ASPECT, P. BOUYER, AND T. BOURDEL. Effect of disorder close to the superfluid transition in a two-dimensional Bose gas. *Phys. Rev. A*, **85** 033602, 2012.
- [139] M. C. BEELER, M. E. W. REED, T. HONG, AND S. L. ROLSTON. Disorder-driven loss of phase coherence in a quasi-2D cold atom system. *New J. Phys.*, **14** 073024, 2012.
- [140] B. GADWAY, D. PERTOT, J. REEVES, M. VOGT, AND D. SCHNEBLE. Glassy behavior in a binary atomic mixture. *Phys. Rev. Lett.*, **107** 145306, 2011.

- [141] S. E. SKIPETROV, A. MINGUZZI, B. A. VAN TIGGELEN, AND B. SHAPIRO. Anderson localization of a Bose-Einstein condensate in a 3D random potential. *Phys. Rev. Lett.*, **100** 165301, 2008.
- [142] J. CHABÉ, G. LEMARIÉ, B. GRÉMAUD, D. DELANDE, P. SZRIFTGISER, AND J.-C. GARREAU. Experimental observation of the Anderson metal-insulator transition with atomic matter waves. *Phys. Rev. Lett.*, **101** 255702, 2008.
- [143] G. LEMARIÉ, H. LIGNIER, D. DELANDE, P. SZRIFTGISER, AND J.-C. GARREAU. Critical state of the Anderson transition: Between a metal and an insulator. *Phys. Rev. Lett.*, **105** 090601, 2010.
- [144] M. LOPEZ, J.-F. CLÉMENT, P. SZRIFTGISER, J.-C. GARREAU, AND D. DELANDE. Experimental test of universality of the Anderson transition. *Phys. Rev. Lett.*, **108** 095701, 2012.
- [145] M. JANSSEN. Statistics and scaling in disordered mesoscopic electron systems. *Phys. Rep.*, **295** 1–91, 1998.
- [146] N. F. MOTT AND W. D. TWOSE. The theory of impurity conduction. *Adv. Phys.*, **10** 107–163, 1961.
- [147] J. T. EDWARDS AND D. J. THOULESS. *J. Phys. C: Solid State Phys.*, **5** 807, 1972.
- [148] D. VOLLHARDT AND P. WÖLFLE. Anderson localization in  $d \leq 2$  dimensions: A self-consistent diagrammatic theory. *Phys. Rev. Lett.*, **45** 842–846, 1980.
- [149] D. VOLLHARDT AND P. WÖLFLE. Diagrammatic, self-consistent treatment of the Anderson localization problem in  $d \leq 2$  dimensions. *Phys. Rev. B*, **22** 4666–4679, 1980.
- [150] M. HILLERY, R. F. O’CONNELL, M. O. SCULLY, AND E. P. WIGNER. Distribution functions in physics: Fundamentals. *Phys. Rep.*, **106** 121–167, 1984.
- [151] C. MINIATURA, R. C. KUHN, D. DELANDE, AND C. A. MÜLLER. Quantum diffusion of matter waves in 2D speckle potentials. *Eur. Phys. J. B*, **68** 353–364, 2009.
- [152] F. C. MACKINTOSH AND S. JOHN. Diffusion-wave spectroscopy and multiple scattering of light in correlated random media. *Phys. Rev. B*, **40** 2383, 1989.
- [153] P. WÖLFLE AND R. N. BHATT. Electron localization in anisotropic systems. *Phys. Rev. B*, **30** 3542–3544, 1984.
- [154] R. N. BHATT, P. WÖLFLE, AND T. V. RAMAKRISHNAN. Localization and interaction effects in anisotropic disordered electronic systems. *Phys. Rev. B*, **32** 569, 1985.
- [155] V. L. BEREZINSKII. *Sov. Phys. JETP*, **38** 620, 1974.
- [156] JOSEPH W. GOODMAN. *Speckle Phenomena in Optics: Theory and Applications*. Roberts and Co, Englewood, 2007.
- [157] F. SAFA AND P. CHAVEL. Speckle dependence on object statistics and on the point-spread function. *J. Opt. Soc. Am. A*, **6** 1835–1845.
- [158] L. LEUSHACKE AND M. KIRCHNER. Three-dimensional correlation coefficient of speckle intensity for rectangular and circular apertures. *J. Opt. Soc. Am. A*, **7** 827, 1990.
- [159] A. GATTI, D. MAGATTI, AND F. FERRI. Three-dimensional coherence of light speckles: Theory. *Phys. Rev. A*, **78** 063806, 2008.

- [160] D. MAGATTI, A. GATTI, AND F. FERRI. Three-dimensional coherence of light speckles: Experiment. *Phys. Rev. A*, **79** 053831, 2009.
- [161] D. CLÉMENT, P. BOUYER, A. ASPECT, AND L. SANCHEZ-PALENCIA. Density modulations in an elongated Bose-Einstein condensate released from a disordered potential. *Phys. Rev. A*, **77** 033631, 2008.
- [162] Y. P. CHEN, J. HITCHCOCK, D. DRIES, M. JUNKER, C. WELFORD, AND R. G. HULET. Phase coherence and superfluid-insulator transition in a disordered Bose-Einstein condensate. *Phys. Rev. A*, **77** 033632, 2008.
- [163] R. C. KUHN, C. MINIATURA, D. DELANDE, O. SIGWARTH, AND C. A. MÜLLER. Localization of matter waves in two-dimensional disordered optical potentials. *Phys. Rev. Lett.*, **95** 250403, 2005.
- [164] S. PILATI, S. GIORGINI, AND N. PROKOF'EV. Superfluid transition in a Bose gas with correlated disorder. *Phys. Rev. Lett.*, **102** 150402, 2009.
- [165] L. BEILIN, E. GUREVICH, AND B. SHAPIRO. Diffusion of cold-atomic gases in the presence of an optical speckle potential. *Phys. Rev. A*, **81** 033612, 2010.
- [166] U. BISSBORT, R. THOMALE, AND W. HOFSTETTER. Stochastic mean-field theory: Method and application to the disordered Bose-Hubbard model at finite temperature and speckle disorder. *Phys. Rev. A*, **81** 063643, 2010.
- [167] G. M. FALCO, A. A. FEDORENKO, J. GIACOMELLI, AND M. MODUGNO. Density of states in an optical speckle potential. *Phys. Rev. A*, **82** 053405, 2010.
- [168] S. PILATI, S. GIORGINI, M. MODUGNO, AND N. PROKOF'EV. Dilute Bose gas with correlated disorder: a path integral Monte Carlo study. *New J. Phys.*, **12** 073003, 2010.
- [169] A. YEDJOUR AND B. A. VAN TIGGELEN. Diffusion and localization of cold atoms in 3D optical speckle. *Eur. Phys. J. D*, **59** 249–255, 2010.
- [170] L. PEZZÉ AND L. SANCHEZ-PALENCIA. Localized and extended states in a disordered trap. *Phys. Rev. Lett.*, **106** 040601, 2011.
- [171] W. KETTERLE, D. S. DURFEE, AND D. M. STAMPER-KURN. Making, probing and understanding Bose-Einstein condensates. In *Proceedings of the International School of Physics Enrico Fermi*, 1999.
- [172] R. GRIMM, M. WEIDEMÜLLER, AND Y. B. OVCHINNIKOV. Optical dipole traps for neutral atoms. *Adv. At. Mol. Opt. Phys.*, **42** 95–170, 2000.
- [173] I. BLOCH, J. DALIBARD, AND W. ZWERGER. Quantum simulations with ultracold quantum gases. *Rev. Mod. Phys.*, **80** 885–964, 2008.
- [174] PIERRE LUGAN. *Ultracold Bose gases in random potentials: Collective excitations and localization effects*. PhD thesis, Ecole Polytechnique, Palaiseau, 2010. <http://tel.archives-ouvertes.fr/tel-00468888/en/>.
- [175] B. SHAPIRO. Expansion of a Bose-Einstein condensate in the presence of disorder. *Phys. Rev. Lett.*, **99** 060602, 2007.
- [176] CORD A. MÜLLER AND DOMINIQUE DELANDE. Disorder and interference: localization phenomena. In *Ultracold Gases and Quantum Information, C. Miniatura et al. eds., Proceedings of the Les Houches Summer School in Singapore 2009: Vol. XCI*, 2011.

- [177] P. BOUYER, J. BILLY, V. JOSSE, Z. ZUO, A. BERNARD, B. HAMBRECHT, P. LUGAN, D. CLÉMENT, L. SANCHEZ-PALENCIA, AND A. ASPECT. Anderson localization of matter waves. In *Proceedings of the XXI International Conference on Atomic Physics*, 2008.
- [178] YU. KAGAN, E. L. SURKOV, AND G. V. SHLYAPNIKOV. Evolution of a Bose-condensed gas under variations of the confining potential. *Phys. Rev. A*, **54** 1753(R), 1996.
- [179] Y. CASTIN AND R. DUM. Bose-Einstein condensates in time dependent traps. *Phys. Rev. Lett.*, **77** 5315, 1996.
- [180] WILLIAM H. PRESS, SAUL A. TEUKOLSKY, WILLIAM T. VETTERLING, AND BRIAN P. FLANNERY. *Numerical Recipes, 3rd Edition*. Cambridge University Press, Cambridge, 2007.
- [181] G. KOPIDAKIS, S. KOMINEAS, S. FLACH, AND S. AUBRY. Absence of wave packet diffusion in disordered nonlinear systems. *Phys. Rev. Lett.*, **100** 084103, 2008.
- [182] S. PALPACELLI AND S. SUCCI. Quantum lattice boltzmann simulation of expanding Bose-Einstein condensates in random potentials. *Phys. Rev. E*, **77** 066708, 2008.
- [183] M. V. IVANCHENKO, T. V. LAPTYEVA, AND S. FLACH. Anderson localization or nonlinear waves: A matter of probability. *Phys. Rev. Lett.*, **107** 240602, 2011.
- [184] R. E. BORLAND. The nature of the electronic states in disordered one-dimensional systems. *Proc. Roy. Soc. A: Math. Phys. Eng. Sci.*, **274** 529–545, 1963.
- [185] N. CHERRORET, T. KARPIUK, C. A. MÜLLER, B. GRÉMAUD, AND C. MINIATURA. Coherent backscattering of ultracold matter waves: Momentum space signatures. *Phys. Rev. A*, **85** 011604, 2012.
- [186] M. PŁODZIEŃ AND K. SACHA. Matter-wave analog of an optical random laser. *Phys. Rev. A*, **84** 023624, 2011.
- [187] ALEKSEI A. ABRIKOSOV, LEV P. GOR'KOV, AND IGOR E. DZIALOSHINSKII. *Methods of Quantum Field Theory in Statistical Physics*. Dover Publications, New York, 1975.
- [188] SYDNEY CHAPMAN AND THOMAS G. COWLING. *The Mathematical Theory of Non-uniform Gases*. Cambridge Mathematical Library, 1991.
- [189] S. HIKAMI. Anderson localization in a nonlinear- $\sigma$ -model representation. *Phys. Rev. B*, **24** 2671–2679, 1981.
- [190] T. PLISSON, B. ALLARD, M. HOLZMANN, G. SALOMON, A. ASPECT, P. BOUYER, AND T. BOURDEL. Coherence properties of a two-dimensional trapped Bose gas around the superfluid transition. *Phys. Rev. A*, **84** 061606, 2011.
- [191] B. C. KAAS, B. A. VAN TIGGELEN, AND AD LAGENDIJK. Anisotropy and interference in wave transport: An analytic theory. *Phys. Rev. Lett.*, **100** 123902, 2008.
- [192] B. A. VAN TIGGELEN, R. MAYNARD, AND A. HEIDERICH. Anisotropic light diffusion in oriented nematic liquid crystals. *Phys. Rev. Lett.*, **77** 639–642, 1996.
- [193] H. STARK AND T. C. LUBENSKY. Multiple light scattering in anisotropic random media. *Phys. Rev. E*, **55** 514–533, 1997.
- [194] U. KUHL, F. M. IZRAILEV, A. A. KROKHIN, AND H.-J. STÖCKMANN. Experimental observation of the mobility edge in a waveguide with correlated disorder. *Appl. Phys. Lett.*, **77** 633, 2000.

- [195] P. BARTHELEMY, J. BERTOLOTTI, AND D. S. WIERSMA. A Lévy flight for light. *Nature (London)*, **453** 495–498, 2008.
- [196] J. KROHA, T. KOPP, AND P. WÖLFLE. Self-consistent theory of Anderson localization for the tight-binding model with site-diagonal disorder. *Phys. Rev. B*, **41** 888–891, 1990.
- [197] K. SLEVIN AND T. OHTSUKI. Corrections to scaling at the Anderson transition. *Phys. Rev. Lett.*, **82** 382–385, 1999.
- [198] B. SHKLOVSKII. Superfluid-insulator transition in dirty ultracold Fermi gas. *Semiconductors*, **42** 909–913, 2008.
- [199] L. FALLANI, C. FORT, AND M. INGUSCIO. Bose-Einstein condensates in disordered potentials. *Adv. At. Mol. Opt. Phys.*, **56** 119–160, 2008.
- [200] G. MODUGNO. Anderson localization in Bose-Einstein condensates. *Rep. Prog. Phys.*, **73** 102401, 2010.
- [201] T. PAUL, P. SCHLAGHECK, P. LEBOEUF, AND N. PAVLOFF. Superfluidity versus Anderson localization in a dilute Bose gas. *Phys. Rev. Lett.*, **98** 210602, 2007.
- [202] T. PAUL, M. ALBERT, P. SCHLAGHECK, P. LEBOEUF, AND N. PAVLOFF. Anderson localization of a weakly interacting one-dimensional Bose gas. *Phys. Rev. A*, **80** 033615, 2009.
- [203] L. FALLANI, J. E. LYE, V. GUARRERA, C. FORT, AND M. INGUSCIO. Ultracold atoms in a disordered crystal of light: Towards a Bose glass. *Phys. Rev. Lett.*, **98** 130404, 2007.
- [204] FRED JENDRZEJEWSKI. *Quantum transport of ultracold atoms in disordered potentials*. PhD thesis, Université Paris-Sud XI, Palaiseau, 2012.
- [205] B. DEMARCO. private communication.
- [206] DAVID J. THOULESS. Percolation and localization. In R. Balian, R. Maynard, and G. Toulouse, editors, *III-condensed Matter*, pages 1–62. North-Holland, 1979.
- [207] M. KAPPUS AND F. WEGNER. Anomaly in the band centre of the one-dimensional Anderson model. *Z. Phys. B*, **45** 15–21, 1981.
- [208] N. P. ROBINS, C. FIGL, S. A. HAINE, A. K. MORRISON, M. JEPPESEN, J. J. HOPE, AND J. D. CLOSE. Achieving peak brightness in an atom laser. *Phys. Rev. Lett.*, **96** 140403, 2006.
- [209] W. GUERIN, J.-F. RIOU, J. P. GAEBLER, V. JOSSE, P. BOUYER, AND A. ASPECT. Guided quasicontinuous atom laser. *Phys. Rev. Lett.*, **97** 200402, 2006.
- [210] A. BERNARD, W. GUERIN, J. BILLY, F. JENDRZEJEWSKI, P. CHEINET, A. ASPECT, V. JOSSE, AND P. BOUYER. Quasi-continuous horizontally guided atom laser: coupling spectrum and flux limits. *New J. Phys.*, **13** 065015, 2011.
- [211] R. ZALLEN AND H. SCHER. Percolation on a continuum and the localization-delocalization transition in amorphous semiconductors. *Phys. Rev. B*, **4** 4471–4479, 1971.
- [212] I. S. GRADSHTEYN AND I. M. RYZHIK. *Table of Integral, Series, and Products*. Academic Press, London, 1980.
- [213] YU. N. BARABANENKOV AND V. D. OZRIN. Asymptotic solution of the Bethe-Salpeter equation and the Green-Kubo formula for the diffusion constant for wave propagation in random media. *Phys. Lett. A*, **154** 38, 1991.

- 
- [214] YU. N. BARABANENKOV AND V. D. OZRIN. Diffusion asymptotics of the Bethe-Salpeter equation for electromagnetic waves in discrete random media. *Phys. Lett. A*, **206** 116, 1995.





## Résumé

Ce mémoire présente une étude du transport quantique et de la localisation d'Anderson d'ondes de matière sans interaction dans des désordres anisotropes. À l'aide d'approches microscopiques, nous étudions l'effet des corrélations du désordre dont nous démontrons qu'elles peuvent considérablement modifier les propriétés du transport quantique à 1D, 2D et 3D. Nous développons des outils généraux et les appliquons à des modèles de désordre continu pertinents pour les expériences d'atomes ultrafroids : les potentiels de tavelures optiques (« speckle »). Dans un premier temps, à une dimension, nous raffinons les précédents modèles du processus de localisation d'un nuage d'atomes froids en expansion dans un potentiel de speckle usuel, et nous montrons que la prise en compte de nouveaux éléments devrait permettre d'expliquer les écarts entre les résultats expérimentaux et théoriques observés précédemment. Nous étudions ensuite le transport quantique et la localisation d'Anderson en dimensions supérieures, plus particulièrement dans des désordres aux corrélations anisotropes, ce qui est naturellement le cas dans la plupart des potentiels de speckle. Nous calculons les propriétés de transport quantique et proposons une nouvelle méthode pour estimer la position du seuil de localisation à 3D (seuil de mobilité). Nos prédictions théoriques sont ensuite comparées aux résultats obtenus par deux expériences récentes ayant observé la localisation tri-dimensionnelle d'ondes de matière. Enfin, nous approfondissons notre étude des effets des corrélations du désordre. Nous démontrons qu'elles peuvent induire l'inversion des anisotropies de localisation et une amplification de la localisation d'Anderson avec l'énergie de la particule, lorsqu'elles sont judicieusement adaptées.

## Abstract

In this thesis we investigate quantum transport and Anderson localization of non-interacting matterwaves in anisotropic disorder. Using microscopic approaches, we study the effect of disorder correlations, which are shown to significantly modify quantum transport properties in 1D, 2D and 3D. We develop general theoretical tools and apply them to particular models of continuous disorder, which are relevant to ultracold atom experiments: speckle potentials. First, in the one-dimensional case we extend previous models for the localization process of ultracold atoms expanding in a standard speckle potential and show that taking into account new ingredients could permit to understand deviations between experiments and theory observed previously. We then study quantum transport and Anderson localization in dimensions higher than one, with special emphasis on anisotropic correlations, which are naturally present in most speckle potentials. We compute quantum transport properties and propose a new method to estimate the 3D localization threshold (mobility edge). Our theoretical findings are compared with the results of two recent experiments which report evidence of 3D localization of matterwaves. Eventually, we further study effects of disorder correlations, which can induce inversion of localization anisotropies and enhancement of Anderson localization with the particle energy, when appropriately tailored.